INFORMATION TO USERS

This manuscript has been reproduced from the microfilm master. UMI films the text directly from the original or copy submitted. Thus, some thesis and dissertation copies are in typewriter face, while others may be from any type of computer printer.

The quality of this reproduction is dependent upon the quality of the copy submitted. Broken or indistinct print, colored or poor quality illustrations and photographs, print bleedthrough, substandard margins, and improper alignment can adversely affect reproduction.

In the unlikely event that the author did not send UMI a complete manuscript and there are missing pages, these will be noted. Also, if unauthorized copyright material had to be removed, a note will indicate the deletion.

Oversize materials (e.g., maps, drawings, charts) are reproduced by sectioning the original, beginning at the upper left-hand corner and continuing from left to right in equal sections with small overlaps.

Photographs included in the original manuscript have been reproduced xerographically in this copy. Higher quality 6" x 9" black and white photographic prints are available for any photographs or illustrations appearing in this copy for an additional charge. Contact UMI directly to order.

Bell & Howell Information and Learning
300 North Zeeb Road, Ann Arbor, MI 48106-1346 USA

UMI®
800-521-0600

DAMAGE IN MMCS

AND

ITS ROLE IN MICROSTRUCTURAL DESIGN

By

DENIS LAHAIE, B. Sc., M. Eng.

A Thesis

Submitted to the School of Graduate Studies

in Partial Fulfillment of the Requirements

for the Degree

Doctor of Philosophy

McMaster University

DAMAGE IN MMCS AND ITS ROLE IN MICROSTRUCTURAL DESIGN

DOCTOR OF PHILOSOPHY
(Materials Science and Engineering)

McMASTER UNIVERSITY
Hamilton, Ontario

TITLE:	Damage in MMCs and its role in microstructural design
AUTHOR:	Denis J. G. Lahaie, B.Sc., M. Eng. (McMaster University)
SUPERVISOR:	Professor J.D. Embury
NUMBER OF PAGES:	xiv,240

ABSTRACT

Metal-matrix composites (MMCs) have potential as load bearing components for particular functional requirements. However, MMCs are more difficult to form than conventional metals and alloys due to the tendency of suffering microstructural damage at low plastic strains. It is thus of importance to understand the forms of microstructural damage, its level and spatial distribution.

In this work, three main areas of investigation related to damage accumulation in MMCs were considered: the hydrostatic extrusion of MMCs, a theoretical investigation of scale effects in MMCs and plane strain compression experiments on model composites to study load transfer and fibre distribution effects on the patterns of plastic flow in the matrix.

In the experiments on the hydrostatic extrusion of particulate MMCs, it was found that damage occurred in the form of reinforcement cracking, that the amount of damage varied linearly with applied plastic strain and that the rate of damage accumulation depended on the morphology of the reinforcement. The extrusion process was examined in regard to its ability to limit or suppress damage through the action of high compressive hydrostatic pressures. A slip-line field analysis was adopted to relate the effect of process parameters such as the amount of reduction and die angle to the magnitude and distribution of hydrostatic pressure in the extrusion dies. The linear relationship between damage and applied plastic strain was explained using a micro-mechanical description of the response of MMCs to plastic flow and the effect of microstructural variables such as volume fraction, shape and size of the reinforcement on the rate of damage accumulation was discussed. In addition, the tensile properties of MMCs subsequent to hydrostatic extrusion were quantified and the effect of previous extrusion was described in terms of the strain hardening of the matrix materials and the damage accumulation in the reinforcement materials and their influence on the stability of the plastic flow process.

In the work on plane strain compression of model composites, the effect of reinforcement distribution on the pattern of flow in Cu-W MMCs was described using maps of equivalent strain obtained from the analysis of deformed surface grids. The level and distribution of strain was found to be related to the spatial distribution of the reinforcements. The fiber distribution also influenced the efficiency of the fibers as obstacles to macroscopic flow. Comparison of the results with numerical analyses allowed a link to be established between the observed damage mechanism of decohesion and the state of stress and local strain level in the composite. An optical method was used to get information on the load transfer process in a Cu-sapphire MMC plastically deformed in plane strain compression. The fracture of the sapphire fiber was related to the measured stress state.

In the theoretical analysis of scale effects in MMCs, scale dependent bounds on strength were developed and scale dependent composite design charts were constructed. The results highlighted the importance of the scale of the reinforcement in MMC design, as well as the importance of the processing route to fabricate MMCs on a fine scale.

The conclusions of the various areas of investigation demonstrated how damage in MMCs links together issues of process design, microstructural optimization and resultant mechanical properties of MMCs.

ACKNOWLEDGEMENTS

I would like to thank Prof. J.D. Embury for his unfailing guidance as a supervisor during my graduate studies. I would also like to acknowledge the contributions made by Prof. D.S. Wilkinson and Prof. J.D. Preston in seeing this work to fruition. In addition, thanks are due to NSERC for its financial support of this work.

Many people were involved with the various investigations of this work. I would like to thank Prof. F. Zok and Dr. M. Kiser for their help with the work on extrusion of MMCs and their hospitality during my frequent stays at UCSB. I would also like to thank Prof. M.F. Ashby for his helpful guidance for the work on scale effects in MMCs and Prof. R. Sowerby for his guidance with the slip-line field analysis. I would also like to express my sincere thanks to Mr. J. Garrett and Mr. B. Collier for their invaluable help in making model composites. I would also like to acknowledge the help provided by Mr. C. Butcher and Mrs. T. Castillo for various aspects of metallographic analysis and Mr. Y. Meng for his help with electron beam lithography. Further, I would like to extend my appreciation to Mr. G. Timmins for his work with Raman spectroscopy.

Special acknowledgement should be given to Mr. J. Berardine for the development of the digitizing software used in the analysis of deformed fiducial grids.

I would also like to mention the invaluable help of both the staff and graduate student body of the Materials Science and Engineering department. Their contribution as a whole was of great importance, both professionally and personally, and I regret not being able to acknowledge everyone by name in this limited space. I would finally like to thank my family and friends for their much needed support throughout the years.

TABLE OF CONTENTS

LIST OF FIGURES

LIST OF TABLES

CHAPTER 1

INTRODUCTION

Composites are materials in which two or more phases are combined, usually with strong interfaces between them. They usually consist of a continuous phase called the matrix and a discontinuous phase in the form of fibers, whiskers or particles called the reinforcement. Considerable interest in composites has been generated in the past because many of their properties can be described by a combination of the individual properties of the constituent phases and their volume fraction in the mixture. This type of simple description of a composite property is termed a law of mixtures. By varying the constituent materials and/or the volume fraction they occupy in the composite, a measure of control over the resultant properties is gained. This has obvious benefits for the design of components. Ideally, composites can be produced to suit particular functional requirements, such as high specific stiffness (ratio of stiffness to density) or high specific strength (ratio of strength to density) for aerospace applications. Thus, the link between the structure of a composite and its properties is a useful tool for materials selection in relation to composite design.

Metal matrix composites (MMCs) are materials that consist of a metallic continuous phase reinforced with a second phase, which usually consists of ceramic particles or strong fibers. The interest in MMCs is due to the relation of structure to properties discussed above and the potential that this implies to produce materials with improved properties such as specific stiffness or specific strength. Ideally, MMCs could be created to combine the advantageous properties of metals, namely ductility and the ability to be formed at high strains, toughness and strength, with some attractive properties of ceramics or strong fibers such as stiffness, density, wear resistance, creep resistance or oxidation resistance. It is this potential benefit in resultant properties which has driven much of the research on MMCs.

However, the potential of tailoring the structure of MMCs for improvements in materials properties has been limited in some instances by the processing routes used to fabricate them. The traditional fabrication routes of liquid phase processing and powder processing have inherent problems in terms of the structural defects they produce as well as the scale of the structure produced. The liquid phase processes involve mixing of the reinforcements with liquid metals. This procedure can lead to various defects in the composite microstructure such as porosity in the matrix, inhomogenous distributions of reinforcements and interfacial problems related to adhesion or chemical reactions. The liquid phase processes also tend to produce metallic matrices with large grains, thus adversely affecting the strength of the metal. The powder processing routes suffer from problems with impurities at grain boundaries due to the large surface areas of metallic powders and from problems of poor bonding at the reinforcement/matrix interfaces. Further, in both these processes, it is difficult and expensive to make complex shapes. This is in sharp contrast to the well established processes in the metals industry. For the production of metals and alloys, many of the problems associated with primary processing steps involving liquids can be rectified in the secondary processes involving solid state forming operations. For instance, gas porosity can be reduced by plastic deformation, grain sizes can be reduced by recrystallisation heat treatments and complex shapes can be produced cheaply. For this reason, there is interest in using these secondary processes to form MMCs, but the challenges involved in applying these is considerable. Typically, MMCs are much less able to tolerate large plastic deformations than conventional metals or alloys. Unless parameters of the forming operation are tightly controlled, the strains will damage the composite structure. The damage is usually described in terms of the loss in load bearing area of the composite and the degradation of mechanical properties that this entails.

In view of its effect on the mechanical properties of MMCs, it is important to be able to understand various issues related to the processes of damage nucleation and evolution in plastically

deforming MMCs. Of primary interest are the forms in which damage may occur, its level and spatial distribution. Typical damage mechanisms include matrix/reinforcement decohesion and reinforcement fracture. For each mechanism, an understanding is needed of the parameters that govern the initiation and growth of damage. The identification of these parameters would be of great help in identifying possible schemes to suppress or limit damage during secondary processing of MMCs. These schemes may involve altering process parameters or microstructural parameters. Further, in the event that damage cannot be suppressed entirely during forming, it is of great importance to develop a basis for its effect on subsequent mechanical performance. The modeling and design of MMC components depends on reliable physical descriptions of the mechanical response of damaged MMCs.

The issues related to damage in MMCs described above are central to the present work. Three main areas of investigation related to damage accumulation in MMCs were considered. The first topic of research dealt with the hydrostatic extrusion of MMCs. In this work, four composites were extruded: a composite of Cu reinforced with continuous W fibers and three particulate metal matrix composites (pMMCs). The matrices of the pMMCs were Al based alloys A356 and 6061 and the three composites tested were A356 reinforced with 10% by volume SiC particles, A356 reinforced with 20% by volume SiC particles and 6061 reinforced with 20% by volume CMS (ceramic microspheres). The second part of this investigation was involved with plane strain compression experiments of model composite systems. Two model composites were tested, the Cu-W system described above and a composite of Cu reinforced with continuous single crystal sapphire fibers. The last area of interest in this thesis was a theoretical investigation of scale effects in MMCs. It was the aim of this work to link the results of these investigations to the central issue of damage in MMCs. The specific objectives for each area of investigation will be discussed in turn.

It was found that the hydrostatic extrusion process created damage in the microstructures of the composites investigated. Thus, one of the objectives of the work on hydrostatic extrusion was to measure the level of damage created and to relate this to various process and microstructural parameters. The process parameters of die angle and reduction were examined in terms of their effect on the stress state in the die during the deformation of the MMCs. In particular, the effect of the hydrostatic pressure component of the stress state was related to the nucleation and growth of damage. The microstructural parameters of reinforcement volume fraction, reinforcement size and reinforcement shape were also considered for their effect on the level and rate of damage with applied plastic strain by extrusion. Further, tensile testing of the extruded composites was conducted in order to clarify the effects of damage on the mechanical properties of MMCs. The effect of the damage created during the extrusion process on the stiffness, strength, work hardening characteristics and tensile instabilities was investigated.

The work on extrusion described above considered the global response of MMCs to plastic deformation. The investigation of model systems in plane strain had as an objective to obtain knowledge of the pattern of flow of the Cu matrix near W fibers. This was done both in terms of the level of strain and its distribution. Comparisons of the flow patterns for various fibre distributions were made and related to the constraints exerted by the reinforcements to the macroscopic direction of plastic flow. In addition, where possible, the patterns of flow observed for the various fibre distributions were compared to experimental and numerical results in the literature. Thus, the experimentally determined strain patterns were related to numerical solutions for the distribution of stresses near the W fibers. From these, a basis was developed to explain the observed damage mechanism of interfacial decohesion in terms of the location and magnitude of interfacial stresses.

The second part of the work on plane strain deformation of model composites was undertaken to complement the results on the patterns of flow in the matrix with some information on the load

transfer to the fibers. This was made possible by an optical technique to measure stresses in chromium doped sapphire single crystals. Using this technique, the residual stresses in a sapphire fibre embedded in a Cu matrix were measured after plane strain compression experiments. The information on the stress state in the fibre due the flow of the matrix was related to the onset of fracture of the reinforcement. The use of this technique can be included in the broader context of understanding how plastic flow in MMCs leads to damage.

The last area of interest of this thesis was a theoretical analysis of the effect of scale on the mechanical properties of MMCs. In this work, scaling laws for several combinations of matrix and reinforcement materials were incorporated into bounds for composite strength. The results were presented in the form of scale dependent composite design charts. The implications of this work for the relationship between the processing route chosen for the composite and its subsequent properties were emphasized, as well as the link between reinforcement size and damage in MMCs.

CHAPTER 2

LITERATURE REVIEW

In reviewing the literature relating to metal matrix composites, it is important to recognize that this topic has been subject to great scrutiny in the past two decades and a number of comprehensive texts (Clyne and Withers, 1995, Chawla, 1987 and Taya and Arsenault, 1989) are available on this topic. Thus, in presenting a review of the literature, it is appropriate to focus attention on the basic themes which link the work presented in the current thesis. Much of the analysis of the micromechanics of composites assumes that the resultant properties reflect the intrinsic properties of the constituents and their volume fractions. However, there is much evidence to suggest that the scale of the constituents is an important variable to be considered and some attention is given to this both in the literature review and the analysis presented in the thesis.

An important relationship in any material system is that of the relationship of properties not only to structure but to processing. In much of the work in the literature, metal matrix composites have been fabricated either by powder techniques or by liquid phase processes such as infiltration and casting. These techniques have some intrinsic drawbacks in terms of defects and scale of reinforcements. Thus it would be of value to be able to process MMCs in the solid state by conventional forming processes. However, this approach is limited by the occurrence of damage in MMCs at relatively modest strains. Thus, attention must be paid both to the quantification of damage and to incorporation into constitutive descriptions of the plasticity of MMCs. This requires careful quantitative experimentation and consideration of damage in relation to the load bearing capacity, stability and fracture of MMCs. These aspects are considered in terms of the current literature.

Finally, the incorporation of damage into plasticity descriptions is related to the analysis and design of forming operations for MMCs and this is explained in the current work in relation to the utilisation of hydrostatic extrusion. Thus, the aspects of the literature presented here do not seek to give a broad overview of the topic but to give the appropriate background for the related topics which are linked together in the fabric of this thesis.

2.1 BASIC COMPOSITE PROPERTIES

One of the basic problems for composite materials is to predict the resultant properties in terms of the properties of their constituents. To illustrate this concept, we will consider an aligned continuous fibre composite, as shown in figure 2.1. An important material property for structural materials is stiffness. It is thus of importance to find the Young's Modulus of the composite in the axial and transverse directions defined in figure 2.1. In the axial direction parallel to the fibres, we can find the elastic modulus by noticing that the two phases must have the same strain for compability requirements to be satisfied. By simple manipulation and use of Hooke's Law, the axial composite stiffness E_3 is given by

$$E_3 = (1-f)E_M + fE_f \qquad \text{eq. (2.1)}$$

where E_M and E_f are the matrix and reinforcement stiffness respectively and f is the volume fraction of the fiber. If the calculation is done in the transverse direction, where it is assumed that the stresses are equal in each phase, the following transverse stiffness E_2 is obtained

$$E_2 = \frac{E_f E_M}{E_M f + (1-f)E_f} \qquad \text{eq. (2.2)}$$

where the variables have been defined above. Note that equation 2.2 will also apply to the other transverse direction, thus $E_1=E_2$. The first point to be made from these results is that, from equation 2.1 and 2.2, for a reinforcement phase that is stiffer than the matrix, the reinforcement imparts stiffness to

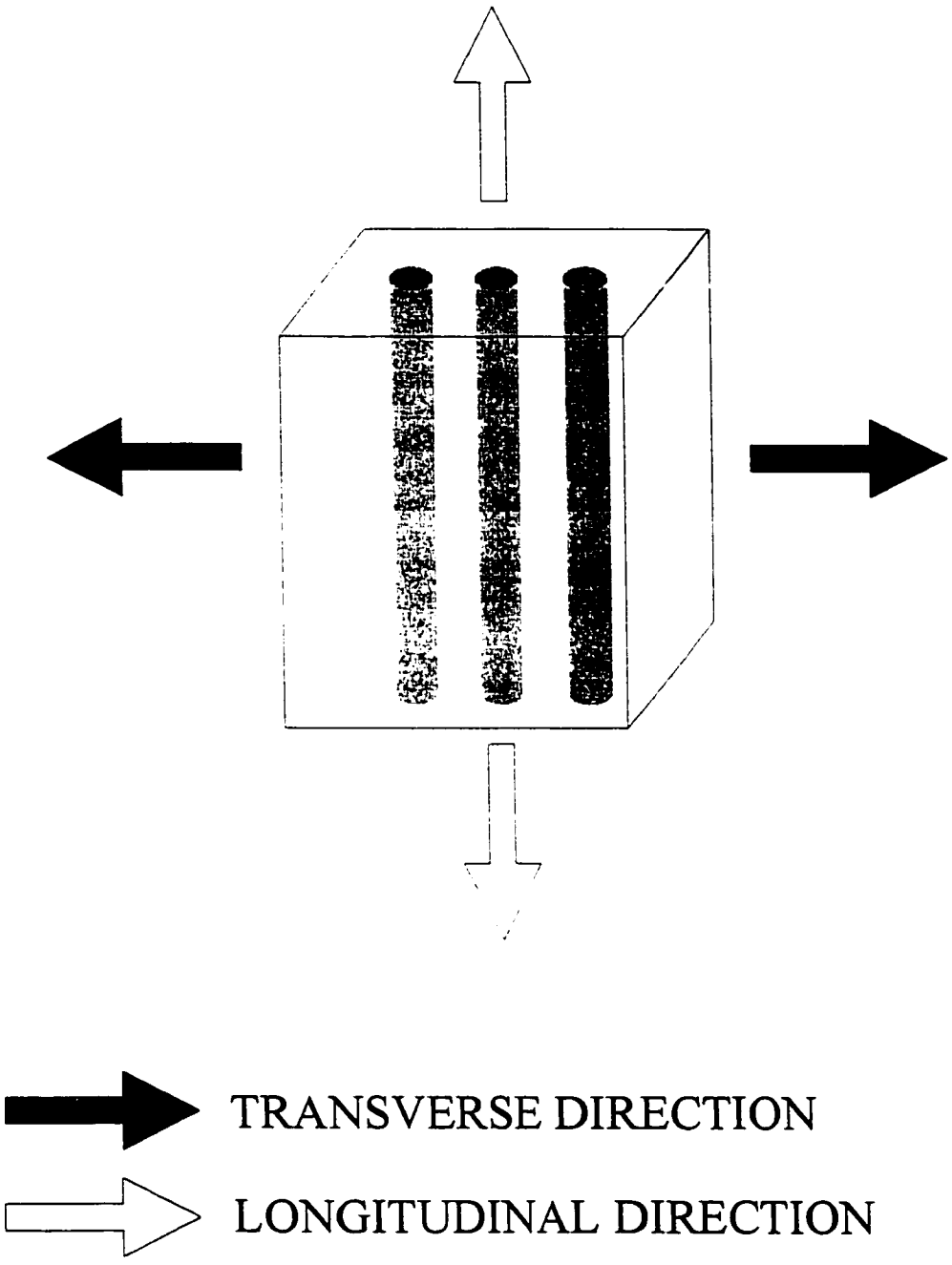

Figure 2.1 Schematic diagram of a continuous fibre composite.

the mixture. This is consistent with experimental results. It is also to be noted that these equations are functions of the intrinsic variables of the constituents only. This is why eq. 2.1 is often referred to as the Rule of Mixtures. It is also called the Voigt relationship (Voigt, 1910). The equal stress model for transverse stiffness is also called the Reuss relationship (Reuss, 1929).

The Rule of Mixtures or Voigt approach is a good approximation for aligned fibre composites where the equal strain condition is approached. However, the Reuss model for transverse stiffness is not a good approximation for aligned fibre composites because the equal stress condition is not satisfied. Although it uses an empirical parameter, a more accurate description for the transverse stiffness is given by the Halpin-Tsai equation

$$E_2 = \left(\frac{E_M (1+\xi\eta f)}{1-\eta f} \right) \qquad \text{eq. (2.3)}$$

where

$$\eta = \left(\frac{E_1/E_M - 1}{E_1/E_M + \xi} \right) \qquad \text{eq. (2.4)}$$

and ξ is the adjustable parameter. Its value is usually of the order of unity.

When the reinforcement phase is not continuous, the Rule of Mixtures approach becomes less accurate due to the invalidity of the constant strain condition. A more accurate model for particulate reinforced composites was adapted from the rigorous treatment by Eshelby (1957) for an isolated ellipsoidal particle. The procedure involved consists of a series of imaginary cutting and welding exercises on the ellipsoidal inclusion. These exercises effectively replace the real inclusion by one made of matrix material which will be equivalent to the real one in terms of the stress field it produces in itself and the matrix. If the effect of other particles is included through an average background stress due to their overlapping stress fields (Pederson, 1983), the composite stiffness tensor C_c is given by

$$C_c = \left[\left[C_M^{-1} - f\left\{(C_I - C_M)\left[S - f((S-I)\right] + C_M\right\}^{-1}(C_I - C_M)C_M^{-1}\right]\right] \qquad \text{eq. (2.5)}$$

where C_M and C_I are the matrix and reinforcement stiffness tensor respectively, f is the volume fraction of the reinforcement and S is the Eshelby tensor. The S tensor is a function of the shape of the particles and thus, the composite stiffness in this model cannot be specified by knowledge of extrinsic component properties only.

The Eshelby model solves for the entire stiffness tensor, if the complete Eshelby tensor is known. This wide applicability has made this method attractive for modeling fibre reinforcements. However, the Eshelby approach requires that the Brown and Clarke (1975) approximation for fibres by elongated ellipsoids be used. It is assumed in these calculations that the stress field at the end of the fibres is similar to the one generated at the end of the model ellipsoid. This has been verified by comparing the Eshelby result to numerical modeling by FEM (finite element method) (Withers et al., 1992). The results are shown in figure 2.2.

With the use of the Eshelby stress fields, the load transfer process from the matrix to the fibre can be quantified. Since load is shed from the matrix, the general yield strength $\sigma^{\wedge}$ of the composite is increased and is given by

$$\sigma^{\wedge} = \sigma_{YM} - \left(\langle\sigma_3\rangle_M^{\wedge} - \langle\sigma_1\rangle_M^{\wedge}\right) \qquad \text{eq. (2.6)}$$

where σ_{YM} is the intrinsic flow stress of the matrix and $\langle\sigma_i\rangle_M^{\wedge}$ are the two principal mean matrix stresses, which are given by

$$\langle\sigma\rangle_M^{\wedge} = -f\,C_M(S-I)\left\{(C_M - C_I)\left[S - f(S-I)\right] - C_M\right\}^{-1}(C_I - C_M)C_M^{-1}\sigma^{\wedge} \qquad \text{eq. (2.7)}$$

where the variables have been defined above. A balance of stresses gives the inclusion stress $\langle\sigma\rangle_I$

$$\langle\sigma\rangle_I = \frac{-(1-f)\langle\sigma\rangle_M}{f} \qquad \text{eq. (2.8)}$$

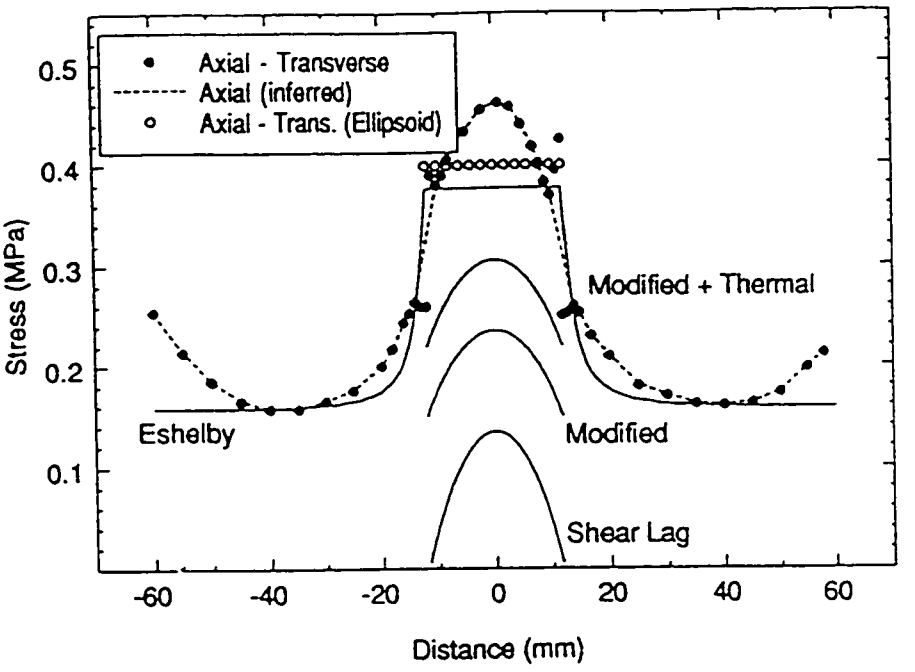

Figure 2.2 Comparison of the stress distribution at a fibre end by FEM with the result of the Eshelby model for an ellipsoidal particle. (from Withers et al., 1992)

This analysis only considers global yielding of the matrix and not the microyielding process near the reinforcements. It also assumes that there is no work hardening in the matrix.

The shear lag model proposed by Cox (1952) gives insight into the microyield process as well as the load transfer process. The mechanism for load transfer in this model assumes that the tensile stress in the fibre is built up from the fibre ends by shear stresses at the interface, so that, in essence, the tensile stress lags behind the shear stress. A force balance at the interface leads to a second order linear differential equation which can be solved for the axial stress in the fibre σ_1 and the shear stress along the fibre τ_1

$$\sigma_1 = E_1 \varepsilon_{3C}\left[1 - \cosh(nz/r_o)\operatorname{sech}(ns)\right] \qquad \text{eq. (2.9)}$$

$$\tau_1 = \frac{n\varepsilon_{3C}}{2} E_1 \sinh(nz/r_o)\operatorname{sech}(ns) \qquad \text{eq. (2.10)}$$

where E_1 is the stiffness of the reinforcement, ε_{3C} is the total strain of the composite in the direction parallel to the length of the fibre, z is the axial distance from the fibre mid-point, r_o is the radius of the fibre, s is the aspect ratio of the fibre defined as the axial half length L divided by r_o and n is a constant defined by

$$n = \left[\frac{2E_M}{E_1(1+\nu_M)\ln(1/f)}\right]^{1/2} \qquad \text{eq. (2.11)}$$

where ν_M is the Poisson's ratio of the matrix. These results are derived by assuming that the axial stress is zero at the fibre ends. To account for transfer of normal stress accross the ends, equation 2.9 is modified and becomes

$$\sigma_1 = \varepsilon_{3C}\left[E_1 - (E_1 - E_M^*)\cosh(nz/r_o)\operatorname{sech}(ns)\right] \qquad \text{eq. (2.12)}$$

where E_M^* is defined as

$$E_M^{\bullet} = \frac{E_f\left[1-\operatorname{sech}(ns)\right]+E_M}{2} \qquad \text{eq. (2.13)}$$

Equations 2.10 and 2.12 show that the axial stress in the fibre increases from the end to the mid-point and that the shear stress at the interface decreases over the same length. This is illustrated schematically on figure 2.3. From this distribution of stresses near a fibre, it is readily observed that matrix yielding will first occur at the fibre ends where the shear stresses are the highest. For a critical matrix yield stress $\tau_i^{\bullet}$. microyield is shown to occur at an applied stress $\sigma_3^{\wedge}$ given by

$$\sigma_3^{\wedge} = \frac{2\tau_i^{\bullet}}{nE_f}\left\{\left[fE_f+(1-f)E_M\right]\coth(ns)-\frac{fE_f}{ns}\right\} \qquad \text{eq. (2.14)}$$

where the variables have been defined previously. Yielding will proceed from the fibre ends and eventually global flow will occur.

The shear lag model also gives information on possible fracture events occuring within the fibre due to load transfer. It has been shown from equation 2.12 that the axial stresses build up from the fibre ends and reach a maximum in the central region. By doing a force balance, the critical length of fibre needed to build up the load to this maximum is found to depend on the strength of the interface $\tau_i^{\bullet}$ and the ultimate strength of the fibre $\sigma_f^{\bullet}$. It is called the critical aspect ratio $S_{\bullet}$ (Clyne and Withers, 1995) and is given by

$$S_{\bullet} = \frac{\sigma_f^{\bullet}}{2\tau_i^{\bullet}} \qquad \text{eq. (2.15)}$$

This critical aspect ratio is a measure of the minimum length of fibre needed to cause a fracture event. It is also a measure of the minimum length for effective load transfer.

We have now discussed the basic ideas of the resultant properties of multiple phases mixed in intimate contact. With the use of simple models, it has been shown how such mixing can produce composite materials with desirable properties. These simple models have also been shown to be of use

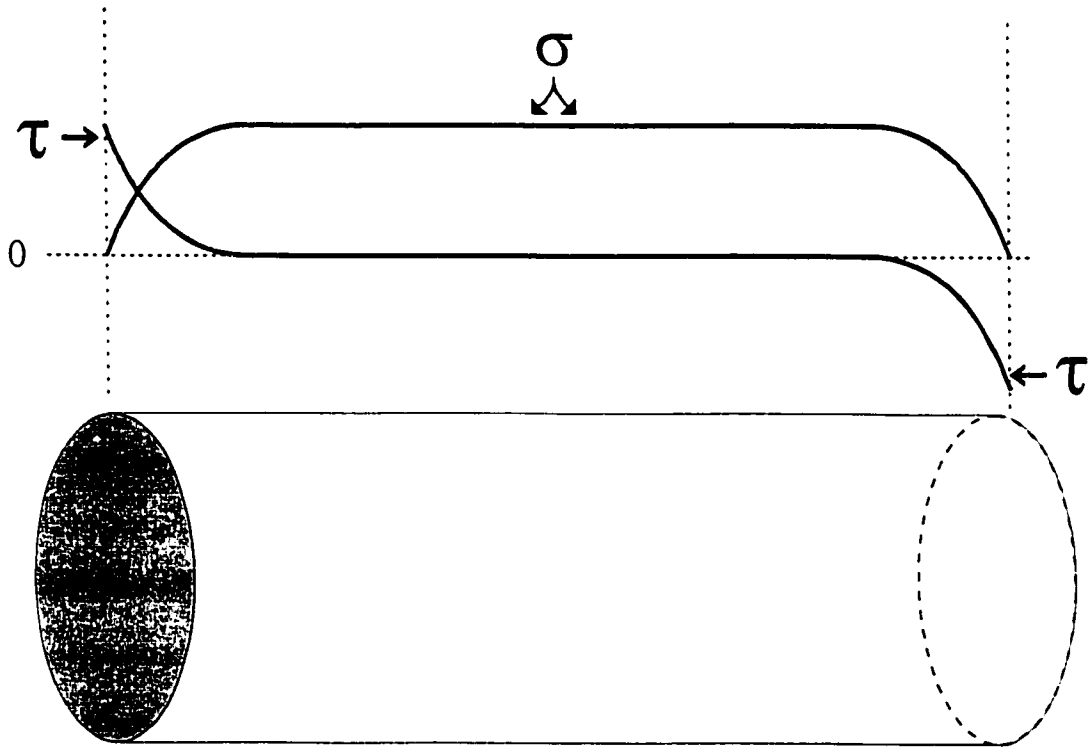

Figure 2.3 Schematic diagram illustrating the axial stress and shear stress distribution along the length of a fibre from the shear lag model.

for materials selection and composite design (Ashby, 1993). The method developed by Ashby allows for selection of the composite phases for optimal performance and for comparison to single phase materials in materials-selection charts. Although this method is applicable to many composite materials properties which can be described by rules of mixture, this work will only discuss the process for determination of strength and elastic modulus. The method consists of developing bounds for composite properties resulting from the mixing of two phases. Precise calculations of the properties would be difficult because of effects such as reinforcement distribution and shape.

The procedure for deriving these bounds for the elastic modulus is straight forward. The upper bound is given by the Voigt iso-strain condition (eq. 2.1) and the lower bound is given by the Reuss iso-stress condition (eq. 2.2). More accurate calculations such as the Eshelby analysis will predict an elastic modulus contained between these bounds. Given that the density of the composite ρ_C will obey the rule of mixtures exactly if there is no reaction between the phases upon mixing, composite materials-selection charts for weight-critical applications can be devised. An example for the elastic modulus of two Al based composites is shown in figure 2.4. The effect of constituent choice on resultant properties is clearly observed from this chart. Depending on whether alumina or beryllium is used as the reinforcement, significant differences in properties result. The improvement of Young's Modulus by adding Be reinforcement to the Al matrix is also clearly observed and demonstrates the merit of this method for materials selection.

2.2 SCALE EFFECTS

It has been shown that the strength of metals depends on the relative ease of dislocation flow and multiplication within them. This motion of dislocations is normally limited by a dominant obstacle type which will control the strength. Such obstacles are grain boundaries, particles, solute atoms or other

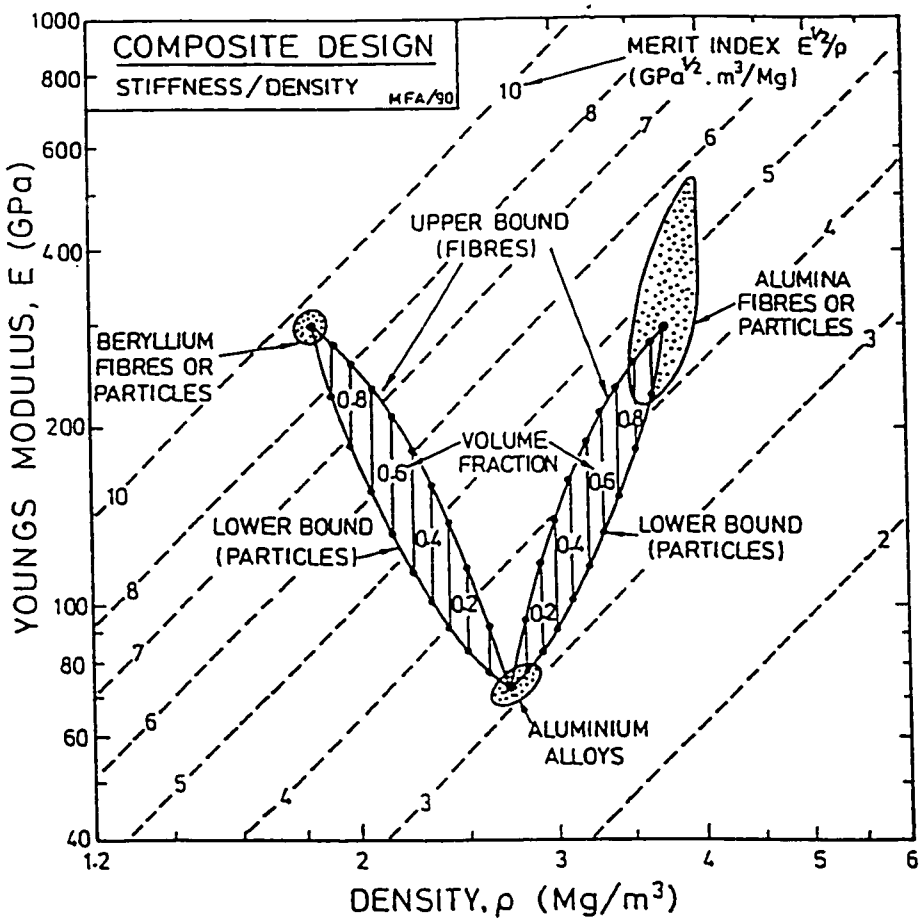

Figure 2.4 Materials-selection chart for composites of Al-Be and Al-Al_2O_3. (from Ashby, 1993)

dislocations. In order to be effective strengthening agents, these obstacles must interact with dislocations over a significant portion of their line length. The scale at which this becomes important is of relevance to scale effects in composites.

To gain an idea of the typical dimensions over which obstacles must operate to affect the strength of metals, we will use grain boundary strengthening as an example. It has been shown by experimentation (Hall, 1951 and Petch, 1953) that the strength of a polycrystalline metal σ_d can be related to its grain size d through the Hall-Petch relation

$$\sigma_d = \sigma_o + \frac{k}{d^{1/2}} \qquad \text{eq. (2.16)}$$

where σ_o is a reference stress related to the friction of the lattice for dislocation flow and k is the barrier strength of the grain boundaries. In metals, k is in the range of 30 to 775 MPa·m$^{1/2}$ (Armstrong et al., 1962). If we arbitrarily define a significant increase in strength as 100 MPa, we find that the grain size necessary to achieve this increment is of the order of 10 μm. This sets a practical boundary for the magnitude of the scale at or below which significant strengthening by grain refinement can occur.

The situation is similar for particles. Small finely distributed particles can impede the flow of dislocations in a plastically deforming metal. The increase in shear stress τ needed to be applied to the dislocations on their glide planes to overcome particles separated by a distance l is given approximately by (Hull and Bacon, 1984)

$$\tau = \frac{Gb}{3l} \qquad \text{eq. (2.17)}$$

where G is the shear modulus and b is the Burgers vector for the dislocation. We can see that strength depends on the inverse of the inter particle distance, a strong effect of scale. More comprehensive models which account for the effects of kinematic and isotropic strain hardening and hardening due to

thermal expansion mismatch between the particles and matrix have been reported (Nan and Clarke, 1996).

The scale effects above operate in metals that deform by dislocation flow. Ceramics at room temperature do not exhibit plastic flow. They tend to deform elastically and fracture in a brittle fashion. The stress at which fracture occurs defines the strength of the ceramic. The pioneering work of Griffith (1920) and the subsequent development of LEFM (linear elastic fracture mechanics) have related the strength of brittle materials to scale. The strength σ_f of a brittle material has been related to the largest flaw of size c in its microstructure by

$$\sigma_c = A\sqrt{\frac{2E\gamma}{\pi c}} \qquad \text{eq. (2.18)}$$

where E is the elastic modulus, γ is the surface energy and A is a geometrical constant. This is called the Griffiths fracture criterion. The effect of scale comes into this process from the fact that the largest possible flaw size in a brittle material is ultimately limited to the scale of the component.

2.3 PROCESSING

It is apparent from the preceding discussion that the microstructure of materials has a direct bearing on the resultant properties. In order to produce materials with the desired microstructure, the appropriate processing techniques must be found. Ideally, the processing step should provide easy control over the shape and microstructure produced. In reality, the situation is much more complicated. For the production of MMCs in particular, processing is a difficult step. Most MMCs are produced from the liquid state. Processes such as squeeze casting, squeeze infiltration, spray deposition and slurry casting are generally used to produce a wide variety of composites (Clyne and Withers, 1995). Some of these primary processing steps are similar to the ones used in making unreinforced metals and alloys.

The secondary processing step which usually involves large deformation strains for the elimination of porosity and for forming into a required shape is more complicated for MMCs. This is due to the presence of the usually brittle reinforcing phase in the microstructure. To avoid damage of this phase during processing, great care must be taken for control of the parameters of the forming operation. This in turn limits control over the microstructure that one will obtain. As an example of this, the forming of Al-SiC pMMCs (particulate reinforced metal-matrix composites) by extrusion is considered. Experimental results (Brusethaug and Reiso, 1991) have found that this forming operation depends critically on conditions of applied strain rate and temperature. For a 15 vol% composite, Brusethaug and Reiso reported that the operating range for successful and efficient extrusion is given by an extrusion speed of 30 to 35 m/min in the temperature range of approximately 410 to 420 °C. This is in sharp contrast to metals and alloys which can be formed successfully over a much wider range of process parameters.

Thus, it is of importance to gain understanding of forming operations for MMCs. More specifically, because of its importance for forming pMMCs, the process of extrusion is of interest. It will be seen by illustrating its potential benefits, that the hydrostatic extrusion process as a subset of the different extrusion methods is of worth for the study of MMC forming.

The concept of all of the extrusion methods is a simple one. A billet is pushed against a die until the forces developed are enough for the billet to deform and for the material to flow through the die (Schey, 1977). In extrusion, the billet is pushed by a ram and is supported in a container to avoid uncontrolled deformation such as buckling. In the hydrostatic extrusion variant, the billet is forced against the die by a pressurized fluid. This fluid pressure provides the axial force that the ram provides in extrusion but also supports the billet in the die without the need for a container. The fluid may also be

used to pressurize the receiving chamber at the exit of the die. This has an effect on the stress state during deformation which will be discussed next.

We will now consider the extrusion of a cylindrical billet into a small angle converging conical die in order to gain an understanding of the pressures needed for extrusion and the stress state created in the die. The process is illustrated in figure 2.5. The simplest treatment of this problem is to assume that the axial stress σ_{xx} is constant from the die wall to the center line and that the die walls are frictionless. The solution to this problem is attributed to Sachs (1927). The axial stress distribution in the die is given by

$$\sigma_{xx} = \sigma_{xf} + \sigma_o \ln\left(\frac{R_f}{R}\right)^2 \qquad \text{eq. (2.19)}$$

where σ_0 is the flow stress of the material, σ_{xf} is the applied back stress at the die exit, R_f is the radius at the die exit and R is the radius of the billet at a position x in the die. The extrusion pressure for this problem is found by substituting R for R_o, the radius at the die entry, into equation 2.19. For a small die angle, σ_{xx} is approximately equal to the extrusion pressure P and it is given by

$$P = \sigma_{xf} + \sigma_o \ln\left(\frac{R_f}{R_o}\right)^2 \qquad \text{eq. (2.20)}$$

Thus, it can be seen from this simple analysis that without back pressure, the extrusion pressure will depend on the flow stress of the material and the reduction imposed on the billet.

If this equilibrium analysis is made more accurate by including Coulomb friction at the die walls, we obtain the following expressions for axial stress in the die and the extrusion pressure

$$\sigma_{xx} = \sigma_o\left[\frac{1+B}{B}\right]\left(1-\left(\frac{R}{R_f}\right)^{2B}\right)+\sigma_{xf}\left(\frac{R}{R_f}\right)^{2B} \qquad \text{eq. (2.21)}$$

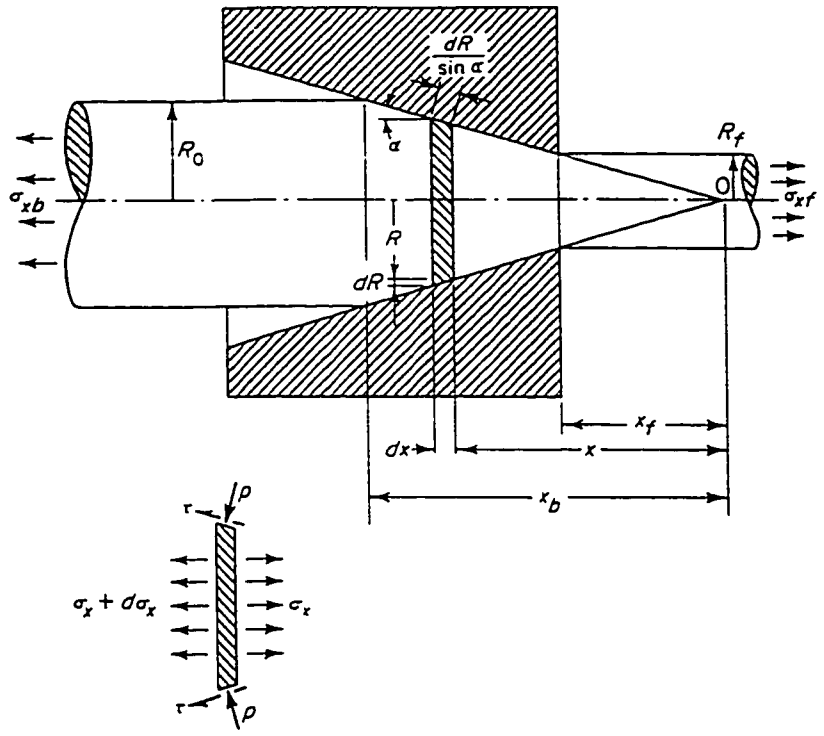

Figure 2.5 Schematic diagram of the extrusion process. (from Avitzur, 1968)

$$P = \sigma_o \left[\frac{1+B}{B}\right]\left(1-\left(\frac{R_o}{R_f}\right)^{2B}\right)+\sigma_{xf}\left(\frac{R_o}{R_f}\right)^{2B} \qquad \text{eq. (2.22)}$$

where B is a positive constant given by $\mu/\tan\alpha$, where μ is the coefficient of friction and α is the die half-angle. Again, when friction is considered, we see that the pressure required for the extrusion depends on the flow stress and the reduction but also on the coefficient of friction and die angle. It is observed from equation 2.21 that the axial stress in this model is compressive everywhere in the die, for any reduction. The effect of back pressure can also be observed. By applying a compressive back pressure, the axial stress becomes more compressive, leading to a more compressive state of hydrostatic stress. Since fracture events are dilatational in nature, they will be suppressed by high compressive hydrostatic pressures. One can see a further benefit of hydrostatic extrusion with back pressure for extruding without creating damage.

The equilibrium or slab analysis above predicts compressive axial stresses everywhere in the die. This result contradicts the experimental evidence of center-burst cracks in extruded metals which are caused by tensile stresses. Thus, the assumption of constant axial stress accross the die is not physically sound.

In order to model the variations of stress state from the die wall to the centre-line of the extrusion, Thomason (1969/70) developed a slip-line field solution for axisymmetric extrusion. The chosen slip-line field is shown in figure 2.6. The equilibrium equations for the α and β slip-lines are given by the following

$$dp + 2k\,d\phi + (\sigma_\theta + p - k\cot\phi)\frac{dr}{r} = 0 \qquad \text{for an } \alpha \text{ line} \qquad \text{eq. (2.23)}$$

$$dp - 2k\,d\phi + (\sigma_\theta + p - k\tan\phi)\frac{dr}{r} = 0 \qquad \text{for a } \beta \text{ line} \qquad \text{eq. (2.24)}$$

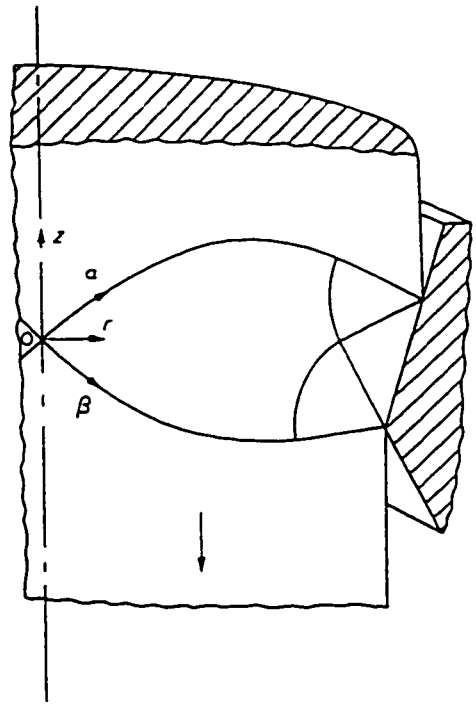

Figure 2.6 Slip-line field for axisymmetric extrusion. (from Thomason, 1969/70)

where p and k are the pressure and maximum shear stress on the plane of the slip-line field, ϕ is the angle between the horizontal and an α line, and r is the radial distance from the centre-line. These equations differ from the similar case of plane strain sheet drawing by the fact that there is an out of plane stress σ_θ that is not given by the plane strain condition. In order to solve equation 2.23 and 2.24, Thomason assumed that σ_θ is given by

$$\sigma_\theta + p = \pm k(1 - r/R_D) \qquad \text{eq. (2.25)}$$

where R_D is the radius of the die. By substituting the appropriate form of equation 2.25 into equation 2.23 and 2.24, we obtain the following equilibrium equations

$$dp + 2kd\phi - k(1 - r/R_D + \cot\phi)\frac{dr}{r} = 0 \qquad \text{for an } \alpha \text{ line} \qquad \text{eq. (2.26)}$$

$$dp + 2kd\phi - k(1 - r/R_D + \tan\phi)\frac{dr}{r} = 0 \qquad \text{for a } \beta \text{ line} \qquad \text{eq. (2.27)}$$

By integrating equations 2.26 and 2.27, the extrusion pressure P can be found and it is plotted as a function of reduction of area for various die half-angles in figure 2.7. Note that this result is for a frictionless die billet interface. It is also possible to find the mean hydrostatic pressure in the material at the billet centre-line. Values of the hydrostatic pressure σ_m are presented in figure 2.8 in terms of reduction in area for various die half-angles. It should be noted that positive values of σ_m /2k are tensile hydrostatic pressures.

From figure 2.8, it is apparent that the slip-line field model can predict the production of tensile stresses in the billet, for certain conditions of die angle and reduction. This is in agreement with the observations of damage in extruded materials in some conditions. The axisymmetric model developed by Thomason does not report hydrostatic stresses away from the centre-line. This may be due to the complication of the mixed mode of deformation away from the centre-line. According to equation 2.25, plane strain conditions only exist at the die billet interface where $r=R_D$. Conversely, for the problem of

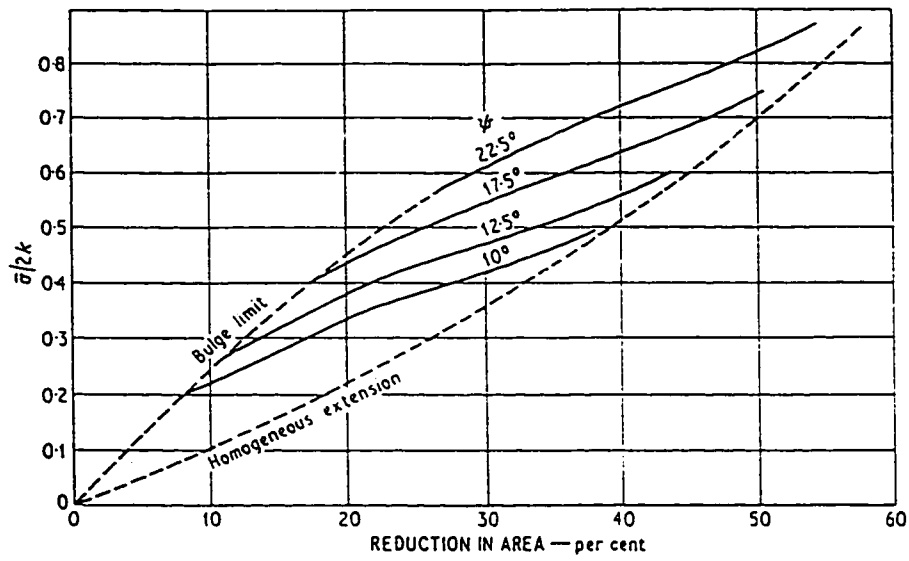

Figure 2.7 Extrusion pressure as a function of reduction in area for various die half-angles. (from Thomason, 1969/70)

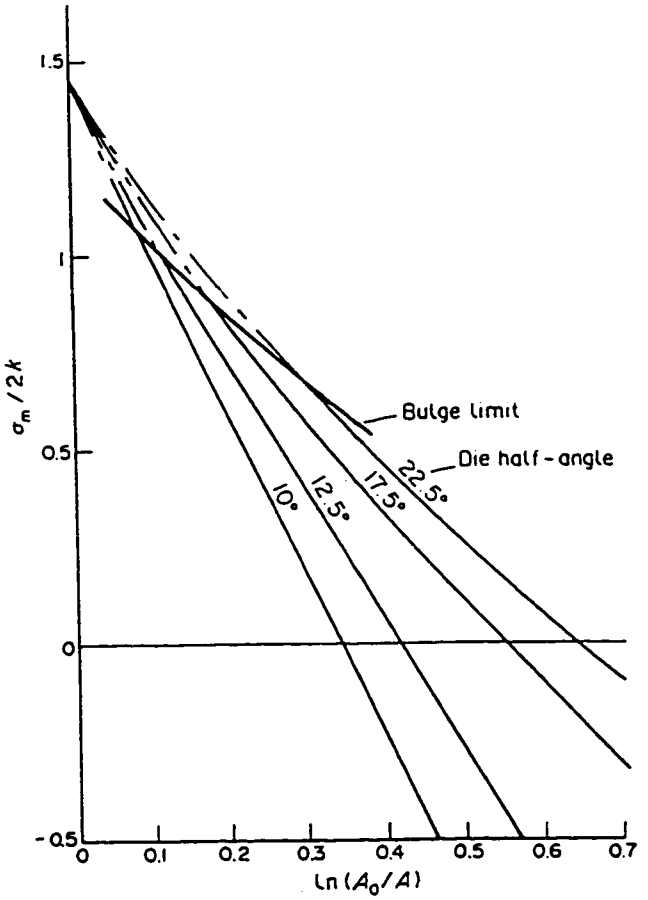

Figure 2.8 Hydrostatic pressure at the billet centre-line for axisymmetric extrusion. (from Thomason, 1969/70)

plane strain sheet extrusion, plane strain conditions dominate over the entire cross-section (Coffin and Rogers, 1967). The solution for hydrostatic stresses in this case is much simpler and is shown in figure 2.9. The state of hydrostatic stress for this case varies from a strong tensile component at the centre-line to a strong compressive component at the die billet interface. Considering the fact that the axisymmetric model also predicts tensile hydrostatic stresses for the same conditions of die angle and reduction and that plane strain conditions are approached from the center-line to the die wall, one would expect the same trend to apply to this case.

The results of the slip-line field models show the importance of the processing parameters such as die angle and reduction for the resultant properties. Damage occurs in the form of voiding and because of the dilatation involved, the sense of the hydrostatic pressure is critical. A compressive hydrostatic pressure will oppose dilatation whereas a tensile hydrostatic pressure will aid it. It thus becomes clear that the choice of extrusion parameters must be made carefully to avoid damage in the product.

2.4 LOAD TRANSFER

In MMCs, damage usually occurs at the metal-reinforcement interface or in the reinforcement itself. The initiation or nucleation of such events are a results of load transfer from the matrix to the reinforcement. Models for load transfer were summarized in section 2.1. The modified Eshelby model of equation 2.8 and the shear lag model of equation 2.9 or 2.12 describe the process of load shedding from the matrix to the particles or fibres and so describe the efficiency of the reinforcement. Implicit in these models is that the interfacial region is strong enough to transfer the load. The interfacial strength depends on many variables such as wettability, propensity for reaction, surface roughness of the reinforcement, processing history and the relative thermal expansion coefficients of the constituents.

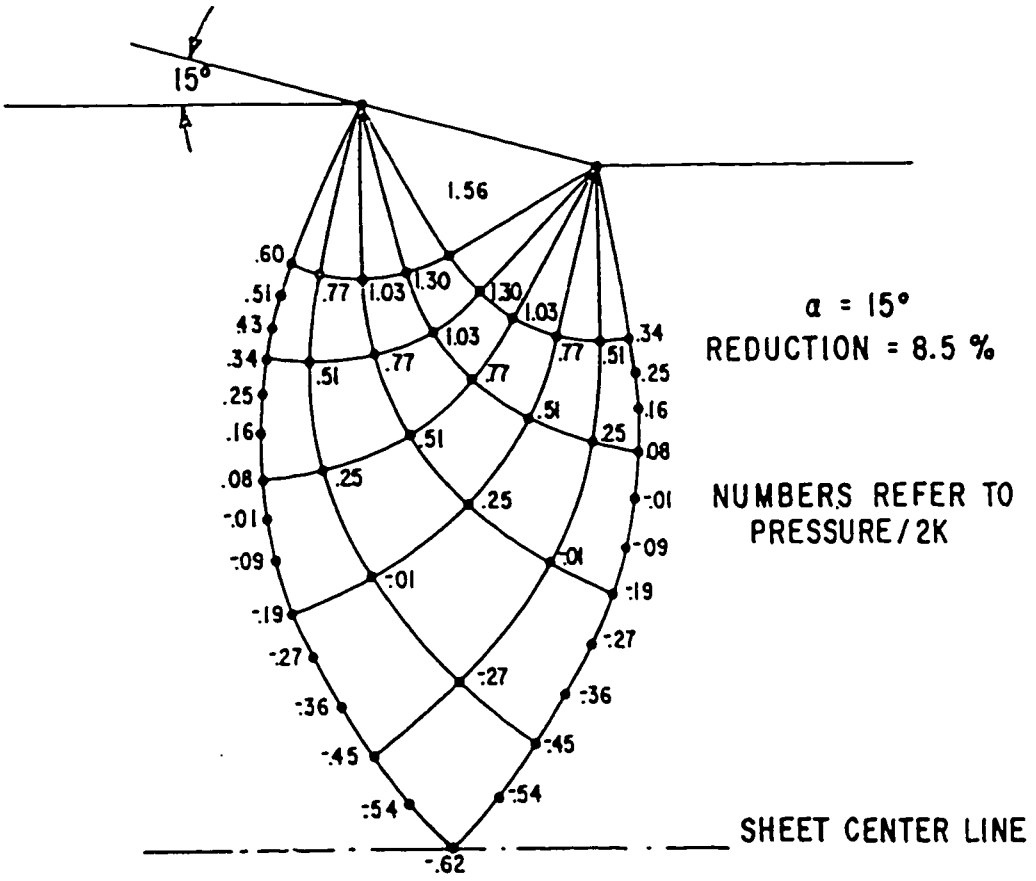

Figure 2.9 Hydrostatic pressure in the die during plane strain sheet extrusion. (from Coffin and Rogers, 1967)

This complexity and variability makes it difficult to gauge the efficiency of the fibres other than by direct measurement.

We will now examine various methods for measurement of the internal stresses in the reinforcements of MMCs. One method is neutron diffraction and it is especially powerful for probing the bulk properties of materials because of the high penetration depth and large sampling volume (Clyne and Withers, 1995). Thus, neutrons can penetrate directly into the matrix of an MMC to the reinforcement. The quantity sought in neutron diffraction is the interplanar spacing d of the crystallographic plane being measured. The spacing is found by Bragg's Law

$$d = \frac{\lambda}{2\sin\theta} \qquad \text{eq. (2.28)}$$

where λ is the wavelength of the neutrons and θ is the angle between the incident and diffracted beams. When the lattice being probed is strained, the difference between the measurement d and the unstressed interplanar spacing d_o will give the elastic strain ε in the direction perpendicular to the plane in question. Assuming that this strain is a principal strain,

$$\varepsilon_{ii} = \frac{d - d_o}{d_o} \qquad \text{eq. (2.29)}$$

If the stiffness tensor of the material being probed and the principal strain tensor ε_{ij} are known, the principal stress in the direction of the measured strain can be found by Hooke's Law

$$\sigma_{ii} = C_{ijij}\varepsilon_{ij} \qquad \text{eq. (2.30)}$$

If this procedure is followed for several planes of the same crystal, its entire stress state may be elucidated.

Another method for determining internal stresses in composites consists in exploiting the birefringent properties of photoelastic materials which have been strained elastically (Clyne and Withers,

1995). In such a strained material, an incident plane polarized wave will be split into two perpendicular components in the direction of the two in-plane principal stresses and will travel with velocities in proportion to the magnitude of the aforementioned stresses. The two split components will interact upon exiting the material and will interfere to create a fringe pattern if observed through an analysing polaroid. The fringe pattern is simply analysed to get the difference in principal stress σ_1-σ_2 with the following relation

$$\sigma_1 - \sigma_2 = \frac{nf}{t} \qquad \text{eq. (2.31)}$$

where n is the fringe order, f is the fringe value (in Nm^{-1}) and t is the thickness of the photoelastic material. Determination of the individual stresses is made by an integration method using

$$\delta\sigma_1 = \frac{2(\sigma_1 - \sigma_2)}{\rho}\delta z \qquad \text{eq. (2.32)}$$

where $\delta\sigma_1$ is the increment in principal stress for an increment δz away from a point of known stress σ_1 and ρ is the radius of curvature of the orthogonal stress direction.

There is another optical method which exploits the piezo-spectroscopic properties of some materials. One such material is sapphire. The stress state of the host alumina lattice affects the energy levels of electrons in substitutional Cr^{3+} impurities. By measuring the shifts in the emission spectrum of these ions, stress measurements can be deduced. It has been found (He and Clarke, 1995) that the piezo-spectroscopic effect for chromium doped sapphire (ruby) can be described in terms of the change in frequency $\Delta\nu$ from the unstressed state. The tensorial equation to describe the effect is given by

$$\Delta\upsilon = \Pi_{ij}\sigma_{ij} \qquad \text{eq. (2.33)}$$

where Π_{ij} are the piezo-spectroscopic coefficients and σ_{ij} is a stress state defined with respect to the crystallographic basis of the sapphire lattice. This basis is defined as the 3-axis corresponding to the c-axis of rhombohedral (trigonal) sapphire and the 1 and 2 axes corresponding to the a and m

crystallographic axes. The choice of these axes is illustrated in figure 2.10 in terms of a sapphire unit cell. If crystal symmetry criteria similar to the ones used for elasticity (Nye, 1993) are valid, Π_{ij} must be symmetric and the off-diagonal terms must be zero when the reference frame chosen is the one shown in figure 2.10. Experimental evidence from bend specimens of the Iosipescu type (Iosipescu, 1967) producing regions of nearly pure shear suggests that shear stresses do not significantly affect R transition frequencies for chromium doped sapphire. Thus, from this result, the full piezo-spectroscopic tensor is found to contain 3 independent coefficients and it is given by

$$\begin{bmatrix} \Pi_{11} & 0 & 0 \\ 0 & \Pi_{22} & 0 \\ 0 & 0 & \Pi_{33} \end{bmatrix} \qquad \text{eq. (2.34)}$$

He and Clarke also found that the two R transitions lines for ruby possess different piezo-spectroscopic coefficients. The piezo-spectroscopic tensor for the R_1 transition is given by

$$\begin{bmatrix} 2.56 & 0 & 0 \\ 0 & 3.50 & 0 \\ 0 & 0 & 1.53 \end{bmatrix} \qquad \text{eq. (2.35)}$$

where the coefficients are in units of $(GPa \cdot cm)^{-1}$. The corresponding tensor for the R_2 transition is

$$\begin{bmatrix} 2.66 & 0 & 0 \\ 0 & 2.80 & 0 \\ 0 & 0 & 2.16 \end{bmatrix} \qquad \text{eq. (2.36)}$$

It is clear from equations 2.33, 2.35 and 2.36 that by measurement of the shift in R transitions in sapphire, the stress state can be solved entirely for special cases or two principal stresses can be described in terms of the third.

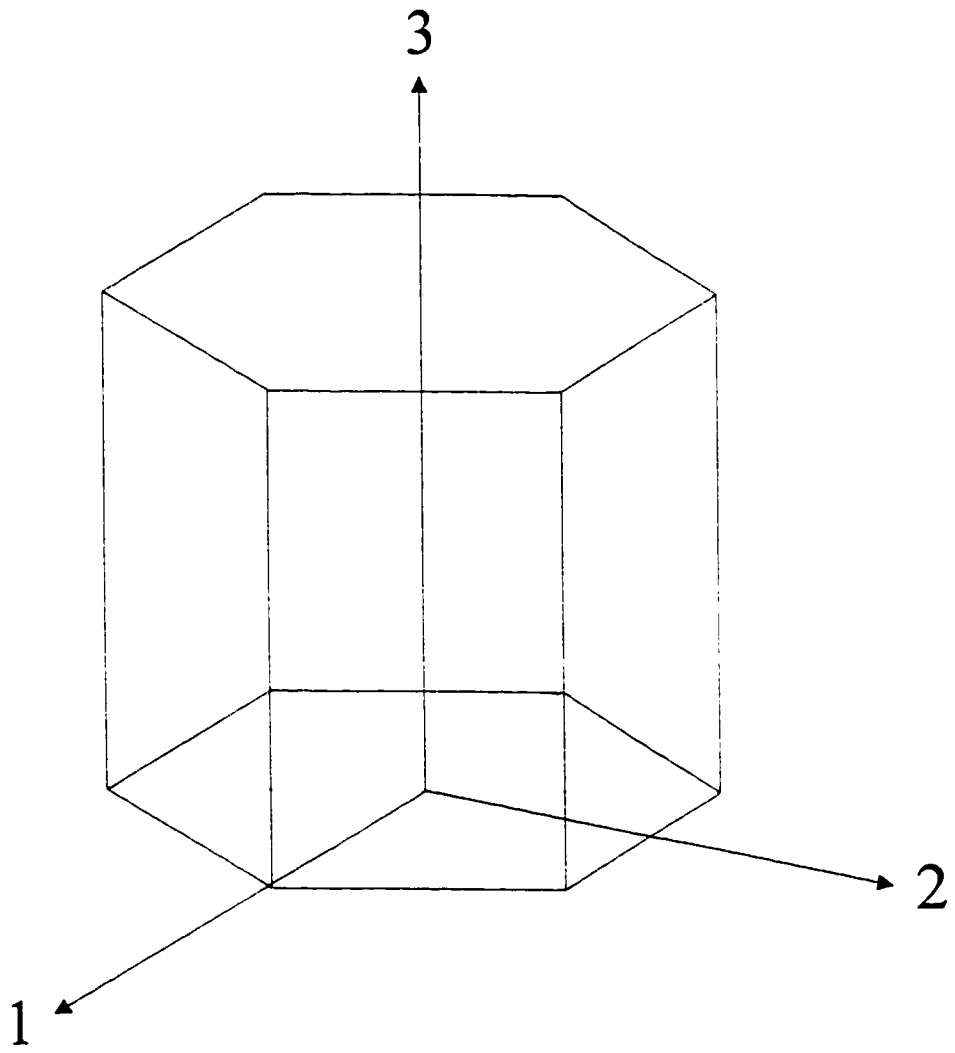

Figure 2.10 Schematic diagram of the crystallographic basis for sapphire.

2.5 SPATIAL DISTRIBUTION EFFECTS

It is clear from the models for load transfer that this process will have a direct influence on the mechanical properties of an MMC and its ability to withstand damage. It is implicit in these models that the matrix away from the immediate vicinity of the reinforcements deforms homogenously in the elastic and plastic state. In the Eshelby model, the effect of other reinforcement particles or fibres is assumed to create an average background stress to be superimposed onto the stress state caused by the reinforcement modelled. In the shear lag model, the fibre is assumed to be surrounded by matrix material strained to a constant level in the far-field condition and no effect of other fibres is considered.

Experimental studies by Poole (1993) and Yip and Wang (1997) have demonstrated the importance of the fibre distribution for the global flow pattern of a composite. These studies showed a strong inhomogeneity of flow in Cu-W and Cu-TiB_2 composites. Inhomogenous distribution effects have also been observed in particulate MMCs (Llorca and Gonzalez, 1998). It is thus apparent from these results that the load transfer process will depend on the location of a reinforcement in an inhomogenously deforming MMC. It is thus important to discuss the effect of spatial arrangement on the flow properties of composites.

In a discussion of relative positions of general objects in space, methods for quantifying spatial distribution are needed. Qualitative attributes such as clustered, regular or random microstructures are not sufficient and represent special cases only. The degree of clustering, periodicity or randomness must be assessed to understand this effect more clearly.

One method used to quantify spatial distribution is the Dirichlet tessellation. This method applies to two dimensional sections of the distribution in question. For MMCs, each reinforcement is

replaced by a point at its center on the two dimensional section. A Dirichlet cell, which corresponds to the area within which every point will be closer to the reinforcement it contains than any other reinforcement, can then be constructed. The boundary of the cell is a line of equidistance between two reinforcements. By applying simple statistics to the cells, Burger et al. (1987) tested the sensitivity of this method to periodicity and clustering. They found that the standard deviation of the near-neighbor distance had a strong correlation with the degree of periodicity and that the standard deviation of cell area, the mean cell aspect ratio and its standard deviation had a strong correlation with the degree of clustering. They also found that by defining a critical separation distance between points, distributions could be compared on a relative basis.

Work by Pyrz (1994) has shown the use of the second-order intensity function K(r) in comparing distributions. This function is defined as

$$K(r) = \frac{A}{N^2} \sum_{K=1}^{N} \omega_K^{-1} I_K(r) \qquad \text{eq. (2.37)}$$

where N is the number of points in the observation area A, $I_K(r)$ is the number of points in the circle of radius r with centre at one of the points. The variable ω_K^{-1} is a correction for edge effects and is given by the proportion of the circumference contained within A to the whole circumference of radius r. To illustrate the comparative power of K(r), six point patterns along with their Dirichlet cells are defined in figure 2.11. They vary in order from regular to clustered to random distributions. The plot for K(r) versus r for these six distributions are shown in figure 2.12. It is seen from these that clustered distributions lie above the Poisson (random) distribution and regular distributions have distinctive steps. Non-clustered distributions lie close to or below the Poisson distribution. It is evident that K(r) is a good tool to assess the characteristics of reinforcement distributions in MMCs.

Once the distribution has been characterized, the question to be resolved is how various distributions affect the mechanical properties of MMCs. Fan et al. (1994) have modified

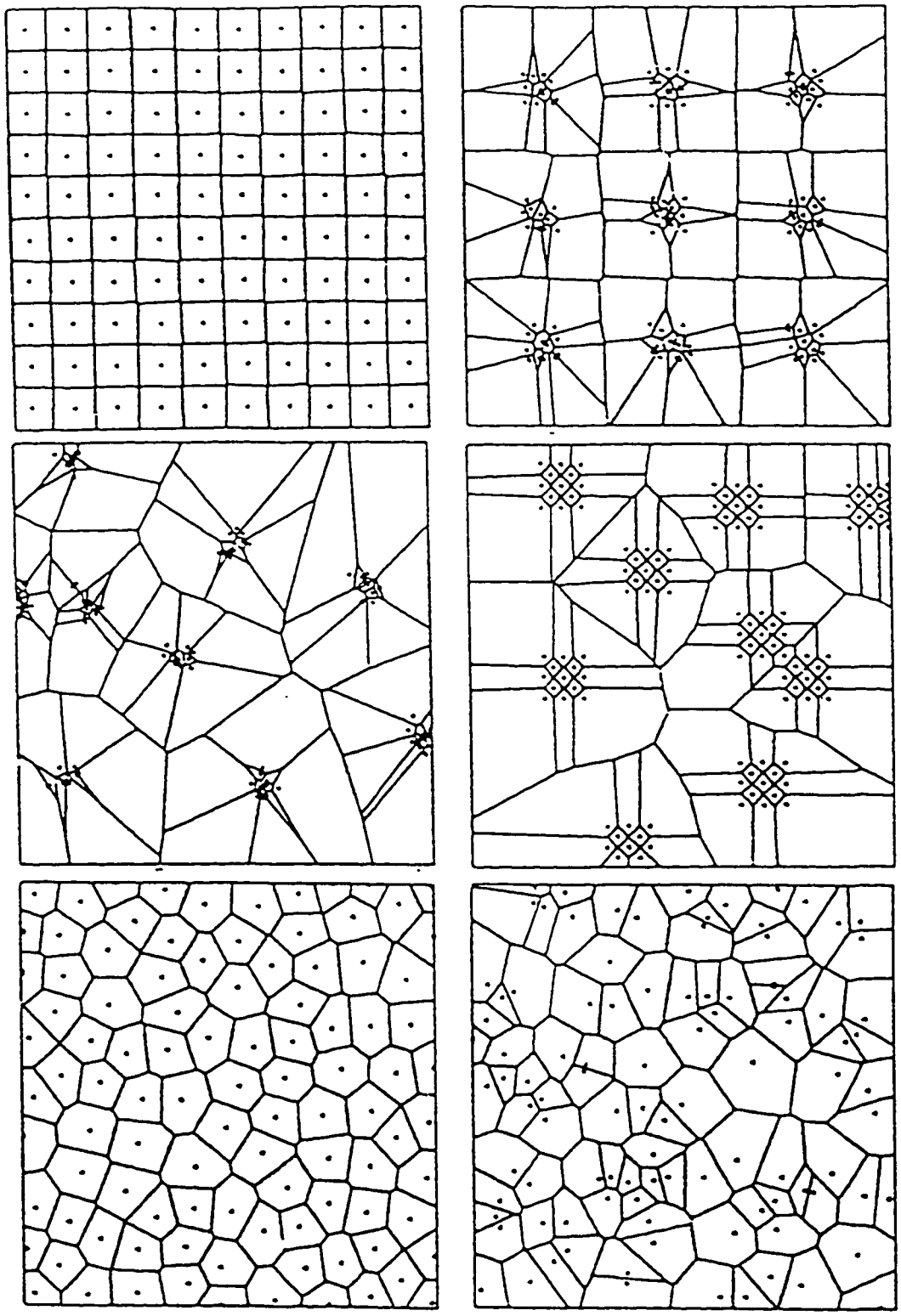

Figure 2.11 Six idealised point patterns and their Dirichlet cells. (from Pyrz, 1994)

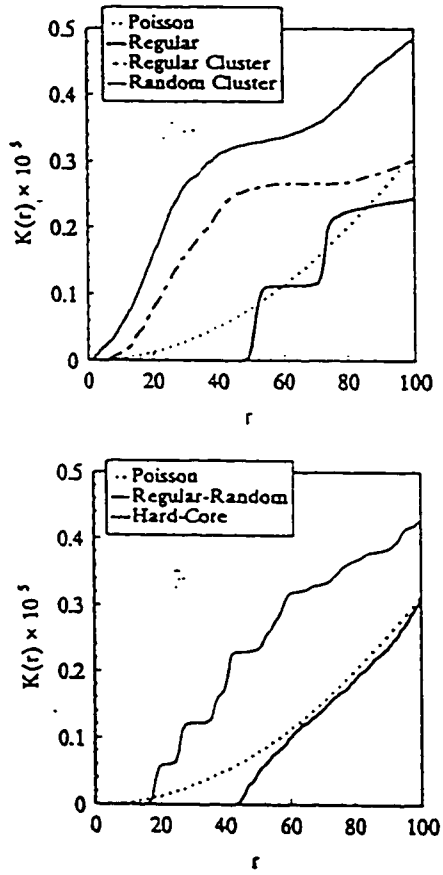

Figure 2.12 Plot of the second-order intensity function K(r) versus r for the six point patterns illustrated in figure 2.11. (from Pyrz, 1994)

the law of mixtures to account for different reinforcement distributions. The law of mixtures for the elastic modulus of the composite E_C, for example, is given by

$$E_c = E_1 f_{1c} + E_2 f_{2c} + E_3 F_s \qquad \text{eq. (2.38)}$$

where E_1 and E_2 are the elastic moduli of the constituents, E_3 is the elastic modulus of a third microstructural feature consisting of clustered areas of phase 1 and 2 where they are very finely separated so that they essentially be regarded as a separate phase. The variables f_{1C}, f_{2C} and F_s are the volume fractions of phase 1,2 and 3 respectively. In order to find E_C from equation 2.38, experimental results must be gathered from metallography to find the volume fractions of the three phases. More importantly, the quantity E_3 must also be found experimentally from separate samples consisting of 100% by volume of the fine mixture of 1 and 2.

There have been other contributions to the goal of understanding fibre distributions effects. Experimental results by Poole et al. (1994) have shown that the distribution of the von Mises strain developed in Cu reinforced with continuous W fibres transversely loaded in compression up to global strains of 30% depends on the distributions of reinforcements. The distribution of von Mises strain for fibres arranged in a regular square array is more inhomogenous than the distribution for fibres arranged in a triangular array for the same volume fractions of material. This result was explained by the necessity to develop a kinematically admissible velocity field in the matrix for compatibility with the imposed global strain and for continuity of the matrix around the non-deforming W fibres. This has been schematized for the triangular and square fibre arrangements on figure 2.13. This simple analysis explains the inhomogenous character of the global flow pattern and the location of extremes in strain level. The inhomogeneity of flow was also observed by Yip and Wang (1997) for Cu-TiB_2 composites. The location and density of slip lines following uniaxial compression perpendicular to the fibres was found to be dependent on the spatial arrangement of the TiB_2 fibres around the area of interest. Similar slip line observations have also shown the inhomogeneity of flow in pMMCs. From

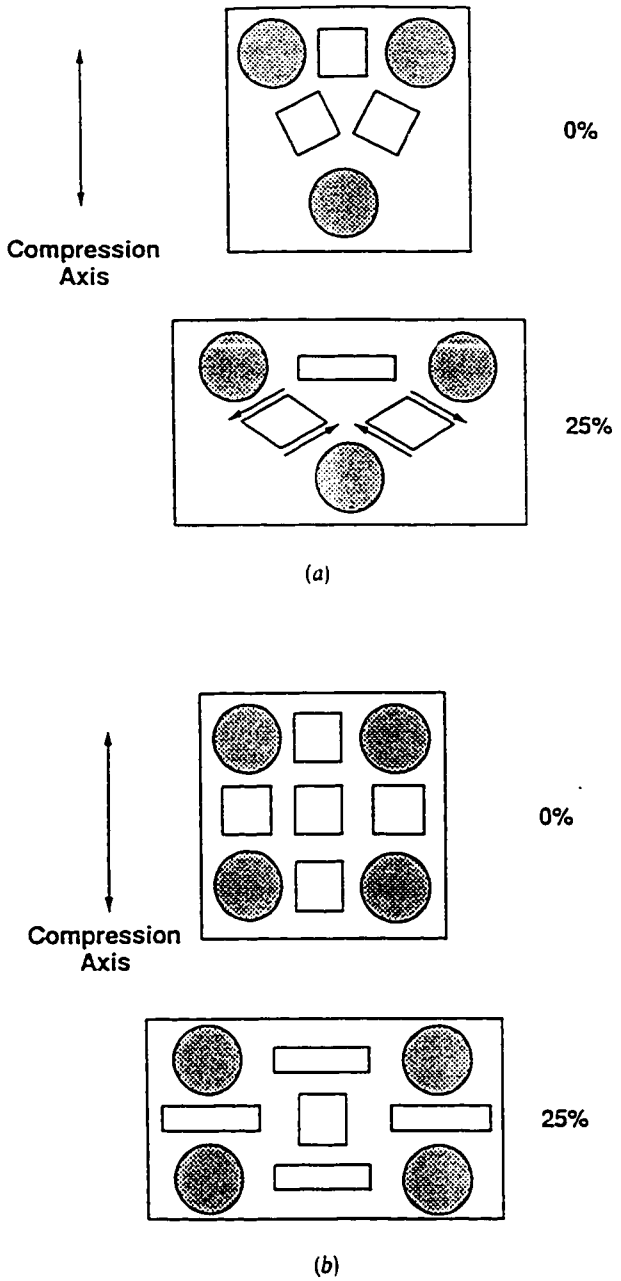

Figure 2.13 Analysis of the effect of local fibre distribution on the matrix strain field during plane strain compression. (from Poole, 1994)

the observation of slip lines on polished faces of an Al-SiC particulate composite deformed at small strains of the order of 0.15%, Corbin (1992) found an effect of particle distribution. The regions of low particle volume fraction was where the initial matrix flow occurred. Thus, the onset of yielding is dependent upon the distribution of reinforcements.

The experimental evidence of particle distribution effects has been corroborated by various numerical analyses by FEM. Poole et al. (1994) were able to match experimental strain distributions in Cu-W composites with the ones generated by FEM analysis. The FEM results also permitted the elucidation of the stress distribution in the composites, thus giving insight into the load transfer process from the matrix to the fibres and the overall stress-strain behaviour. In a numerical analysis by Brockenbrough et al. (1991), the tensile stress strain response in the transverse direction of an aligned continuous fibre MMC varied appreciably from one chosen fibre distribution to the other. Further FEM work on modeling of plane strain loading of continuous fibre composites was done by Lesne et al. (1995) and Yip and Wang (1997). Their results also showed the inhomogenous distribution of stress and strain in 1 and 2 fibre arrangements. Of particular interest in these results is the effect of the orientation of the two fibre arrangement to the loading axis. The location of maximum shear stress and of the maximum-normal stress combination varies as the angle to the loading axis is varied and as the distance between fibres is varied.

2.6 INSTABILITIES

The inhomogeneity of flow in MMCs has consequences for their forming properties. Forming of materials by plastic deformation is often limited by the formation of plastic instabilities. These flow instabilities develop locally where the work hardening ability of the material is overcome by a softening process, be it geometrical or materials-based, causing all further deformation to be concentrated in that

region. Continuation of local flow will eventually lead to fracture. It is thus of interest to examine how inhomogenous flow in the matrix of MMCs will aid in the development of instabilities.

The flow stress of metals is a function of many variables such as strain ε, strain rate $\dot{\varepsilon}$ and temperature T. The total material-based work hardening of the material denoted $\frac{d\sigma}{d\varepsilon}$ can thus be expressed as

$$\frac{d\sigma}{d\varepsilon} = \left(\frac{\partial\sigma}{\partial\varepsilon}\right) + \left(\frac{\partial\sigma}{\partial\dot{\varepsilon}}\right)\left(\frac{\partial\dot{\varepsilon}}{\partial\varepsilon}\right) + \left(\frac{\partial\sigma}{\partial T}\right)\left(\frac{\partial T}{\partial\varepsilon}\right) + \ldots. \qquad \text{eq. (2.39)}$$

The condition for stable flow is that the right hand side of equation 2.39 be greater than zero. If any of the terms on the right hand side of equation 2.39 becomes sufficiently negative, softening will occur and unstable flow will result. If equation 2.39 is examined term by term, it is found that only $\left(\frac{\partial\sigma}{\partial T}\right)$ is negative. All others are positive and cannot lead to softening. It thus becomes important for stable flow that $\left(\frac{\partial\sigma}{\partial T}\right)\left(\frac{\partial T}{\partial\varepsilon}\right)$ not become sufficiently large to overcome the hardening processes. This is a concern when an increment in strain locally causes an increment in temperature that is not dissipated quickly enough. This is a condition of adiabatic heating and will only occur in metals at high strain rates. Under such conditions, further localization tendencies such as the presence of reinforcing fibres could aid the softening process.

Although adiabatic deformation is the main process that can lead to materials-based instabilities, metals can also become plastically unstable due to geometrical softening. An example of this is for metals in uniaxial tension. In this case, the work hardening capacity of the material is overcome by the softening due to the loss of load bearing area. We can express the increment in tensile load dF by

$$dF = \sigma dA + A d\sigma \qquad \text{eq. (2.40)}$$

where σ is the tensile stress and A is the load bearing area perpendicular to σ. We find from equation 2.40 that unstable flow will ensue if for an increment in tensile strain $d\varepsilon$, dF becomes zero

$$\frac{dF}{d\varepsilon} = 0 = \sigma \frac{dA}{d\varepsilon} + A \frac{d\sigma}{d\varepsilon} \qquad \text{eq. (2.41)}$$

Re-arranging equation 2.41 yields the geometrical instability criterion

$$\frac{d\sigma}{d\varepsilon} = -\sigma \frac{dA}{A d\varepsilon} \qquad \text{eq. (2.42)}$$

For uniaxial tension $d\varepsilon = dl/l$ and by constancy of volume for plastic flow $dA/A = -dl/l$, equation 2.42 simplifies to

$$\frac{d\sigma}{d\varepsilon} = \sigma \qquad \text{eq. (2.43)}$$

Equation 2.43 is the well known Considere criterion for instability in uniaxial tension. It states that unstable flow in metals will occur when the work hardening rate is equal to the flow stress. This is of importance for MMCs in tension where localization of flow could reduce the strain at which equation 2.43 is satisfied. Llorca and Gonzalez report that, although it is not strictly valid for damaging MMCs, that the onset of plastic instability in tension is followed closely by the Considere criterion (Llorca and Gonzalez, 1998 and Kiser et al., 1996).

2.7 DAMAGE

It has been shown in previous sections that the mechanical properties of MMCs are affected by scale effects, distribution effects and the process of load transfer to the reinforcement. The presence of reinforcing fibres will also affect the processes of damage accumulation and fracture. The incorporation of damage into constitutive laws for MMCs becomes an important endeavour for modeling and design of

structural components. This section will review the different modes of damage and the efforts made to model them.

In a review by Embury (1993), three modes of damage were identified for MMCs, namely local plastic buckling and localized shear, surface degradation and dilatent damage and fracture. In general, these modes of damage depend on many parameters such as stress state, strain path, temperature and microstructural variables such as scale, reinforcement distribution and volume fraction of reinforcement.

The plastic buckling and localized shear mode of damage has been observed in an aligned in-situ Al-Ni composite (Tao and Embury, 1993). It was found that a process of kinking occurred when this material was compressed parallel to the aligned direction of the fibres. The stress σ_C at which this process occurred is given by

$$\sigma_c = \frac{\tau_m}{\phi} \qquad \text{eq. (2.44)}$$

where τ_m is the matrix shear yield stress and ϕ is the initial misalignment of the fibres in the buckled region. The process described by equation 2.44 was also found to evolve with added compression strain. The misalignment ϕ was found to increase slightly with strain and the width of the kink band was found to increase drastically with increasing compressive strain, leading to failure.

The surface degradation mode of damage is mainly found to be of significance in practical deformation processes such as ironing. In such processes where large strains may be involved along with complex strain paths, surface damage may be involved in the complex interactions of the workpiece and die which occur in galling (Heymes, 1992).

The mode of damage and fracture by dilatent processes has been much more thoroughly investigated than the surface degradation and plastic buckling modes. The subject has been reviewed in a comprehensive manner by Thomason (1990). The approach in this review is to separate the process of dilatent damage into the three distinct steps of damage nucleation, growth and coalescence. These will be examined in turn along with the formalisms developed to incorporate damage into quantitative descriptions of large strain plasticity.

The nucleation of dilatent damage can be separated into the two distinct processes of decohesion and fracture. The process of decohesion at the interface of submicron particles has been described by Brown and Stobbs (1976). At the interface of these small particles, the local stress is raised by strain hardening. It was found that the critical nucleation strain for decohesion ε_1^n is given by

$$\varepsilon_1^n = Kr(\sigma_c - \sigma_m) \qquad \text{eq. (2.45)}$$

where σ_c is the critical cohesive strength of the particle matrix interface, σ_m is the hydrostatic component of the applied stress tensor, r is the radius of the particle and K is a material constant related to the particle volume fraction. This model is not valid for particles larger than 1 μm since the strain hardening due to the presence of such particles is negligible. In this case, the model by Argon et al. (1975) has been found more suitable. Their approximate analysis states that decohesion will occur at a critical normal stress to the interface. This critical stress σ_c has been shown to be approximated by the superposition of the equivalent stress $\bar{\sigma}$ and the hydrostatic component of the stress tensor σ_m. Thus

$$\sigma_c = \bar{\sigma} + \sigma_m \qquad \text{eq. (2.46)}$$

where

$$\bar{\sigma} = \left\{1/2\left[(\sigma_1 - \sigma_2)^2 + (\sigma_1 - \sigma_3)^2 + (\sigma_2 - \sigma_3)^2\right]\right\}^{1/2} \qquad \text{eq. (2.47)}$$

and the stresses σ_I for I=1,3 denote the principal stresses. A third model for damage has been proposed in the case where the hydrostatic component of stress is small. In such cases, the proposed decohesion criterion would be one of critical shear stress where the effective stress defined in equation 2.47 is equal to σ_{DC}. This critical shear stress may be constant or a function of σ_m. The second process of damage nucleation is by particle cracking. An estimate of the critical stress to cause fracture σ_c for particles containing flaws is given by the Griffiths criterion, equation 2.18. Implicit in this criterion is the size dependence of the fracture stress of the reinforcement. This implies a stress controlled process which is also stochastic. The use of statistical methods to describe damage in MMCs has been discussed by Maire et al. (1997). For elongated particles, or fibres, the critical stress for fracture can be estimated from the build-up of axial stresses by the shear lag model, equation 2.12.

Once holes have nucleated by decohesion or fracture, further microstructural damage can occur by growth of the voids. An idealised model for an isolated spherical particle in a non-hardening matrix subjected to a uniform remote strain rate field was developed by Rice and Tracey (1969). Their result for $\dot{R}_k$, the rate of change of the radius in the direction of the principal strain rate $\dot{\varepsilon}_k$ is

$$\dot{R}_k = \left\{(1+E)\dot{\varepsilon}_k + \left(\tfrac{2}{3}\dot{\varepsilon}_i\dot{\varepsilon}_i\right)^{1/2} D\right\}R \qquad \text{eq. (2.48)}$$

where (1+E) is 5/3 for low values of hydrostatic pressure and 2 for high values, $\dot{\varepsilon}_i$ are the principal remote strain-rates, R is the radius of the void and D is given by

$$D = 0.558\sinh\left(\frac{3}{2}\frac{\sigma_m}{Y}\right) + 0.008\upsilon\cosh\left(\frac{3}{2}\frac{\sigma_m}{Y}\right) \qquad \text{eq. (2.49)}$$

where Y is the uniaxial flow stress of the material and v is the Lode variable defined as $v = \dfrac{-3\dot{\varepsilon}_2}{\dot{\varepsilon}_1 - \dot{\varepsilon}_3}$.

Modifications to this model to account for linear work hardening use equation 2.48 in its original form with (1+E) equal to approximately 5/3 and D equal to 0.75 σ_m/Y. By integration of equation 2.48, the

volume change of the void can be calculated to give insight into the relative contributions of deviatoric and dilatational void growth. It turns out that the total volume of the void does not contribute significantly to the total strain up to high strains of the order of 0.2 and at high values of tensile hydrostatic stresses. This effect is even more pronounced if linear work hardening of the material is considered. The Rice and Tracey model thus predicts almost purely deviatoric growth for voids.

The void growth only becomes strongly dilatational when the deformation becomes localised on a plane Σ. On this plane, a sheet of voids coalesces by internal necking and will cause ductile fracture. In a two dimensional plane strain model, the normalised tensile stress σ_1 required to initiate this process is given by

$$\frac{\sigma_1}{2K} = \frac{\sigma_n}{2K_n}\left(1+\sqrt{V_f}\right)^{-1} = \frac{1}{2} + \frac{\sigma_m}{2K} \qquad \text{eq. (2.50)}$$

where V_f is the void volume fraction on the plane Σ, σ_n is the mean tensile stress required to initiate localised necking in a porous solid, and K_n is the corresponding yield shear stress. It was found by Thomason that this simple criterion did not differ much from a more complicated three dimensional model. It is important to note that this localisation process does not contribute much to the overall failure strain ε_1^f which is approximately given by

$$\varepsilon_1^f = \varepsilon_1^n + \varepsilon_1^g \qquad \text{eq. (2.51)}$$

where the superscripts n and g refer to nucleation and growth of voids respectively.

It is important to review the ways in which the physical modeling of damage accumulation and fracture presented above can be incorporated into phenomenological constitutive equations. Extensive work of this type has been done for the uniaxial creep process. A theoretical analysis by Onat (1986) of the original work of Kachanov (1958) was made for materials which can be described by the following representation and for an applied stress state that does not change with time t

$$\frac{d\varepsilon(t)}{dt} = f(\omega(t), \sigma) \qquad \text{eq. (2.52a)}$$

$$\frac{d\omega(t)}{dt} = g(\omega(t), \sigma) \qquad \text{eq. (2.52b)}$$

where $\varepsilon(t)$ and σ represents the strain and stress tensor respectively and where $\omega(t)$ represents the effects of changes in internal structure on the current mechanical behaviour. This latter parameter is zero for a state of no damage and is equal to one for a completely damaged state. If the Helmholtz free energy of the system ψ is assumed to depend on ω and σ, we can define the thermodynamic force Σ as

$$\Sigma = \frac{d\psi(\omega, \sigma)}{d\omega} \qquad \text{eq. (2.53)}$$

If there is a one to one mapping of ω to Σ for a fixed σ then ω is a function of Σ and σ and so are the constitutive functions f and g. The functions can then be written in terms of a potential function Ω that defines the mechanical behaviour of the material completely

$$f(\omega, \sigma) = \frac{d\Omega(\Sigma, \sigma)}{d\sigma} \qquad \text{eq. (2.54a)}$$

$$g(\omega, \sigma) = -\frac{d\Omega(\Sigma, \sigma)}{d\Sigma} \qquad \text{eq. (2.54b)}$$

Onat further proves that although the formalism above does not violate thermodynamics, it is not a consequence of thermodynamics. Other formalisms exist which will also satisfy thermodynamic requirements. Keeping this caution in mind, we now proceed to review the models developed using this formalism. Leckie (1986) has reported a model for creep damage. He has defined the parameter ω as the deviation from the steady-state creep rate $\dot{\varepsilon}_s$ corresponding to the applied stress in the tertiary creep range of the creep curve. This has been defined by Lemaitre and Chaboche (1990)

$$\omega = \frac{\dot{\varepsilon} - \dot{\varepsilon}_s}{\dot{\varepsilon}} \qquad \text{eq. (2.55)}$$

The parameter ω is introduced into the Kachanov (1958) constitutive equation for f and g given by

$$f(\sigma,\omega)=\dot{\varepsilon}_o\left\{\frac{\sigma}{\sigma_o(1-\omega)}\right\}^n \qquad \text{eq. (2.56a)}$$

$$g(\sigma,\omega)=(\lambda-1)(\sigma/\sigma_o)^\nu/\left(\lambda n t_o(1-\omega)^\eta\right) \qquad \text{eq. (2.56b)}$$

where $\dot{\varepsilon}_o$ and t_o are the creep rate and rupture time for a reference uniaxial stress σ_o respectively, σ is the applied uniaxial stress, $\eta=\frac{\lambda n}{\lambda-1}-1$ and n,ν,λ are constants to be determined using experimental results.

Constitutive equation of a similar form to equation 2.56a and 2.56b have also been developed for multiaxial stress states. Instead of solely being dependent on a reference stress σ_o, the rupture time t_o is related to a surface Δ in stress space called the isochronous surface. This surface is given by

$$\Delta(\sigma_{ij}/\sigma_o)=\left[\alpha(\sigma_1/\sigma_o)+\beta(\bar{\sigma}/\sigma_o)+\gamma(J_1/\sigma_o)\right]=1 \qquad \text{eq. (2.57)}$$

where α,β and γ are constants for which $\alpha+\beta+\gamma=1$, σ_1 is the maximum principal stress, $\bar{\sigma}$ is the effective stress defined by equation 2.47 and J_1 is the first invariant of the stress tensor and is equal to $(\sigma_1+\sigma_2+\sigma_3)$. The relative magnitudes of α,β and γ reflect the sensitivity of a material's creep rupture time to σ_1, $\bar{\sigma}$ and J_1 respectively.

It has been shown (Leckie, 1986) that the form of f and g derived from the potential function Ω of equation 2.54 depends on the nature of the damage mechanism. The constitutive equation 2.56 is but one example for a damage mechanism of dilatent damage defined by the experimentally determined increment in creep rate from the steady-state creep rate and continuum damage mechanics. Theoretical formalisms can be developed for various damage mechanisms (Leckie, 1986). It is thus clear that an understanding of the underlying mechanism of damage in MMCs could be of great worth for the development of constitutive equations for their mechanical response.

CHAPTER 3

EXPERIMENTAL PROCEDURES

3.1 MICROSTRUCTURE AND COMPOSITION OF Al BASED PARTICULATE COMPOSITES

Three particulate reinforced aluminum matrix composites were investigated in this work. The material was supplied by Alcan Inc. Two of the composites were Duralcan based products consisting of aluminum alloy A356 reinforced with angular SiC particles of 15 μm average diameter. Their mechanical properties have been reported previously (Corbin, 1992). The composition of the alloy is given in Table 3.1. One composite was reinforced with 10% SiC by volume and the other had a volume fraction of 20%. The other composite supplied was a 6061 Al alloy reinforced with 20% by volume of proprietary spherical ceramic particles (Smith et al., 1993) of 14 μm average diameter. These ceramic microspheres, henceforth termed CMS in the present investigation, consist of a fine polycrystalline mixture of 3 phases with the following ranges of compositions in weight percent: 30% to 90% mullite ($3Al_2O_3{\cdot}2SiO_2$), 10% to 70% corundum (Al_2O_3) and 0% to 10% pseudobrookite {$(Fe,Al)_2TiO_5$}. Table 3.1 lists the chemical composition of the 6061 alloy.

Table 3.1 - Compositions in wt. % of Al alloys in MMCs

ALLOY	Si	Fe	Cu	Mn	Mg	Cr
A356	6.5-7.5	0.2 max	0.2 max	0.1 max	0.25-0.45	-
6061	0.4-0.8	0.7 max	0.15-0.40	0.15 max	0.8-1.2	0.04-0.35

Unless otherwise stated, the composites were given the following heat treatment, corresponding to the T4, or natural ageing condition. After a solution heat treatment at 540°C, the composites were quenched in warm water at a temperature of approximately 30°C. They were then aged at ambient

temperature for at least 14 days prior to testing. Examples of typical microstructures taken by optical metallography are given in figures 3.1 to 3.3 for the A356-10% SiC, A356-20% SiC and 6061-20% CMS respectively. The applied heat treatments have resulted in precipitates of Si in the A356 alloy and precipitates of Mg_2Si in the 6061 alloy in addition to the reinforcing phases.

3.2 HYDROSTATIC EXTRUSION OF THE PARTICULATE COMPOSITES

The particulate composites were hydrostatically extruded on an Innovac Inc., model 06 hydrostatic extrusion press designed for constant pressure extrusions. A schematic of the apparatus is shown in figure 3.4. The composites were extruded through one of two streamlined dies, one which produced a total plastic strain of 0.5 and the other which produced a total plastic strain of 1.0. The dimensions of the billets for these strain levels are shown in figure 3.5.

Prior to extrusion, the billet surface was ground with 800 grit SiC paper , coated with $MoSi_2$ and teflon tape to aid lubrication. The sample was introduced into the extrusion chamber and seated into the die. After sealing the chamber, the load applied to the pressurizing fluid was increased slowly. The load and displacement of the pressurizing ram were monitored. At a certain load, displacement would increase at a constant rate without application of additional force. On the load-displacement diagram, this is seen as a plateau region, which signalled the start of the extrusion. Due to friction, stick slip could occur so that the extrusion pressure for two samples of the same material could vary. In the same way, the extrusion rate also varied. When a specified displacement was obtained, the pressure was reduced to ambient pressure to stop the extrusion. The product length was cut and the remaining part of billet was pressed out of the die.

3.3 STRAIN AND DAMAGE MEASUREMENTS IN THE EXTRUDED PARTICULATE MMCs

To observe the effects of the extrusion process on the microstructure of the composites, the samples were sectioned longitudinally and were mounted in epoxy. The grinding and polishing was done

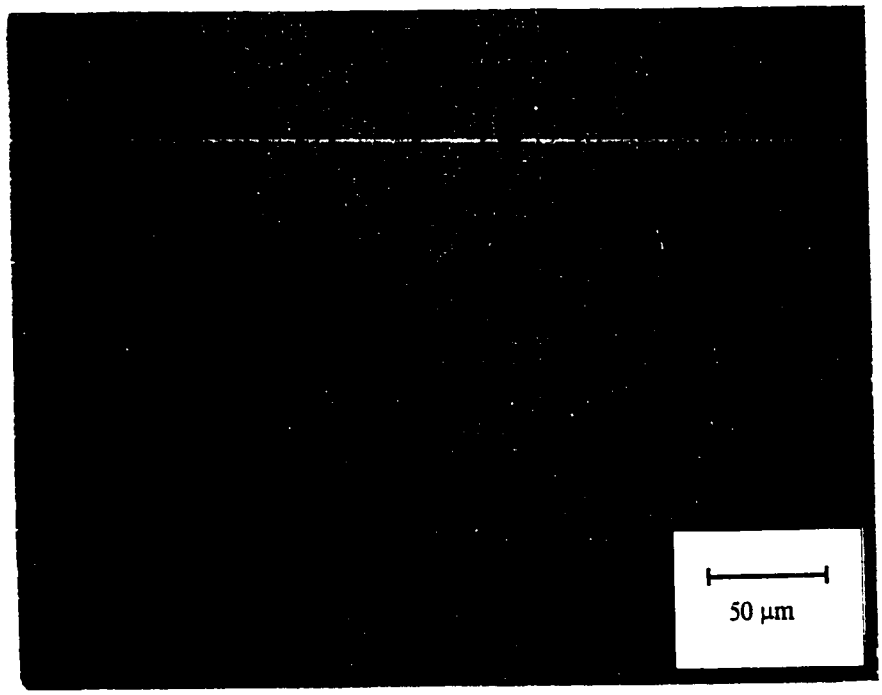

Figure 3.1 Microstructure of the A356-10% SiC composite.

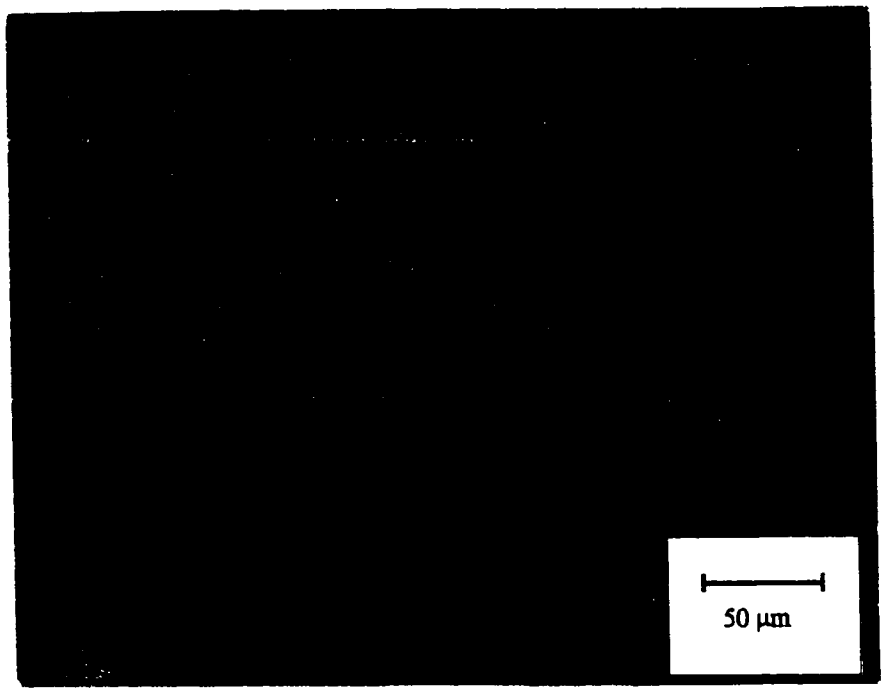

Figure 3.2 Microstructure of the A356-20% SiC composite.

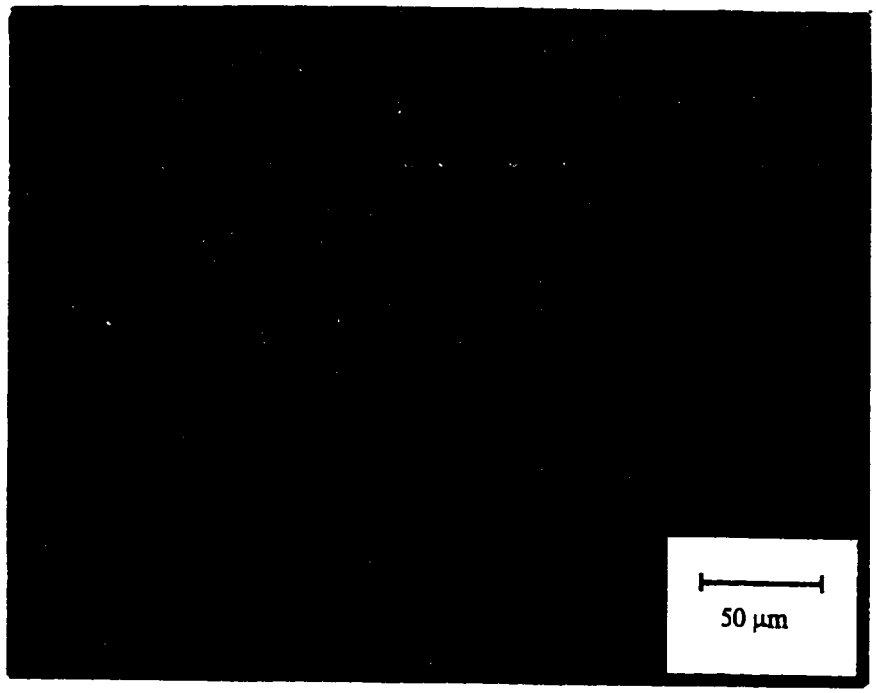

Figure 3.3 Microstructure of the 6061-20% CMS composite.

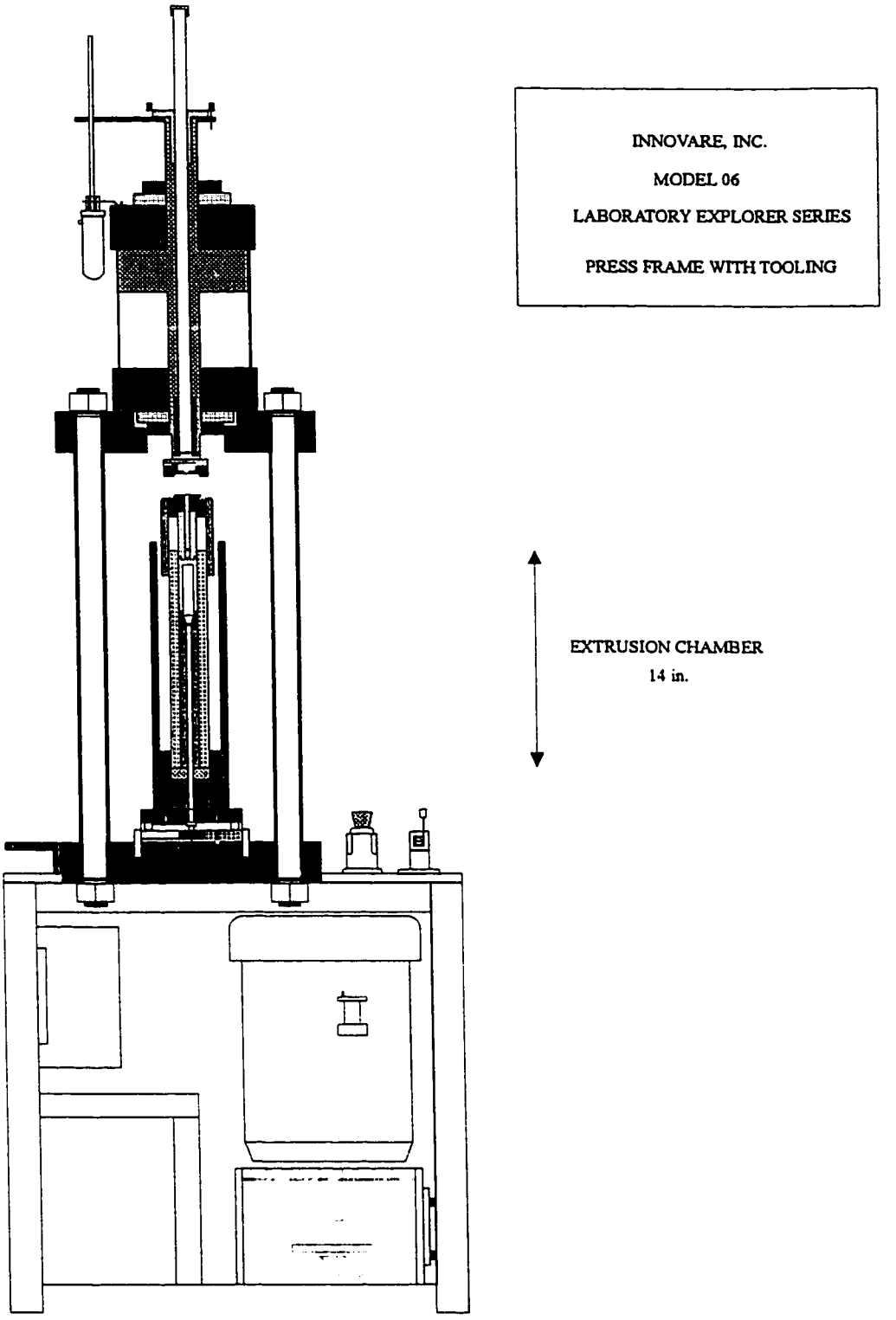

Figure 3.4 Schematic diagram of the hydrostatic extrusion press used in this study.

0.50 STRAIN BILLET

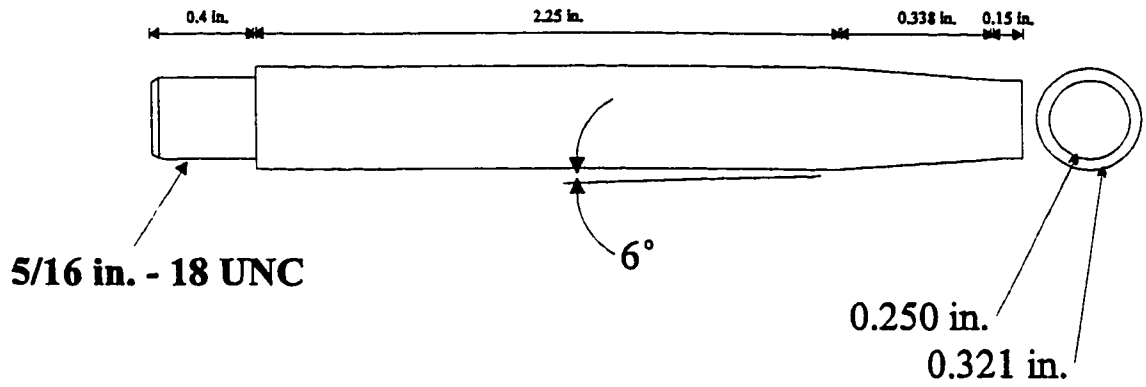

1.00 STRAIN BILLET

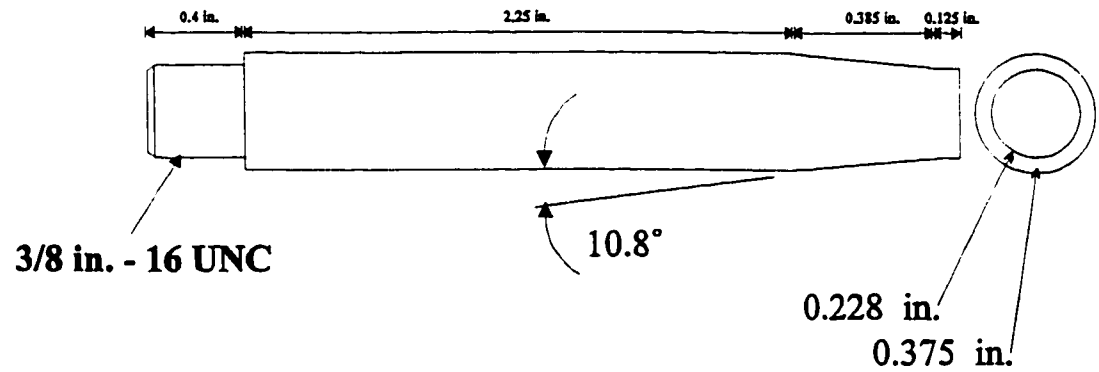

Figure 3.5 Schematic diagram of the billet dimensions for extrusion to strains of 0.5 and 1.0.

on an automatic polishing machine under a load of approximately 150 N. Three sheets of SiC abrasive paper were used for 20 seconds each in the following order of grit size: 180,320,500,1000 and 1200. Polishing was done for 10 minutes using the 6 μm diamond spray and then 5 minutes using the 3 μm diamond spray.

The true plastic strain ε at each point along the billet section is given by

$$\varepsilon = 2\ln\left(\frac{D_o}{D}\right) \qquad \text{eq. (3.1)}$$

where D_o is the initial billet diameter and D is the diameter at the point of interest.

Diameters were measured from photographs taken at specified points x along the length of the section. The measurement of the points x was accurate to 0.1 mm. The diameters taken from the photographs were measured to an accuracy of approximately 0.01 mm. Corrections had to be applied to the diametral measurements because the sections were eccentric. Assuming that the billets were sectioned on a plane which did not contain the extrusion axis, the corrected diameter (in mm) is given by

$$D_{cor} = 2\sqrt{(mx+b)^2 + \left(\frac{D_{photo}}{2}\right)^2} \qquad \text{eq. (3.2)}$$

where D_{photo} is the diameter (in mm) measured from the photographs at point x and the constants b and m are given by

$$b = \sqrt{\left(\frac{D_o}{2}\right)^2 - \left(\frac{D_{photo@x=x_o}}{2}\right)^2} \qquad \text{eq. (3.3)}$$

$$m = \frac{\sqrt{\left(\frac{D_f}{2}\right)^2 - \left(\frac{D_{photo@x=x_f}}{2}\right)^2} - b}{x_f - x_o} \qquad \text{eq. (3.4)}$$

where the subscripts o and f refer to the values in the product and unextruded regions of the billet respectively.

To obtain a measure of damage as a function of the applied strain defined above, the area fraction of cracked particles was counted for the three particulate composites as a function of x. Thus, the damage is defined as

$$\text{DAMAGE} = \frac{\%\ \text{OF TOTAL AREA OF DAMAGED PARTICLES}}{\%\ \text{OF TOTAL AREA OF PARTICLES}} \qquad \text{eq. (3.5)}$$

The denominator in eq. (3.5) is equivalent to the particle volume fraction if it is assumed that the reinforcement is distributed isotropically. Metallographic evidence of damage was mainly in the form of fractured particles. For each longitudinal location defined by x, nine images were acquired and analysed to calculate the amount of damage. The area sampled for each x corresponded to approximately 2.5×10^{-8} m^2.

3.4 MECHANICAL TESTING OF COMPOSITES

The composites were tested in tension to compare the change in mechanical properties occuring due to the extrusion. In order to make a quantitative comparison, the materials were tested both prior to extrusion and after extrusion. Since the extruded products had a diameter less than 6.5 mm, a tensile specimen had to be designed so that its largest diameter did not exceed the aforementioned value. Figure 3.6 shows the dimension of the specimen chosen. This geometry was chosen in accordance with ASTM standard E8 for round specimens.

The tensile testing was performed on the MTS Testar hydraulically driven system. The tests were conducted at a displacement rate of 0.005 mm/sec. This corresponds to an inital strain rate of 4.4×10^{-4} sec^{-1} for the standard specimens described above. The load cell used was rated for 100 kN and it had a resolution of approximately 3.4 N. The displacement was measured with an LVDT in the actuator and a

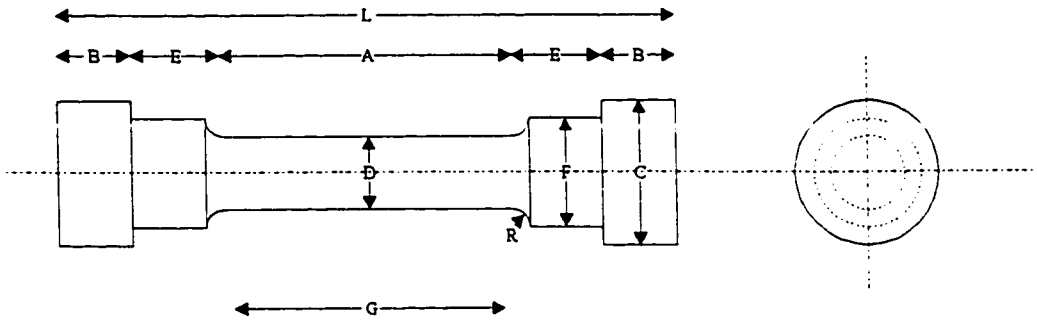

DIMENSIONS

A - LENGTH OF REDUCED SECTION - 0.625 + 0.005 in.
B - LENGTH OF END SECTION - 0.139 +/- 0.005 in.
C - DIAMETER OF END SECTION - 0.198 +/- 0.002 in.
D - DIAMETER - 0.113 +/- 0.002 in.
E - LENGTH OF SHOULDER AND FILLET - 0.208 +/- 0.005 in.
F - DIAMETER OF SHOULDER - 0.141 +/- 0.002 in.
G - GAGE LENGTH - 0.450 +/- 0.005 in.
L - OVERALL LENGTH - 1.319 +/- 0.005 in.
R - RADIUS OF FILLET - 3/32 in.

Figure 3.6 Dimensions of the specimens for tensile testing of extruded composites.

MTS model 632.41C-01 extensometer on the sample. The linearity and calibration of the extensometer is reported elsewhere (Gharghouri, 1996). The data acquisition system recorded time, LVDT displacement, load and extensometer displacement at a rate of about 2 points/sec.

Similar tensile tests were conducted on samples with an hourglass gauge section. The dimensions of these samples are given in figure 3.7. The materials machined into these shapes were the A356-10% SiC and the 6061-20% CMS particulate composites. The tests were conducted at a displacement rate of 0.005 mm/sec. During the test, photographs of the gauge section were taken at 20 second intervals to monitor the dimensions of the sample as a function of time.

A tensile test was also done on a specimen of larger size than the one described by figure 3.6. The reason for the specimen change was to maximize the gauge section volume for density measurements on 6061-20% CMS following the tensile testing. The sample dimensions are shown on figure 3.8. To increase the number of points acquired for the test compared to the tests described above, a displacement rate of 0.001 mm/s was chosen. This displacement rate corresponds to an initial strain rate of 7.1×10^{-5} sec^{-1}, which is approximately one order of magnitude smaller than what was used for the tests conducted on the smaller samples. After the test, pieces of the gauge section were cut away from the specimen, making sure that the material chosen was well away from the neck. Density measurements were made on both these pieces and undeformed specimens using the Archimedean method. The mass of the materials was measured in pure water and in air and the density was found using:

$$\rho_c = \frac{m_a \rho_w - m_w \rho_a}{m_a - m_w} \qquad \text{eq. (3.6)}$$

where m refers to the mass, ρ refers to the density and the subscripts c,w,a refer to the composite, water and air respectively. To reduce the error involved with the mass of the suspending wire in the fluid, a 10 micron diameter Kevlar 49 fibre of density 1.44 g/cm^3 was chosen. The temperature of the fluids used for

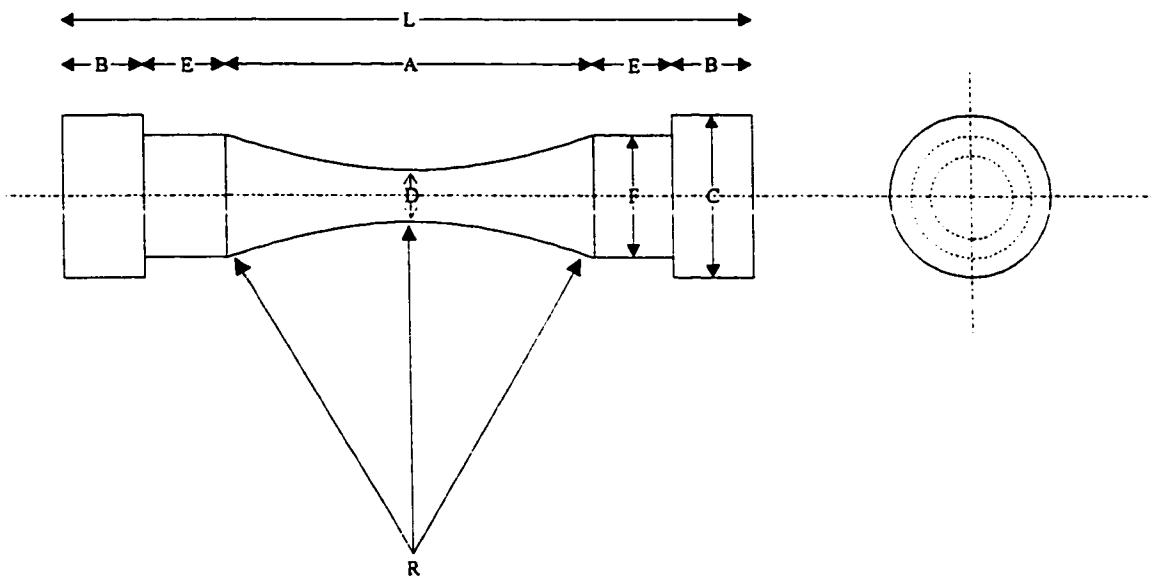

DIMENSIONS

A - LENGTH OF REDUCED SECTION - 0.625 +/- 0.005 in.
B - LENGTH OF END SECTION - 0.250 +/- 0.005 in.
C - DIAMETER OF END SECTION - 0.375 +/- 0.005 in.
D - DIAMETER - 0.125 max
E - LENGTH OF SHOULDER - 0.350 +/- 0.005 in.
F - DIAMETER OF SHOULDER - 0.250 max
L - OVERALL LENGTH - 1.825 in.
R - RADIUS OF FILLET - 0.453 in.

Figure 3.7 Dimensions of the tensile specimens with an hourglass shaped gauge section.

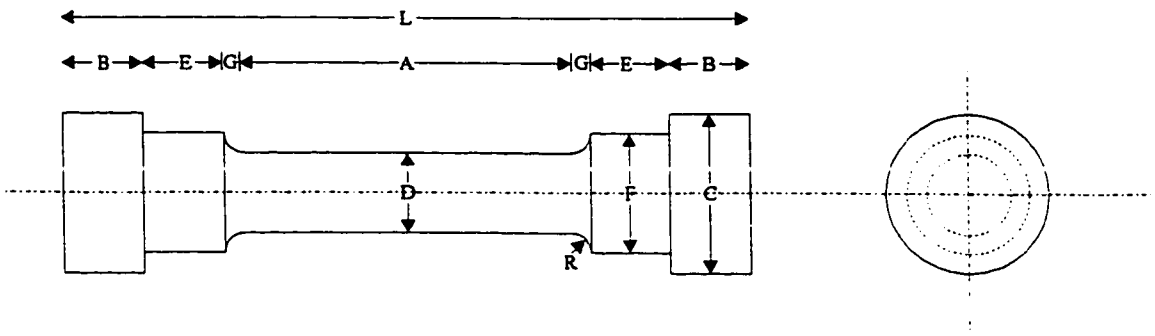

DIMENSIONS

A - LENGTH OF REDUCED SECTION - 0.625 + 0.005 in.
B - LENGTH OF END SECTION - 0.250 +/- 0.005 in.
C - DIAMETER OF END SECTION - 0.375 +/- 0.002 in.
D - DIAMETER - 0.200 +/- 0.002 in.
E - LENGTH OF SHOULDER - 0.350 +/- 0.005 in.
F - DIAMETER OF SHOULDER - 0.250 +/- 0.002 in.
G - LENGTH OF FILLET - 0.094 +/- 0.002 in.
L - OVERALL LENGTH - 2.013 +/- 0.005 in.
R - RADIUS OF FILLET - 3/16 in.

Figure 3.8 Dimensions of the tensile specimen used for subsequent density measurements.

the weighing media (air and water) was monitored by a thermometer to within ± 1°C. This reading was used to account for the variation of density of air and water with temperature. A standard table (Reed, 1988) was consulted for the temperature dependent densities. The weighings were done 10 times for each sample and the error was estimated as the standard deviation to the average density calculated by eq. (3.6).

3.5 FABRICATION OF COPPER-TUNGSTEN AND COPPER-SAPPHIRE COMPOSITES

The copper matrix composites were reinforced with continuous reinforcements of Tungsten or single crystal sapphire (Al_2O_3). The main objective in the fabrication process was to control the resulting fibre distribution in the finished product. In order to achieve this control over the reinforcement location, a liquid infiltration method was devised to cast copper around fiber arrangements held stationary by carbon spacers.

Under a vacuum of approximately 50 mtorr, an ingot of Cu was heated by an induction coil in one of two high density carbon split moulds shown schematically in figure 3.9. Fibres were affixed to the spacers by introducing them into machined holes having the required geometrical distribution. Larger holes were also made into the top spacer to permit infiltration of the liquid Cu. The mould and its contents were heated slowly in the coil until the Cu was observed to melt. The mould was then pulled out of the induction coil at an approximate speed of 57 mm/hr.

The chemical compositions of the Cu and W, based on the work of Poole (1993), are presented in Table 3.2 and Table 3.3. Table 3.4 lists the impurity levels (in parts per million) in the sapphire fibres, as reported by Saphikon Inc.

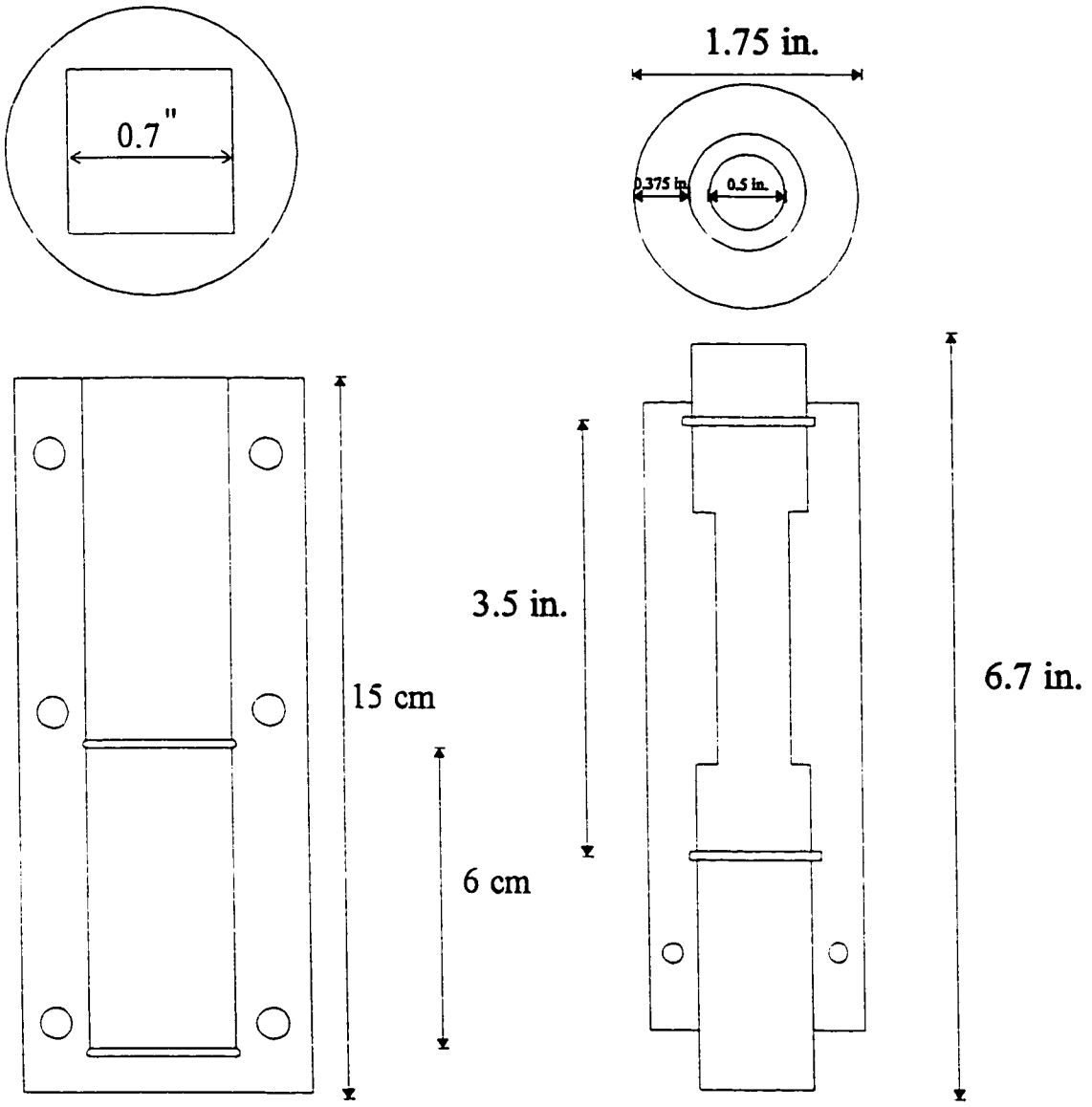

Figure 3.9 Schematic diagram of the carbon split moulds used for the fabrication of continuous fibre composites.

Table 3.2 - Chemical analysis of Cu (concentrations of impurities in parts per million)

Bi	Cd	Pb	Hg	O_2	P	Se	S	Te	Zn
<1	<1	4	<1	3	2	<1	9	<1	<1

Table 3.3 - Chemical analysis of W fibres (concentrations of impurities in parts per million)

Al	Ca	Cr	Cu	Fe	Mg	Mn	Ni	Si	Sn	Na	K	Mo	C
8	<1	2	<1	5	<1	<1	2	1	1	<5	62	<8	10

Table 3.4 - Chemical analysis of Al_2O_3 fibres (concentrations of impurities in parts per million)

Li	B	Na	Mg	Si	S	Ca	Ti	Cr	Mn	Fe	Mo
0.01	0.3-3	0.5-5	~2	10-30	2-7	1-10	0.2-2	0.2-8	0.2-2	2-10	1-10

3.6 HYDROSTATIC EXTRUSION OF Cu-W COMPOSITES

Hydrostatic extrusion billets to result in a total strain of 0.5 were machined out of the fabricated Cu-W composites. The geometry of the billets and the extrusion procedure corresponded to the one outlined in Section 3.2. Three billets were made with a square distribution of 1 mm diameter fibres. This geometry is illustrated in figure 3.10. One billet was made with a single 2 mm W fibre centered into the Cu matrix. This billet was longitudinally sectioned through the middle of the fibre by electrical discharge machining, a square gold grid of size 36.7 ± 0.2 μm was deposited on the polished surface and the 2 halves were mechanically joined. The procedure used to make the fiducial grid is outlined in the following section.

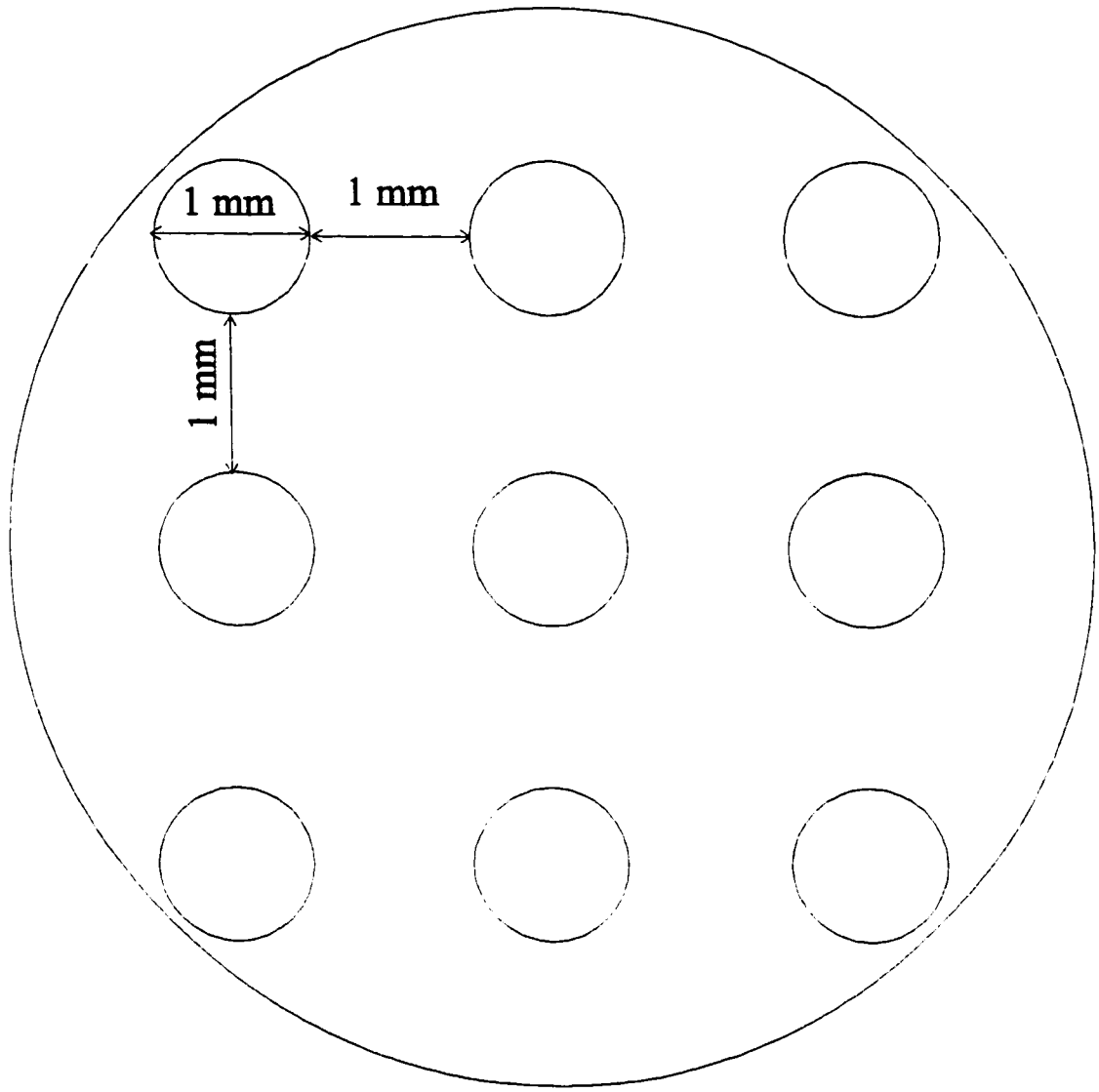

Figure 3.10 Distribution of W fibres in the Cu-W extrusion billets.

3.7 FABRICATION OF FINE METALLIC GRIDS

In order to make accurate microstrain measurements on surfaces of composites with high spatial resolution, fine, regular grids were made by an electron lithography method (Attwood and Hazzledine, 1976). Figure 3.11 shows the steps involved in making metallic grids. The cross-section to be gridded was polished to a 1 μm finish. A few drops of chlorobenzene/ 6% polymethylmethacrylate (PMMA) solution were dropped onto the surface. The solution was supplied by KTI Chemicals Inc.. The PMMA had a molecular weight of 496000 ± 10% (g/mol of chains) which corresponds to 5600 mers (repeat units) per chain. The samples were spun for 20 seconds at a speed of 4000 rpm. According to data furnished by the supplier, this produces a film thickness of about 0.4 μm. The film was then baked at 175^{0}C for 1 hour. The exposure of the electron resist in a Phillips 501B scanning electron microscope (SEM) was optimized for the following conditions:

a) accelerating voltage: 30 kV

b) working distance: ~30 mm

c) magnification: 20x

d) spot size: ~1000 nm

e) line time: 1 sec/line

f) number of lines: 250

Under these conditions, the area of film adequately exposed was a square of approximately 6 x 6 mm. Development was done in a bath of 75% 4-butanone (MEK)/25% ethanol under ultrasonic agitation for 75 seconds. The sample was then etched in a 10% $FeCl_3$ solution for 5 seconds. Following etching, gold was sputtered onto the sample. The mask was then lifted by agitation in chlorobenzene. A final grid is shown in figure 3.12 which corresponds to the grid deposited on the split billet for hydrostatic extrusion described in section 3.6.

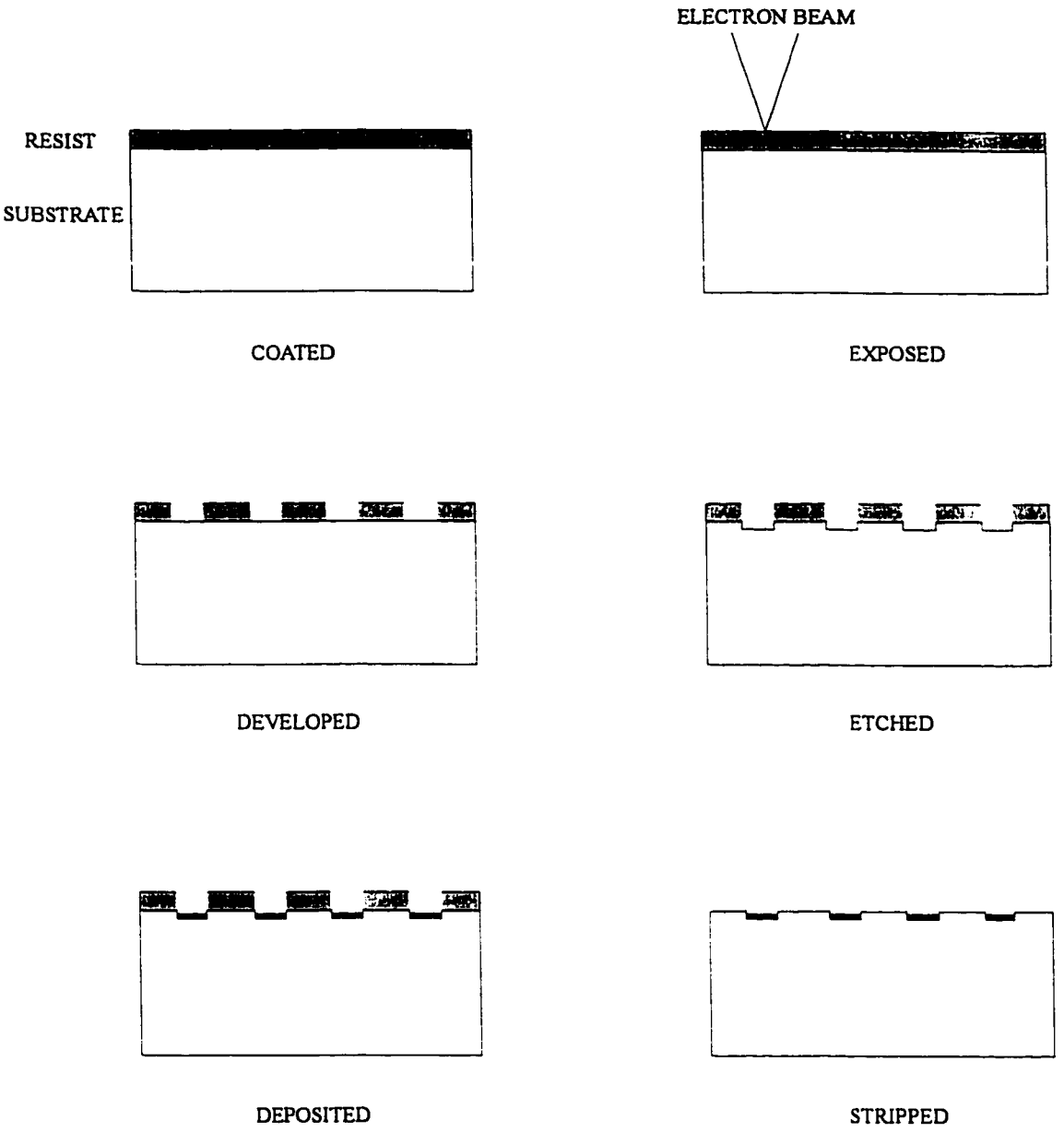

Figure 3.11 Schematic diagram illustrating the steps involved in electron beam lithography.

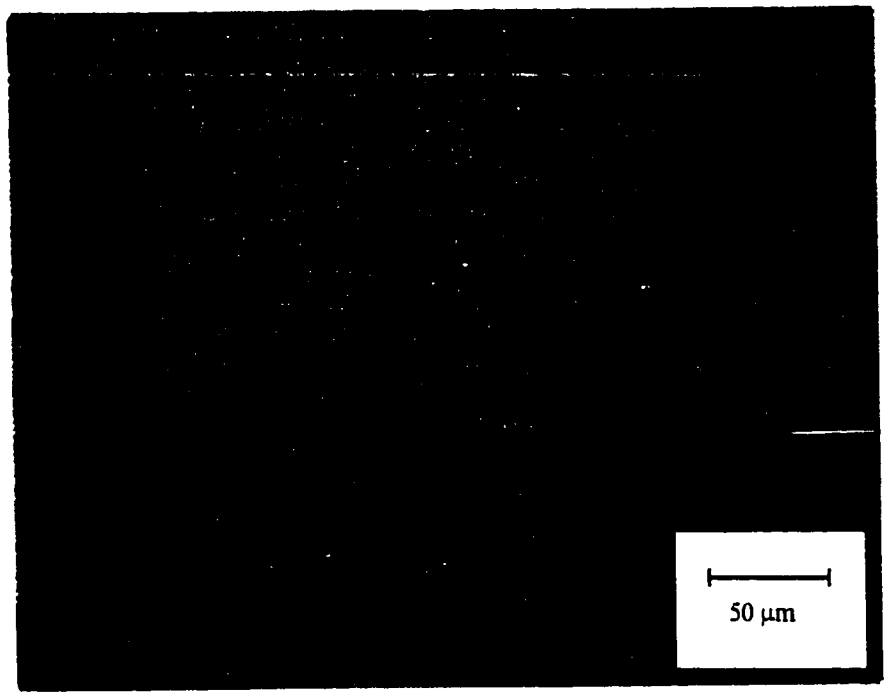

Figure 3.12 Fiducial grid deposited on the Cu-W split extrusion billet.

Typical grids had a spacing ranging between 20-30 μm with a line width of 1-3 μm. The accuracy of the grid spacing was measured within 1.5 μm. The angle between the vertical and horizontal lines, which define the orthogonality of the grid, was within ±2.5° of 90°. This angle was measured to an accuracy of 0.5°.

3.8 PROCESSING AND PLANE STRAIN COMPRESSION TESTING OF Cu-W COMPOSITES

Inspection of the composite billets revealed some amount of gas porosity, especially near the top of the billets. This was minimal for single and double fibre composites but more severe for the arrayed fibre arrangements which will be discussed below. Following cutting and machining of the billets, care was taken to discard the top portions of the billets affected by the gas porosity.

In order to investigate the effect of spatial distribution of fibres on the plastic flow of MMCs, rectangular samples were produced from the as-fabricated billets. Composites with various fibre arrangements were produced. Single centered fibre billets were made to investigate the effect of one fibre embedded in a Cu matrix. Other billets were fabricated consisting of two tungsten fibres separated by a distance of 1mm. Samples were machined from these billets to yield three arrangements of these fibres with respect to the plane strain compression axis. These arrangements, denoted 0°, 45° and 90° are shown schematically in figure 3.13 a).

The simple arrangements described above do not represent practical distributions of fibres. Billets with more realistic arrangements in terms of the volume fraction of reinforcement were fabricated. The first of these, denoted the clustered arrangement, is illustrated in figure 3.13 b). This composite consisted of a regular square array of 6 x 6 fibres with one extra fibre in the centre. The

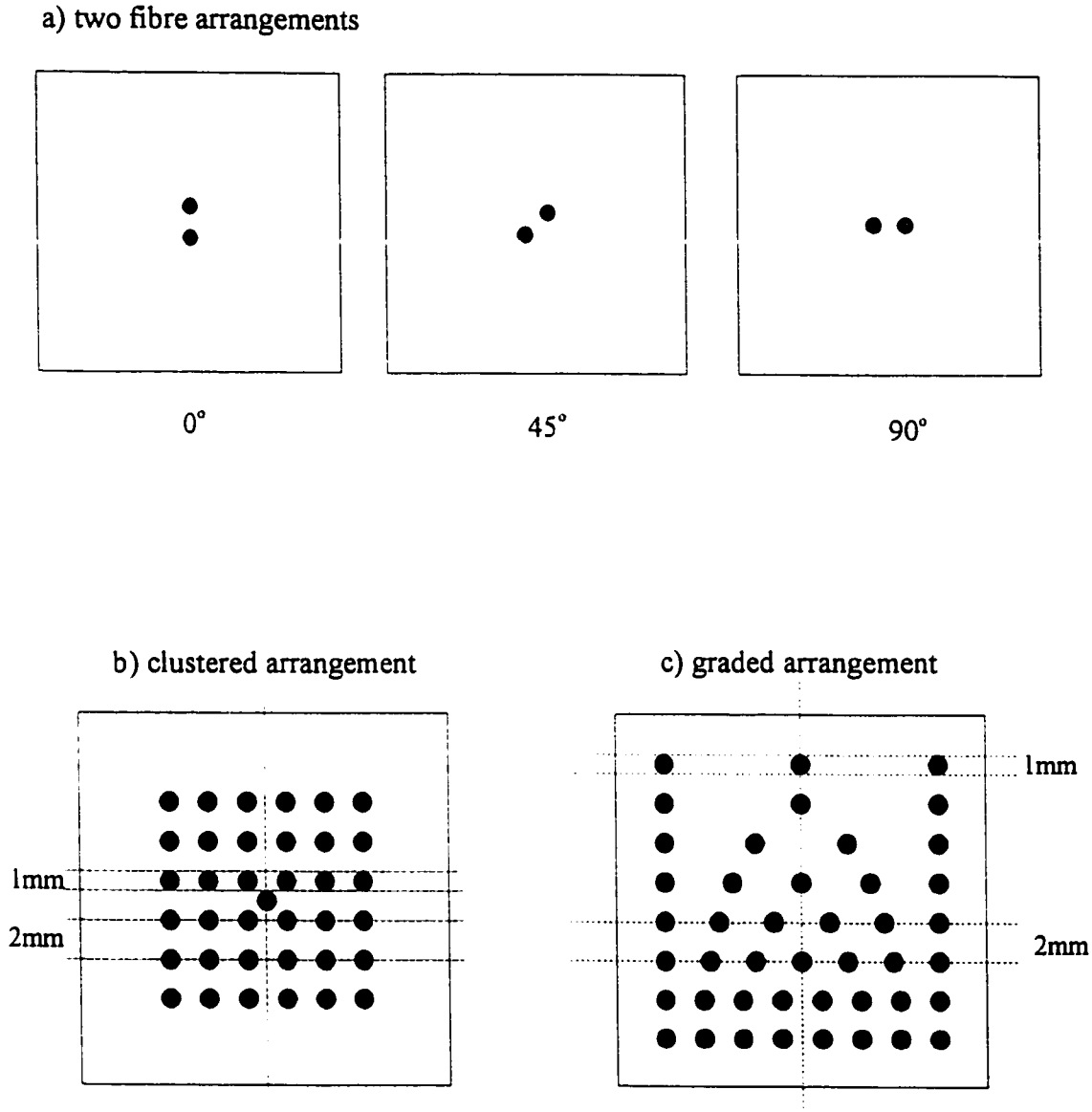

Figure 3.13 Schematic diagram representing the arrangement of fibres in the Cu-W model composites.

purpose of this extra fibre was to effectively create a region of higher local fibre volume fraction in the composite, or in other words, a cluster. The second arrangement, called the graded arrangement, is shown on figure 3.13 c) and consists of a composite where the local volume fraction of fibres varies with the height of the sample. Thus, in this work, the volume fraction in the graded composites was varied from 3 fibres per cross-section at the top of the sample to 8 fibres per cross-section at the bottom of the sample.

An extra requirement for the plane strain compression samples was that the Cu matrix grain size should be fine enough so that the matrix could be modelled as a continuum. For this condition to be valid, the grains had to be at least an order of magnitude smaller than the fibre diameter. The fabrication process described in Section 3.5 produced very large grains in the Cu, due to the very slow cooling rate. In order to refine the grains, a thermo-mechanical treatment was applied to cause recrystallisation of fine Cu grains in the samples.

The mechanical part of the treatment consisted of deformation in plane strain to a strain of between 5-10%, dependent on the fibre volume fraction. Composites with arrays of many fibres, the clustered and graded arrangements described above, were deformed to 5% and the composites with low volume fractions were deformed 10%. Rotating the samples 90^0 to the plane strain axis, the procedure was repeated. The procedure was executed on an MTS Testar system described previously, at a deformation rate of 0.01 mm/sec. The apparatus used to constrain the compression specimens is described elsewhere (Deschamps, 1994). The composite was then given a recrystallisation heat treatment at 600^0C for 1 hour. The resulting microstructure of the Cu following this treatment is shown in figure 3.14. It can be seen that the grain size of the Cu is of the order of 50 microns, which satisfies the requirement of grain size to fibre diameter ratio described above. It is also to be noted that this procedure closed existing pores from fabrication to a significant extent.

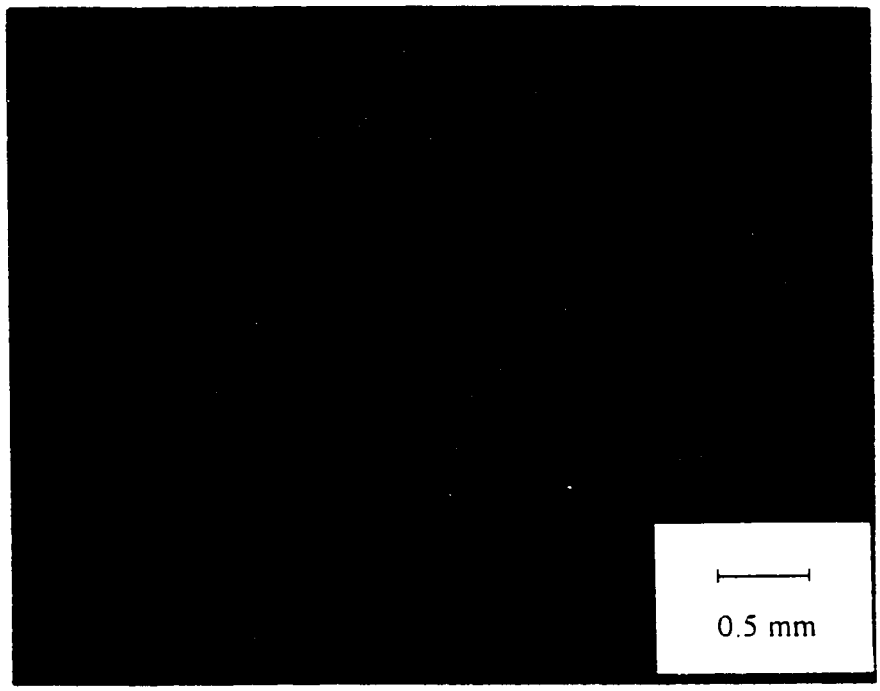

Figure 3.14 Microstructure of the recrystallized Cu matrix following thermo-mechanical processing of the fabricated Cu-W composite billets.

The recrystallised samples were then milled to produce flat, orthogonal surfaces parallel to the fibres. The faces of the rectangular specimens were ground flat. One of the faces was then further polished to a 1 μm finish. A metallic grid was applied to this surface by following the procedure outlined in Section 3.7. The sample was then deformed using the MTS Testar system in the plane strain compression apparatus discussed above. The deformation rate was 0.01 mm/sec and the total applied strain was varied from one sample to another in order to gauge the effect of applied strain on the plastic flow of the composites.

The strain field created by the flow of the composites was determined by measuring the coordinates of deformed grid elements and applying the method outlined by Sowerby (1985). In this analysis, a vector **x** defining a vertex on the deformed grid, is mapped to **X**, the vector defining the same vertex prior to deformation, by $\mathbf{x} = \mathbf{F}\ \mathbf{X}$, where F is defined as the deformation gradient tensor. This tensor has four coefficients for a fiducial grid deformed in plane strain. These coefficients are found using the coordinates of the deformed and undeformed grids, as illustrated in figure 3.15. The tensor F is most easily expressed in the following matrix form

$$\begin{matrix} F_{11} \\ F_{12} \\ F_{21} \\ F_{22} \end{matrix} = D \begin{bmatrix} Y_2 & -Y_1 & 0 & 0 \\ -X_2 & X_1 & 0 & 0 \\ 0 & 0 & Y_2 & -Y_1 \\ 0 & 0 & -X_2 & X_1 \end{bmatrix} \begin{vmatrix} x_1 \\ x_2 \\ y_1 \\ y_2 \end{vmatrix} \qquad \text{eq. (3.7)}$$

where D is defined as $1/(X_1Y_2 - X_2Y_1)$. We can now express U and V, the right and left stretch tensors respectively, in the following way

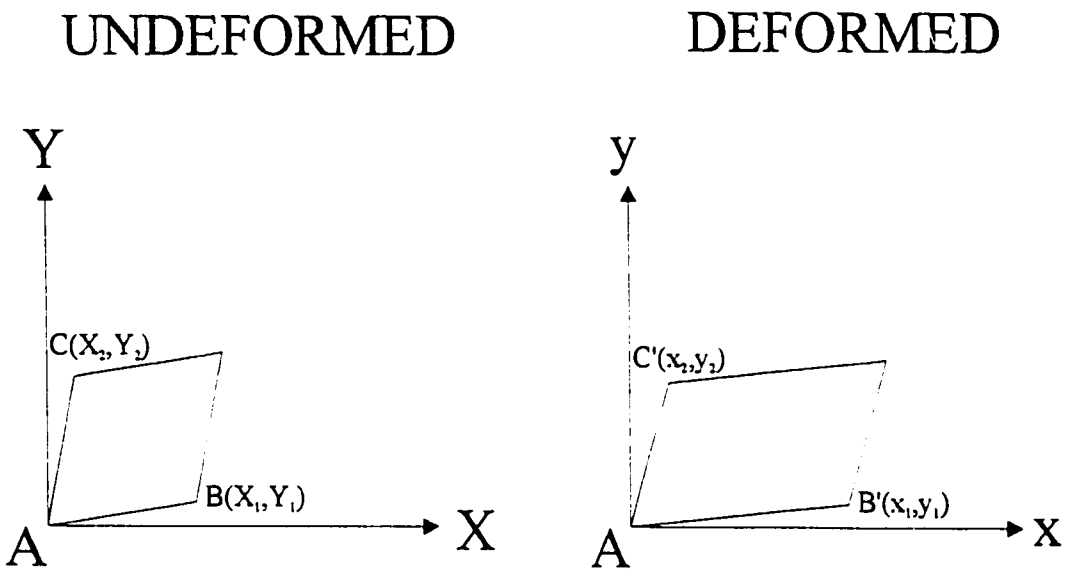

Figure 3.15 Schematic diagram of the coordinate system used for grid analysis.

$$\begin{aligned} R \cdot U &= F \\ V \cdot R &= F \\ R \cdot R^T &= I \end{aligned} \qquad \text{eq. (3.8)}$$

where R and its transpose R^T are the rigid body rotation tensors. It follows that

$$\begin{aligned} U^2 &= F^T \cdot F \\ V^2 &= F \cdot F^T \end{aligned} \qquad \text{eq. (3.9)}$$

The eigenvalues or principal values of U^2 and V^2 are identical. For convenience, we can define a vector C such that $C=U^2$. The components of C are given below in terms of the components of F

$$\begin{aligned} C_{11} &= F_{11}^2 + F_{21}^2 \\ C_{12} = C_{21} &= F_{11}F_{12} + F_{21}F_{22} \\ C_{22} &= F_{12}^2 + F_{22}^2 \end{aligned} \qquad \text{eq. (3.10)}$$

The principal values of C, λ^2_{11} and λ^2_{22}, are given by

$$\lambda_{11}^2, \lambda_{22}^2 = \frac{C_{11} + C_{22}}{2} \pm \sqrt{\left(\frac{C_{11} - C_{22}}{2}\right)^2 + C_{12}^2} \qquad \text{eq. (3.11)}$$

The true principal strains ε_{11} and ε_{22} are thus given by

$$\varepsilon_{11} = \ln \lambda_{11}, \quad \varepsilon_{22} = \ln \lambda_{22} \qquad \text{eq. (3.12)}$$

In plane strain compression, the equivalent strain $\bar{\varepsilon}$ is given by

$$\bar{\varepsilon} = \sqrt{\frac{2}{3}\left(\varepsilon_{11}^2 + \varepsilon_{22}^2\right)} \qquad \text{eq. (3.13)}$$

This equivalent strain can be plotted to represent the spatial distribution of strain in a deformed specimen. In order to expedite the above numerical procedure, a computer program was written in the FORTRAN language. The source code for this program is listed in Appendix A. The input data for the program was the coordinates of the deformed grid elements and the dimensions of the undeformed grid. The output consisted of the equivalent strain in eq. (3.13) corresponding to the aforementioned coordinates.

3.9 PLANE STRAIN TESTING AND OPTICAL MEASUREMENTS IN Cu-SAPPHIRE

Following the production procedure outlined in Section 3.5, a Cu-sapphire billet with one centered fibre was prepared for plane strain compression testing and optical measurements. The thermomechanical treatment outlined in Section 3.8 to recrystallise the matrix in the Cu-W samples could not be utilised for Cu-sapphire due to fibre cracking at low strains. It was thus necessary to test this composite as-fabricated. This meant that the matrix grain size was large, of the order of several millimeters on cross-sections defined by perpendiculars along the fibre direction. Similar to the Cu-W composites, orthogonal sides were milled parallel to the fibre and the faces were subsequently ground flat. One face was polished to a 1 μm finish for optical measurements and the deposition of a fiducial grid around the fibre.

Optical measurements of the R_1 and R_2 transitions of the Cr^{3+} impurities in the sapphire lattice were conducted on an ISA MOLE S300 Raman spectrometer. An argon laser operating at an excitation wavelength of 514.5 nm and a power of 20 mW was focused through a 10x objective lens at least 2mm into the sapphire. The spectrum was acquired for a minimum of 1.5 minutes. In order to monitor and compensate for the effects of temperature variations on the acquired spectra, a characteristic 14431.118 cm^{-1} transition in Ne was acquired before and after every test on the sapphire.

Spectra were recorded for a free fibre, the as-fabricated composite and for the composite following plane strain deformations in increments of 0.60± 0.05 % up to a total plastic strain of 1.2 %. The plane strain compressions were conducted as outlined in Section 3.8.

CHAPTER 4

EXPERIMENTAL RESULTS

In this chapter, results pertaining to the investigation of the mechanical properties of particulate and model composites will be presented. The experimental campaign outlined in Chapter 3 was chosen so that a clearer understanding be gained of the resultant mechanical properties of MMCs following plastic deformation and of the consitutive laws to describe these properties.

The results of the extrusions of the three particulate composite systems will be summarized and the salient observations will be described in Section 4.1. In Section 4.2, the form and level of damage induced in these composites will be identified and quantified. The effect of extrusion on the constitutive laws to describe the mechanical behaviour of the composites will be examined in Section 4.3, through the use of tensile tests. The results of these tensile tests will be compared for the three composite systems as fabricated and after extrusion. The tensile tests will be analysed for comparison of composite stiffness, flow stress and instability properties. The damage level induced in an as-fabricated 6061-20% CMS sample tested in tension will be evaluated from density measurements, in order to measure the amount of dilatation at the point of tensile instability. The work on tensile instabilities and the incorporation of damage in constitutive laws in extruded and as-fabricated composites will be expanded in Section 4.4 by making damage and dilatation measurements on tensile samples with hourglass gauge sections.

The particulate composite systems with which this work is concerned are complex due to many microstructural variables such as particle volume fraction, size, shape as well as the statistical and spatial variations of these quantities in the microstructure. Thus, model composite systems, where control of the aforementioned variables was possible, were fabricated and tested. It was hoped that the control over these microstructural variables would help define the effect of a single parameter on the mechanical

behaviour of composite materials. The next three sections of this chapter deal with experiments done on these model continuous fibre composites. The first of these, Section 4.5, will deal with the hydrostatic extrusion of model Cu-W composites and the salient features of the resulting extruded microstructures. The following section, Section 4.6, will outline the results of the investigation of reinforcement distribution effects on the global and local plastic flow patterns of the Cu matrix in the model continuous Cu-W fibre composites. The last section will report on the use of optical measurements in a single crystal sapphire fibre embedded in a Cu matrix for direct measurements of residual stresses in fibres due to fabrication and plastic deformation.

4.1 HYDROSTATIC EXTRUSION OF PARTICULATE COMPOSITES

The three particulate MMCs described in Section 3.1 were hydrostatically extruded into a chamber which was at ambient pressure. The two billet geometries and the corresponding tooling of the extruder were selected to achieve total true strains of 0.5 and 1.0 at the die exit, as described in Section 3.2.

The pressure on the ram as well as the displacement of the pressurizing ram were recorded for all tests. To illustrate the results of the extrusions, this pressure displacement trace is plotted for the A356-10% SiC, A356-20% SiC composites and the unreinforced matrix on figure 4.1. All three traces correspond to extrusions to a strain of 0.5.

Some general observations can be made about the effect of reinforcements on the ease of extrusion. If we equate this ease of extrusion with the maximum load needed to complete the operation, it can be seen from figure 4.1 that it becomes more difficult to extrude the pMMCs as the volume fraction of reinforcement increases. This trend was general and also applied to the 6061-20% CMS composite.

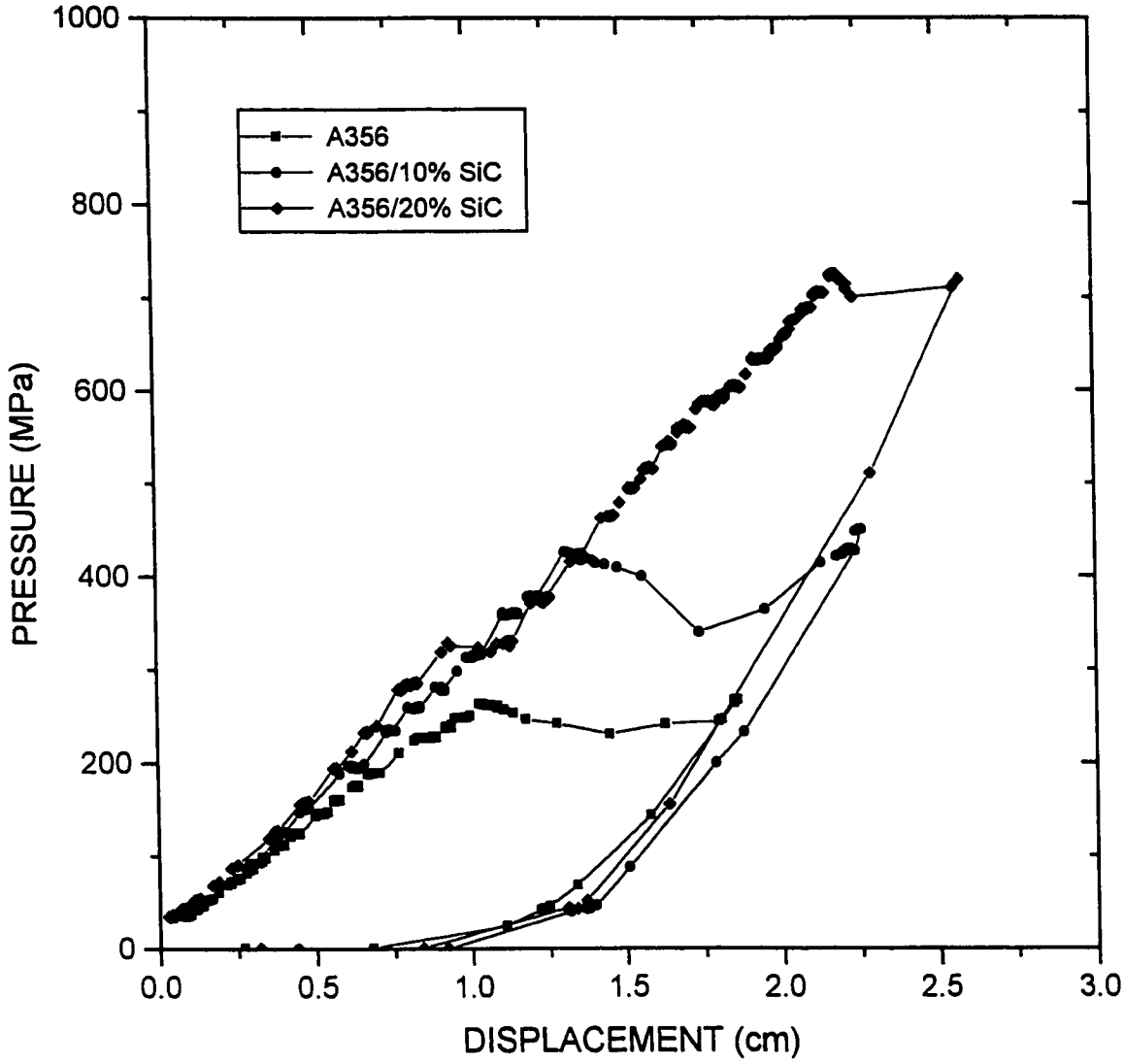

Figure 4.1 Extrusion curves for A356, A356-10% SiC and A356-20% SiC.

A simple analysis of the extrusion process was presented in Chapter 2, with the result that the required pressure P for extrusion is given by

$$P = \sigma_o \ln\left(\frac{R_F}{R_o}\right)^2 \qquad \text{eq. (4.1)}$$

where R_f and R_o are the initial and final radii of the extrusion billet respectively. Equation 4.1 predicts that extrusion pressure will be proportional to the flow stress σ_o. It will be shown later in Section 4.1 that the flow stress of A356 is not increased by more than 40% by adding 20% by volume SiC particles, yet the pressure required to extrude A356-20% SiC is 3x higher than the one required to extrude unreinforced A356. It thus seems that the effect of volume fraction of reinforcement on extrusion P cannot be explained by the change in flow stress only. As discussed in Chapter 2, by considering the contribution of friction at the die wall, eq. (4.1) is modified and becomes

$$P = \sigma_o\left(\frac{1+B}{B}\right)\left(1-\left(\frac{R_o}{R_F}\right)^{2B}\right) \qquad \text{eq. (4.2)}$$

where $B=\mu/\tan\alpha$. Thus, in eq. (4.2), the pressure required for extrusion is not only related to the flow stress of the material, but also to the coefficient of friction μ and the die half angle α. An increase in the coefficient of friction at the die wall due to the addition of hard wear resistant particles may thus help explain the large differences in extrusion pressures between the composites and the unreinforced matrix materials.

The effect of the total reduction was similar. For the same billet material, increasing the total strain from 0.5 to 1.0 resulted in an increase in maximum extrusion pressure. This effect was most clear for the A356-20% SiC material. The pressure required to extrude this material to a strain of 0.5 was 550 MPa compared to a pressure of 1.3 GPa for a strain of 1.0 extrusion. For these reductions, eq. (4.1) predicts a doubling of the extrusion pressure. The results in the present work are thus in general agreement with the predictions of eq. (4.1). The predictions of eq. (4.2) cannot be reported due to the

unknown magnitude of the coefficient of friction. It should be noted that the extrusion to a strain of 1.0 was only successfully conducted once on A356-20% SiC. The die suffered damage in the form of surface scratches, probably due to the SiC particles at the surface of the billet. Subsequent attempts failed to produce full extrusion in this material, even at the maximum capacity of 1.4 GPa of the equipment. This result seems to corroborate the evidence for increased friction at the die wall due to the reinforcing ceramic particles.

4.2 STRAIN AND DAMAGE MEASUREMENTS IN pMMCs

The extruded composites were sectioned and analyzed according to the methods outlined in Section 3.3 in order to follow the evolution of damage as a function of imposed true plastic strain during extrusion. The result is plotted on figure 4.2 for the three particulate MMCs investigated in this work. It should be noted here that no radial dependence of damage could be measured in the sectioned billets.

The predominant damage mechanism in all three pMMCs was observed to be particle cracking. Examples of damaged microstructures are shown in figure 4.3, figure 4.4 and figure 4.5 for the A356-10% SiC, A356-20% SiC and 6061-20% CMS composites respectively. Since this form of damage was identified as predominant, the damage plotted on figure 4.2 can be defined as

$$\text{DAMAGE} = \frac{\%\ \text{OF TOTAL AREA OCCUPIED BY FRACTURED PARTICLES}}{\%\ \text{OF TOTAL AREA OCCUPIED BY PARTICLES}} \qquad \text{eq. (4.3)}$$

This is in contrast to the more general definition of damage of eq. (3.5).

The errors involved in measuring damage arose mainly from the difficulty in phase identification and in crack identification using the image analysis method. The former error, phase identification, is due to the effect of surface relief between the hard reinforcement and the soft matrix

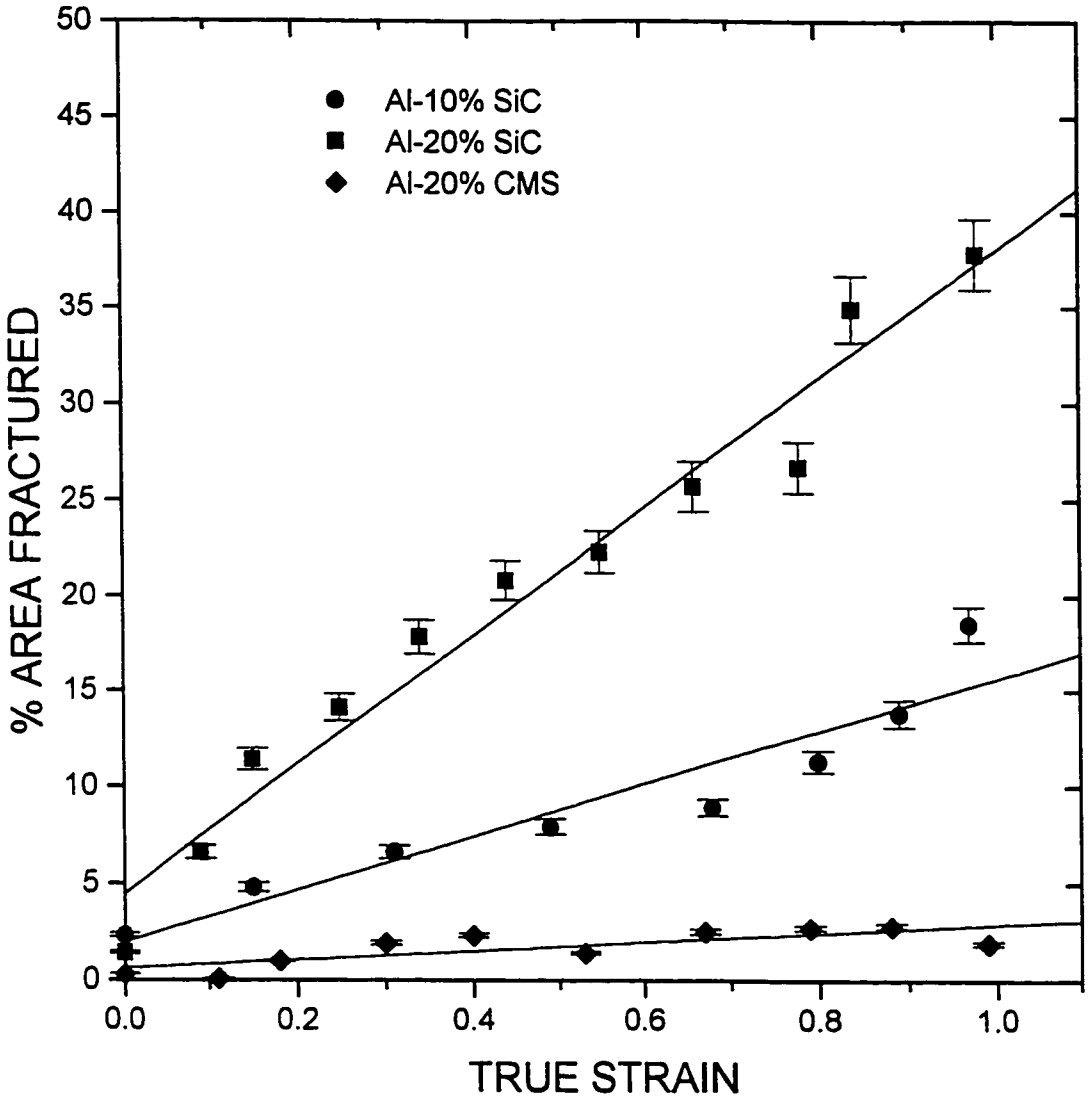

Figure 4.2 Plot of damage in the pMMCs with applied plastic strain by extrusion.

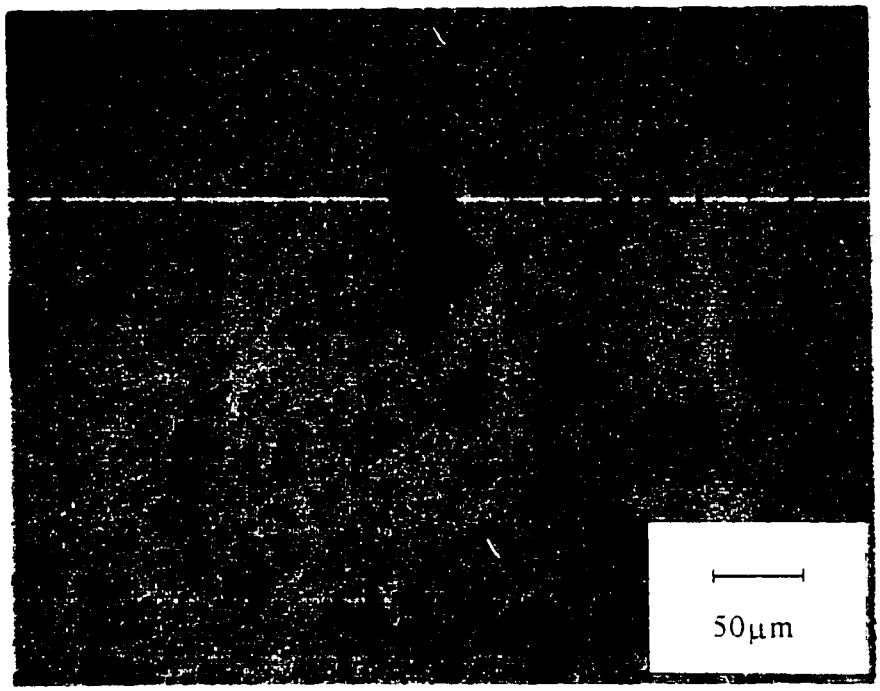

Figure 4.3 Micrograph of the damaged microstructure of A356-10%$_v$ SiC after hydrostatic extrusion to a strain of 0.37

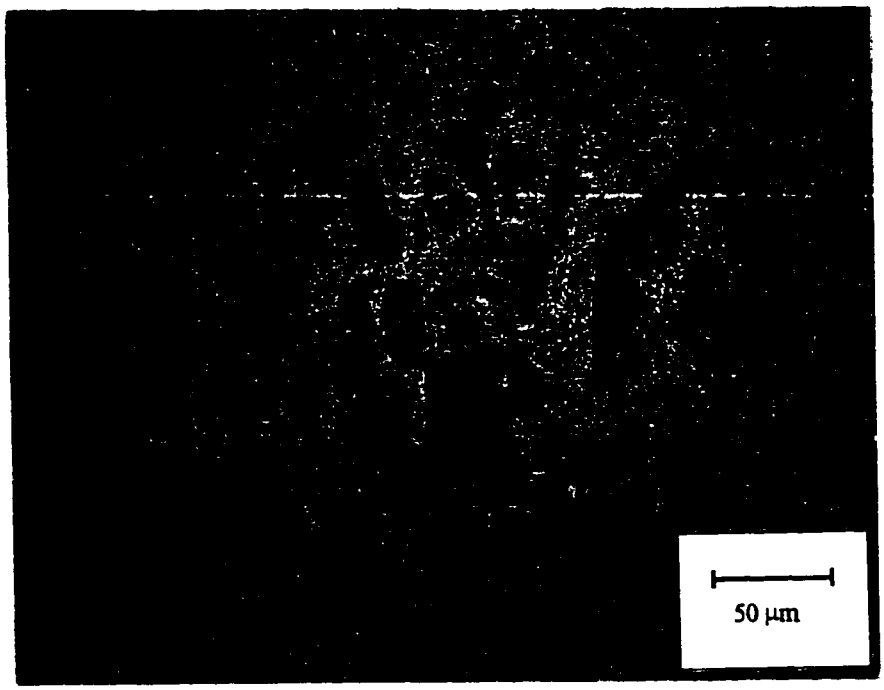

Figure 4.4 Micrograph of the damaged microstructure of A356-20% SiC after hydrostatic extrusion to a strain of 0.37

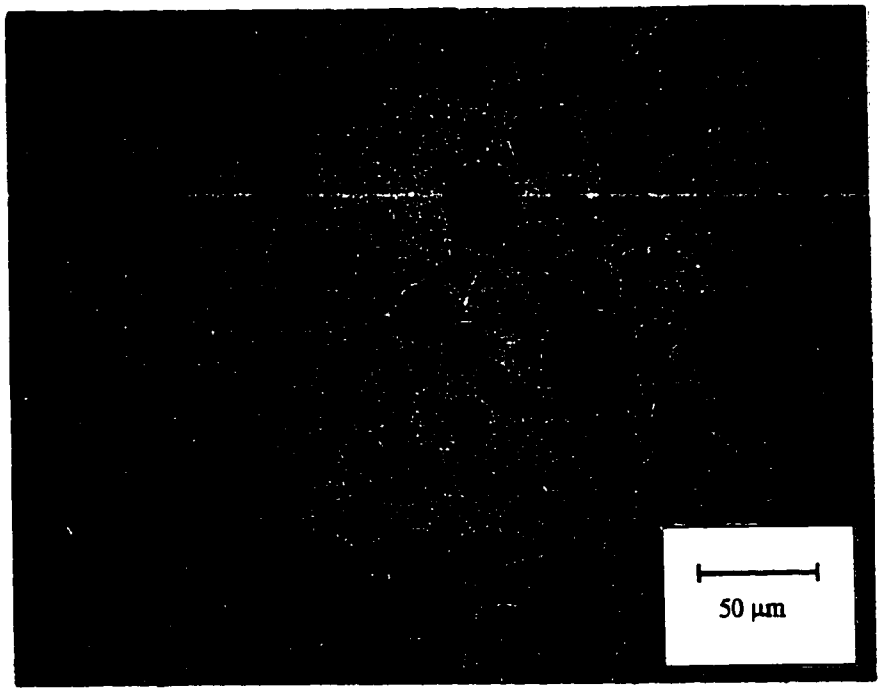

Figure 4.5 Micrograph of the damaged microstructure of 6061-20% CMS after hydrostatic extrusion to a stram of 0.37.

that is created in the sample preparation procedure outlined in Section 3.3. This surface relief caused errors in delineating accurately the matrix/reinforcement interface on the polished section. The identification of cracks in particles was limited to the resolution of the system at the magnification used (200x in this case). The combination of these two errors on the final measurement is difficult to assess and so the error was estimated to be 10% of the measurement. The errors involved in measuring strain were found simply by spatial measurement accuracy and were calculated to be of the order of ± 0.01. This is very small compared to the errors involved in the damage measurements, so error bars were only shown for the error in damage on figure 4.2.

It is observed from the plot of damage versus strain that there is an essentially linear relation in the plotted strain range for all three composites investigated. The damage is thus strongly dependent on the applied plastic strain during extrusion. Further, the slope of the damage-strain plots are an indication of the rate of damage accumulation in these MMCs. In this regard, comparison between the different composite materials yields information about the influence of volume fraction of reinforcement as well as reinforcement shape. For instance, the rate of damage accumulation in the A356 alloy reinforced with 10% SiC is approximately 2.5 times lower than the corresponding rate for the same alloy reinforced with 20% SiC. It is thus apparent that the damage rate is directly dependent on the volume fraction of reinforcement. It is also useful to compare the effect of reinforcement shape on the rate of damage accumulation. The 6061 alloy reinforced with 20% spherical CMS particles has a damage rate about 15 times lower than for the A356 alloy reinforced with 20% angular SiC. This suggests a very strong effect of particle shape, although the comparison cannot be taken as direct, considering the chemical dissimilarity and different preparation routes of the reinforcement particles. This observation is further emphasized by the fact that the damage rate in 6061-20% spherical CMS is about 6 times lower that the corresponding rate for the A356-10% angular SiC system. Thus, the effect of particle shape is stronger than the effect of reinforcement volume fraction from these results.

4.3 TENSILE TESTING OF pMMCs

The mechanical properties in tension of the three particulate materials were characterized, as well as the unreinforced constituent matrix materials. Tensile tests were performed as described in Section 3.4. The true stress-true strain curves are plotted on figure 4.6 to figure 4.12.

The errors involved with measuring strains was estimated at ±0.0005, from the accuracy of the extensometer used and the error in the initial gauge length. The corresponding stresses had an error associated with the error in strain mentioned above, plus the error in load, estimated as 10N. Thus the error in stress was estimated as ±5 MPa. No error bars were plotted on figure 4.6 to figure 4.10 as the errors on individual points fell within the scatter of the many adjacent points. Thus, the scatter band was thought to reflect the errors in an appropriate manner. The tensile tests were done on at least 2 specimens for each material and the scatter bands for the different tests were found to overlap in every case.

Many quantities can be compiled from the data presented in figures 4.6 to figure 4.12. One of these quantities is the elastic modulus, the initial slope of the true stress-true strain curves. Table 4.1 shows the computed values of these slopes, along with the errors involved , for all materials tested. The values of E, the elastic modulus, were calculated for tensile tests of the materials in the undeformed state (denoted UNDEFORMED), deformed by extrusion to a final strain of 0.5 (denoted ε=0.5), deformed by extrusion to a final strain of 1.0 (denoted ε=1.0), deformed by extrusion to a final strain of 0.5 and heat-treated back to the original T4 temper (denoted ε=0.5 + T) and deformed by extrusion to a final strain of 1.0 and heat-treated back to the original T4 temper (denoted ε=1.0 + T). For conciseness, this notation is used in

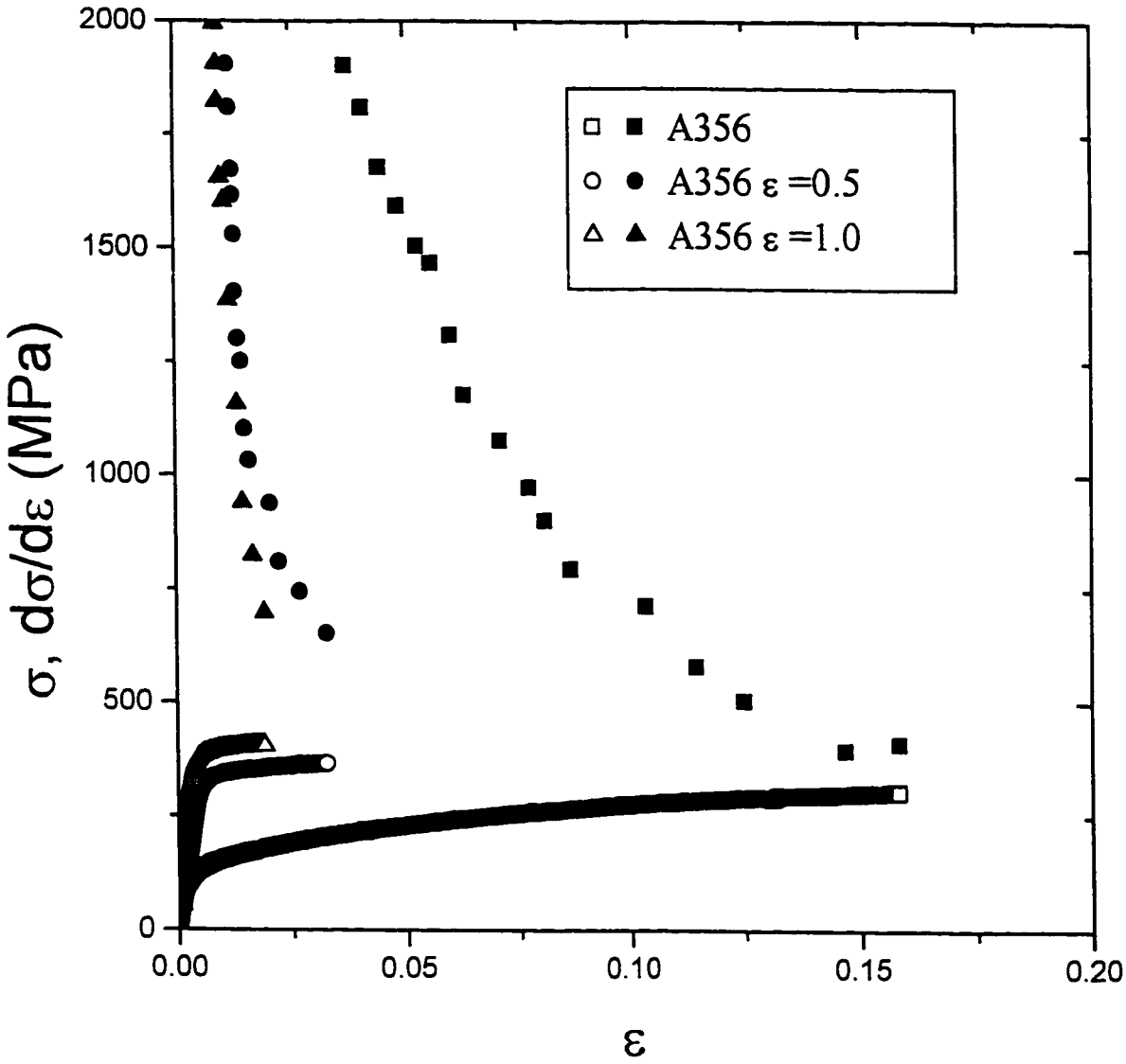

Figure 4.6 Stress-strain curves for the A356 alloy in the undeformed state, subsequent to extrusion to a final strain of 0.5 and subsequent to extrusion to a final strain of 1.0.

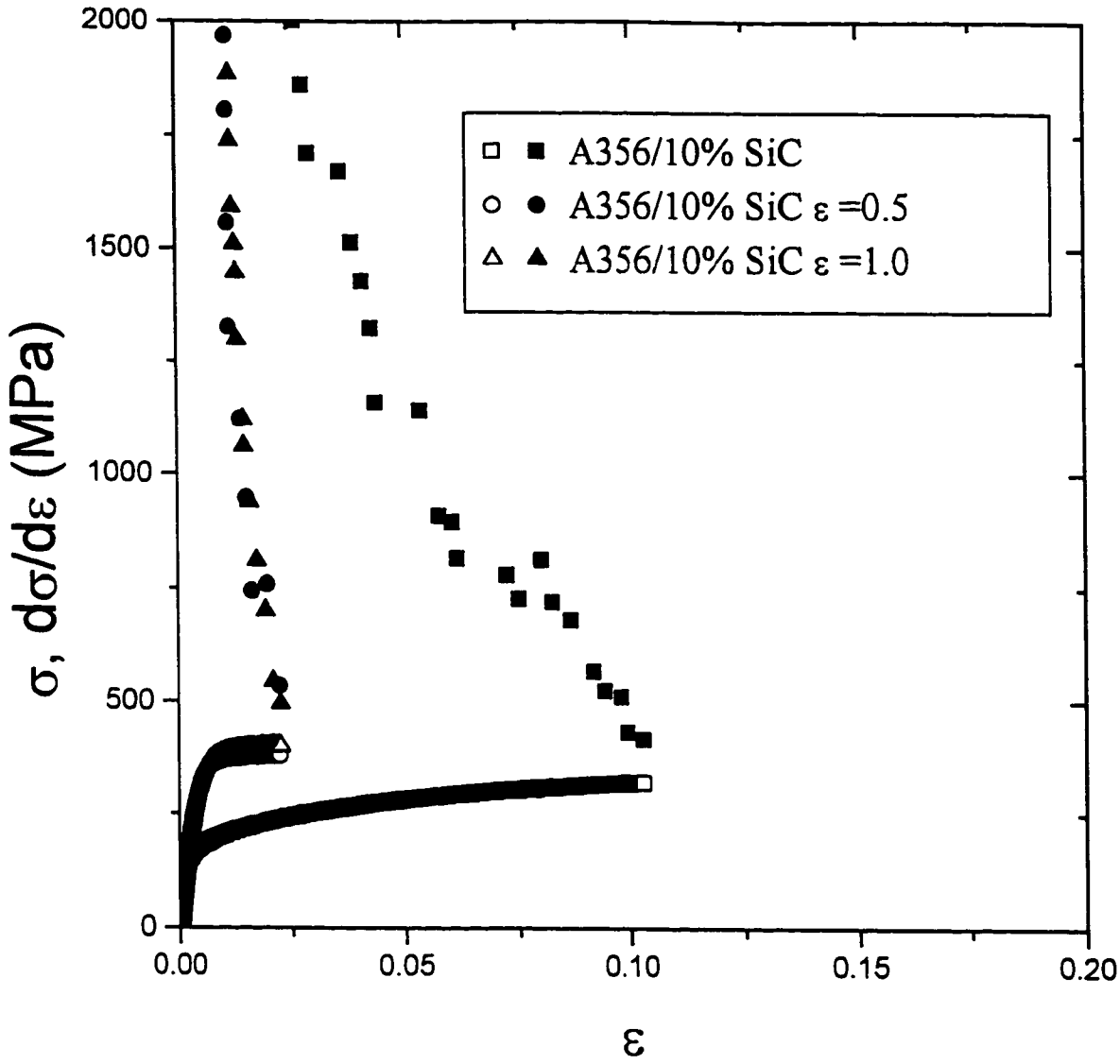

Figure 4.7 Stress-strain curves for the A356-10% SiC composite in the undeformed state, subsequent to extrusion to a final strain of 0.5 and subsequent to extrusion to a final strain of 1.0.

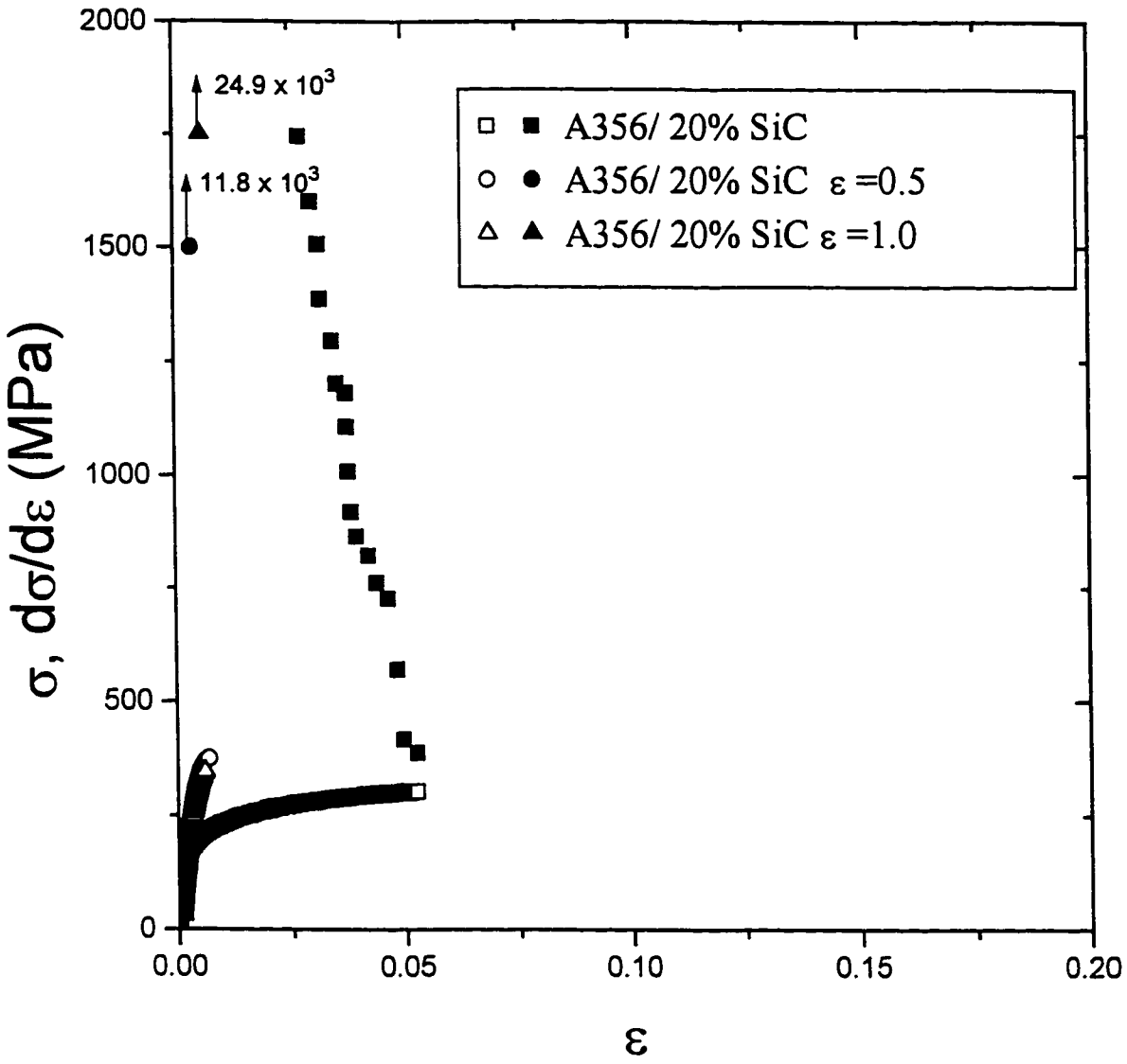

Figure 4.8 Stress-strain curves for the A356-20% SiC composite in the undeformed state, subsequent to extrusion to a final strain of 0.5 and subsequent to extrusion to a final strain of 1.0.

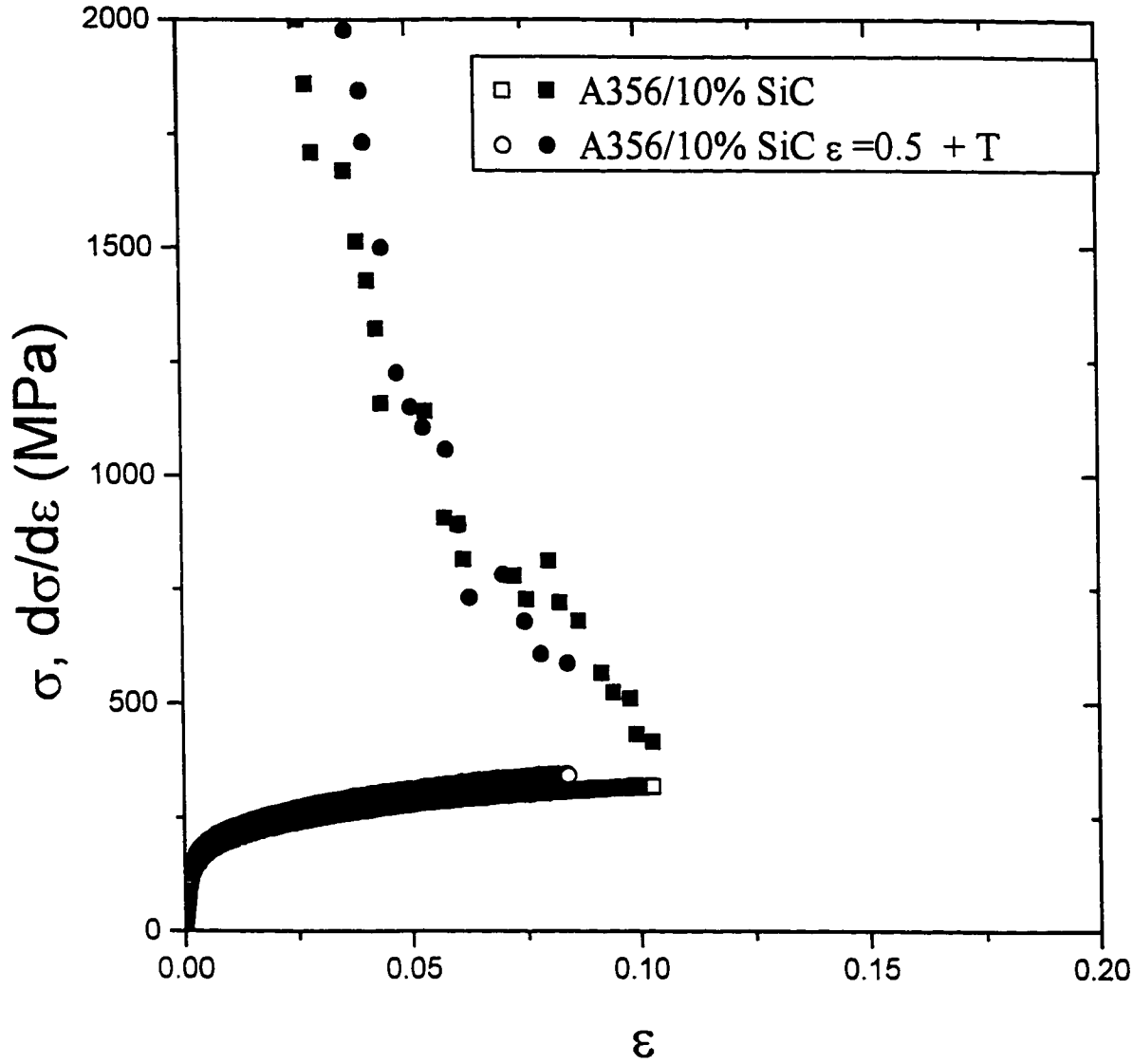

Figure 4.9 Stress-strain curves for the A356-10% SiC composite in the undeformed state and for A356-10% SiC which was extruded to a strain of 0.5 and heat treated back to the T4 temper.

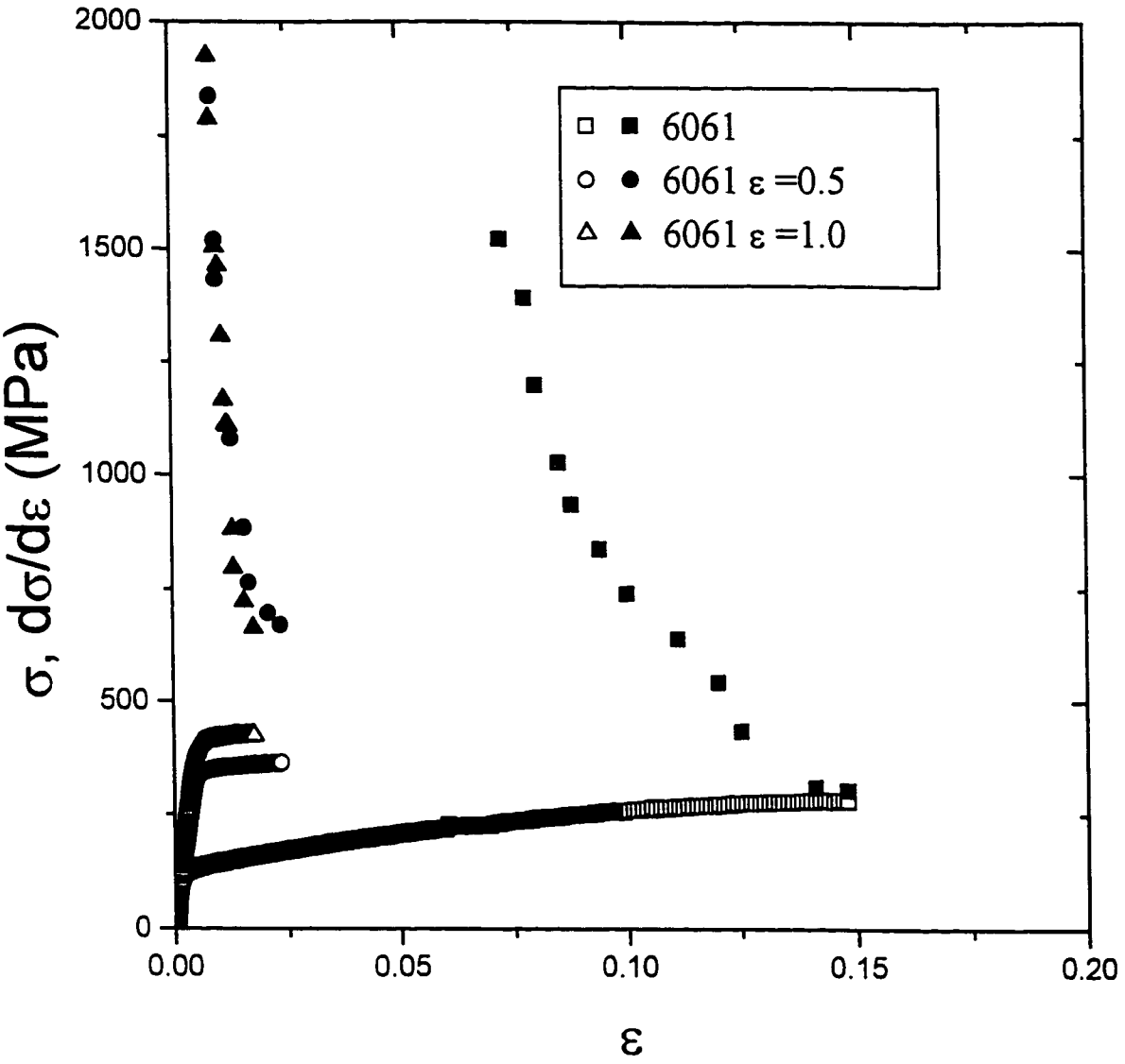

Figure 4.10 Stress-strain curves for the 6061 alloy in the undeformed state, subsequent to extrusion to a final strain of 0.5 and subsequent to extrusion to a final strain of 1.0.

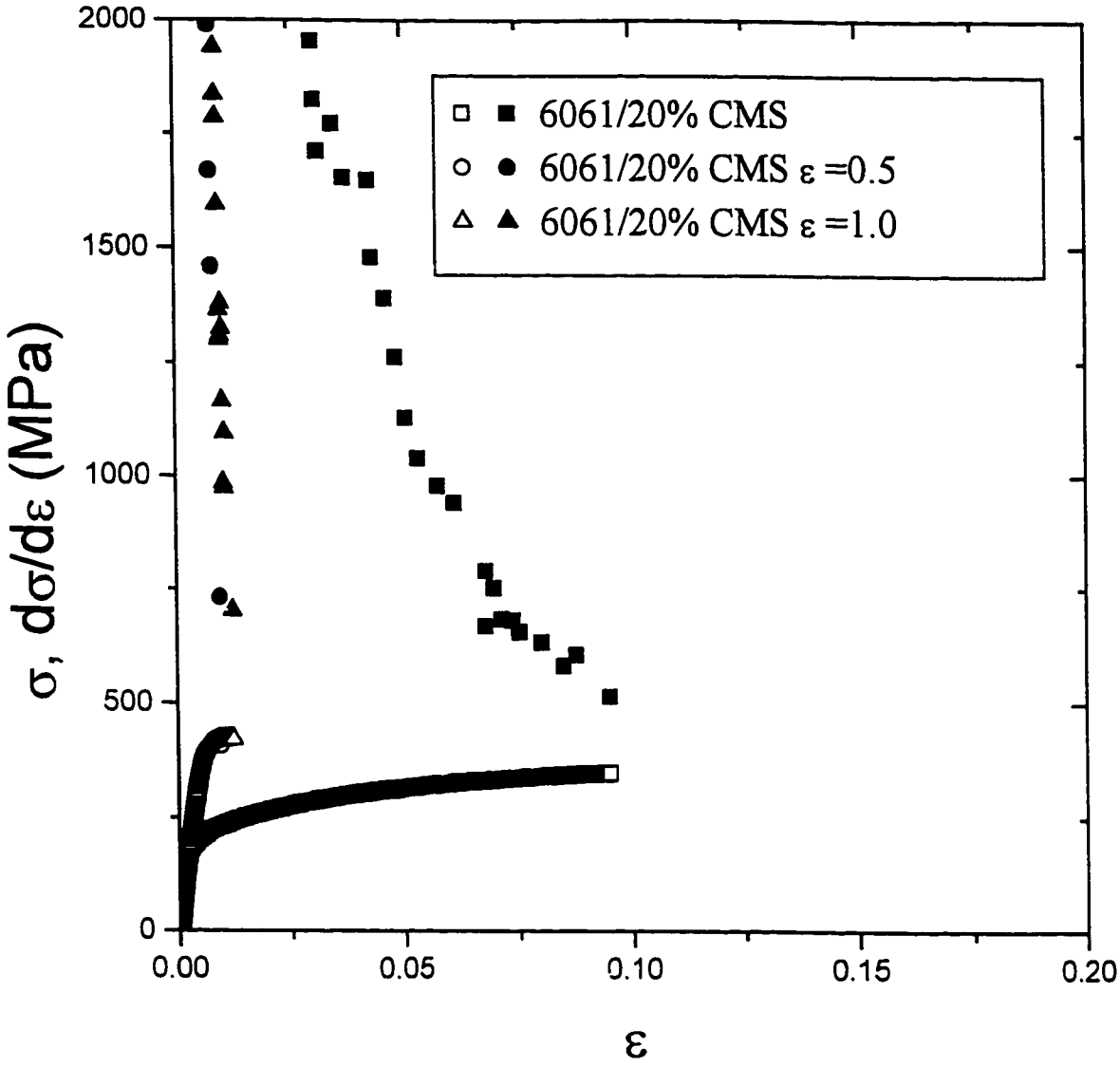

Figure 4.11 Stress-strain curves for the 6061-20% CMS composite in the undeformed state, subsequent to extrusion to a final strain of 0.5 and subsequent to extrusion to a final strain of 1.0.

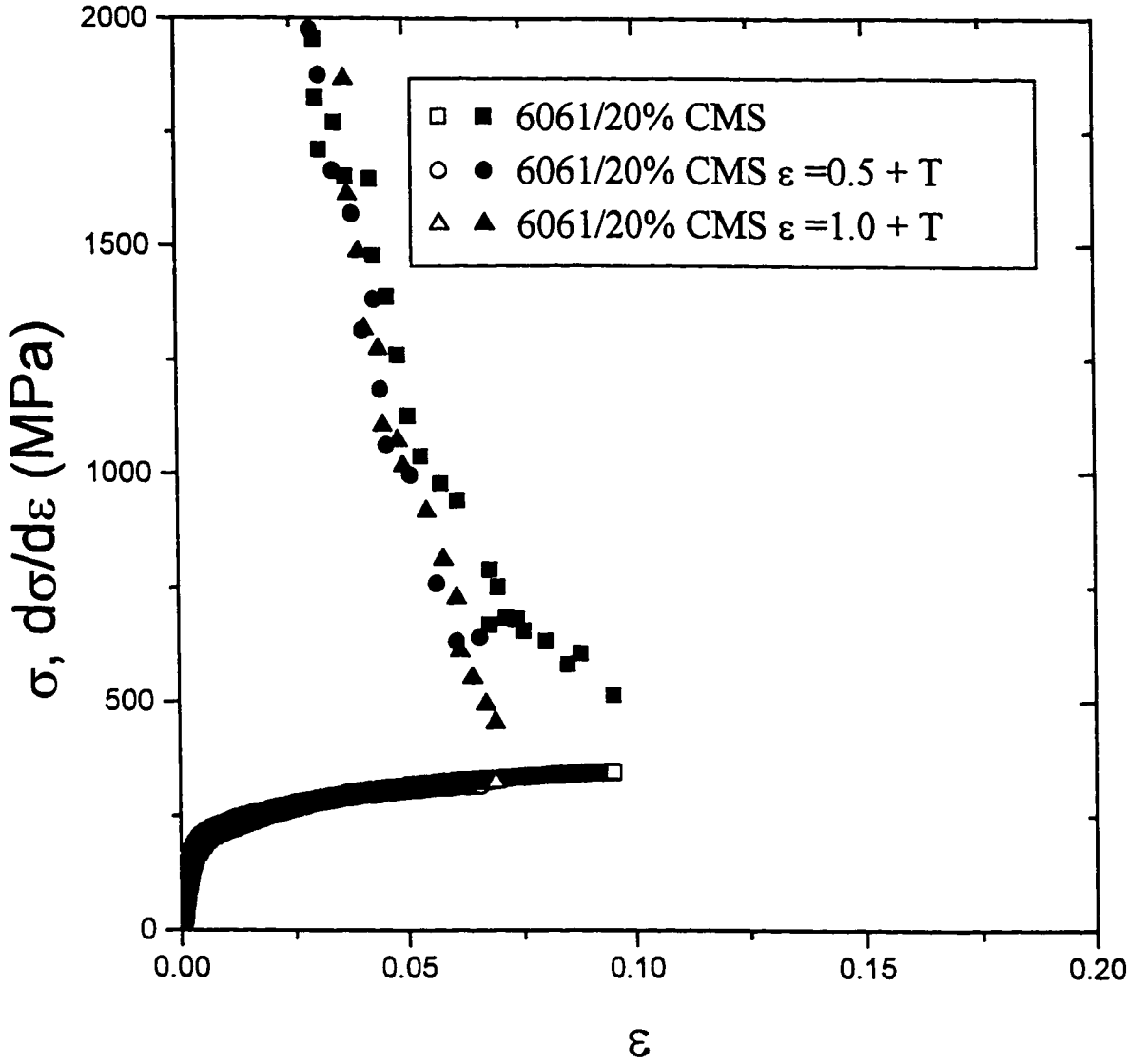

Figure 4.12 Stress-strain curves for the 6061-20% CMS composite in the undeformed state, for 6061-20% CMS which was extruded to a strain of 0.5 and heat treated back to the T4 temper and for 6061-20% CMS which was extruded to a strain of 1.0 and heat treated back to the T4 temper.

all the tables in which there is a need to describe the thermal and mechanical history of the materials tested. The values quoted are averages from at least two tests.

Table 4.1 Elastic Moduli from Tensile Tests

	E(GPa)				
MATERIAL	UNDEFORMED	ε=0.5	ε=1.0	ε=0.5 + T	ε=1.0 + T
A356	71 ± 10	73 ± 10	71 ± 10	N/A	N/A
6061	62 ± 10	71 ± 10	73 ± 10	N/A	N/A
A356-10% SiC	88 ± 10	71 ± 10	79 ± 10	79 ± 10	N/A
A356-20% SiC	109 ± 10	70 ± 10	65 ± 10	N/A	N/A
6061-20% CMS	94 ± 10	93 ± 10	81 ± 10	79 ± 10	78 ± 10

The errors quoted in Table 4.1 reflect the difficulty in making this measurement. Errors arise in E due to many effects. The first cause of non-linearity of the elastic part of the stress-strain curve is due to grip effects. At small applied loads, the sample re-aligns in the grips, causing a total displacement that is not wholly due to the stiffness of the sample. The resultant non-linearity in the stress-strain curve caused by this phenomenon was found to be significant up to approximately 50 MPa in most cases. A second cause of non-linearity is due to microyielding behavior at loads which approach the load required for general yielding. The range of this effect is more difficult to measure. Thus, the stress range of data to be chosen must be above the one where grip effects have terminated and below the stress for the onset of microplasticity. It is not known in any test if the range chosen was valid because of the possibility of overlap of the two regions. This was especially true in materials with low flow stresses. The linearity of the data was evaluated from the correlation coefficient of the best fitting line to the data in the range chosen. Other errors in the measurements are due to machine stiffness effects and error in the stress and strain measurements, although these last two effects are considered to be small with respect to the previous two sources. In view of the standard deviations from the average values and the errors discussed above, it was estimated that the error in the modulus measurements was ± 10 GPa.

The results of Table 4.1, even though large errors cause overlap in the data, indicate trends in elastic properties due to the effect of reinforcing particles and due to previous straining by extrusion. It is a general trend that the addition of high stiffness particles into both the A356 and 6061 Al alloys increases their stiffness. The increase is also seen to increase with the volume fraction added. The effect of prior strain by extrusion is also general, though less clear due to the large errors on the elastic moduli. Hydrostatic extrusion in all cases reduced the stiffness of the material from its value in the undeformed state. Compared to the as-extruded samples, no change in E was observed due to heat treatment to the original T4 temper.

The yield stress, a measure of the tensile stress required for general yielding, is also a quantity that can be extracted from the stress strain data. In materials such as Al that do not exhibit a sharp yield point, the yield stress is generally defined at an offset strain of 0.2%. From this offset, a line drawn with a slope equal to the elastic modulus found previously is constructed. The stress corresponding to the intersection of the line with the flow curve is the yield stress. The average 0.2% offset yield stress, designated $\sigma_{0.2}$ is tabulated in Table 4.2 for all the materials tested, along with the associated errors in the measurement.

Table 4.2 0.2% Offset Yield Stress from Tensile Tests

	$\sigma_{0.2}$ (MPa)				
MATERIAL	UNDEFORMED	ε=0.5	ε=1.0	ε=0.5 + T	ε=1.0 + T
A356	130 ± 10	330 ± 10	385 ± 10	N/A	N/A
6061	125 ± 10	345 ± 10	400 ± 10	N/A	N/A
A356-10% SiC	165 ± 10	350 ± 10	365 ± 10	180 ± 10	N/A
A356-20% SiC	180 ± 10	370 ± 10	N/A	N/A	N/A
6061-20% CMS	200 ± 10	405 ± 10	405 ± 10	185 ± 10	185 ± 10

It is to be noted that for some materials that failed at very low strains of the order of 0.2% , the 0.2% offset line did not intersect the stress-strain curve and thus the yield stress data was unavailable. The errors in Table 4.2 were estimated from the errors in stress and elastic modulus, discussed previously.

The results in Table 4.2 demonstrate a general trend for all materials. In all cases, the yield stress increases with the amount of previous strain by hydrostatic extrusion. The yield stress of A356 is increased from 130 MPa to 165 MPa and 180 MPa for SiC additions of 10% and 20% by volume respectively. Similarly, the addition of 20% CMS particles increases the yield stress from 130 MPa to 200 MPa. Heat treating the composites to the original T4 temper has the effect of reducing the yield stress drastically to values that are closer to the unextruded samples.

The true stress-true strain curves can also be analyzed to measure the strain at which the plastic flow in the materials changes from a homogenous or general nature to a localized or unstable nature. This point is called the tensile instability or onset of necking. These were computed for all materials tested by finding the load maximum. The method utilized for this measurement consisted of picking a subset of data points from the load-strain curve near the load maximum and fitting a second order polynomial to the data. The instability strain was found by differentiating the polynomial fitting equation and setting the derivative to zero. The average instability strains and corresponding average instability stresses from several tests are given in Table 4.3 and Table 4.4 respectively. The errors were estimated from the standard deviations to the average and the uncertainty in finding the load maximum from the method described above.

Table 4.3 Instability Strains from the Tensile Tests

	INSTABILITY STRAIN				
MATERIAL	UNDEFORMED	ε=0.5	ε=1.0	ε=0.5 + T	ε=1.0 + T
A356	0.149±0.008	0.028±0.004	0.019±0.004	N/A	N/A
6061	0.145±0.008	0.025±0.004	0.020±0.004	N/A	N/A
A356-10% SiC	0.106±0.005	0.023±0.002	0.020±0.002	0.072±0.008	N/A
A356-20% SiC	0.052±0.005	0.006±0.001	N/A	N/A	N/A
6061-20% CMS	0.095±0.005	0.010±0.001	0.011±0.001	0.074±0.008	0.077±0.008

Table 4.4 Instability Stresses from the Tensile Tests

	INSTABILITY STRESS (MPa)				
MATERIAL	UNDEFORMED	ε=0.5	ε=1.0	ε=0.5 + T	ε=1.0 + T
A356	300 ± 10	365 ± 10	400 ± 10	N/A	N/A
6061	280 ± 10	365 ± 10	415 ± 10	N/A	N/A
A356-10% SiC	320 ± 10	380 ± 10	400 ± 10	325 ± 10	N/A
A356-20% SiC	300 ± 10	360 ± 10	320 ± 10	N/A	N/A
6061-20% CMS	345 ± 10	410 ± 10	420 ± 10	320 ± 10	320 ± 10

The data of Table 4.3 show that the instability strain, if one is reached at all, is lowered as the amount of previous strain by extrusion is increased. The data also shows that by heat treatment after extrusion, the instability strain increases compared to materials tested directly after the extrusion, but that the instability strain corresponding to the undeformed MMCs is not fully recovered. The effect of particulate additions to the A356 and 6061 alloys is to reduce the magnitude of the instability strain and this effect is greater for greater additions of SiC to A356.

Along with the stress-strain curves, figure 4.6 to 4.12 also show the work hardening characteristics of the materials tested. The points plotted correspond to the slope of the stress-strain curve for the given strain. This is also called the tangent modulus. The method used to obtain this data was similar to the method used to find the elastic moduli of the tensile samples. The entire stress-strain dataset was divided into smaller subsets of approximately 50 points. The size of these subsets was

increased from 50 to several hundred points in some cases as the stress-strain curve flattened out, in order to get enough points to overcome the natural scatter. The work hardening rate was then calculated as the slope of a linear regression fit to the points. Of special interest is the value of the work hardening coefficient at the instability strain. This value was measured by examining the data preceding this point and choosing the maximum number of points for which no deviation to linearity could be observed for the best fit line. The average work hardening rates at the tensile instability are given in Table 4.5.

Table 4.5 Work Hardening Rate at the Tensile Instability

	$d\sigma/d\varepsilon$ (MPa)				
MATERIAL	UNDEFORMED	ε=0.5	ε=1.0	ε=0.5 + T	ε=1.0 + T
A356	435 ± 50	660 ± 50	675 ± 50	N/A	N/A
6061	280 ± 50	630 ± 50	715 ± 50	N/A	N/A
A356-10% SiC	390 ± 50	560 ± 50	520 ± 50	530 ± 50	N/A
A356-20% SiC	390 ± 50	20000±2000	22000±2000	N/A	N/A
6061-20% CMS	580 ± 50	685 ± 50	1900 ± 200	565 ± 50	450 ± 50

The errors associated with the high work hardening region of the stress-strain curves are estimated at ± 10 GPa, reflecting the similarity of this measurement with the one for the elastic modulus. As the stress-strain curve flattens out and the work hardening rate drops below about 30 GPa, the percent errors increase with the decrease in slope because of the larger error contribution of the natural scatter. The errors at lower average work hardening rates was thus estimated to be of the order of 10% of the measurement of the slope of the best fit line, corresponding to an error of approximately ± 50 MPa at the instability.

The work hardening properties of the materials can be compared as a function of the amount of previous strain by extrusion. For the same strain, the work hardening rate drops as the prior strain by extrusion increases. Similar to the trend with instability strain, some work hardening capacity is

recovered in the MMCs by heat treatment, but it is not recovered to the level observed for the undeformed composites.

In order to get better load resolution and more material in the gauge section, a larger tensile sample of the undeformed 6061-20% CMS was machined according to the dimensions given in figure 3.8 and tested in tension at a lower strain rate. The details of this test are in Section 3.4. The stress-strain curve for this test is shown on figure 4.13, along with the work hardening characteristics. The errors involved in theses quantities have been discussed previously. Density measurements were made on the undeformed material and on material from the gauge section cut from a region outside the neck. Ten density measurements were made using the Archimedean method detailed in Section 3.4 and they are shown in Table 4.6.

Table 4.6 Density of Deformed and Undeformed 6061-20% CMS

MEASUREMENT	$\rho_{undeformed}$	$\rho_{deformed}$
1	2.8387	2.8264
2	2.8385	2.8268
3	2.8383	2.8263
4	2.8379	2.8274
5	2.8392	2.8266
6	2.8385	2.8278
7	2.8391	2.8257
8	2.8379	2.8257
9	2.8384	2.8269
10	2.8380	2.8254

The average density of the undeformed composite is 2.8385 ± 0.0005 g/cm^3 and the corresponding density of the material from the gauge section is 2.8265 ± 0.0007 g/cm^3. The errors quoted for both densities were taken to be the standard deviation of the ten measurements. The porosity is given by the ratio

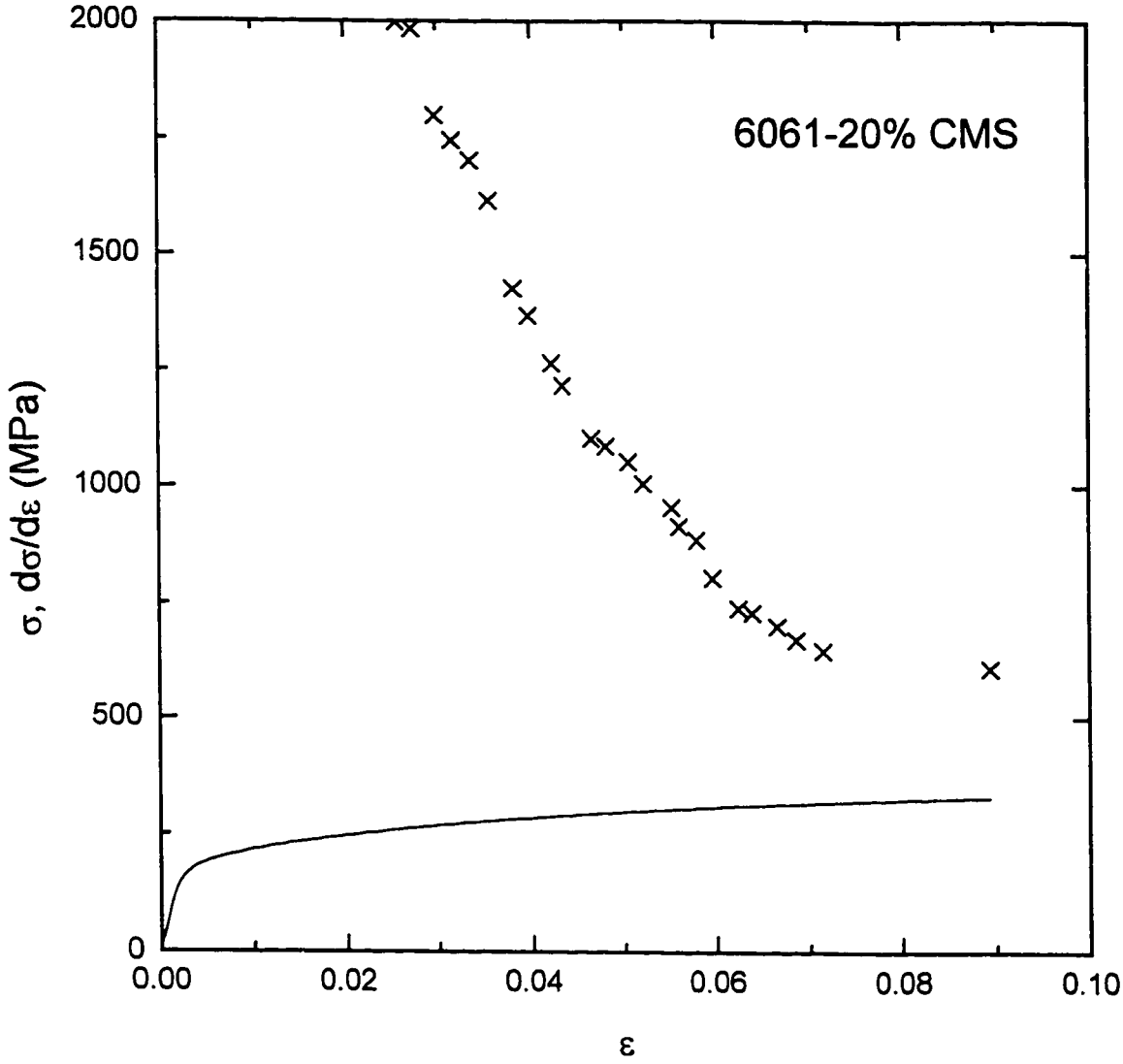

Figure 4.13 Stress-strain curve for the large tensile specimen that was used to measure the density of the damaged 6061-20% CMS.

$$\%\text{POROSITY} = \left(\frac{\rho_{\text{undeformed}} - \rho_{\text{deformed}}}{\rho_{\text{undeformed}}} \right) \times 100\% \qquad \text{eq. (4.4)}$$

The tensile test thus produced a 0.42 ± 0.05 % porosity change in the material.

4.4 STRESS AND DAMAGE MEASUREMENTS IN HOURGLASS SPECIMENS

Tensile tests were conducted on samples of 6061-20% CMS with a variable diameter gauge section in order to get information on the damage created in tension as a function of applied stress. To monitor the stress-strain behavior for this experiment, photographs with about 7x magnification were taken of the gauge section at 20 second intervals for the duration of the test. Examples of such photographs taken at 0, 60 and 140 seconds of one test are shown on figure 4.14 to figure 4.16 respectively.

From the photographs, the diameter of the sample at the center of the gauge section (i.e. the minimum diameter) was measured for each time interval. The corresponding true strain was calculated using eq. (3.1) and the stress was calculated from the recorded load divided by the minimum cross-sectional area calculated from the measured diameter. The Bridgman correction for the stress was applied to the data. It will be seen later that this correction was approximately 0.97 for the duration of the tensile test. The error in strain from measurements on the photographs was estimated by RMS analysis at $\pm$ 0.5% and the corresponding error in stress was $\pm$ 5 MPa. The true stress-true strain curve generated from the photographs is shown in figure 4.17 along with the stress-strain curve for a sample with a constant diameter gauge section.

At strains lower than approximately 2.5%, there is good agreement between the two plots of figure 4.17. Above this strain, the stress-strain curve measured for the hourglass specimen is lower than

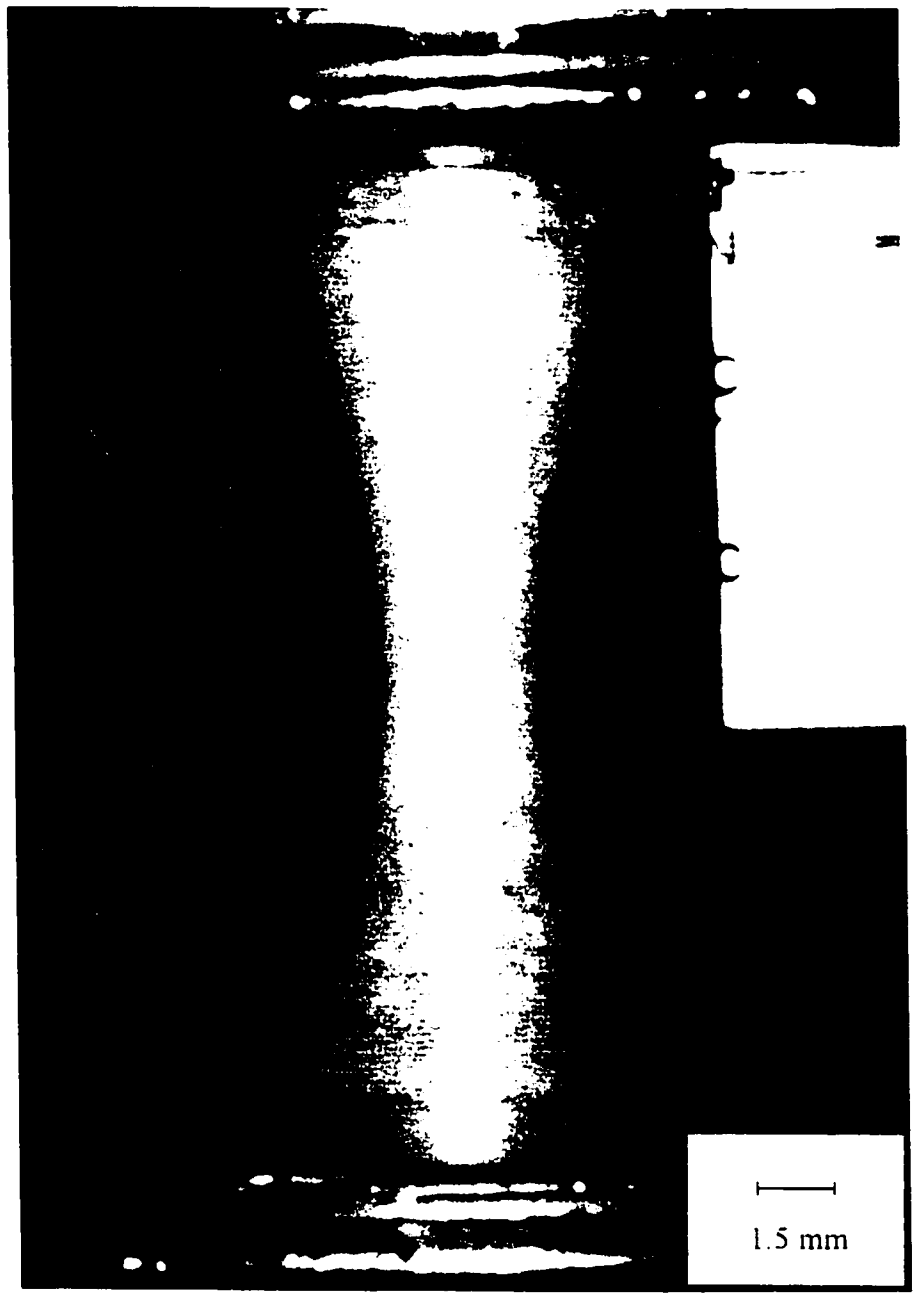

Figure 4.14 Photograph of the hourglass shaped tensile sample prior to tensile testing.

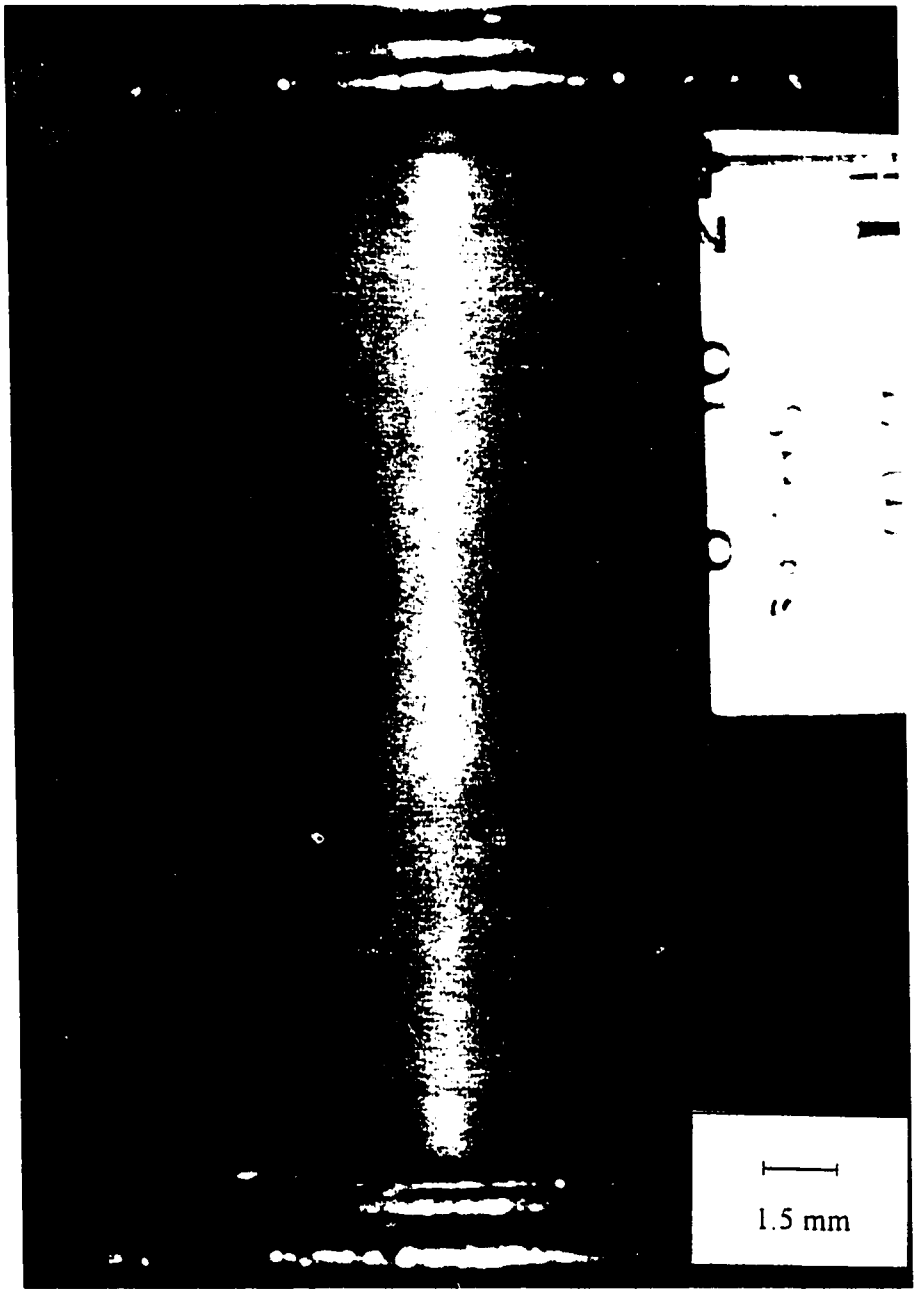

Figure 4.15 Photograph of the hourglass shaped tensile specimen 60 sec. after the start of the tensile test.

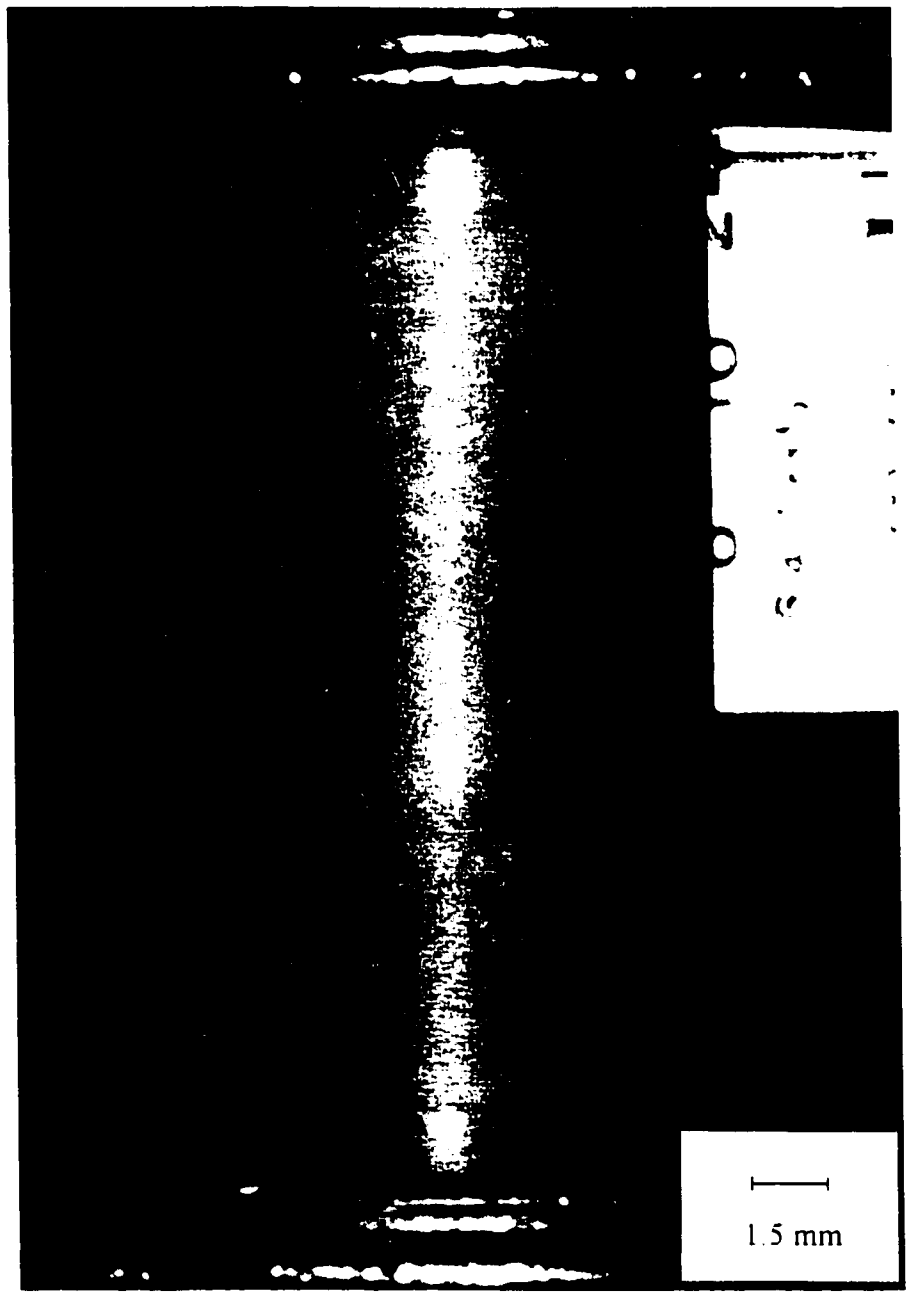

Figure 4.16 Photograph of the hourglass shaped tensile specimen 140 sec. after the start of the tensile test.

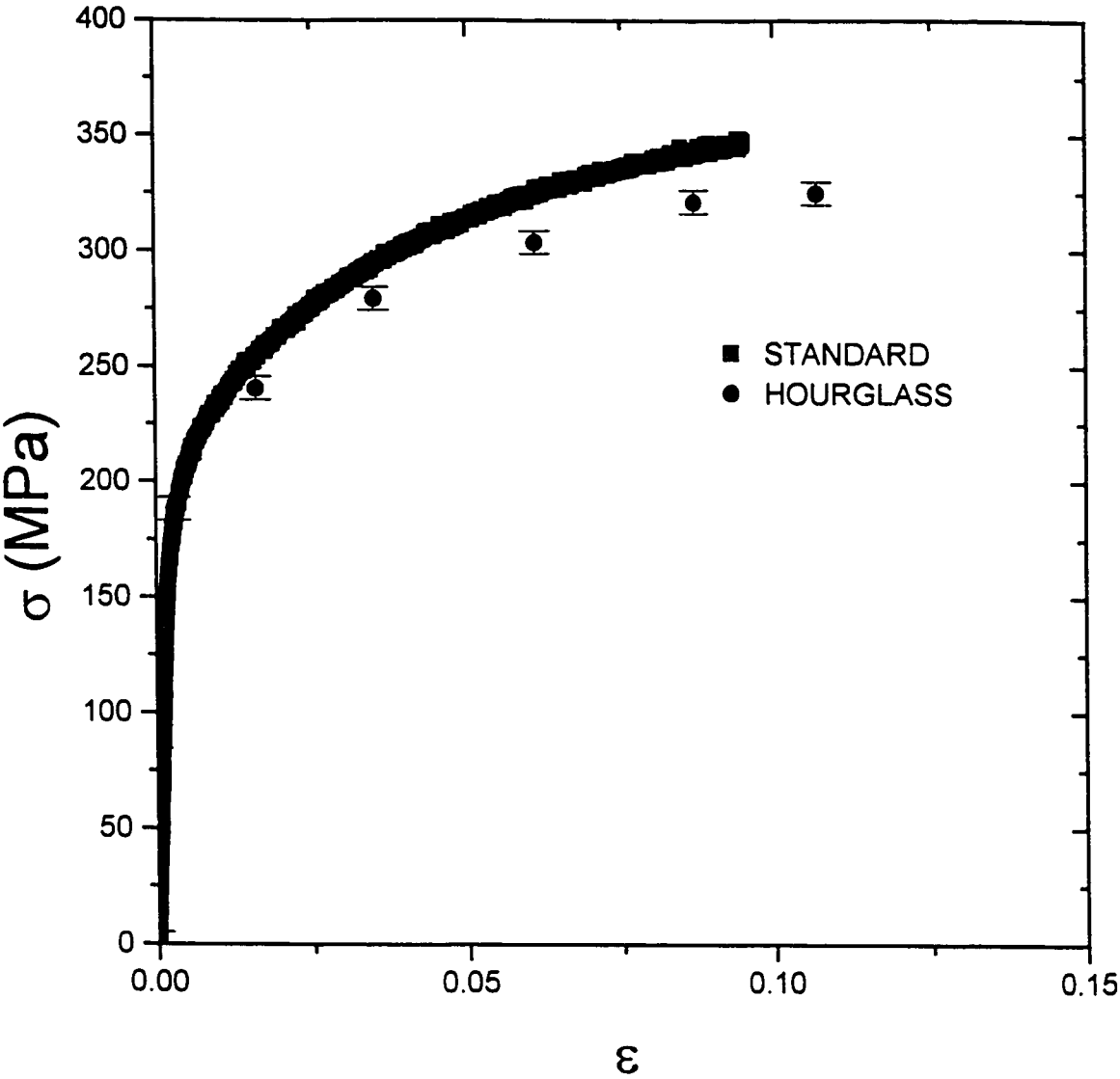

Figure 4.17 Stress-strain curve for the 6061-20% CMS composite calculated from the load cell data for the tensile test and from dimensional measurements of the cross section of the hourglass gauge section.

the one measured for the standard specimen. Also, the difference between the two curves increases with strain.

Longitudinal sections of the hourglass tensile specimens were polished and observed for evidence of damage. Similarly to the extruded composites, the form of damage was particle cracking and thus damage could also be described by eq.(4.3). The damage was quantified by image analysis according to the procedure outlined in Section 3.3. The diameter of the section where the damage measurements were made was recorded. It was thus possible to find the stress on the given section from the maximum load attained in the tensile test and the load bearing area calculated from the diameter. The damage was thus related to the maximum applied true stress and the result is plotted in figure 4.18.

Along with damage, the area fraction of voids was calculated from the polished sections. The intention of this measurement was to add to the dilatational information from the density measurements of Section 4.4, to get a measure of the dilatation of the material as a function of stress. It was assumed that the area fraction of voids measured was equal to the volume fraction of voids. The result is presented on figure 4.19. The dimensionless variable describing the volume of the sample is V divided by V_o, where V, the total volume, is equal to the addition of the initial damage free volume V_o and the dilatation ΔV.

The results of the damage measurements reveal several features related to damage evolution in the 6061-20% CMS composite. The first such feature is the effect of stress state on the evolution of damage. From figure 4.2, for extrusion of 6061-20% CMS up to a strain of 1.0, the level of damage is around 3%. In figure 4.18, the damage level in the same composite tested to a stress of 353 MPa is close to 35%. This stress of 353 MPa can be related to a strain if it is assumed that every element of the

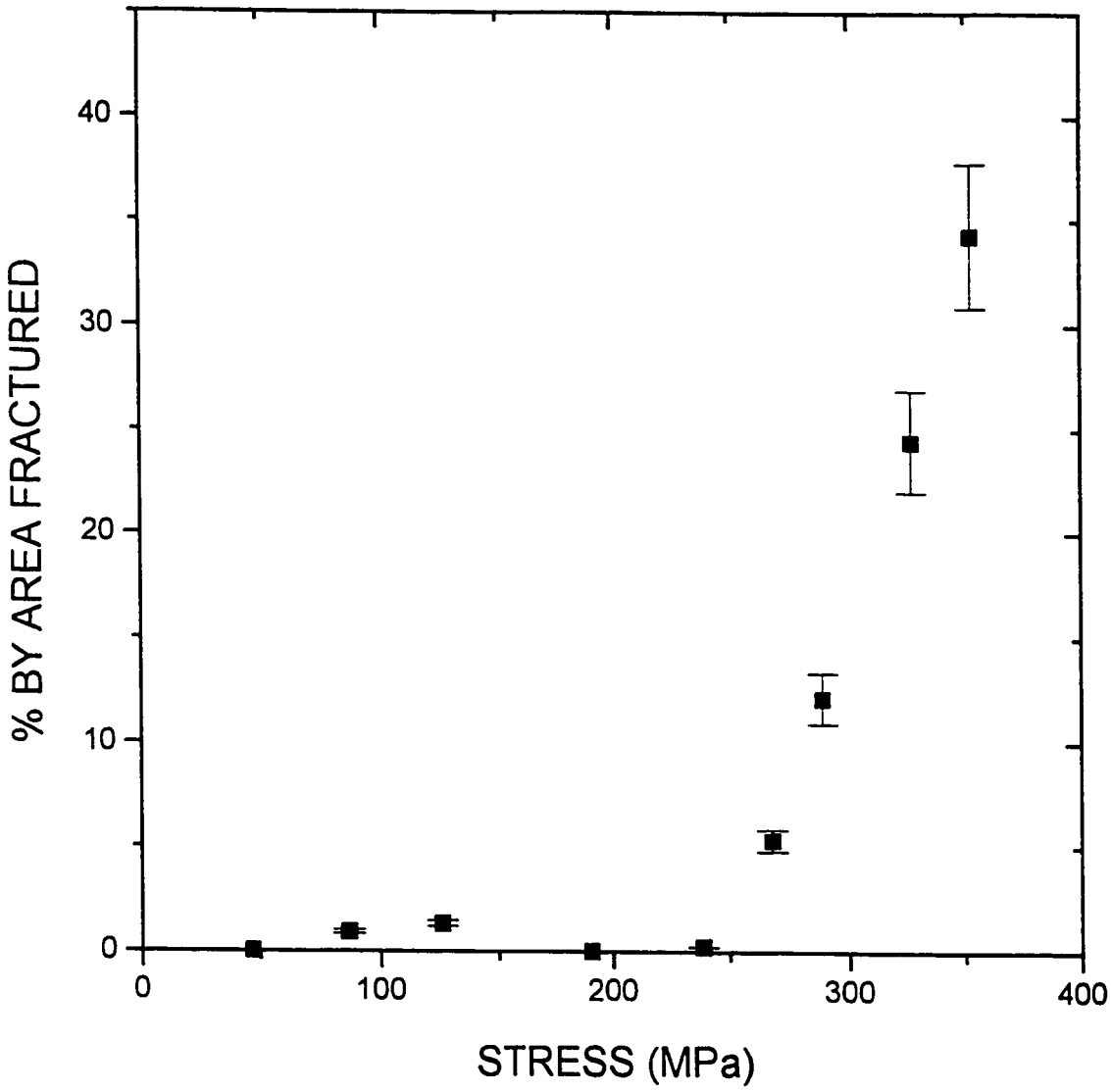

Figure 4.18 Plot of damage in 6061-20% CMS as a function of the maximum applied tensile stress in the hourglass shaped tensile specimen.

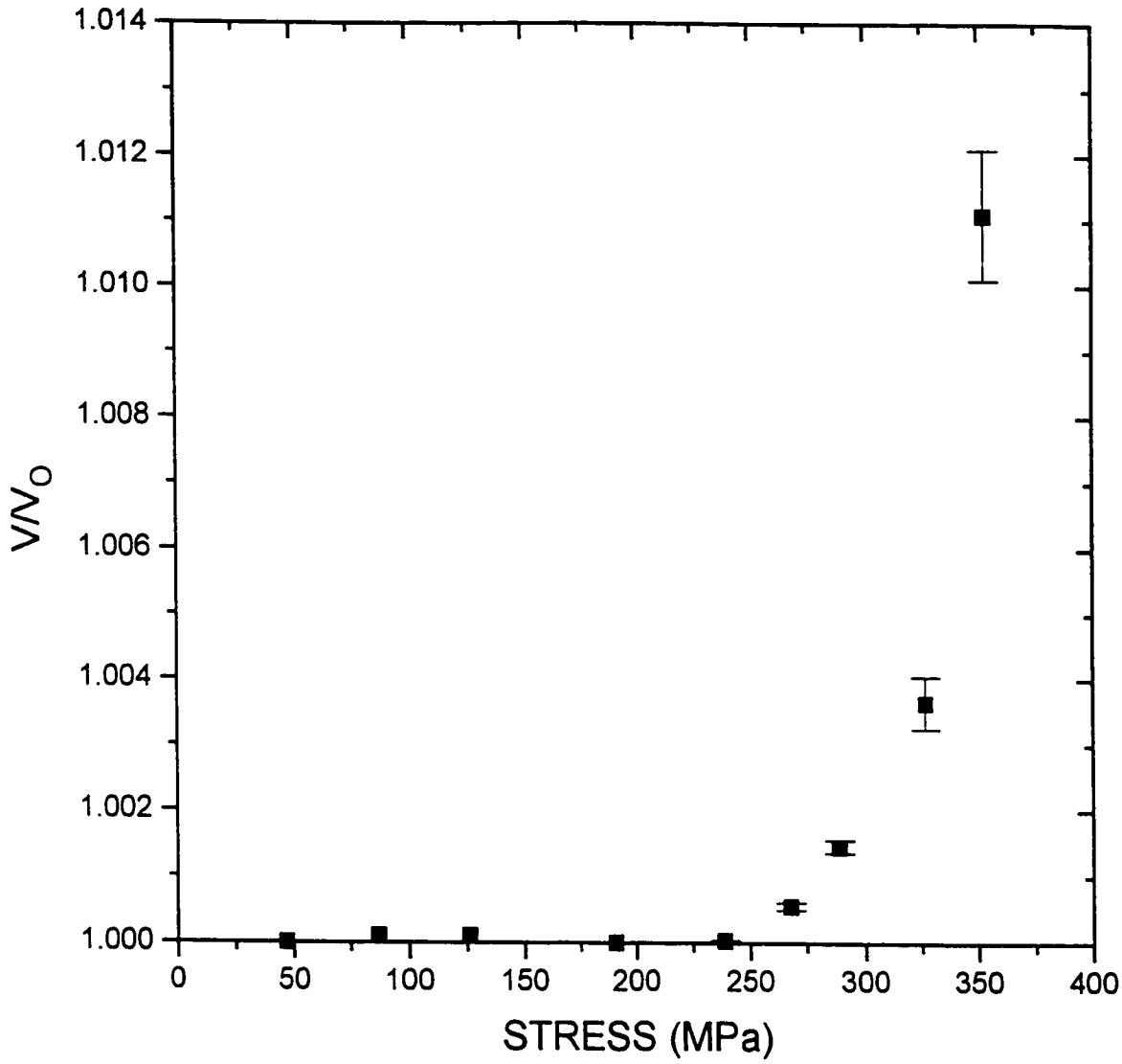

Figure 4.19 Plot of dilatation (V/V_o) in 6061-20% CMS as a function of the maximum applied tensile stress in the hourglass shaped tensile specimen.

hourglass section of the specimen follows the same strain path. The radius of curvature of the hourglass section was designed to approach such a condition. In a necked section, during plastic flow in tension, the corrected stress at the minimum section is given by the following equation by Bridgman (1944)

$$\sigma = \frac{\sigma_{avg}}{(1+2R/a)\left[\ln(1+a/2R)\right]} \qquad \text{eq. (4.5)}$$

where R is the radius of curvature of the neck, a is the radius of the neck and σ_{avg} is the average stress calculated by dividing the applied load by the cross sectional area. The stress σ in the Bridgman equation is a correction to the average stress that accounts for the triaxial stress state created in the neck due to axial constraint. Thus, the ratio of corrected stress to average stress is a measure of the degree of triaxiality and of the deviation of the stress state from its initial uniaxial condition. From the hourglass sample dimensions given in figure 3.7, the ratio of corrected stress to average stress is 0.967, so that the stress state at the centre of the sample does not differ much from the initial uniaxial state. From the photograph on figure 4.16 taken right before fracture, it was determined that the Bridgman correction was 0.965, remaining essentially unchanged and small. Consideration of this result shows that the assumption of equivalent strain paths in every element of the hourglass section is reasonable. The stress in the section can thus be related in a rough manner to the strain in the following way. From figure 4.18, the 6 points in the strain range 0.02 to 0.11 were fitted to a best fitting power law line. The plastic strain corresponding to points below this strain range was considered to be zero. This fit, together with the experimental points, is shown on figure 4.20. Using this line, the stresses calculated from the damage measurements were converted to strains. Thus, the damage in tension was plotted against true tensile strain on figure 4.21. It was assumed that the contribution of elastic strain to the total true tensile strain was small so that the strain in figure 4.21 is essentially equal to the plastic strain in tension. In this way, a direct comparison to the damage created by plastic strain by extrusion could be made. The highest strain in tension is about 0.14 and the damage level, defined by the percent area of particles that

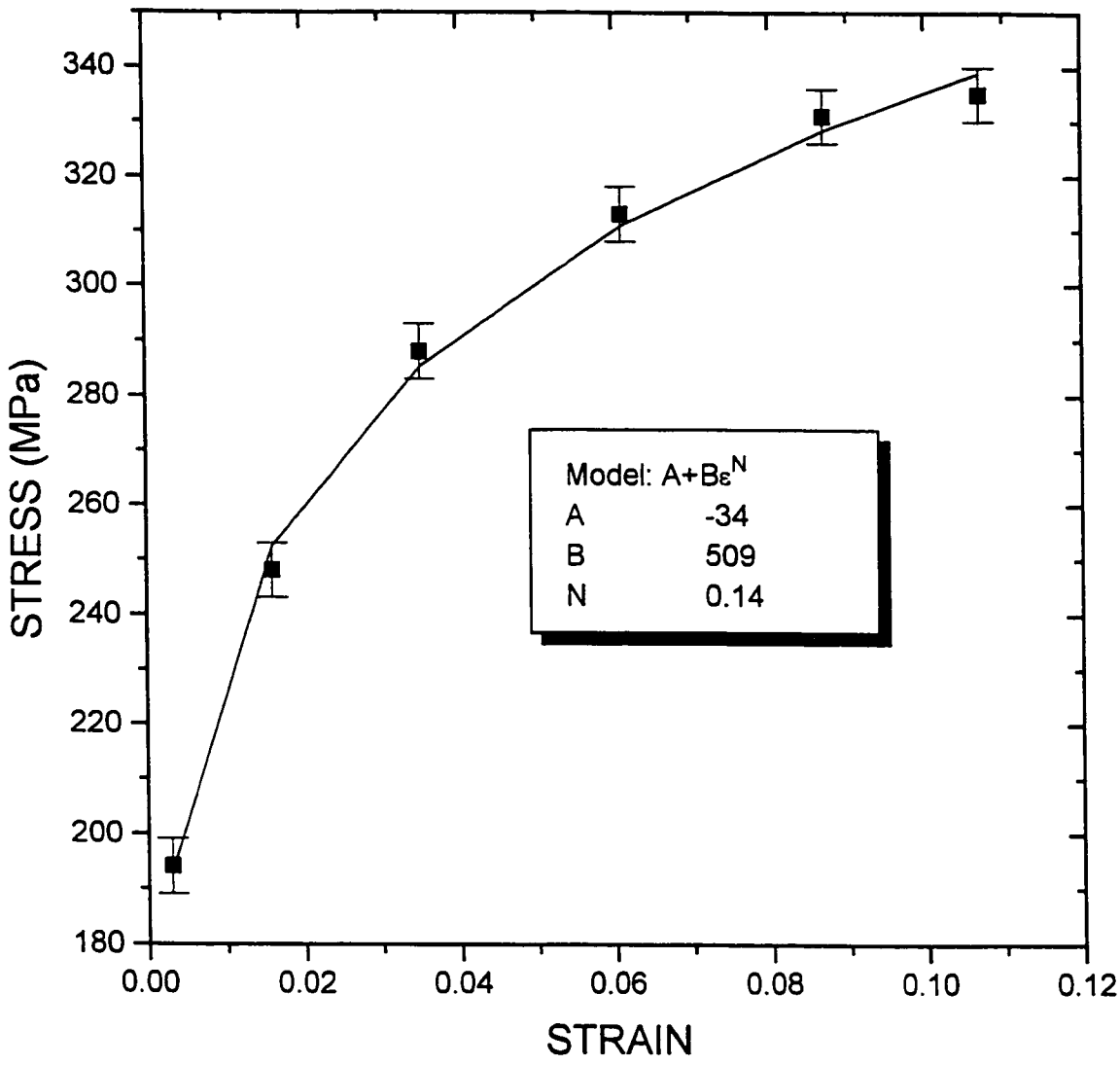

Figure 4.20 Plot showing a power-law fit to the stress-strain data for the hourglass shaped 6061-20% CMS tensile specimen .

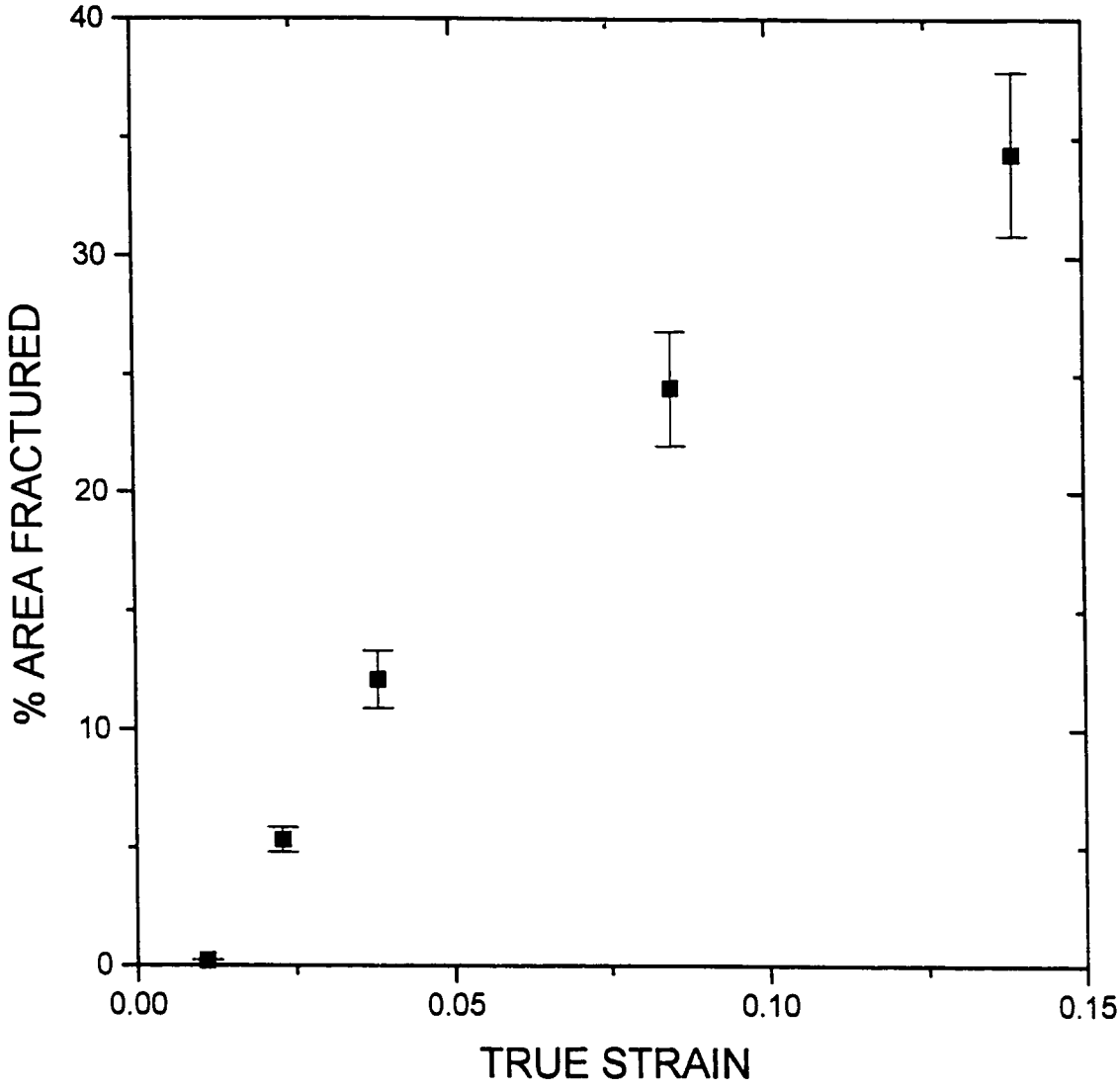

Figure 4.21 Plot of damage in 6061-20% CMS as a function of applied tensile plastic strain.

are cracked, is close to 35% compared to 3% damage for extrusion to a strain of 1.0. Thus, in tension, 7 times less strain creates approximately 10 times more damage in the form of cracked particles. Even considering the approximate correlation between stress and strain in figure 4.20, the effect of stress state is clear.

4.5 HYDROSTATIC EXTRUSION OF Cu-W COMPOSITES

Three billets of Cu reinforced with continuous W fibers were made into billets and hydrostatically extruded according to the procedure outlined in Section 3.5. The billets were extruded to a strain of 0.5 and the pressure extension traces for the procedure were similar to figure 4.1 for the particulate composites, with an extrusion pressure of 400 MPa.

Following extrusion, the samples were sectioned longitudinally, mounted and polished for microscopic examination. From this observation, it was apparent that the deformation in one of the three billets was different from the other two. Two of the samples showed significant microstructural damage in the form of fractured fibers. This type of behavior is illustrated in figure 4.22. The average length of the W fibre fragments was calculated to be 2.0 ± 0.5 mm. The other type of behavior was one of co-deformation of both phases, with the W fibers showing multiple necks. This is illustrated in figure 4.23. In view of these inconsistent microstructures, three more billets with one 2 mm W fibre were extruded. All of these served to verify the trend for fracture of the W. The co-deformed sample appears to be an exception rather than the general behavior for the composite.

In order to clarify the relative properties of the W fibers in the composites, microhardness measurements were made. The average hardness results for the fibers in the fully extruded and undeformed regions of the billets are presented in Table 4.7.

Figure 4.22 Cross section of a Cu-W billet extruded to a strain of 0.5, showing brittle fracture of the W fibers.

Figure 4.23 Cross section of a Cu-W billet extruded to a strain of 0.5, showing plastic deformation of the W fibers.

Table 4.7 Vickers Hardness of W fibers in Composite Extrusion Billets

	VICKERS HARDNESS (kg/mm^2)	
SAMPLE (mechanism)	UNDEFORMED	FULLY EXTRUDED
1 (fracture)	N/A	490 ± 10
2 (co-deformation)	485 ± 10	560 ± 10
3 (fracture)	490 ± 10	500 ± 10

The errors in Table 4.7 were estimated from the measurement uncertainty of the indentation size, namely ± 0.4 μm. It is to be noted that there is no significant difference in hardness between samples in the undeformed state. The W in the billets with fractured fibers had a comparable hardness as in the undeformed state. This suggests that the tungsten failed in a brittle manner, with no significant plastic flow. This is in contrast to the co-deformed sample, in which the fully extruded W fibers exhibit a higher hardness, further corroboration for the evidence for plastic flow and work hardening of the tungsten. The reason for the embrittlement of the W during composite fabrication is not known. There is, however, evidence in the literature (Neges et al., 1995) that work hardened W can be embrittled by heat treatment at temperatures as low as 1100°C. Considering the fabrication process for the Cu-W composites requiring liquid infiltration of Cu (m.p. 1084°C) around 1100°C, it is possible that the W fibres were heat-treated and embrittled. This may also explain the result of one ductile specimen, if the processing temperature for the production of that composite stayed below the critical embrittlement temperature.

The plastic flow characteristics in the Cu matrix were also investigated for the billets with fractured fibers. Microhardness measurements were made in Cu as a function of distance into the die. An example of the microstructure of the Cu-W composite in the die is shown in figure 4.24. In addition, indentations were made at regular intervals in the fully extruded section of figure 4.22. Using the approximation that the flow stress in metals can be estimated by the Vickers hardness divided by 3, the flow stress was plotted as a function of true strain by extrusion in figure 4.25. The experimental curve is

Figure 4.24 Cross section of a Cu-W extrusion billet extracted from the die.

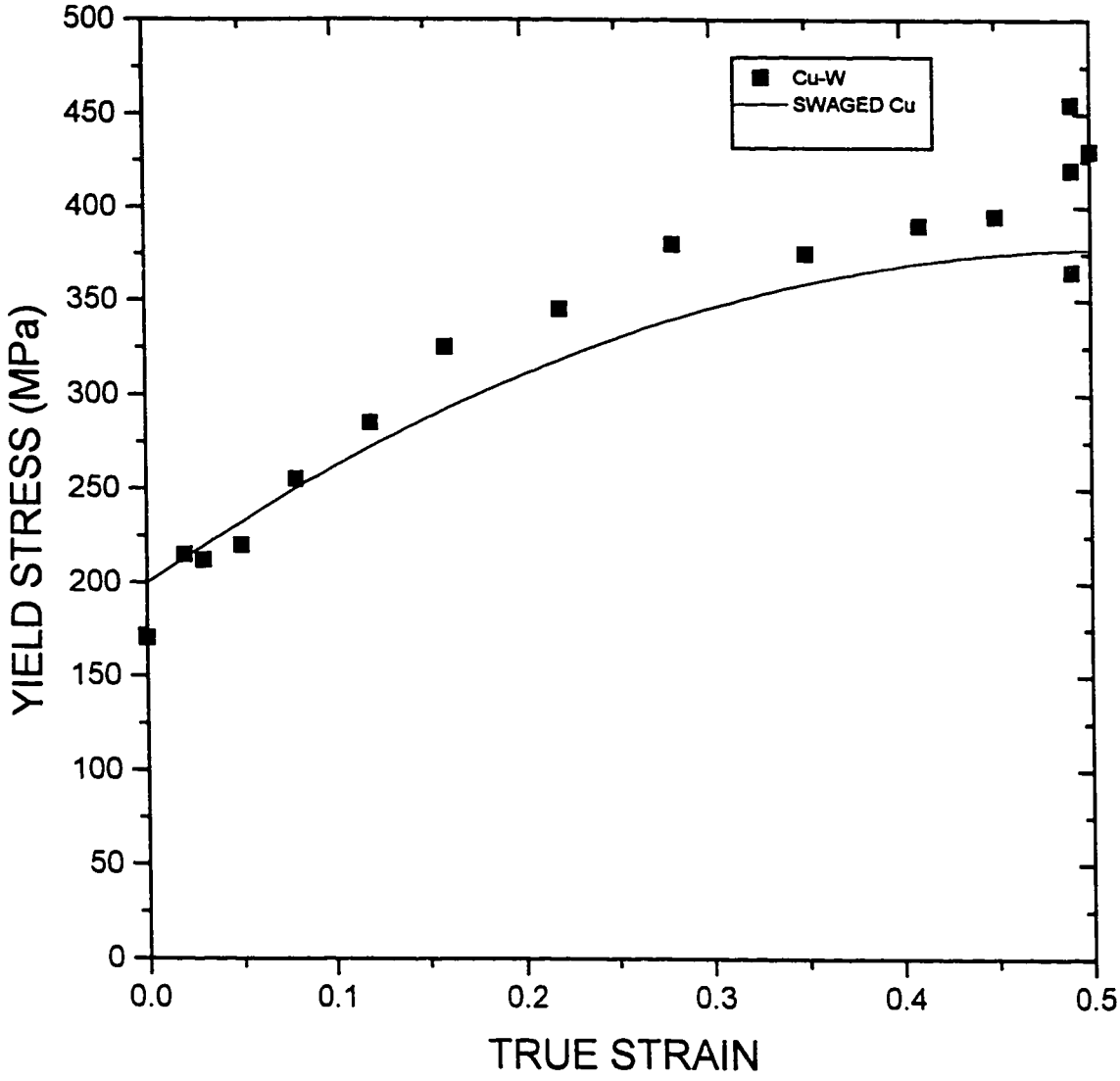

Figure 4.25 Plot of the flow stress in the Cu matrix of a Cu-W composite as a function of applied plastic strain by extrusion.

compared to a curve generated by swaging pure Cu in a similar strain range. From the plot, it can be seen that the matrix flow stress in the composite seems to follow closely the expected trend for pure Cu at low strains. However, at strains approaching 0.5, the flow stress of the Cu matrix in the composite is scattered between 310 and 430 MPa. This indicated a condition of inhomogeneous flow, where some regions of the matrix deform and work harden to a larger extent than others.

Further corroboration of this inhomogeneity in plastic flow was obtained by recrystallising the Cu matrix at a temperature of 450°C for 1 hour. A micrograph of the resulting microstructure is shown in figure 4.26. It is clearly seen from this that the recrystallisation occurred only near fibre fractures. As the driving force for recrystallisation is the reduction of stored energy, highly deformed regions will recrystallise more easily. It is thus further evidence that inhomogenous flow occurred in the composite, with much of the local strain being concentrated near the locations of the fibre fractures.

The results for an extruded internally gridded billet described in Section 3.5 were used to quantify this localization of strain during the hydrostatic extrusion process. The location of the deposited grid with respect to the tungsten fibre is shown in figure 4.27a) and the position of the grid after extrusion is shown in figure 4.27b). The grid was analyzed following the procedure outlined in Section 3.8 and the resulting strain map is shown in figure 4.28. The position of the fibre is schematized along with the map to help visualization. It is clear from this result that at or near the fibre fracture, the strain can be amplified by 40%, compared to the macroscopically imposed strain (0.5 in this case).

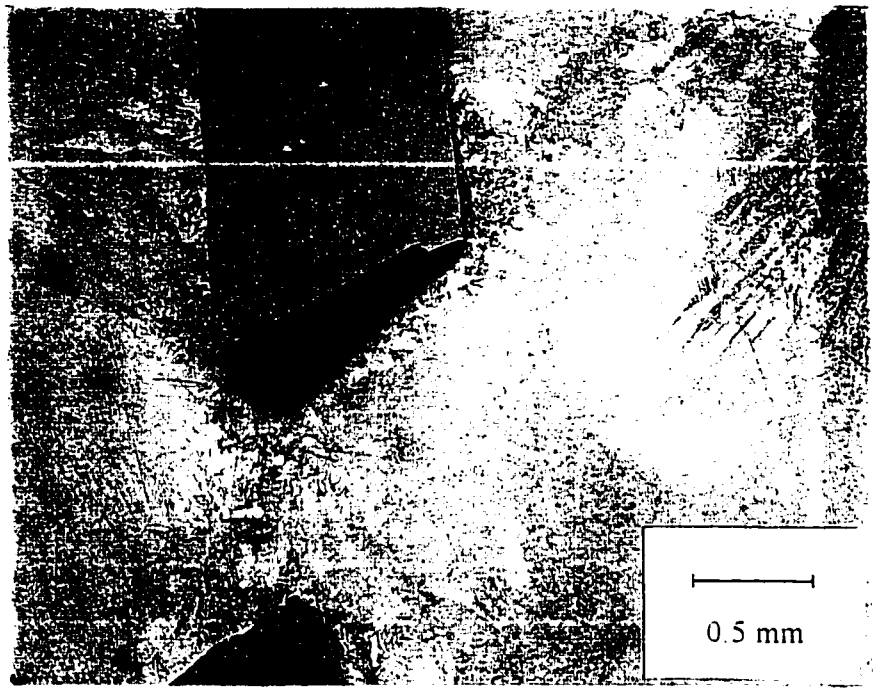

Figure 4.26 Micrograph of the recrystallised Cu matrix in an extruded Cu-W composite.

a)

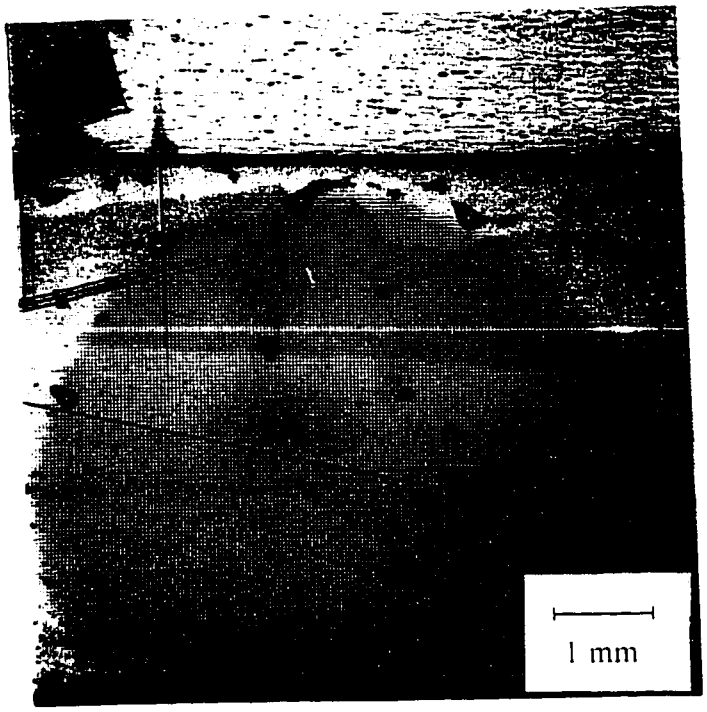

b)

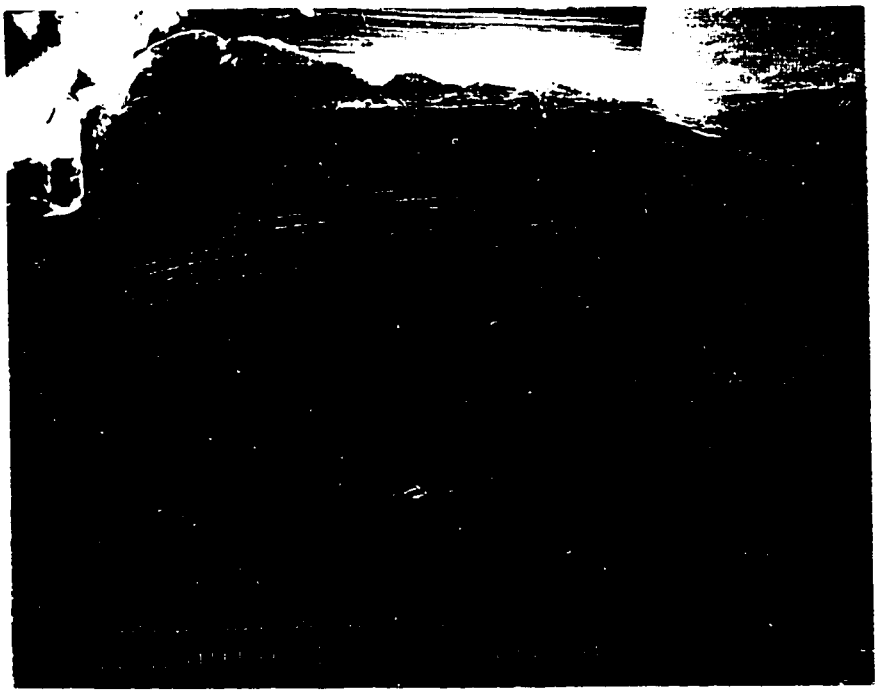

Figure 4.27 Position of the deposited fiducial grid in an internally gridded Cu-W composite extrusion billet. a) before extrusion and b) after extrusion to a strain of 0.5

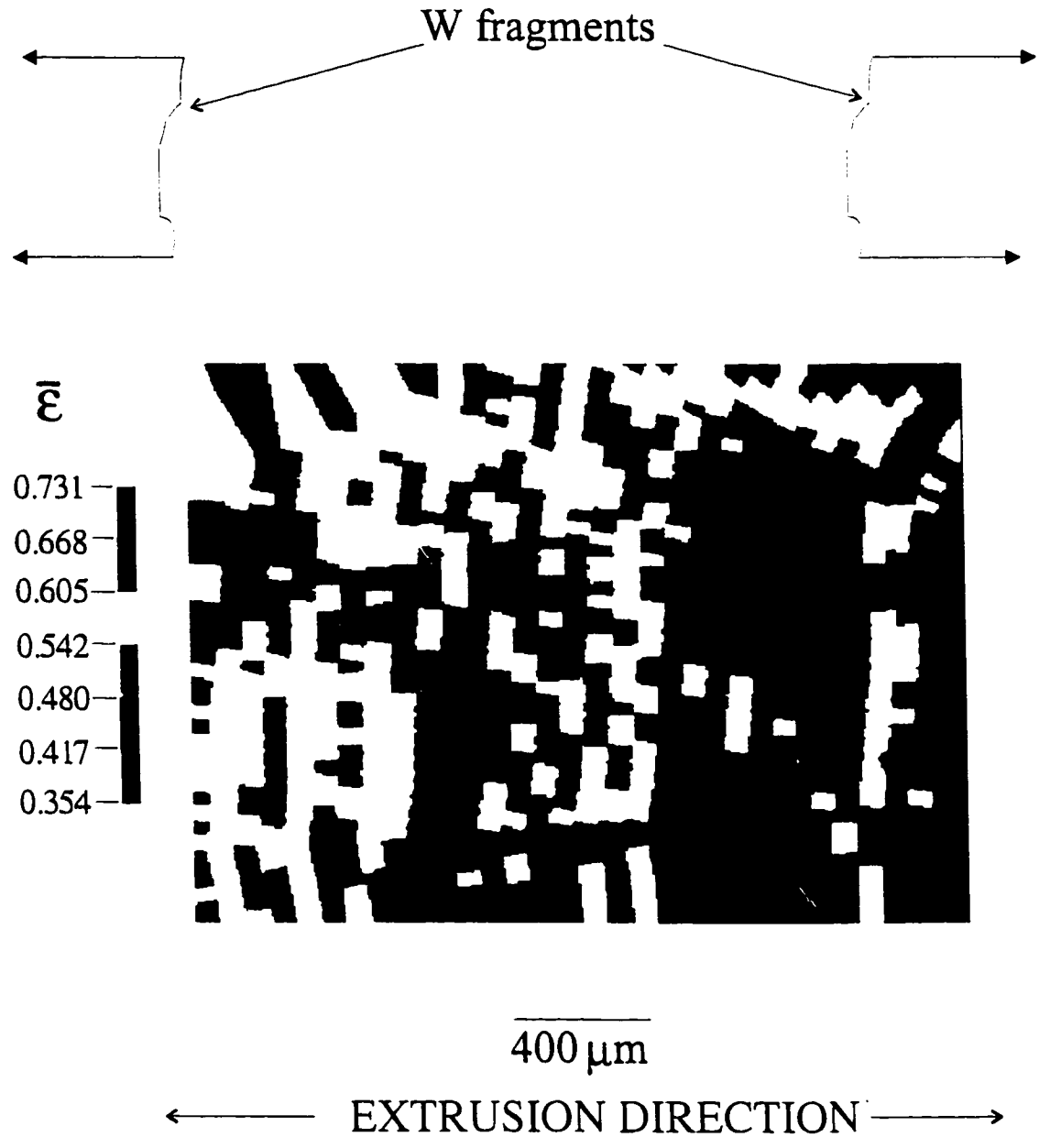

Figure 4.28 Map of the equivalent strains near a fractured W fibre of an internally gridded Cu-W composite extruded to a strain of 0.5.

4.6 PLANE STRAIN COMPRESSION OF Cu-W COMPOSITES

This section will present the results obtained by deforming the model Cu-W composites described in Section 3.8 and deformed in plane strain according to the procedure outlined in Section 3.3. The composites were deformed in plane strain in the transverse direction to the aligned fibres in order to limit the plastic deformation to this transverse plane, where fiducial grids were deposited following the method described in Section 3.7. Thus, the deformed grids give a picture of the way in which the pattern of strain in the matrix is modified by the presence and the spatial distribution of fibres and gives insight into the occurrence of damage by decohesion.

To verify the degree to which plane strain was approached, the longitudinal dimensions of the plane strain samples were measured before and after every test. It was found that the average out of plane strain was 0.4 ± 0.2 % for these tests. It is thought that these strains were the results of the squeezing out of the soft teflon tape used as lubricant for the tests. Considering that the transverse plastic strain imposed on these samples was varied from 10% to 30% depending on the test, it is thus clear that conditions of plane strain were closely approached.

During the tests, the load and displacement of the lower ram were monitored. Due to loads in some tests approaching 90 kN, the deflection of the machine contributed to the ram displacement, as well as the deflection of the teflon lubricant in the load train. Thus, the change in length of the composite was not equal to the displacement of the ram. Hence, it was not possible to construct true stress - true strain curves from the data. In addition, the friction between the sample and pushrods alter the stress state of the test from pure compression to a mixed mode. With these errors in mind, it was still thought to be of worth for comparative and illustrative purposes to construct plots of engineering stress and engineering strain for some of the tests. The engineering stress was calculated as the load divided by the

original cross-sectional area of the sample and the engineering strain was calculated by the change in lower ram displacement divided by the original height of the sample. Examples of the resulting curves are shown in figure 4.29 for the composite consisting of one centered fibre and tested to 12.4%, 20.5% and 28.5% total engineering strain. The initial part of the curves, corresponding to deflections of the lubricant and alignment of the load train, was deleted and the curves were shifted arbitrarily to lower strain. After this shift, it is found that there is general agreement in the slope of these curves at strains above 10 %. The same can be said for figure 4.30, which is a comparison in the response between the various distributions of the two-fibre composites described by figure 3.13b) and deformed to engineering plastic strains of 20 ± 2%. It is thus apparent that globally, the response of the composites in plane strain does not seem to depend on the orientation of the two reinforcing fibres with respect to the axis of compression. This result is not surprising in view of the fact that the global volume fraction of W is small for these samples, so that the overall mechanical response is mainly due to the response of the matrix. The question is whether the fibres affect the flow behaviour locally and this is examined next.

The local effect of the rigid W fibres on the flow pattern of the Cu matrix was obtained from the analysis of deformed fiducial grids on the faces of plane strain compression samples. The strain range over which the compression tests were conducted was limited by the occurrence of damage. For the Cu-W composites in this present study, damage occurred by decohesion of the fibre matrix interface and the magnitude of the strain needed to initiate this process was found to depend on the spatial arrangement of the fibres. In view of this observation, the experimental strain range was varied for different arrangements of reinforcement. The samples with one centered fibre were tested from 10% to 30% plastic strain, at approximate intervals of 10% strain, without damaging. The two fibre samples were also tested at the same strain intervals, but decohesion of the fibre matrix interface was observed in the samples deformed close to 30% plastic strain. The clustered and graded composites were deformed to about 10% and 20% plastic strain. By visual inspection, it was found that there was decohesion

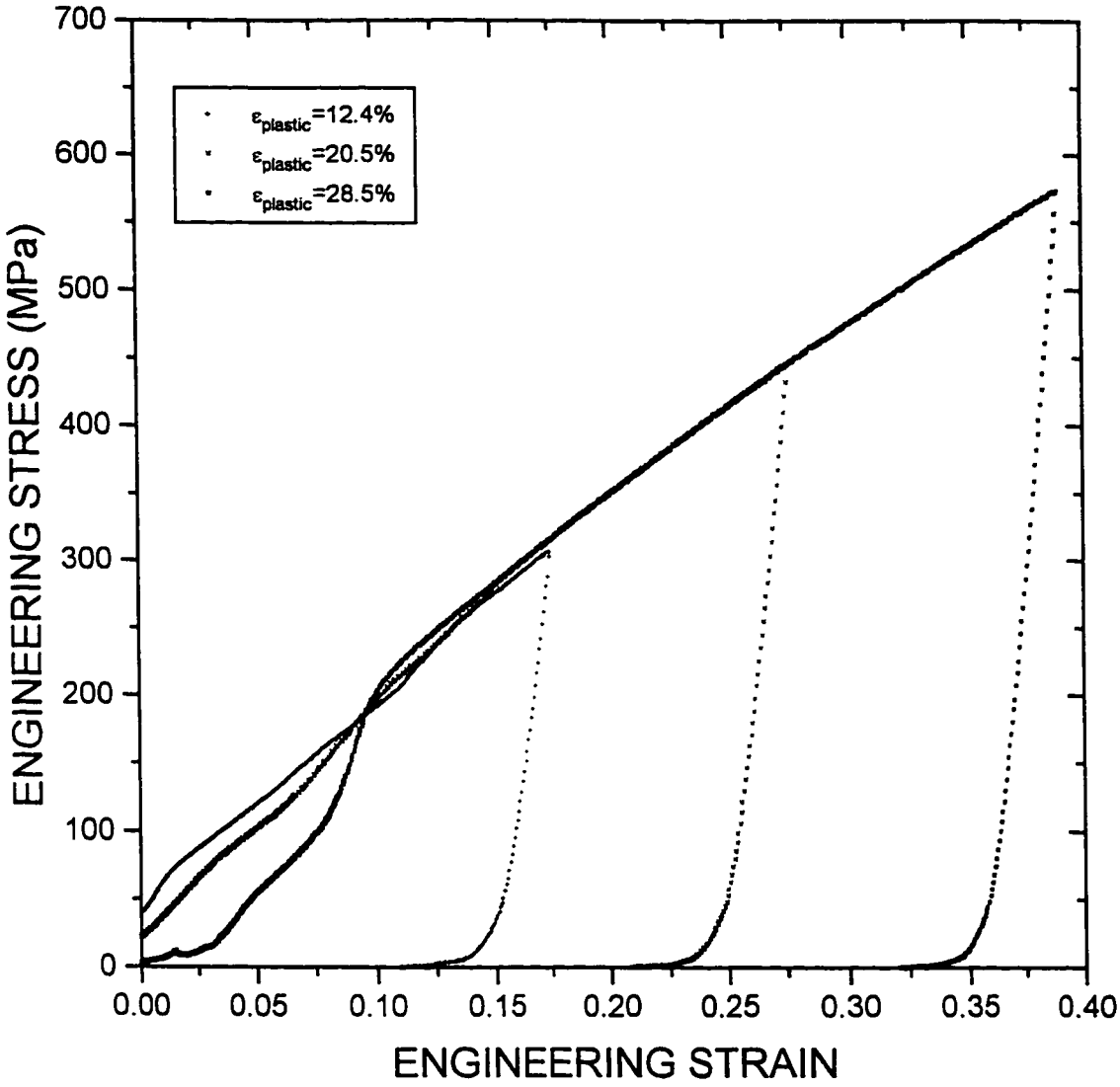

Figure 4.29 Plot of the engineering stress strain curves for one-fibre Cu-W composites deformed in plane strain compression to total strains of 12.4%, 20.5% and 28.5%.

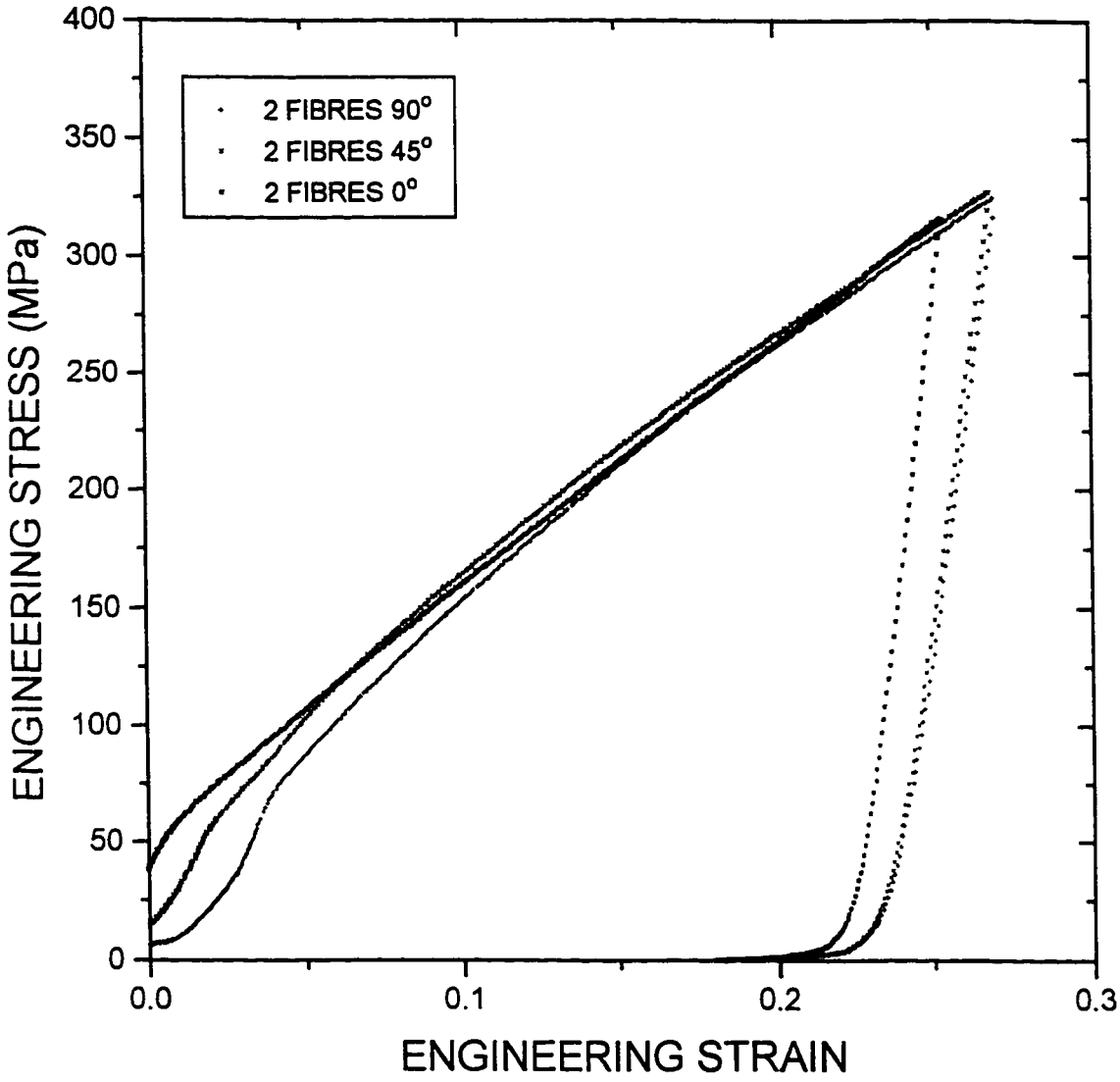

Figure 4.30 Plot of the engineering stress strain curves in plane strain compression for two-fiber Cu-W composites deformed to a total strain of 20±2% for the following arrangements: 0° to the compression axis, 45° to the compression axis and 90° to the compression axis.

between the matrix and fibres for both arrangements at 20% applied plastic strain. Thus, an intermediate strain of around 15% was chosen for the third test on these composites with arrayed fibres.

The analysis of the deformed grids was restricted to samples that exhibited no or very little damage. In this way, the pattern of flow and its dependence on the distribution of reinforcement could be monitored before the occurrence of damage. This was important to relate the conditions of flow before the damage event to strain localization and constraint exerted by the fibres. An example of a deformed grid corresponding to a region on the arrayed composite with a graded distribution of fibres deformed to a total strain of 13.9% is presented in figure 4.31. The errors involved in calculating the strains were estimated from the assumption that the largest uncertainty in the measurements was in the digitizing of the deformed grids. Micrographs on the same scale as figure 4.31 were converted to bitmaps with a resolution of approximately 1 micron per pixel. It was estimated that the coordinates of any grid vertex could be specified to within 1 pixel. Thus, the error in digitizing was estimated at $\pm$ 1 μm. The original grid elements were of the order of 25 $\pm$ 1.4 μm in size. A simple RMS analysis for the homogenous compression of a grid element with the errors discussed above returned an error in strain of $\pm$ 5%. This was considered to be the error in measurement of one deformed grid element. However, a negative error in one element will result into a positive one in the adjacent element which shares the same vertex and vice-versa. Hence, as the strain maps were plotted using averaging routines for an array of data, it was thought that these errors with opposite signs for adjacent points will statistically be reduced, so that the error in strain for any one point on the strain map is thought to be somewhat less than 5%. In view of these errors in strain of a few percent, up to possibly 5%, it was considered that the analysis of samples deformed to a macroscopic strain of 10% would not yield very accurate information. Thus, the decision was made to analyse the deformed grids on the following samples: the composite with one centered fibre deformed to a strain of 20.5%, the composite with one centered fibre deformed to a strain of 26.7%, the two fibre composite at 0° to the compression axis deformed to a strain of 20.1% , the two fibre composite

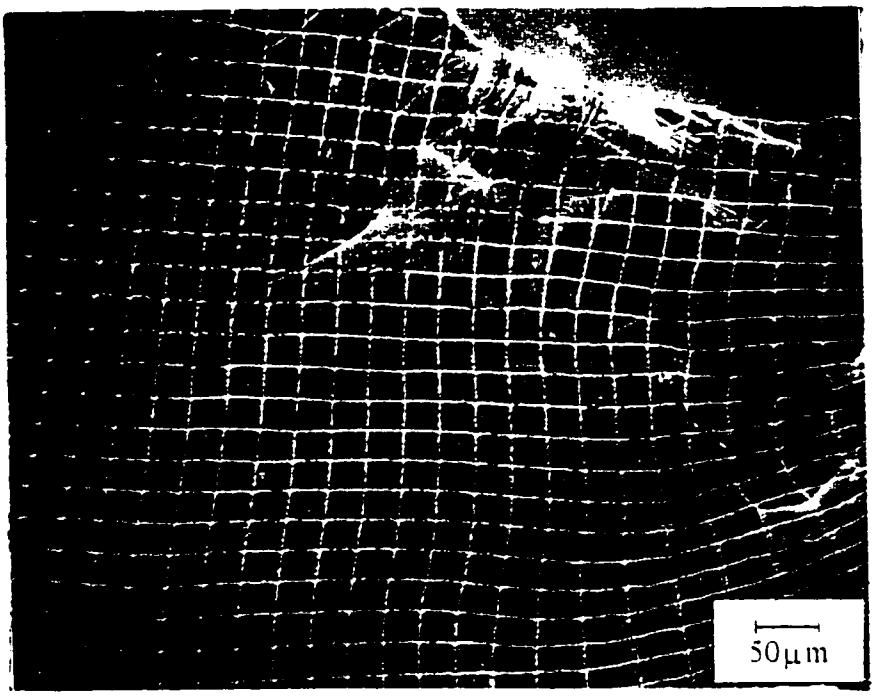

Figure 4.31 Micrograph of a deformed grid from on a Cu-W composite with a graded distribution of reinforcement after 13.9% deformation in plane strain compression.

at 45° to the compression axis deformed to a strain of 21.3%, the two fibre composite at 90° to the compression axis deformed to a strain of 18.3%, the composite with a clustered array deformed to a strain of 14.3% and the the composite with a graded array deformed to a strain of 13.9%. The corresponding strain maps for these samples are presented in figure 4.32 to figure 4.40. To better illustrate the pattern of flow between the fibres in the composite with a clustered array of fibres, the map shown on figure 4.37 was reflected both horizontally and vertically. The result is shown in figure 4.41.

Some general observations can be made from the strain mapping in the Cu matrix near W fibres. It is clear from the maps that the presence of a fibre or many fibres affects the location and intensity of the plastic strain in the Cu matrix. In some cases, it is observed that the strain can be magnified by up to 5 times the value that was imposed globally on the sample. The magnitude of the strain is determined by the stiffness of the fibres, the interfacial strength and the pattern of fibre reinforcement. It can also be generally observed that the location and extent of extremes in strain depends on the proximity to a fibre as well as the distance to the nearest neighbour, if any, and how they are distributed with respect to the axis of compression.

The effect on the local flow pattern created by adding one central fibre in a Cu matrix can be visualised using figure 4.32 and figure 4.33 which correspond to samples deformed globally to strains of 20.5% and 26.7% respectively. For both these samples, it can be seen that the local strain near the fibres is magnified to approximately 3 times the macroscopically applied strain. These high strain regions occur close to the fibre and are located at angles of about 0° and 90^0 to the compression axis. Further, minima in strain are roughly located at 45^0 to the compression axis, and the strain in these regions can be smaller in magnitude than the macroscopic applied strain. This pattern of flow is clearer for the sample deformed to 20.5% strain. At 26.7% strain, the pattern near the fibre varies more sharply and the area fraction of high strain seems to rise. This suggests that, with increasing globally applied

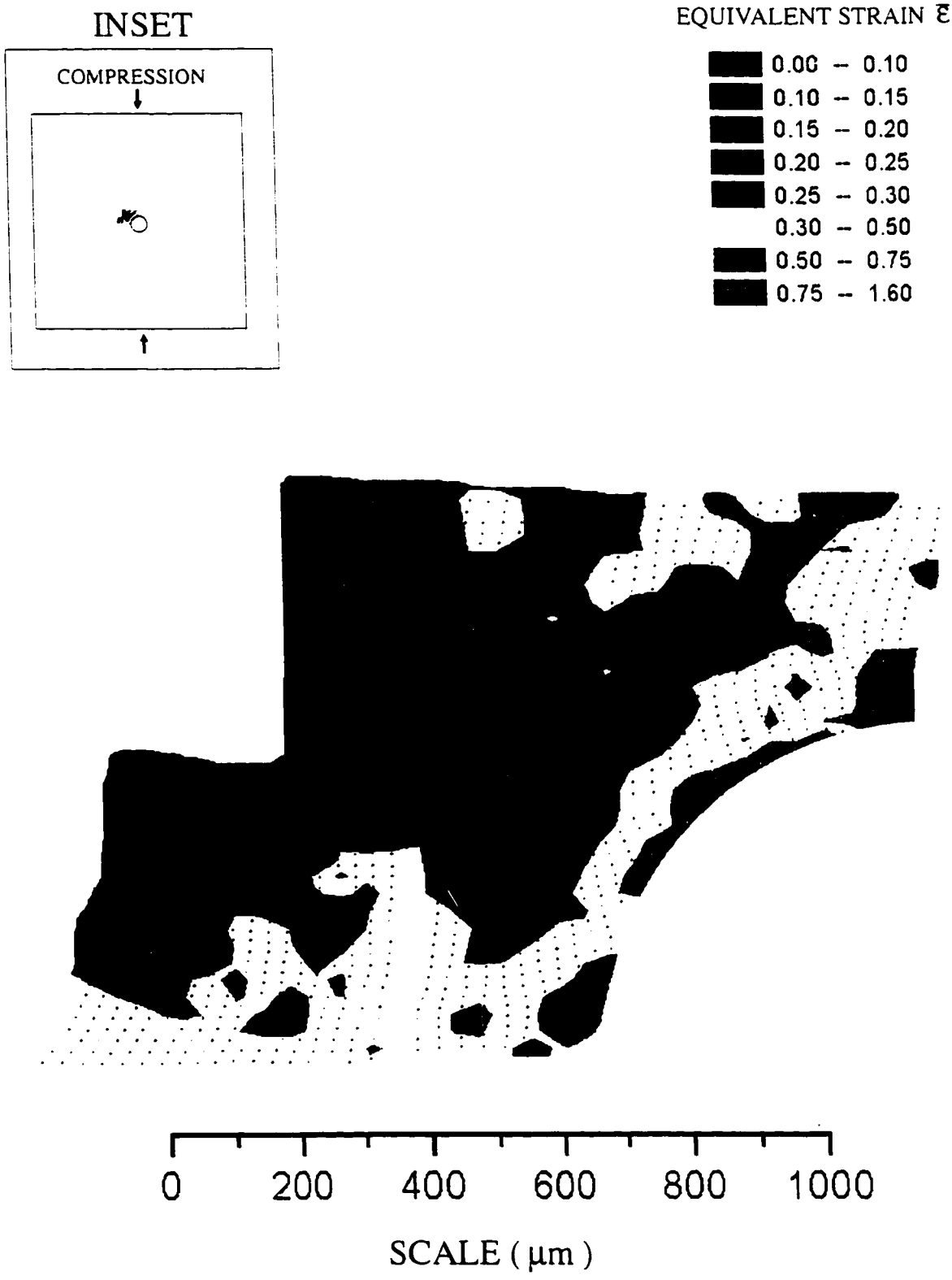

Figure 4.32 Map of equivalent strains in a one-fibre Cu-W composite deformed 20.5% in plane strain compression.

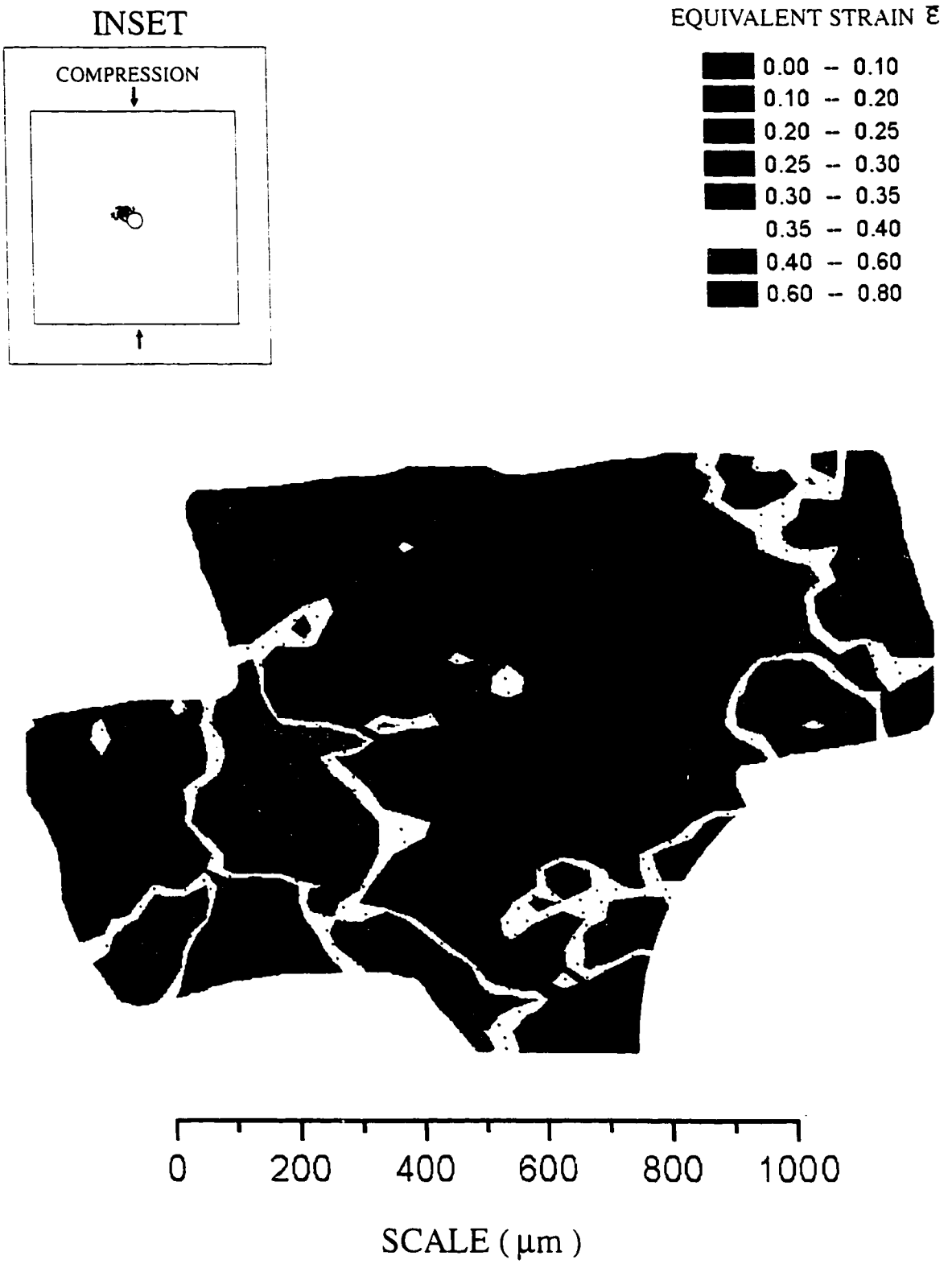

Figure 4.33 Map of equivalent strains in a one-fibre Cu-W composite deformed 26.7% in plane strain compression.

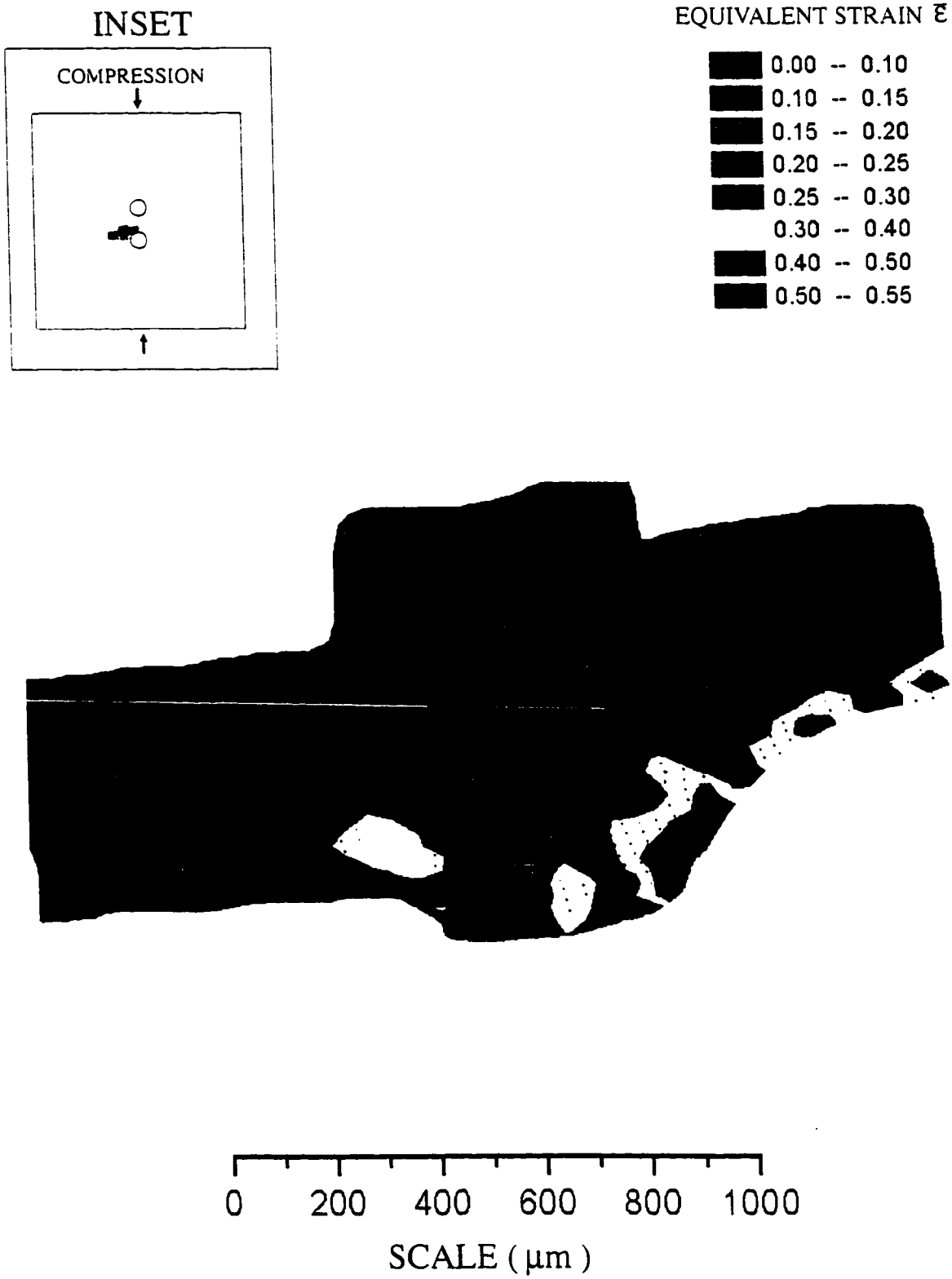

Figure 4.34 Map of equivalent strains in a two-fibre Cu-W composite with the fibre arrangement oriented 0° to the compression axis deformed 20.1% in plane strain compression.

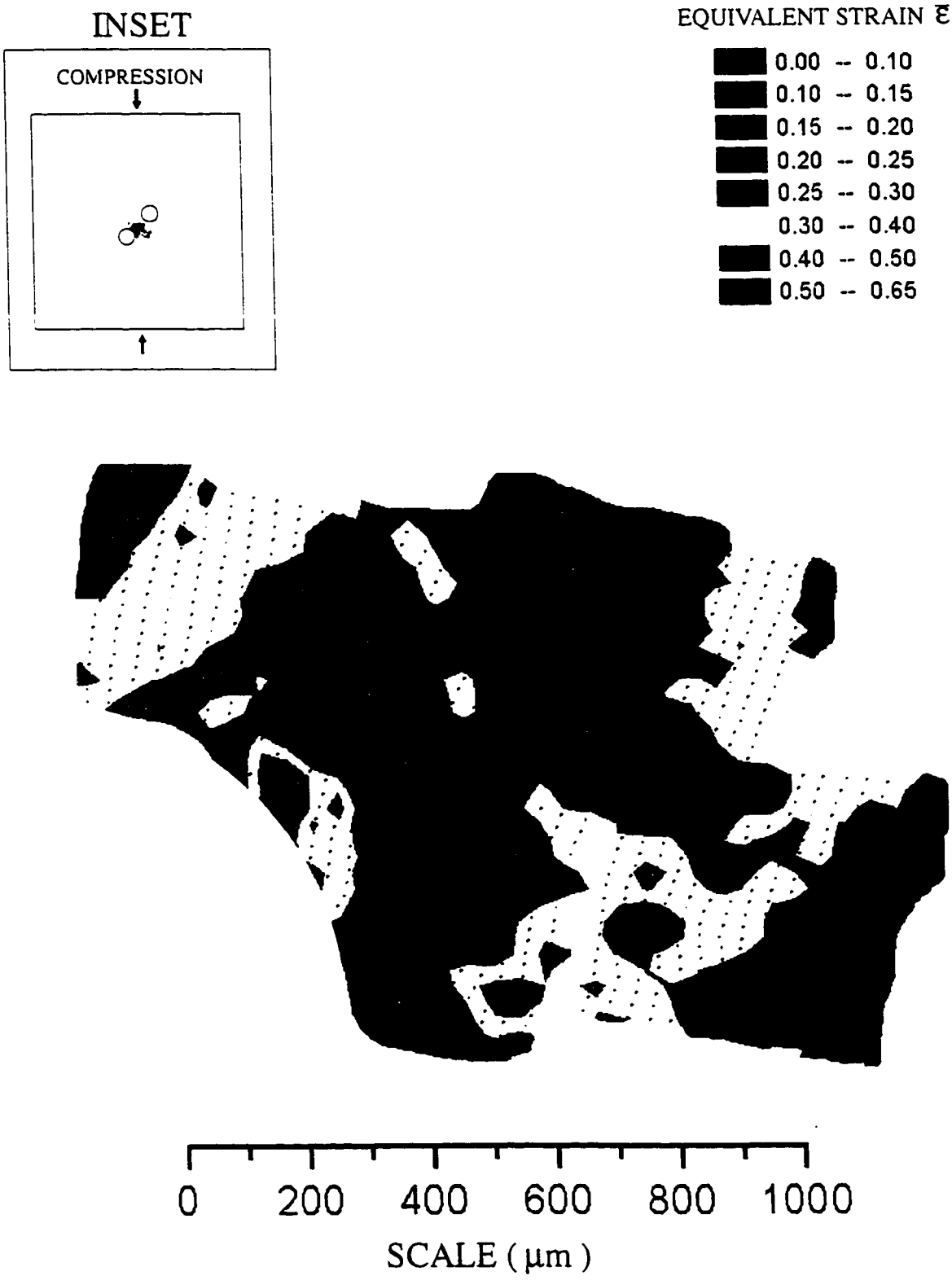

Figure 4.35 Map of equivalent strains in a two-fibre Cu-W composite with the fibre arrangement oriented 45° to the compression axis deformed 21.3% in plane strain compression.

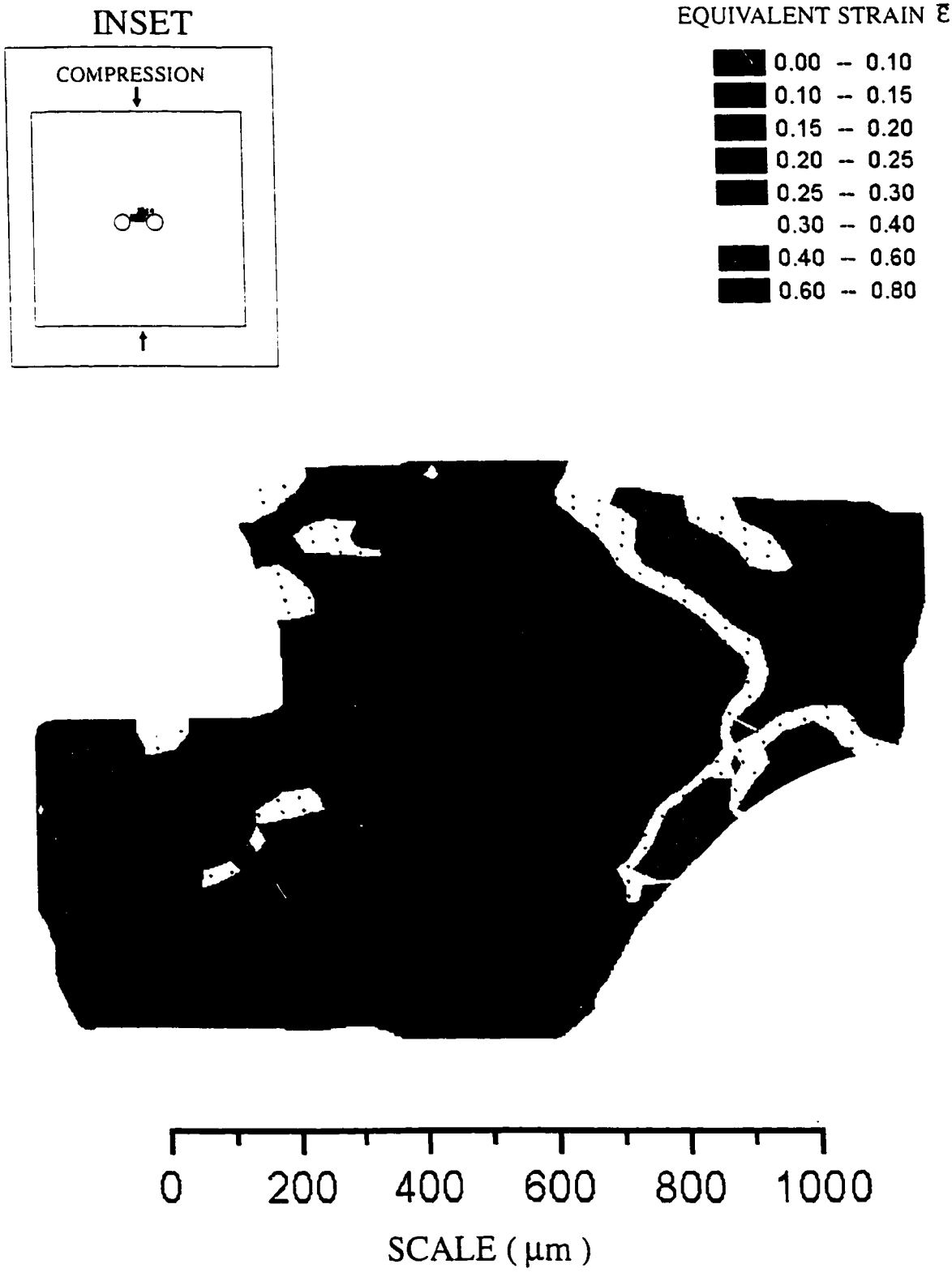

Figure 4.36 Map of equivalent strains in a two-fibre Cu-W composite with the fibre arrangement oriented 90° to the compression axis deformed 18.3% in plane strain compression.

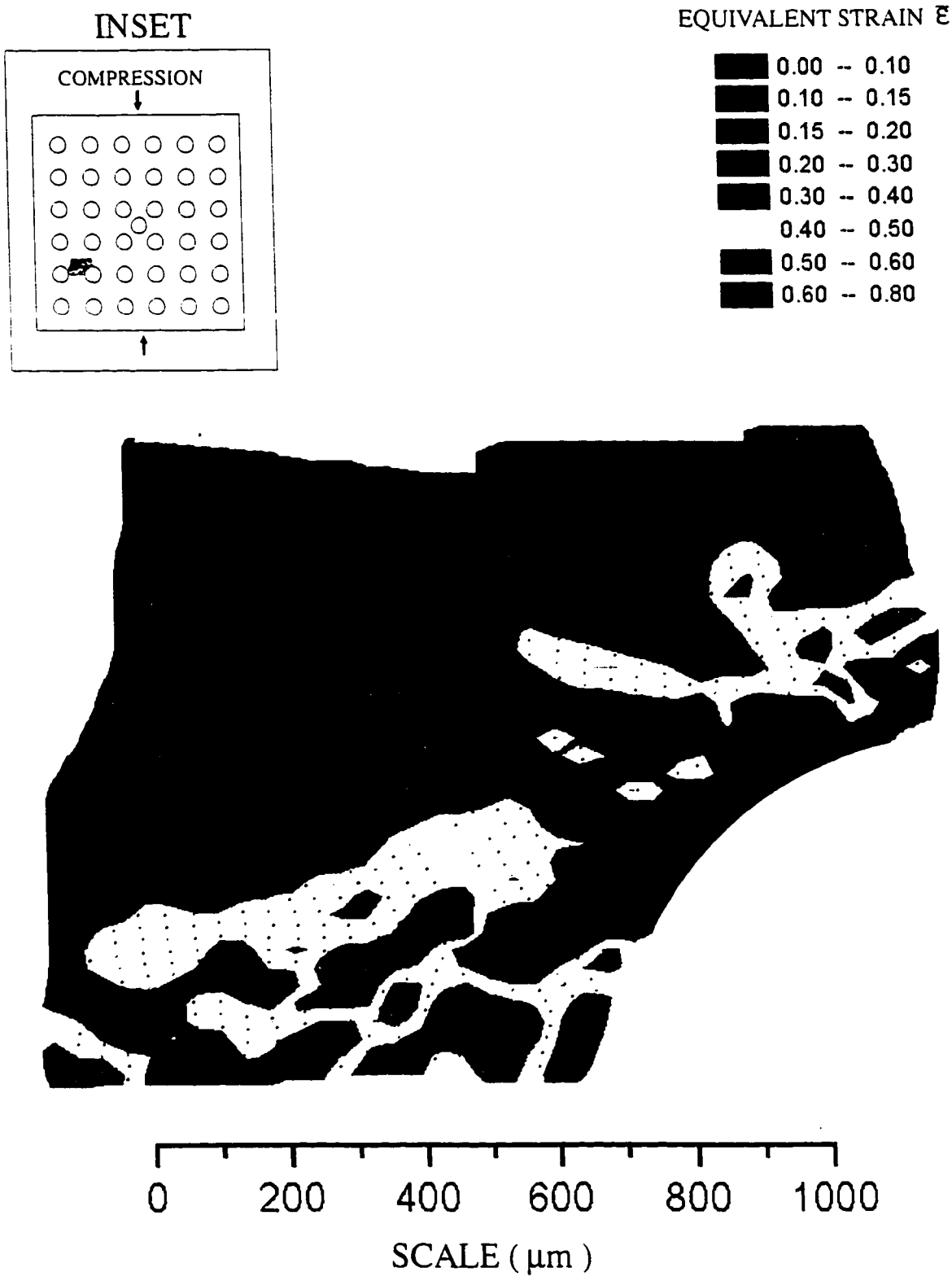

Figure 4.37 Map of equivalent strains in the clustered Cu-W composite deformed 14.3% in plane strain compression. The region mapped is one well away from the cluster.

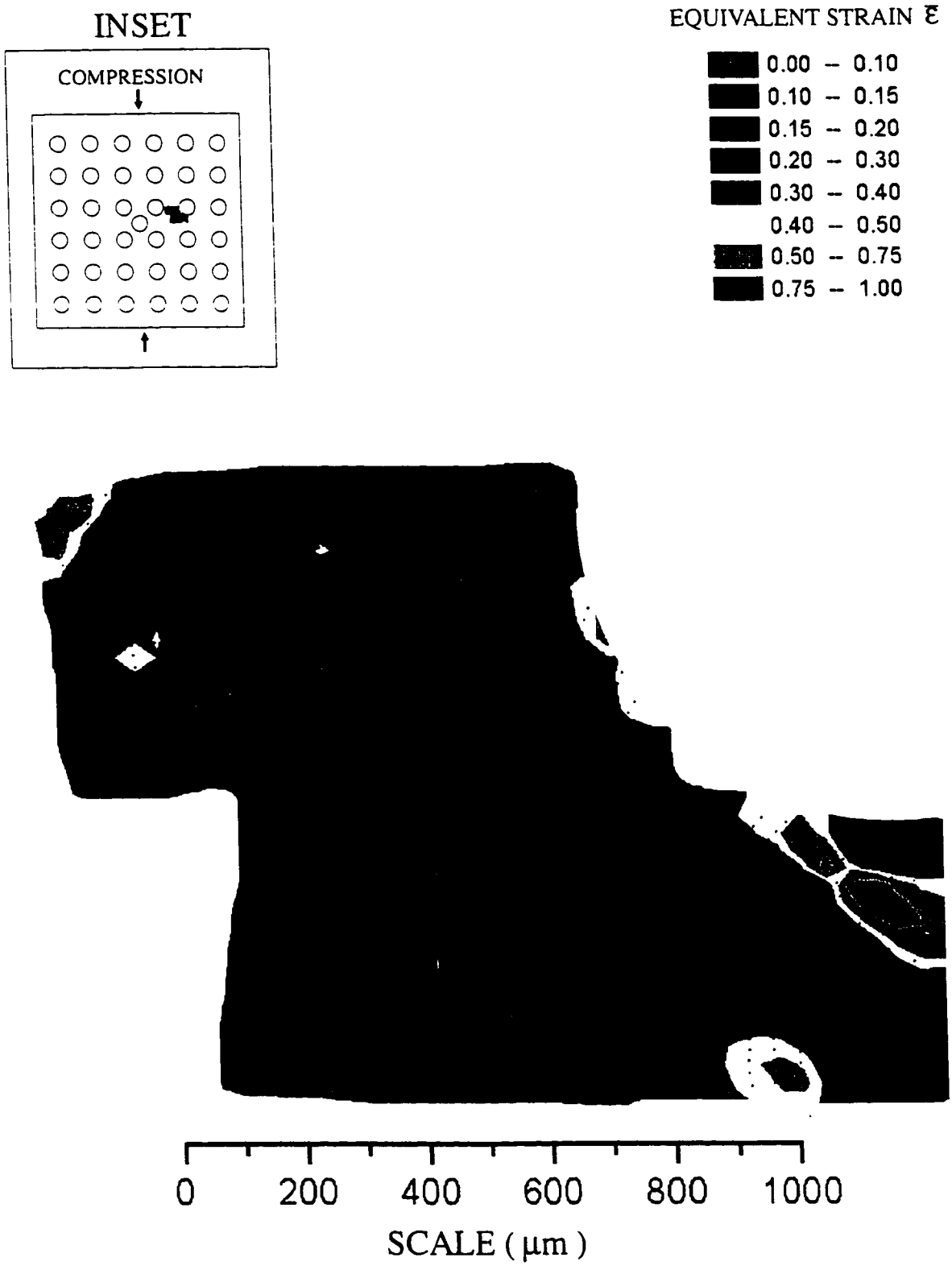

Figure 4.38 Map of equivalent strains in the clustered Cu-W composite deformed 14.3% in plane strain compression. The region mapped is one near the cluster.

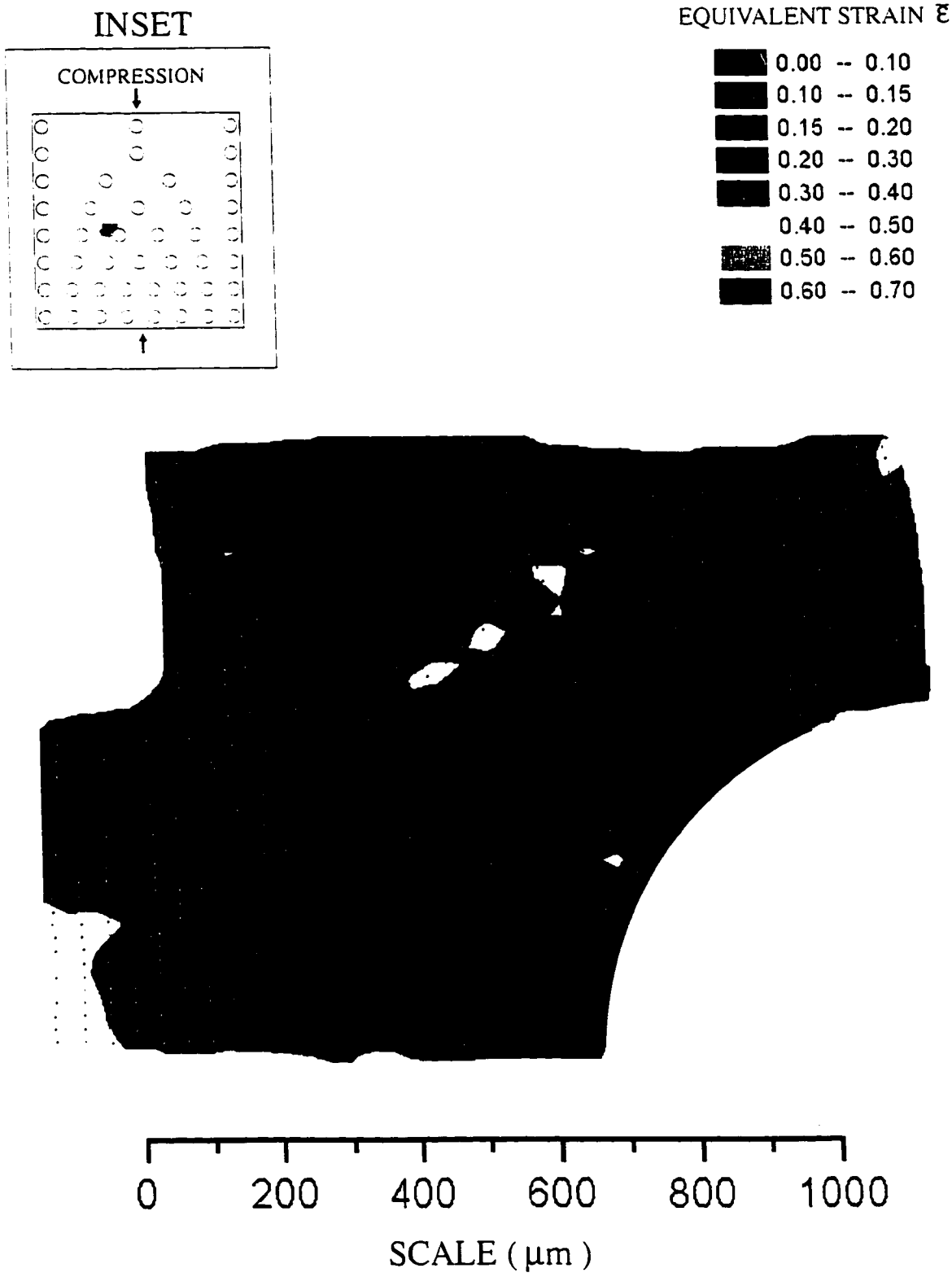

Figure 4.39 Map of equivalent strains in the graded Cu-W composite deformed 13.9% in plane strain compression. The region mapped is one of low local volume fraction of W.

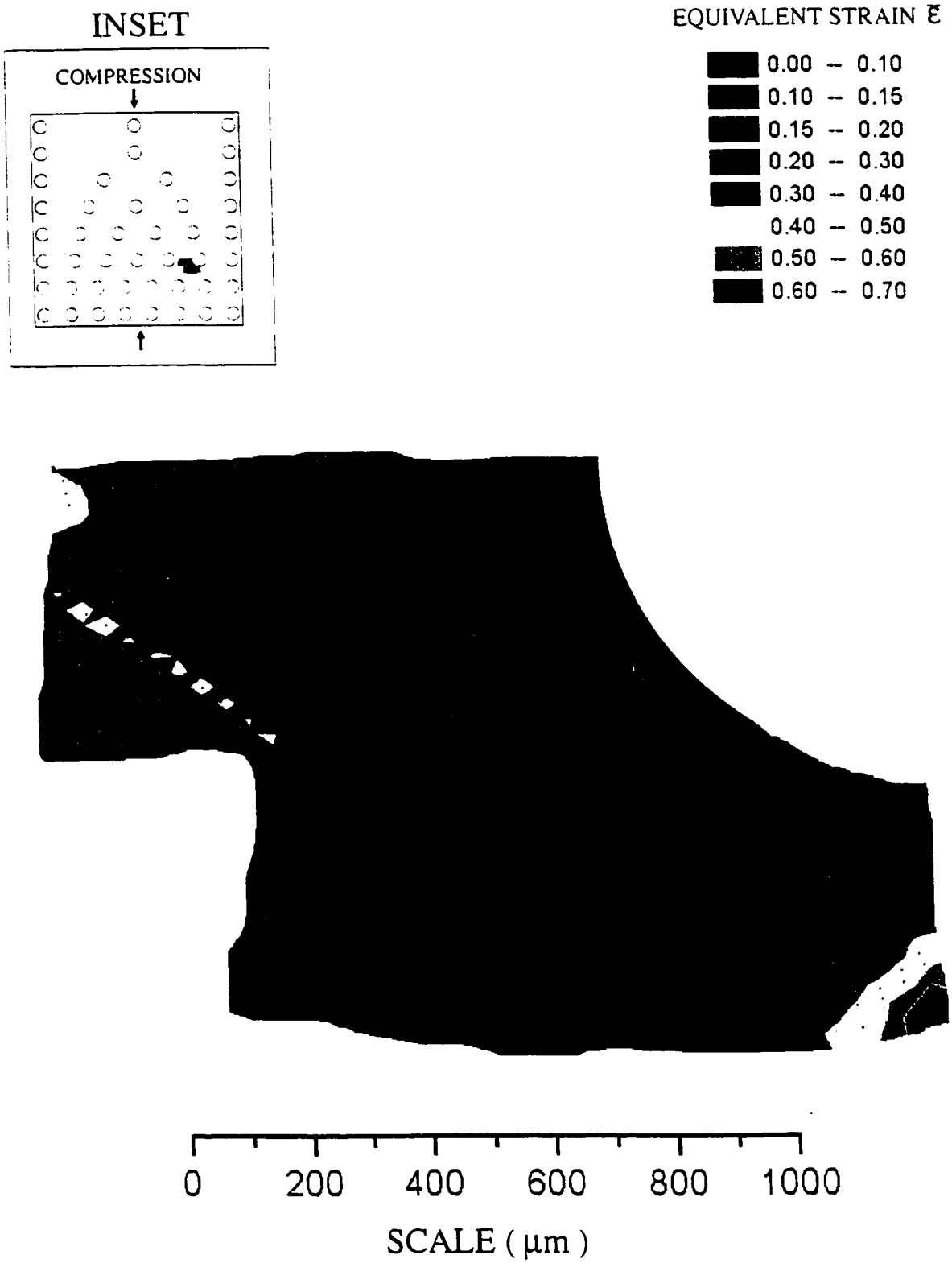

Figure 4.40 Map of equivalent strains in the graded Cu-W composite deformed 13.9% in plane strain compression. The region mapped is one of high local volume fraction of W.

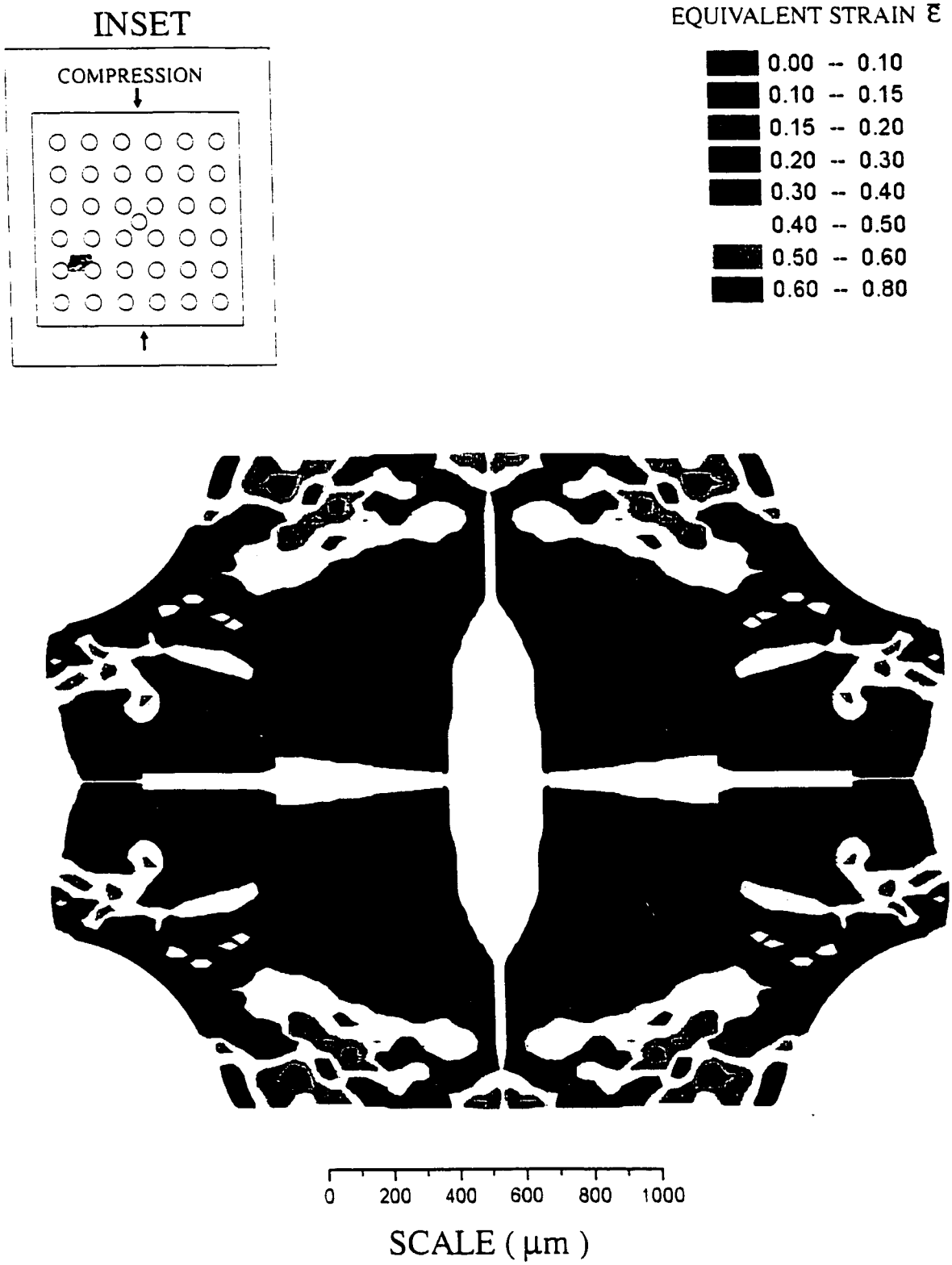

Figure 4.41 Reflected map of figure 4.37 showing the pattern of flow between the W fiber in the clustered Cu-W composite deformed 14.3% in plane strain compression.

strain, the average strain magnification near the fibre increases and that regions of higher than average strain grow at the expense of the low or average strain regions.

Comparison of the 3 arrangements of double fibres also yields useful insights into the effect of the angle of the fibres to the compression axis. These two-fibre composites are compared for the same nominal strain of 20 ± 2 % in figure 4.34, figure 4.35 and figure 4.36 for the 0°, 45° and 90° arrangements respectively. The similarities between the strain maps are that, as in the samples with one fibre, strains are inhomogenously distributed near the fibres. In all three, some regions have deformed to a high level of strain equivalent to about 60%, which is about 3 times the macroscopically imposed strain. The location and extent of these regions of low strain depends on the fibre arrangement. The 90° arrangement of figure 4.34 features regions of low strain at about 45° and 90° to the compression axis and strain amplification near the fibre matrix interface at roughly 0° to the direction of compression. Thus, the presence of the other fibre creates a zone of lower than average strain where a zone of higher than average strain was created in the one fibre samples. The second fibre has restricted the local flow of the matrix along the symmetry axis through the fibre diameters. This is in contrast to the results for the 45° arrangement of fibres which show no extensive regions of low strain. Similar to the 90° arrangement, the matrix strain is magnified near the fibre at 0° to the compression axis. However, the comparison of the results between the 90° and 45° arrangements differ in the 90° direction, where the strain is amplified in the 45° arrangement, although to a lesser extent than in the 0° direction for that sample. The 0° arrangement of fibres from figure 4.34 also has unique characteristics. The strain map shows a broad region of lower than average strain at an angle of about 45° to the direction defined by the axis of compression, with some limited regions of high strain near the fibre in the 0° direction and approaching the 90° direction. It is thus an interesting result that globally, from figure 4.30, the behaviour of the composites is indistinguishable but that locally, near the fibres, marked differences in

local strains occur. These differences are in terms of both the magnitude of the strains and also the inhomogeneity of the pattern of strain around the fibres.

The pattern of flow in the Cu-W composites with arrayed fibre arrangements was obtained from the deformed fiducial grids following plane strain compression. The resulting strain maps enabled an examination of the flow characteristics near a fibre and also of the matrix flow pattern between neighbouring fibres. Hence, two gridded regions of the clustered composite described in Section 3.8 were analysed. The first region's position and the local distribution of strain in it are shown in figure 4.37. This is a region well away from the cluster. At angles of 0° and 90° to the compression axis were regions of high strain, reaching up to 5 times the macroscopically imposed strain of 14.3%. At 45° to the compression axis and about 600 microns away from the fibre are regions of low strain. Figure 4.38 depicts the distribution of strain nearer to the cluster. Similar features are seen, namely high strain regions near the fibre at angles of about 0° and 90° to the compression axis and a low strain region at approximately 45° to the direction of compression. However, this region of low strain is much nearer to the fibre, about 100 microns away.

The analysis of deformed grids was also made for two regions of the graded composite which was deformed to a global strain of 13.9%. These two regions, which can be seen on the insets of figure 4.39 and figure 4.40, correspond to areas of low local volume fraction of reinforcement and high local volume fraction of reinforcement respectively. Inhomogenous flow patterns were observed in both areas, but there was much less variation in strain in the lower volume fraction region. The higher local volume fraction region has locations where the strain is magnified up to 5 time the global strain. This is in contrast to the lower local volume fraction region where the highest strains recorded were of the order of 3 times the globally applied strain. The high strains in the high local volume fraction region are concentrated at a distance of about 200 microns from the fibre, at an angle of 0° to the compression axis.

This direction of high strain coincides with the direction of increasing local volume fraction of reinforcement in the graded array. Another interesting feature of the strain map in figure 4.40 is the large region around the fibre where the strain is close to the globally imposed nominal strain of 15%. The highest strains recorded for the region of lower local volume fraction, from figure 4.39, are located mainly at a distance of about 700 microns away from the fibre, at a 90° angle to the compression axis. This direction corresponds to the region of the highest local reinforcement volume fraction. A region of lower than average strain is located about 600 microns away from the fibre at approximately 45° to the compression axis.

4.7 DETERMINATION OF INTERNAL STRESSES IN Cu-SAPPHIRE

Section 4.6 dealt with the changes in the pattern of flow in the Cu matrix reinforced with rigid W fibres. No information was obtained for the load transfer to these fibres. Therefore, residual stress information was obtained from optical measurements on a single crystal sapphire fibre centered into a Cu matrix and deformed in plane strain compression. The details of composite fabrication, processing and testing are outlined in Section 3.5 and Section 3.9.

The spectra for the composite as-fabricated and for a free fibre were acquired in order to get a measure of the thermal residual stresses induced in the fibre during the solidification process. To monitor instrumental shifts, spectra for a characteristic Ne line were acquired before and after the tests.

To validate a test, it was determined that the Ne spectral peaks acquired before and after the test should not differ by more than 0.01 cm^{-1}. This was done so that confidence could be gained of instrumental stability during the test on the sapphire. The Ne lines acquired before and after the test on the free standing fibre are shown in figure 4.42a) and figure 4.42b) respectively, along with the best

a)

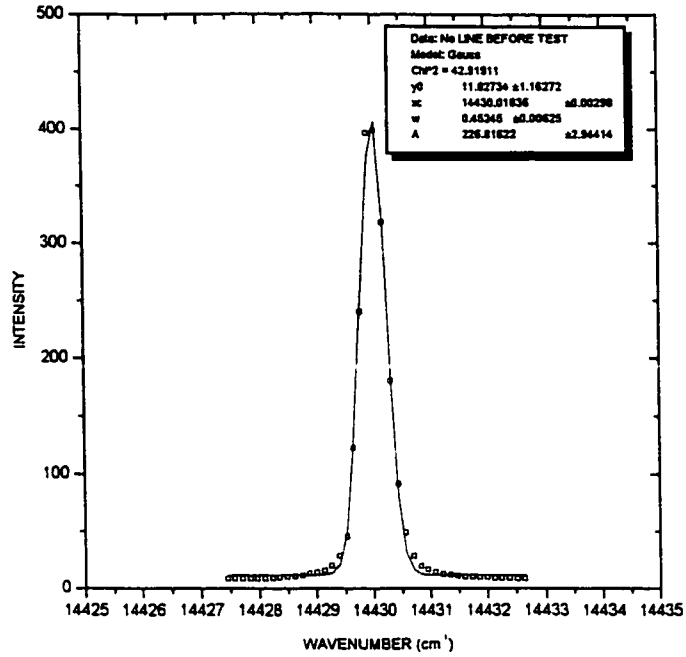

b)

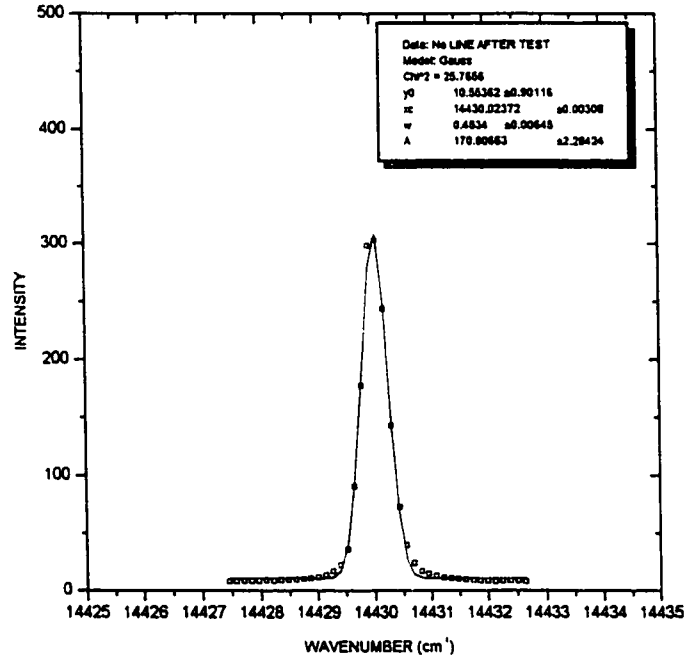

Figure 4.42 Spectrum acquired for a Ne characteristic line, a) before and b) after the piezospectroscopic measurements in a sapphire fiber.

fitting Gaussians to them. From the fitting routines, it was found that figure 4.42a) had a peak center given by 14430.018 ± 0.003 cm^{-1} and that the peak corresponding to figure 4.42b) was 14430.023 ±0.003 cm^{-1}. The difference between the two measurements is 0.005 ± 0.004 cm^{-1}, validating the test. The average position of the Ne peak is 14430.021 ± 0.004 cm^{-1}. This peak should be positioned at 14431.118 cm^{-1} from electron transition tables (Wiese et al., 1966). The difference between the experimental and theoretical values is 1.097 cm^{-1}. In order to compare the sapphire spectral shifts relative to the same baseline, the spectrum acquired for the free standing fibre was thus shifted by 1.097 cm^{-1}. The spectrum for the sapphire is thus plotted in figure 4.43, along with a best fitting double Lorentzian. The center of the peaks corresponding to the R_1 and R_2 transitions for Cr^{3+} in sapphire from the Lorentzian fits are 14402.996 ± 0.007 cm^{-1} and 14432.766 ± 0.010 cm^{-1} respectively. The peaks acquired from the composite were validated and shifted using the procedure detailed above. The spectrum is shown in figure 4.44 and the peak centers are 14402.984 ± 0.007 cm^{-1} and 14432.766 ± 0.009 cm^{-1} for the R_1 and R_2 transitions respectively. The shifts of the R_1 and R_2 transitions due to the thermal residual stress state in the composite is thus given by the difference between the peak centers quoted above and so

$$\Delta\nu_{R_2} = -0.012 \pm 0.014 cm^{-1}$$
$$\Delta\nu_{R_1} = 0.000 \pm 0.014 cm^{-1}$$

The errors in these shifts were calculated by an RMS error analysis using the error in peak center as 0.01 cm^{-1}, the maximum uncertainty for validation of a test.

Using the correlations from He and Clarke given by eq. (2.33), the shifts obtained above are related to the principal stress tensor defined by the crystallographic axes. Knowing that the sapphire fibers are oriented along the c-axis, that the basal plane is isotropic both in terms of elasticity and thermal expansion coefficient and that the Cu matrix surrounding the fibre is completely isotropic in terms of thermal expansion, we can equate the two basal plane stresses σ_{11} and σ_{22}. Solving eq. (2.33), we obtain the following result for the residual thermal stresses

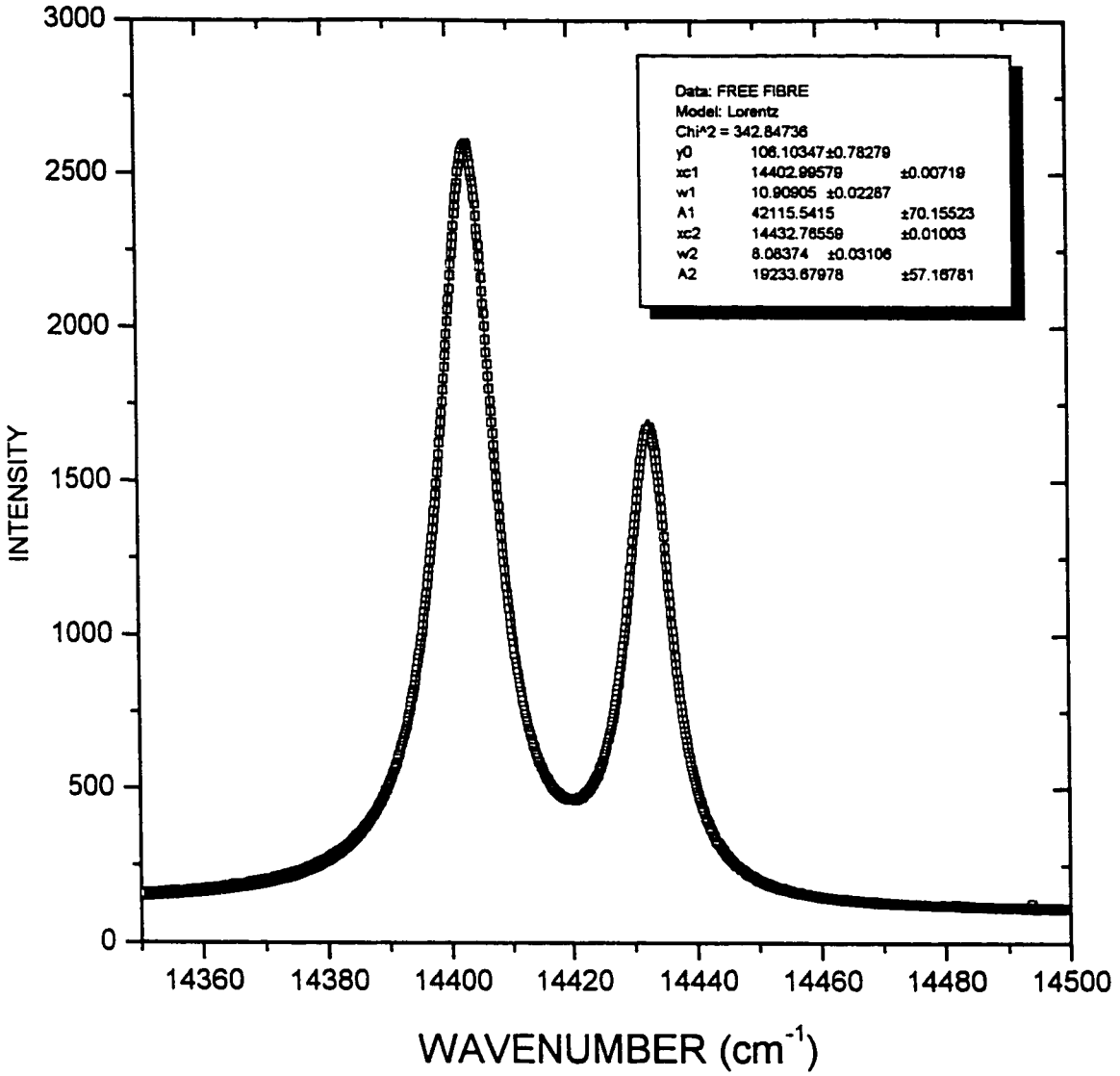

Figure 4.43 Spectrum acquired for the R_1 and R_2 transitions of Cr^{3+} in sapphire.

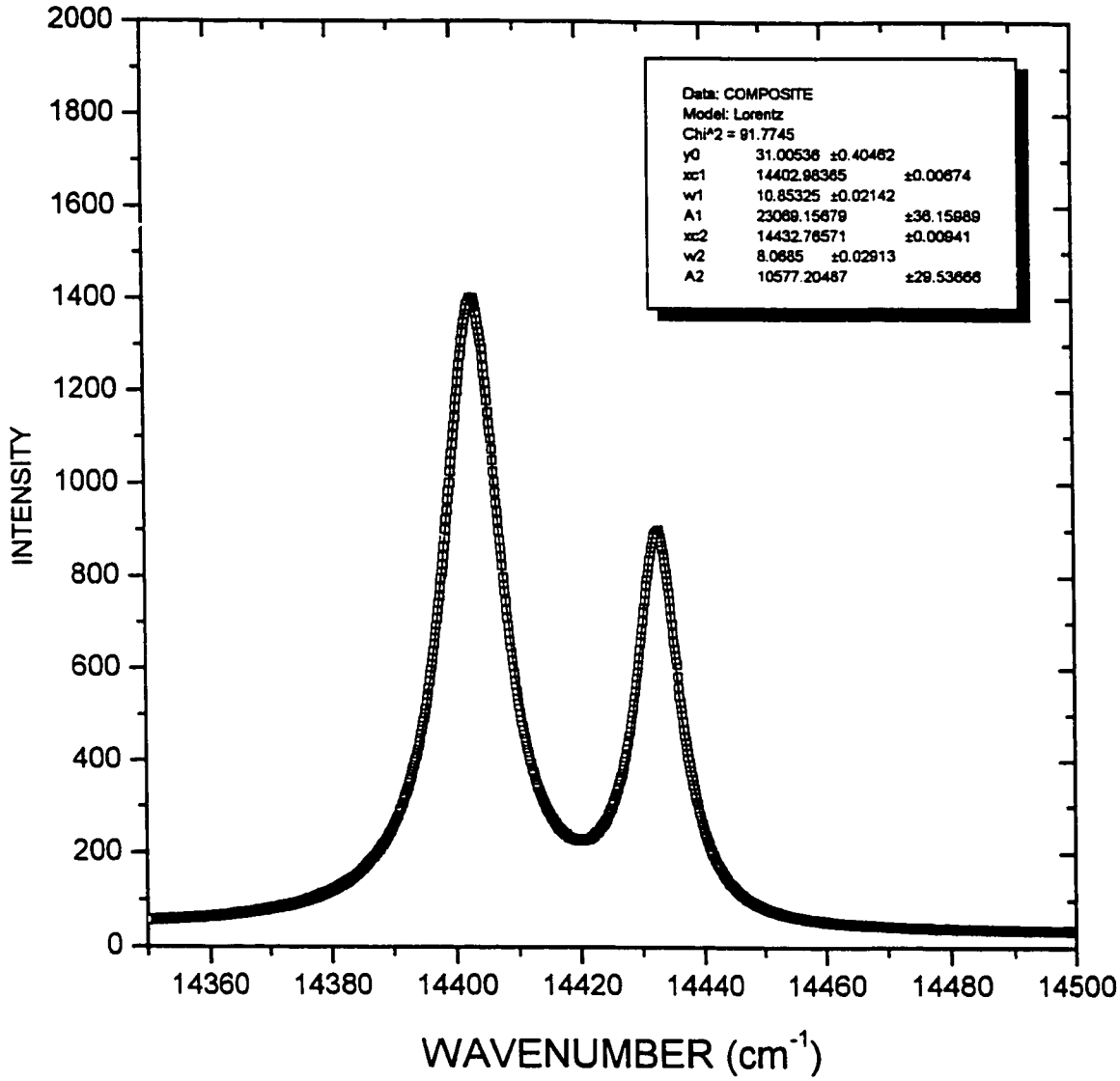

Figure 4.44 Spectrum acquired for the R_1 and R_2 transitions of Cr^{3+} in the sapphire fiber of a Cu-sapphire composite.

$$\sigma_{11} = -5 \pm 6 \text{ MPa}$$

$$\sigma_{22} = -5 \pm 6 \text{ MPa}$$

$$\sigma_{33} = 14 \pm 24 \text{ MPa}$$

The errors were calculated by an RMS method using the errors in peak shift listed above. It is to be noted that, within experimental error, these stresses are close to 0, giving the result that the composite is relatively stress free in the as-fabricated state.

The composite described above was deformed in plane strain in increments of 0.6% and the residual stress state following deformation was monitored using the peak shift of the optical R_1 and R_2 transitions of Cr^{3+} described above. The fibre fractured during the straining to 1.8% and thus, only two measurements could be made of the stress state, at 0.6% and 1.2% total imposed plastic strain.

The spectra acquired following 0.6% and 1.2% strains are presented in figure 4.45 and figure 4.46 respectively. The spectral shift due to 0.6% strain is given by -0.206 ± 0.014 cm^{-1} and -0.202 ± 0.014 cm^{-1} for $\Delta\upsilon_{R_1}$ and $\Delta\upsilon_{R_2}$ respectively. The R_1 and R_2 peak shifts for 1.2% strain are -0.185 ± 0.014 cm^{-1} and -0.198 ± 0.014 cm^{-1} respectively.

Thickness measurements were made after each compression test to verify the plane strain condition. It was found that a thickness change could not be measured within the 0.01mm accuracy of the vernier calipers used. This ensures that the strain in the fibre direction was at most one order of magnitude smaller than the imposed plastic strain of 0.6% and 1.2%. If it is assumed that this thickness strain is zero and that the sapphire deformation is elastic, we can determine the value of the axial fibre stress σ_{33} in terms of the radial stresses σ_{11} and σ_{22}. The full compliance tensor for single crystal sapphire (Simmons and Wang, 1971) is

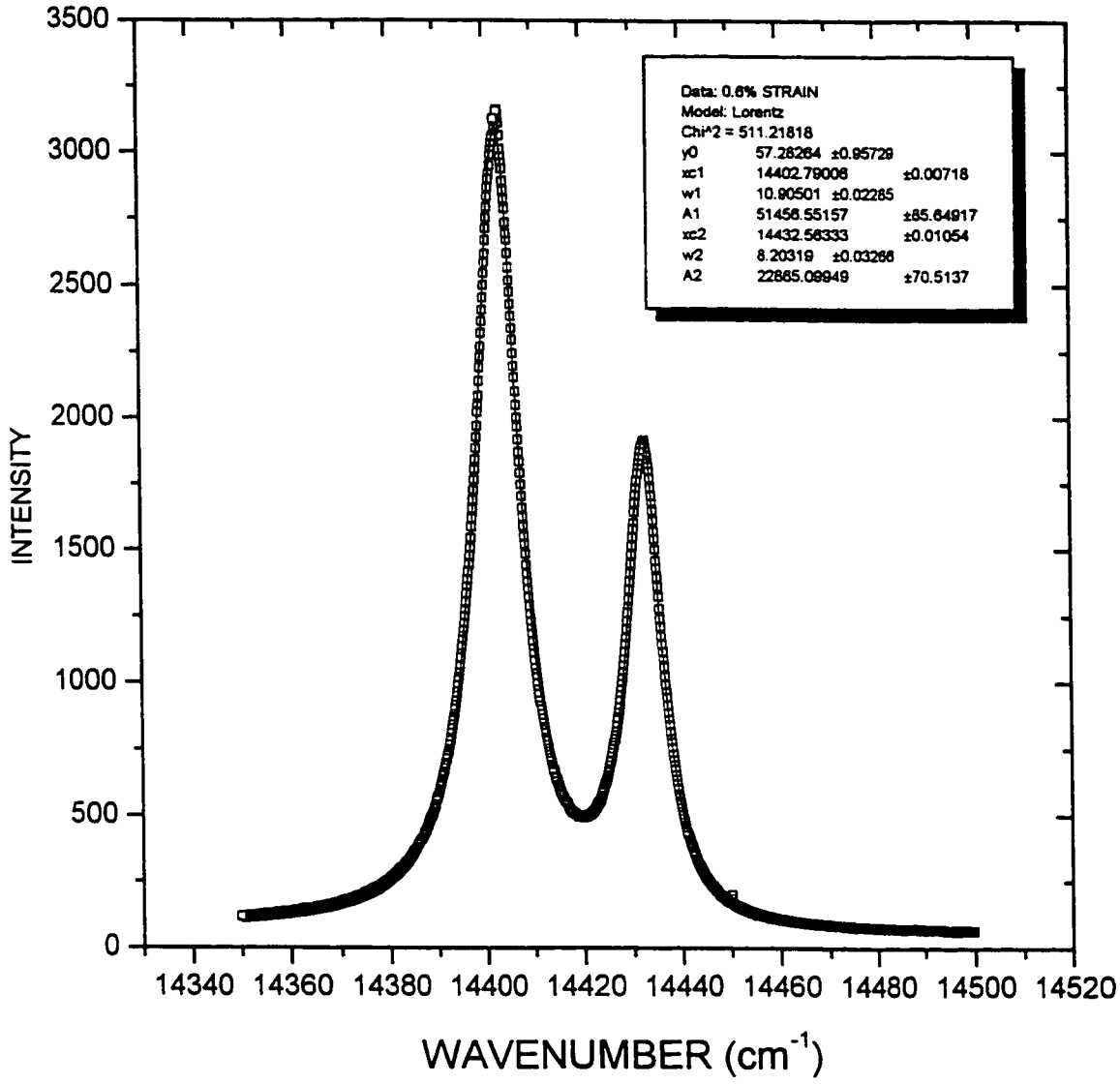

Figure 4.45 Spectrum acquired for the R_1 and R_2 transitions for Cr^{3+} in the sapphire fibre of a Cu-sapphire composite deformed 0.6% in plane strain compression.

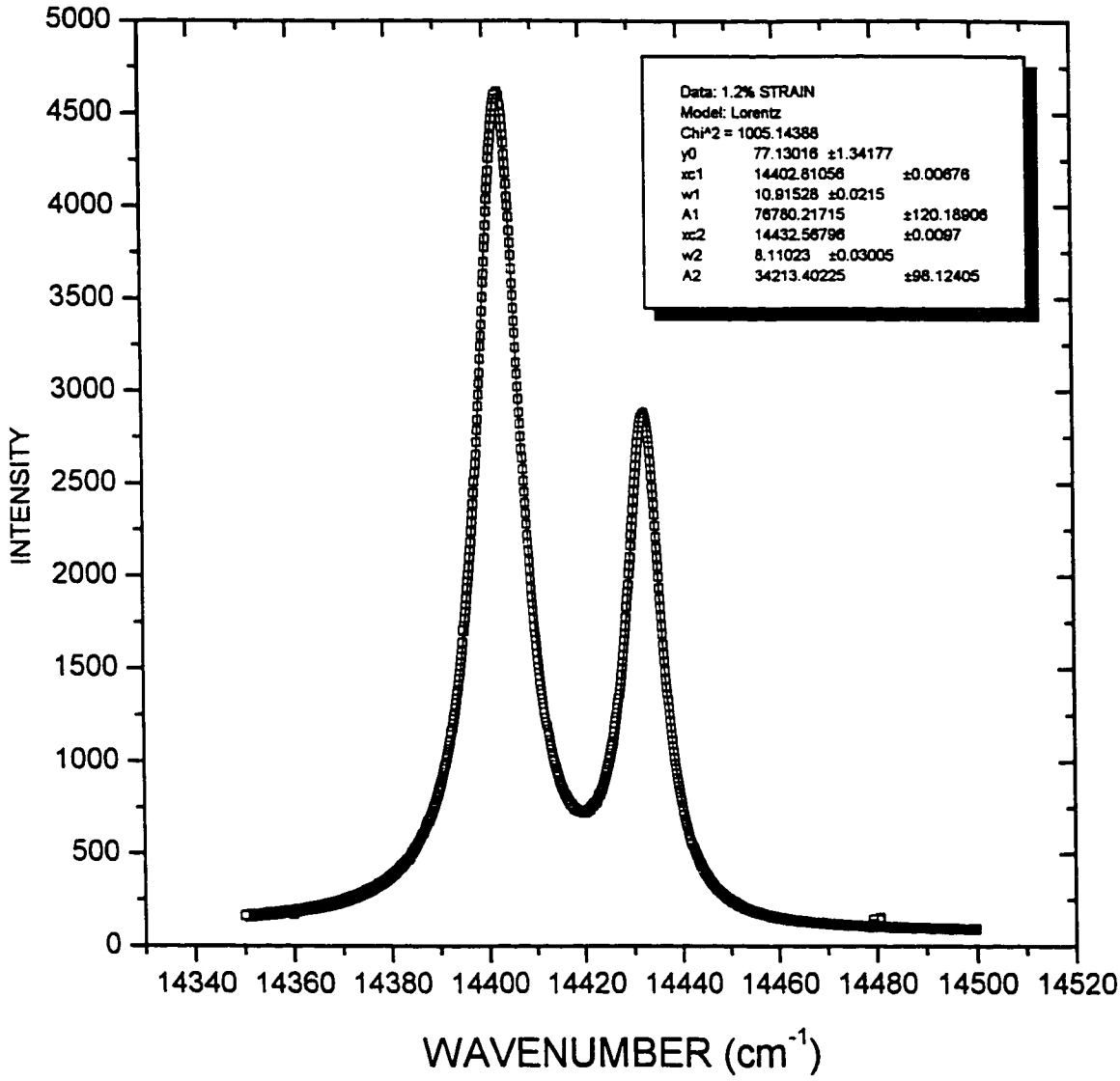

Figure 4.46 Spectrum acquired for the R_1 and R_2 transitions for Cr^{3+} in the sapphire fibre of a Cu-sapphire composite deformed 1.2% in plane strain compression.

$$\begin{bmatrix} 2.353 \times 10^{-3} & -7.16 \times 10^{-4} & -3.68 \times 10^{-4} & 4.91 \times 10^{-4} & 0 & 0 \\ -7.16 \times 10^{-4} & 2.353 \times 10^{-3} & -3.68 \times 10^{-4} & -4.91 \times 10^{-4} & 0 & 0 \\ -3.68 \times 10^{-4} & -3.68 \times 10^{-4} & 2.168 \times 10^{-3} & 0 & 0 & 0 \\ 4.91 \times 10^{-4} & -4.91 \times 10^{-4} & 0 & 6.940 \times 10^{-3} & 0 & 0 \\ 0 & 0 & 0 & 0 & 6.940 \times 10^{-3} & 9.82 \times 10^{-4} \\ 0 & 0 & 0 & 0 & 9.82 \times 10^{-4} & 6.138 \times 10^{-3} \end{bmatrix} \quad \text{eq.(4.6)}$$

The entries in the tensor above are in units of GPa^{-1} . Thus, for zero axial strain along the fibre axis, direction 3,

$$\sigma_{33} = 0.1697(\sigma_{11} + \sigma_{22}) \qquad \text{eq. (4.7)}$$

We can thus use eq. (4.7) to substitute for the axial stress σ_{33} in eq.(2.33) and solve for the stress tensor. Following a strain of 0.6% the stress state is given by

$$\sigma_{11} = -44 \pm 32 \text{ MPa}$$

$$\sigma_{22} = -22 \pm 24 \text{ MPa}$$

$$\sigma_{33} = -11 \pm 7 \text{ MPa}$$

At a plastic strain of 1.2% the residual stress state is

$$\sigma_{11} = -65 \pm 32 \text{ MPa}$$

$$\sigma_{22} = 0 \pm 24 \text{ MPa}$$

$$\sigma_{33} = -11 \pm 7 \text{ MPa}$$

Because of the small magnitude of the residual stresses measured above, it is difficult to clearly establish trends in the fibre loading due to plastic strain. It is clear that σ_{11} becomes more compressive with strain. No real conclusion can be drawn for the variation of the other two principal stresses, σ_{22} and σ_{33}. A clearer picture is obtained by separating the stress tensor into its deviatoric and hydrostatic components. The results are shown in Table 4.8.

Table 4.8 Deviatoric and Hydrostatic Components of the Stress State in Sapphire

	STRESS (MPa)			
CONDITION	σ_H	σ'_{11}	σ'_{22}	σ'_{33}
AS-FABRICATED	1 ± 8	-4 ± 10	-4 ± 10	13 ± 25
0.6% STRAIN	-26 ± 17	-18 ± 36	4 ± 29	15 ± 18
1.2% STRAIN	-25 ± 17	-40 ± 36	25 ± 29	14 ± 18

The hydrostatic pressure σ_H was calculated by $(\sigma_{11} + \sigma_{22} + \sigma_{33})/3$ and the deviatoric stresses, denoted σ'_{ii}, are calculated by subtracting the hydrostatic pressure from the principal axial stresses σ_{ii}. Although the errors are large compared to the measurements, it is seen that σ'_{11} becomes more compressive with increasing applied plastic strain, whereas σ'_{22} becomes more tensile, as compared to the as-fabricated state. The results of Table 4.8 suggest that σ'_{33} does not deviate much from its original value in the as-fabricated state.

CHAPTER 5

SCALE EFFECTS

It is of value to provide diagrams of the form shown in figure 2.4 in order to explore the properties which can result from fabricating composites of given components. However there is much evidence to suggest that the scale of the components in composites exerts a major influence on the properties which can be attained. An interesting example of such scale effects arises in the codeformation of phases such as Cu and Nb by wire drawing. The strength levels attained depends not only on the volume fraction of the BCC Nb phase but on the scale of the structure which is then determined by the imposed strain. Thus, as shown in figure 5.1, the strength levels attained in the drawn product are much higher than those predicted by a simple law of mixtures which assumes parallel fibres of Nb embedded in Cu (Bevk et al., 1978). It is particularly appropriate to consider the influence of scale on the properties of composites because a wide variety of methods are now available for the prodution of ultra fine scale composites. These are summarized in Table 5.1 (Nastasi et. al., 1993).

Table 5.1 - Fabrication methods for fine scale composites

METHOD	DESCRIPTION OF PRODUCT
Chemical Vapour Deposition (CVD)	layered composite
Metal Organic Chemical Vapour Depostion (MOCVD)	layered composite
Electrodepositon	layered composite
Chemical Precipitation	assembly of clusters
Gas Condensation	assembly of clusters
Mechanical Attrition	recrystallized material

In considering the effects of scale, we need to consider how the properties of the composite matrices are themselves influenced by scale and how the scale influences the interaction of the phases by changing the constraints exerted by the matrix on the embedded phase. In developing a view of the

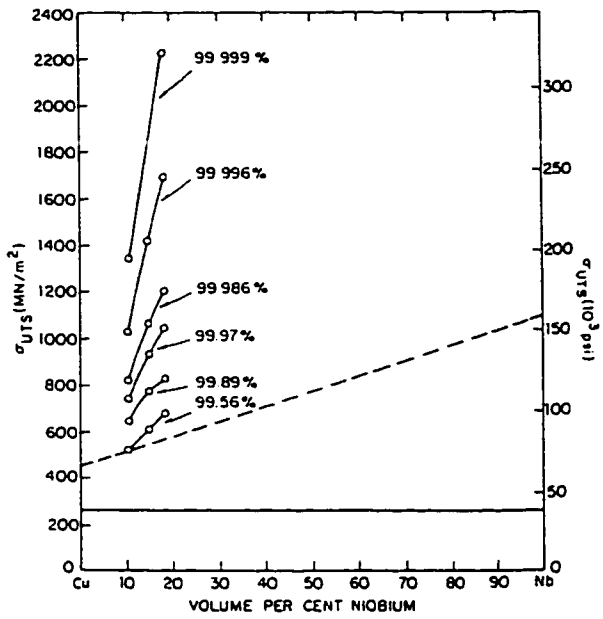

Figure 5.1 Plot of Cu-Nb composite strength as a function of volume percent of Nb for various reductions by wire drawing. (from Bevk, 1978)

influence of scale on composite properties, it is appropriate to consider not the elastic stiffness but the plastic properties in terms of the predicted yield strength.

In Ashby's method (Ashby, 1993), the bounds for strength are slightly more complicated than the ones derived for stiffness. The upper bound is found by loading both phases in the mixture to their respective strengths. This is given by the Rule of Mixtures

$$\sigma_c^u = f\sigma_i^* + (1-f)\sigma_M^* \qquad \text{eq. (5.1)}$$

where σ_c^u is the upper bound for composite strength, σ_M^* and σ_i^* are the matrix and reinforcement strength respectively and f is the volume fraction of reinforcement. A lower bound which is generally applicable is more difficult. Ashby devised a worst case scenario where the strength of the composite is the matrix strength slightly enhanced by the plastic constraint of the reinforcement phase. This plastic constraint was found to be dependent on the ratio of size of the reinforcement h and on the average spacing of the reinforcement t. This ratio h/t and the increase in flow strength can be easily related to volume fraction of reinforcement f by

$$\sigma_c^L = \sigma_M^*\left(1+1/16\left(\frac{f^{1/2}}{1-f^{1/2}}\right)\right) \qquad \text{eq. (5.2)}$$

It has been reported by Drucker (1965) that, for reinforcement sizes ranging from 0.1 to 10 μm with identical h/t ratios, flow strength varied. This means that the constraint itself is scale dependent. Thus, the implicit assumption for the bounds on strength in eq.(5.1) and (5.2) is that the constituent phases can be modelled as continua. In effect, this means that the dominant microstructural feature for strengthening of the phases must be on a scale smaller than the scale of the composite. This means that for the continuum approach to be valid, the main obstacle to dislocation flow cannot be the reinforcement. When this condition breaks down, the constituent phases interact and cannot be treated separately. The following will be concerned with this eventuality. The bounds of eq. (5.1) and eq. (5.2) can be modified by using simple scaling laws to change σ_m and σ_f as the scale of the composite changes.

As outlined in Section 2.2, the strength of materials depends on the microstructural features contained within them. It was shown that the failure strength of brittle materials can be related to the size of flaws in their microstructure and that the yield strength of metals will depend on the spacing of obstacles to dislocation flow. Using this knowledge, scale dependent bounds for strength can be developed for MMCs. The five following systems were chosen to illustrate the method: $Al/Si_{(f)}$, $Al/Be_{(f)}$, $Al/Al_2O_{3(f)}$, $Mg/SiC_{(f)}$ and $Ti/Si_3N_{4(f)}$, where the subscript f denotes the reinforcement phase. Two composite morphologies were considered, a particulate composite with uniformly distributed spherical particles and a lamellar composite with constant layer thicknesses.

Brittle reinforcements such as Si, SiC, Al_2O_3, and Si_3N_4 are limited in strength by the flaws contained within them. Without the presence of such imperfections, one could expect such materials to reach theoretical strengths of approximately E/30, where E is the elastic modulus. In such a material, the largest possible flaw can be considered to be of the order of the lattice parameter b and the theoretical strength can thus be written as

$$\sigma_f^{theo} = \frac{K_{1c}}{\sqrt{\pi b}} \approx \frac{E}{30} \qquad \text{eq. (5.3)}$$

where K_{1C} is the fracture toughness of the reinforcement. In reality, the reinforcements contain flaws such as cracks or grain boundaries which will reduce the strength from E/30. The largest possible flaw size can be taken as the diameter 2r of the particles or of the layer thickness 2r for lamellar structures. There has been evidence for such scaling of strength with size in the literature (Kelly and MacMillan, 1986). Thus, the strength σ_f can be related to fracture toughness

$$\sigma_f = \frac{K_{1c}}{\sqrt{\pi r}} \qquad \text{eq. (5.4)}$$

Substituting for K_{1C} in eq.(5.3), a scale dependent expression for σ_f is obtained

$$\sigma_f = \frac{E}{30}\sqrt{\frac{b}{r}} \qquad \text{eq. (5.5)}$$

The case for metal reinforcements such as Be is different. They may yield before fracture. In this case, the relevant strength is the yield strength. Beryllium has been found to obey the Hall-Petch relation for yield stress σ_y (in MPa) (Webster and London, 1979 and Turner and Lane, 1977)

$$\sigma_y = 114 + \frac{0.37}{d^{1/2}} \qquad \text{eq. (5.6)}$$

where d is the grain size in μm. For the Beryllium particles or layers, a grain size of 10 μm was assumed for r greater than 10 μm resulting in a fracture strength of 230 MPa from eq. (5.6). For $r \leq 10$ μm, it was assumed that a grain size of the order of particle or layer size r so that eq. (5.6) becomes

$$\sigma_f = 114 + \frac{0.37}{r^{1/2}} \qquad \text{eq. (5.7)}$$

In metallic alloys, Hall-Petch behaviour has been verified down to grain sizes on the nanometre scale (Valiev et al., 1993). Reviews by Was and Foecke (1996) and Lesuer et al. (1996) on microlaminated composites have summarized the dominant features for determination of strength. From the literature, it can be concluded that the strength of laminated composites followed a Hall-Petch relationship down to grain sizes of the order of 10 nm. It was also concluded by Was and Foecke that the grain size d controlled the flow stress when $d<5l$, where l is the thickness of the matrix layers. When $d>5l$, the thickness controlled the flow stress. Another finding of the survey was that grain size scales with thickness for microlaminates. Thus, d is usually of the same order as l and the following scaling law can be written

$$\sigma_m = \sigma_{HP} + kl^{-1/2} \qquad \text{eq. (5.8)}$$

where σ_m is the matrix strength, σ_{HP} and k are the Hall-Petch reference stress and locking parameter respectively. For laminates, l is the spacing between consecutive reinforcement layers and from geometry

$$l = \frac{2r(1-f)}{f} \qquad \text{eq. (5.9)}$$

where r and f are the reinforcement size and the volume fraction respectively. By combining equation (5.8) and equation (5.9), we obtain a simple scaling law for σ_m

$$\sigma_m = \sigma_{HP} + k\left(\frac{f}{2r(1-f)}\right)^{1/2} \qquad \text{eq. (5.10)}$$

In particulate composites, the strength of the matrix material will be scale dependent when the spacing between reinforcements is small enough to impede dislocation flow. The strength can be described by the equation for Orowan bowing described in Section 2.2:

$$\sigma_m = \sigma_o + \frac{Eb}{3l} \qquad \text{eq. (5.11)}$$

where b is the Burgers vector of the material, E is the elastic modulus and σ_o is a reference strength and l is the spacing between the particles. For a totally flexible dislocation line (Gerold and Haberkon, 1966), the spacing is given as a function of volume fraction f and size r of the particles

$$l = \frac{(2\pi)^{1/2} r}{(3f)^{1/2}} \qquad \text{eq. (5.12)}$$

The scale dependent matrix strength is thus

$$\sigma_m = \sigma_o + \frac{Eb(3f)^{1/2}}{3(2\pi)^{1/2} r} \qquad \text{eq. (5.13)}$$

The strength of both the lamellar and particulate composites will also depend on their processing history. If the matrix has been work hardened to a strain ε, the increase in strength could be approximated as

$$\Delta\sigma_m = \alpha\mu\sqrt{\frac{bf\varepsilon}{r}} \qquad \text{eq. (5.14)}$$

where α is a constant and μ is the shear modulus.

By substituting the scale dependent expressions developed above for σ_f and σ_m into eq. (5.1) and eq. (5.2), composite design charts similar to the ones reported by Ashby (1993) were constructed for sizes ranging from 100 to 0.001 μm. Care was taken such that the constituents did not exceed their theoretical strength. The lower limit given by eq. (5.2) is only valid for constituents on a macroscopic scale. A reasonable lower limit for submicron reinforcements was taken to be given by the matrix strength only. Figure 5.2 shows examples of the composite design charts for Al reinforced with 1 μm and 0.01 μm Al_2O_3 particles respectively. Figure 5.3 to figure 5.7 illustrate the results for the five composite systems of interest on three dimensional plots with size as the third axis. For clarity, note that the reciprocal of density was plotted for systems where the reinforcement is lighter than the matrix.

The scale dependent design charts of figure 5.3 to figure 5.7 clearly show the effect of size on the bounds for strength of a composite. The upper and lower limits for strength can be increased by orders of magnitude by microstructural refinement. To verify the applicability of these bounds, a 2 dimensional cut on the scale axis of the lamellar $Al/Al_2O_{3(f)}$ design chart was made for comparison with experimental data (Alpas et al., 1990). The 2 dimensional section is shown in figure 5.8. It is clear that the data is contained within the bounds. This is an indication that the scaling laws used and the bounds developed with them were adequate to model real scale effects.

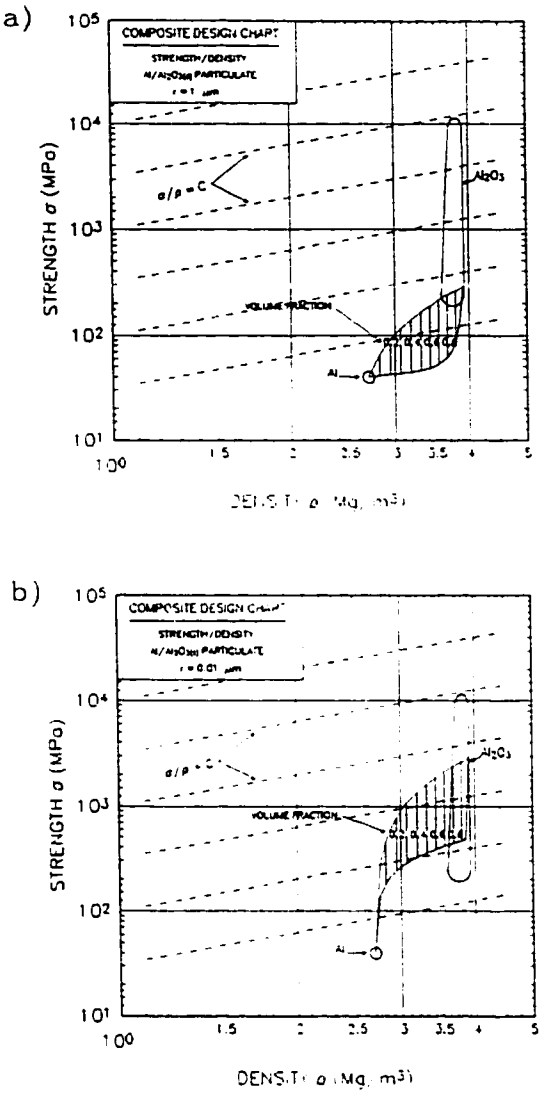

Figure 5.2 Composite Design charts for $Al/Al_2O_{3(0)}$: a) r=1 μm, b) r=0.01 μm.

a)

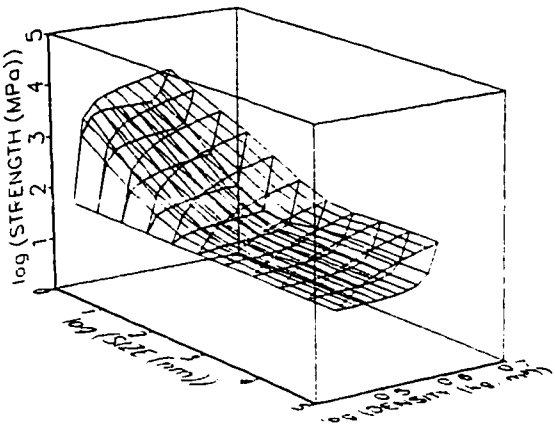

b)

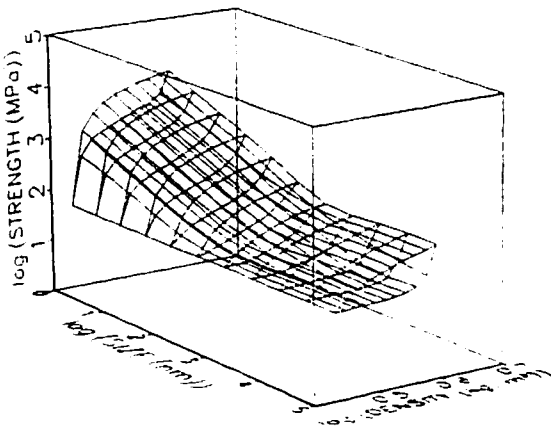

Figure 5.3 Scale Dependent Composite Design Charts for $Al/Al_2O_{3(f)}$: a) particulate reinforcement, b) lamellar reinforcement.

a)

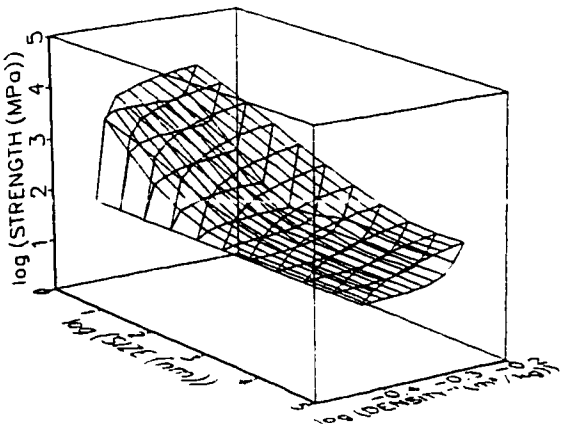

b)

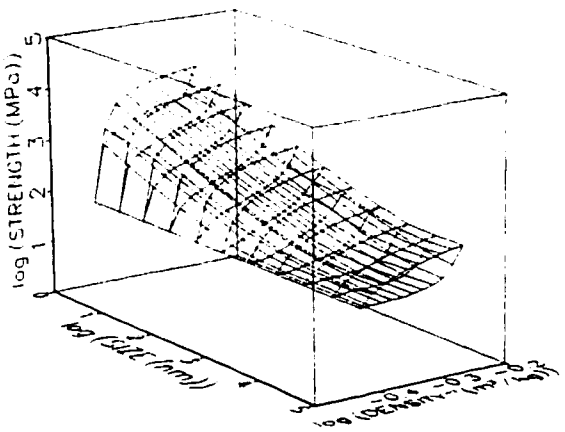

Figure 5.4 Scale Dependent Composite Design Charts for Al/$Be_{(f)}$: a) particulate reinforcement, b) lamellar reinforcement.

a)

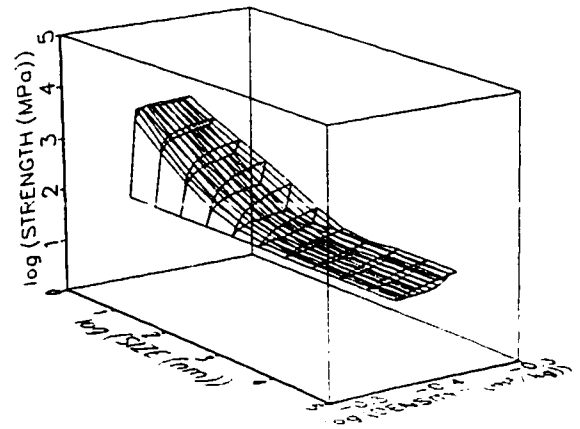

b)

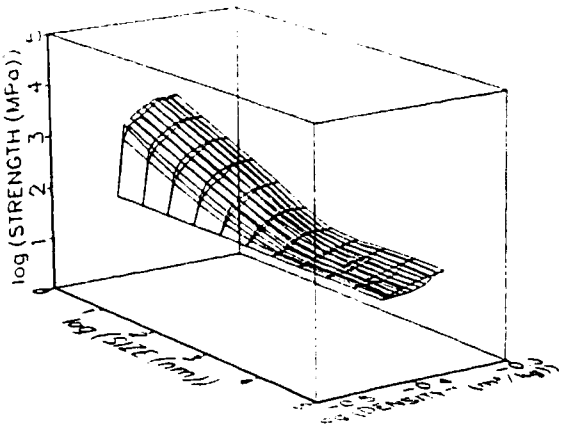

Figure 5.5 Scale Dependent Composite Design Charts for Al/$Si_{(f)}$: a) particulate reinforcement, b) lamellar reinforcement.

a)

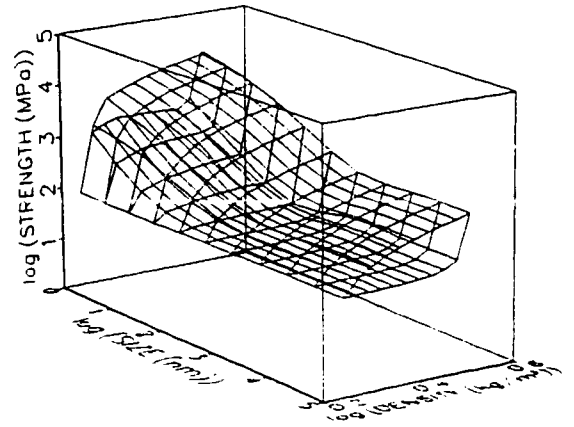

b)

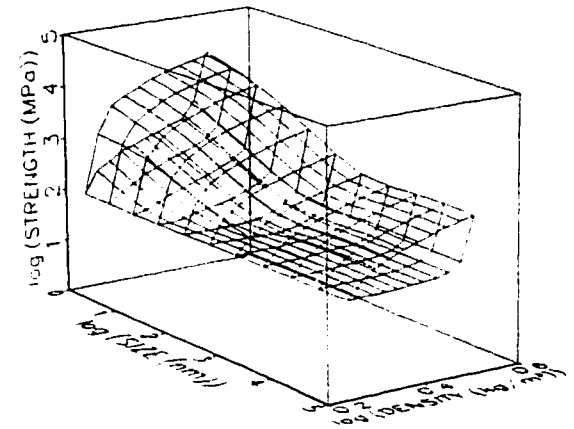

Figure 5.6 Scale Dependent Composite Design Charts for Mg/$SiC_{(f)}$: a) particulate reinforcement, b) lamellar reinforcement.

a)

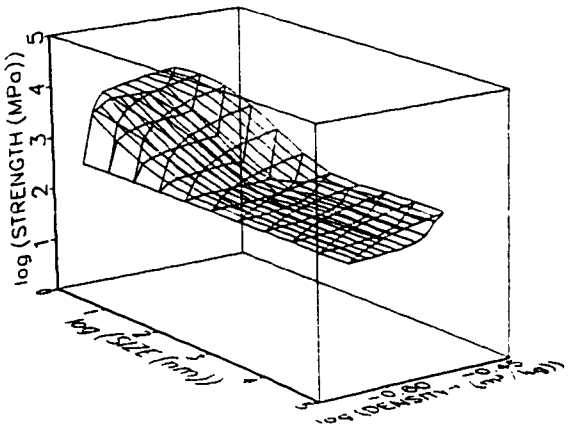

b)

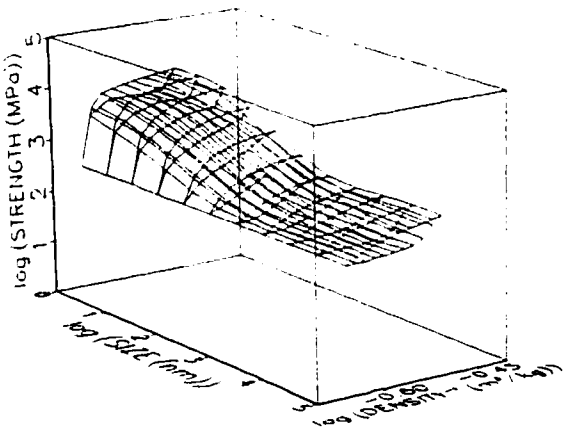

Figure 5.7 Scale Dependent Composite Design Charts for $Ti/Si_3N_{4(f)}$: a) particulate reinforcement, b) lamellar reinforcement.

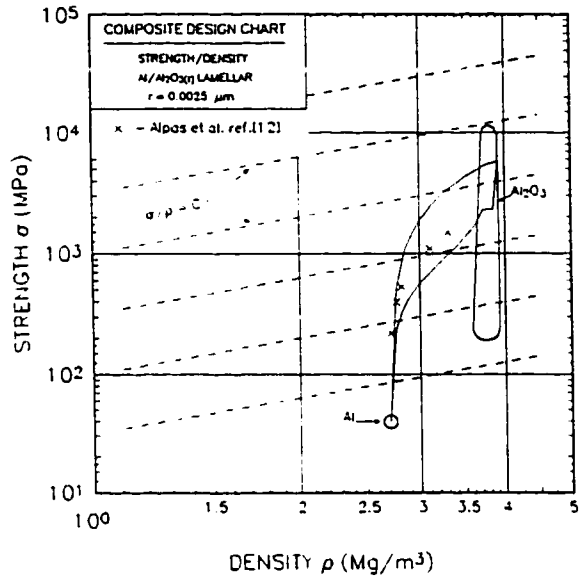

Figure 5.8 Comparison between prediction and experimental data for a lamellar $Al/Al_2O_{3(f)}$ composite.

Despite the good agreement with experimental data, it is important to understand the limitations of the formalism developed here. This method assumes that the constituent phases are manufactured to be in intimate contact but that this step does not result in chemical reaction between the phases. It is also assumed that the reduction of scale by large strain deformation of the constituents does not affect their stability. In the literature, there has been evidence of dissolution of pearlite in heavily cold drawn steel wires (Languillaume et al., 1997). This has been attributed to increases in free energy due to the increase in interfacial area. Spheroidization or cylinderization in Cu-Fe or Ni-W alloys has been observed following large strain deformations and annealing (Malzahn Kampe et al., 1989). These instabilities have also been linked to increases in interfacial area. Although such stability effects are expected to gain importance as the scale of a composite is reduced, this work assumed that the components remain in a state of thermodynamic equilibrium over the range of scale considered in this work. It must also be emphasized that this treatment is intrinsically a low temperature limit. As the scale of composite structures is reduced, alternate thermally activated flow processes may occur even at temperatures as low as 0.2 T_m , where T_m is the melting point (Embury and Lahaie, 1993). These effects are not considered here.

The effect of morphology of the reinforcement is also important in delineating the bounds for composite strengths. The two morphologies examined in this work represent extremes in dimensional constraint. Lamellar reinforcements exert a 2 dimensional constraint and the particulate reinforcements are essentially 1 dimensional obstacles. From the results, it can be seen that neither morphology consistently imparts the most strength to the matrix. The most efficient morphology depends on volume fraction and size, as well as where within the bounds the experimental data will fall.

The inclusion of size as a variable is useful for the optimization process of materials selection involving strength as a parameter. Performance indices (Ashby, 1992) which include strength can now

be examined as a function of volume fraction, scale and morphology. Systems which may not have had good performance indices at macroscopic sizes may become suitable or even the best choice if they can be produced on a finer scale. To illustrate the potential of fine scale, we will consider the five composite systems investigated here for use as spring materials. A spring has the ability to do work by releasing stored elastic strain energy. For uniaxial tension in the elastic range, this energy U is given simply by

$$U = \frac{0.5\,\sigma^2}{E} \qquad \text{eq. (5.15)}$$

where σ is the stress imposed and E is the elastic modulus. From eq.(5.15), it is thus clear that the ability of a material to store energy depends on the strength and elastic modulus. We will assume for simplicity that the elastic moduli of the composites are given by the upper bound law of mixtures of eq. (2.1), that the components of the composite reach their ultimate strength simultaneously and that the composite strength is given by the upper bound of eq. (5.1). The ultimate strength of the components will be at best the theoretical strength, given approximately by E/50. This is the strength level that may be approached in very fine scale composites, as discussed previously. Table 5.2 shows the maximum potential for energy storage of fine scale composites with a reinforcement volume fraction of 0.3. For comparison, the corresponding values of U for low alloy steel and diamond are shown. From these results, the

Table 5.2 - Potential of fine scale composites for spring materials

MATERIAL	σ (GPa)	E(GPa)	U(MJ/m^3)
$Al/Si_{(f)}$	1.6	85	15
$Al/Be_{(f)}$	2.8	140	28
$Al/Al_2O_{3(f)}$	3.2	160	32
$Mg/SiC_{(f)}$	3.1	155	31
$Ti/Si_3N_{4(f)}$	3.3	165	33
low alloy steel	1.6	200	6
diamond	5.0	1000	13

possible efficiency of composite springs can exceed the capacity of materials such as steel or diamond by a significant margin in some cases. Some of the composites have the potential to store elastic energy up to about 30 MJ/m^3, which exceeds by a factor of 5 the potential storage capacity of a very strong steel. In light of the previous example, it is expected that many materials selection criteria which depend on one or several scale dependent properties could demonstrate the potential for improvement in performance of composites produced on a fine scale.

CHAPTER 6

DISCUSSION

In the present chapter, the main results of the experimental work will be discussed. The aims of the discussion are to deal with the central issue of damage accumulation in MMCs. This will be done in various ways. As was outlined in Chapter 1, the issue of forming MMCs is an essential one for their possible application and widespread use. Thus, the first goal of this chapter will be to clarify the relationship of plastic flow during hydrostatic extrusion to the appearance of damage in MMCs. This topic will be dealt with in the first two of the five main sections in this chapter. The first section will present a theoretical basis for the extrusion process in order to gain some understanding of damage accumulation and nucleation in relation to the operative state of stress. The second section will discuss the relationship between the microstructure of the MMCs and the amount of damage created during hydrostatic extrusion. The damage introduced into the MMC microstructure by extrusion has repercussions on their subsequent load bearing capacity and ductility. Thus, the third section of the discussion will consider the tensile response of MMCs subsequent to hydrostatic extrusion and will relate the results to the description of the microstructure, both in terms of the level of damage and its thermo-mechanical history. Due to the extrusion process, changes in both the reinforcement and matrix were observed. In order to understand the composite behavior as a whole, the changes in its components effected by the extrusion process must also be understood. Hence, this section will be divided further into three subsections, the first two which will discuss the effect of hydrostatic extrusion on the matrix materials and reinforcement materials respectively. The third subsection will then deal with the observed mechanical properties of the extruded MMCs in terms of the previously examined properties of the components. In the last two sections of this chapter, the work on model composite systems will be discussed and their importance in understanding the conditions leading up to damage events will be emphasized. The fourth section of this chapter will deal with the results of the plane strain compression

experiments and the insights that they yield into the pattern of flow around various distributions of fibers. The fifth and last section will discuss the piezospectroscopic method for finding internal stresses in sapphire fibers and its potential for an in-depth understanding of the load transfer process in MMCs.

Thus, this chapter will be divided into five main sections which will deal with: the hydrostatic extrusion process, the microstructural aspects of damage accumulation during extrusion, the effects of extrusion on the mechanical properties of MMCs, fibre distribution effects in model MMCs and load transfer in Cu-sapphire. The third section, which will discuss the effects of hydrostatic extrusion on the mechanical properties of MMCs will be divided into three subsections dealing separately with the effect of hydrostatic extrusion on the matrix materials, the reinforcement materials and the composites respectively.

6.1 THE HYDROSTATIC EXTRUSION PROCESS

It is clear from Section 4.1 and Section 4.5 that the stress state created in the die during the hydrostatic extrusion of the particulate MMCs and the model Cu-W composite leads to microstructural damage in the form of particle or fibre cracking. At some point during the extrusion process, the loads transferred to the reinforcement build up until the fracture limit of the reinforcement is reached.

From the literature, it has been shown that hydrostatic pressure is a parameter which has great influence on the initiation and accumulation of damage in materials (Zok, 1988). This has been documented for metal forming processes (Coffin and Rogers, 1967) and for MMCs tested in tension with superimposed hydrostatic pressures (Newell, 1990). The basic conclusions from these studies is that compressive hydrostatic pressures hinder the nucleation of damage in the form of voids and that tensile hydrostatic pressures aid this process. The success of metal forming operations to large plastic strains

relies on the application of large compressive stresses for this reason. Considering the high pressures generated during hydrostatic extrusion, it is of interest to examine the variation of the hydrostatic pressure throughout the deforming MMC during the process. A method which enables this type of information to be gathered is the slip line field method (Hill, 1967 and Johnson and Sowerby, 1970). This method was developed for deformation problems in plane strain. Plane strain sheet extrusion slip line fields have been reported in the literature (Coffin and Rogers, 1967) as well as a modification to this solution for axisymmetric extrusion (Thomason, 1969/70). The details of the method and the literature dealing with extrusion are outlined in Section 2.3.

In short, the slip line field method involves finding the characteristics of the plane strain equilibrium equations (Johnson and Sowerby, 1970), defined in terms of the plane pressure p and k, the shear yield stress. The characteristics form two families of curves, called α and β lines. The α and β lines are orthogonal and form a network called the slip line field. Further, the α and β lines represent the trajectories of the maximum shear stress in the deforming solid.

In view of the information which slip line fields yield on pressure distributions in a deforming solid, it was decided to use this method to obtain an estimate of the hydrostatic stresses in the die during hydrostatic extrusion of the MMCs in the present work. From the literature review in Section 2.3, it was thought that the model by Thomason (1969/70) was most suitable because of its ability to predict some experimentally observed damage modes in extruded metals and alloys (Avitzur, 1967), namely arrowhead cracking and fir-tree cracking. It was also chosen for its ability to model axisymmetric extrusion by modifying the slip line field solution developed for plane strain sheet extrusion. As outlined in Section 2.3, the method applies to a rigid-plastic material. If it is assumed that the Tresca criterion for yielding applies to this material, the equations of equilibrium along the α and β slip lines are given by Hill (Hill, 1967) and are

$$dp + 2kd\phi + (\sigma_\theta + p - k\cot\phi)\frac{dr}{r} = 0 \qquad \text{on } \alpha - \text{line} \qquad \text{eq. (6.1a))}$$

$$dp - 2kd\phi + (\sigma_\theta + p - k\tan\phi)\frac{dr}{r} = 0 \qquad \text{on } \beta - \text{line} \qquad \text{eq. (6.1b))}$$

where p and k are the pressure and shear yield stress on the meridian plane and σ_θ is the out of plane principal stress. The coordinate system and the definition of the angular coordinate ϕ of the slip line are defined in Section 2.3. The equations 6.1a) and 6.1b) are reduced to hyperbolic form for conditions of plane strain on the meridian plane and the solution reduces to the one for plane strain sheet extrusion (Hill, 1967). Thomason's assumption for the axisymmetric problem of extrusion through converging conical dies is that σ_θ varies linearly from the center line of the billet to the die wall in the following fashion

$$\sigma_\theta = -p - k\left(1 - r/R_D\right) \qquad \text{eq. (6.2)}$$

where R_D is the radius of the die at a distance z into it, from figure 2.6. If equation 6.2 is substituted into equation 6.1a) and equation 6.1b), the equilibrium equations become

$$dp + 2kd\phi - k\left(1 - r/R_D + \cot\phi\right)\frac{dr}{r} = 0 \qquad \text{on an } \alpha - \text{line} \qquad \text{eq. (6.3a))}$$

$$dp - 2kd\phi - k\left(1 - r/R_D + \tan\phi\right)\frac{dr}{r} = 0 \qquad \text{on a } \beta - \text{line} \qquad \text{eq. (6.3b))}$$

It was then assumed that the slip line field on the meridian plane for the solution of equations 6.3a) and 6.3b) are the same as for the plane strain sheet extrusion problem. The mean meridian plane stress at the center line of the die p_o is obtained by numerically integrating equation 6.3b) for the β line at the die exit, knowing that the resolved axial force F_z integrated over the cross-section must be zero for extrusion without applied back pressure. The numerical integration was performed using the finite difference form of equation 6.3a) and 6.3b)

$$\Delta p = -k\left(2\Delta\phi - \left(1 - \bar{r}/\bar{R}_D + \cot\bar{\phi}\right)\Delta r/\bar{r}\right) \qquad \text{on an } \alpha - \text{line} \qquad \text{eq. (6.4a))}$$

$$\Delta p = k\left(2\Delta\phi + \left(1 - \bar{r}/\bar{R}_D + \tan\bar{\phi}\right)\Delta r/\bar{r}\right) \qquad \text{on a } \beta - \text{line} \qquad \text{eq. (6.4b))}$$

where the average quantities denoted with a bar are defined by

$$\bar{r} = 1/2\left(r_{n+1} + r_n\right) \qquad \text{eq. (6.4c))}$$

$$\bar{R}_D = 1/2\left(R_{D,n+1} + R_{D,n}\right) \qquad \text{eq. (6.4d))}$$

$$\cot\bar{\phi} = 1/2\left(\cot\phi_{n+1} + \cot\phi_n\right) \qquad \text{eq. (6.4e))}$$

$$\tan\bar{\phi} = 1/2\left(\tan\phi_{n+1} + \tan\phi_n\right) \qquad \text{eq. (6.4f))}$$

and the differences denoted by a preceding Δ and are defined by

$$\Delta\phi = \left(\phi_{n+1} - \phi_n\right) \qquad \text{eq. (6.4g))}$$

$$\Delta r = \left(r_{n+1} - r_n\right) \qquad \text{eq. (6.4h))}$$

for the integration between point n and n+1 on the chosen line. From the calculated p_o, Thomason obtained the hydrostatic pressure σ_{HO} at the die center line using equation 6.2 and this is defined by

$$\sigma_{HO} = -\left(p_o + k/3\right) \qquad \text{eq. (6.5)}$$

Thomason thus reported the hydrostatic pressure at the die center line for various reductions and die-angles, but at no other location.

In view of the importance of the hydrostatic pressure on damage nucleation, it was decided to use Thomason's model to produce a map of hydrostatic pressure in the die during extrusion. As in Thomason's analysis, the die walls were assumed to be frictionless, so that the slip lines meet the walls at 45°. The reductions were chosen to reproduce the experimental reductions of 39.3% (equivalent to a strain of 0.5) and 63.2% (equivalent to a strain of 1.0). Two angles for the conical dies were chosen for each reduction, at 5° intervals. The lowest die angle chosen was the lowest multiple of 5° for which the slip line field could be constructed, from geometrical considerations. Thus, for the reduction of 39.3%,

die angles of 10° and 15° were chosen and the die angles chosen for a reduction of 63.2% were 20° and 25°. The slip line field used in Thomason's model is the centered fan field defined by Hill (1967) for plane strain sheet extrusion and shown in figure 6.1. For this analysis, in order to get good spatial accuracy, equiangular nets of 1° interval defined by circular arcs of equal radii were chosen. The coordinates of the slip lines were calculated using Hill's exact solution for the radius of curvature R of the α lines shown in figure 6.1. This solution is

$$|R| = |r|\left[I_0\left\{2\sqrt{|ab|}\right\} + \sqrt{\left|\frac{b}{a}\right|}\, I_1\left\{2\sqrt{|ab|}\right\}\right] \qquad \text{eq. (6.6)}$$

where I_0 and I_1 are the modified Bessel functions of the first kind, r is the radius of the circular fan and where a and b are the coordinates of the α and β lines respectively, as referred to a curvilinear basis. The coordinate b is constant on an α line and the coordinate a is constant over a β line. If ϕ, the angular coordinate of the slip line, is defined as the counter-clockwise angle to the axis Ox on figure 6.1, then b=0 on the α line through O and a is related to b from

$$\phi = a + b \qquad \text{eq. (6.7)}$$

Using the known coordinates of the β line through O, the entire net can be constructed from α lines and their Cartesian coordinates are

$$X_{m,n} = X_{m-1,n} + \int_{\phi_{m-1,n}}^{\phi_{m,n}} R\cos\phi d\phi \qquad \text{eq. (6.7a))}$$

$$Y_{m,n} = Y_{m-1,n} + \int_{\phi_{m-1,n}}^{\phi_{m,n}} R\sin\phi d\phi \qquad \text{eq. (6.7b))}$$

where m and n refer to the values of a and b on the 1° equiangular grid.

The coordinates of the slip line field were calculated using the mathematical software package MAPLE ™. The program listing written for this purpose is presented in Appendix B. The program shown in Appendix B corresponds to a 1° equiangular net of 90° circular arcs of radius 1. This radius

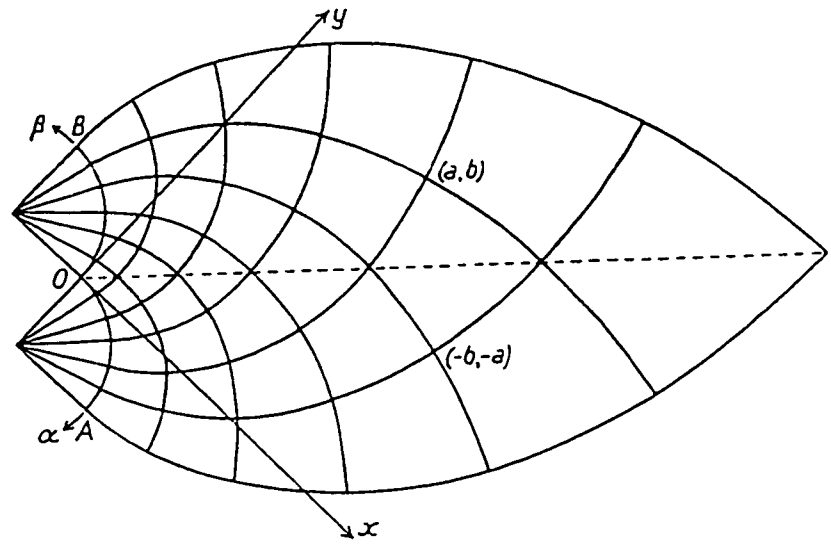

Figure 6.1 Diagram of a centered fan slip line field. (from Hill, 1967)

was chosen as a trial for comparison with published results for 15° equiangular nets of 90° circular arcs of radius 1 (Johnson and Sowerby, 1970). A comparison of the coordinates computed with the published results showed that there was agreement between the two fields to at least 3 decimal places. The results in this method are considered more accurate because of the use of the exact solution for R compared to the published data generated by an approximate method which may be in error by up to 0.1%, according to Hill (1967).

Thus, the slip line fields were constructed for the reductions and die angles discussed previously. In this analysis, the bounding slip line at the die exit was an α line. Thus, the numerical integration was carried out according to equation 6.4a) to obtain p_o, the pressure on the meridian plane at the axis of symmetry. Using this value of p_o, the meridian pressure p was calculated at every point in the net using equation 6.4a) or equation 6.4b) for α and β lines respectively. The hydrostatic pressure σ_H was calculated at every point using

$$\sigma_H = \frac{\sigma_{ii}}{3} = \frac{-2p + \sigma_\theta}{3} \qquad \text{eq. (6.8)}$$

and from the definition of σ_θ in equation 6.2

$$\sigma_H = -p - k/3\left(1 - r/R_D\right) \qquad \text{eq. (6.9)}$$

It is important to note here that a negative value of σ_H represents a tensile hydrostatic stress.

The results of this analysis can be compared to Thomason's results by looking at the center line hydrostatic pressure p_o. The value of p_o for extrusion to a strain of 0.5 (39.3% reduction in area) is 0.435 and 0.007 for the 10° and 15° dies respectively. The value of p_o for extrusion to a strain of 1.0 (62.3% reduction in area) is 0.691 and 0.375 for the 20° and 25° dies respectively. Figure 6.2 is a reproduction of Thomason's results, along with plotted points from the present analysis. For extrusion to a strain of 0.5, it is clear that the present results are consistent with the trends shown, although the

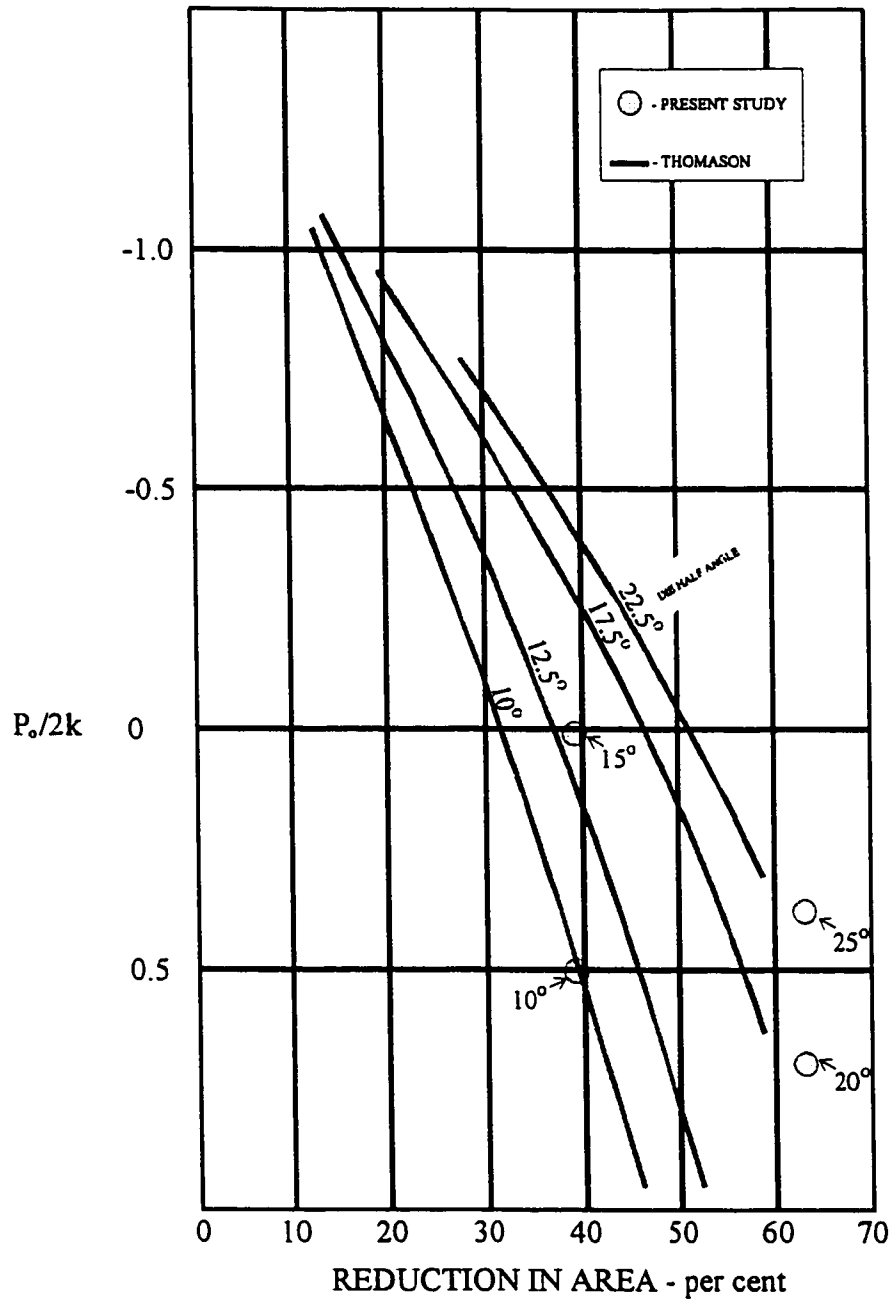

Figure 6.2 Comparison of the present results with the literature (Thomason, 1969/70) for the centre-line plane pressure p_o for various combinations of die angle and reductions.

published analyses were made for differing die angles. It is more difficult to compare the results for extrusion to a strain of 1.0 in view of the fact that the literature results are only plotted for extrusion up to strains of about 0.7. However, it can be said that the data for extrusion to a strain of 1.0 from the present analysis seem to follow the trend expected by extrapolation. Thus, it seems from figure 6.2 that there is good agreement between Thomason's results and the results of the present work.

Thus, with some confidence on the hydrostatic pressure data, the pressure maps were constructed and are shown in figure 6.3 to figure 6.6 for the 4 combinations of reduction and die angle chosen. The pressure on the aforementioned figures was plotted as the dimensionless quantity $\sigma_H/2k$. The points corresponding to the equiangular nets were also plotted with the pressure maps.

Some common trends can be observed from the results in figure 6.3 to figure 6.6. The locations of high pressure and low (or even negative) pressure coincide for all combinations of die angle and reduction. The high pressure region is located near the die entrance and near the die wall, whereas the low pressure regions were situated near the die center line and towards the die exit.

In view of the importance of the sign and magnitude of the hydrostatic pressures for the processes of damage in materials, the effect of reduction and die angle on the hydrostatic pressure distributions in the dies will be examined in terms of the hydrostatic pressure extremum values and the relative volume occupied by tensile and compressive hydrostatic pressures in the dies. For constant reductions, the effect of increasing the die angle was to create hydrostatic pressures of a more tensile nature near the center line of the die. Increasing die angles do not seem from the present results to decrease the magnitude of the highest compressive hydrostatic pressure. It does, however, have the effect of reducing the volume fraction of the die where there are compressive hydrostatic pressures. From the present results, it is not possible to compare the effect of the reduction for constant die angles. However,

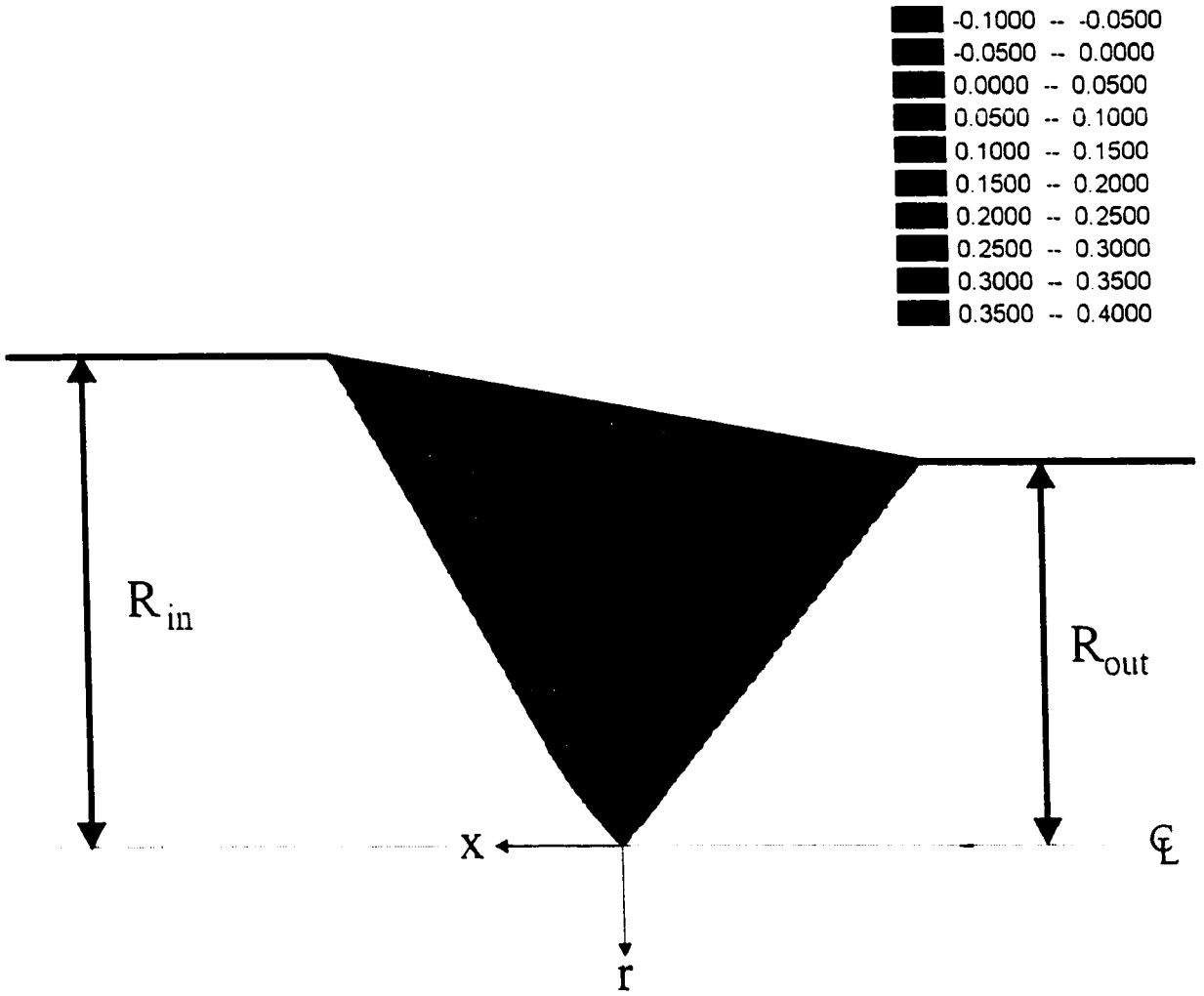

Figure 6.3 Map of the hydrostatic pressure ($\sigma_H/2k$) during extrusion in a 10° die for a reduction of 39.3%.

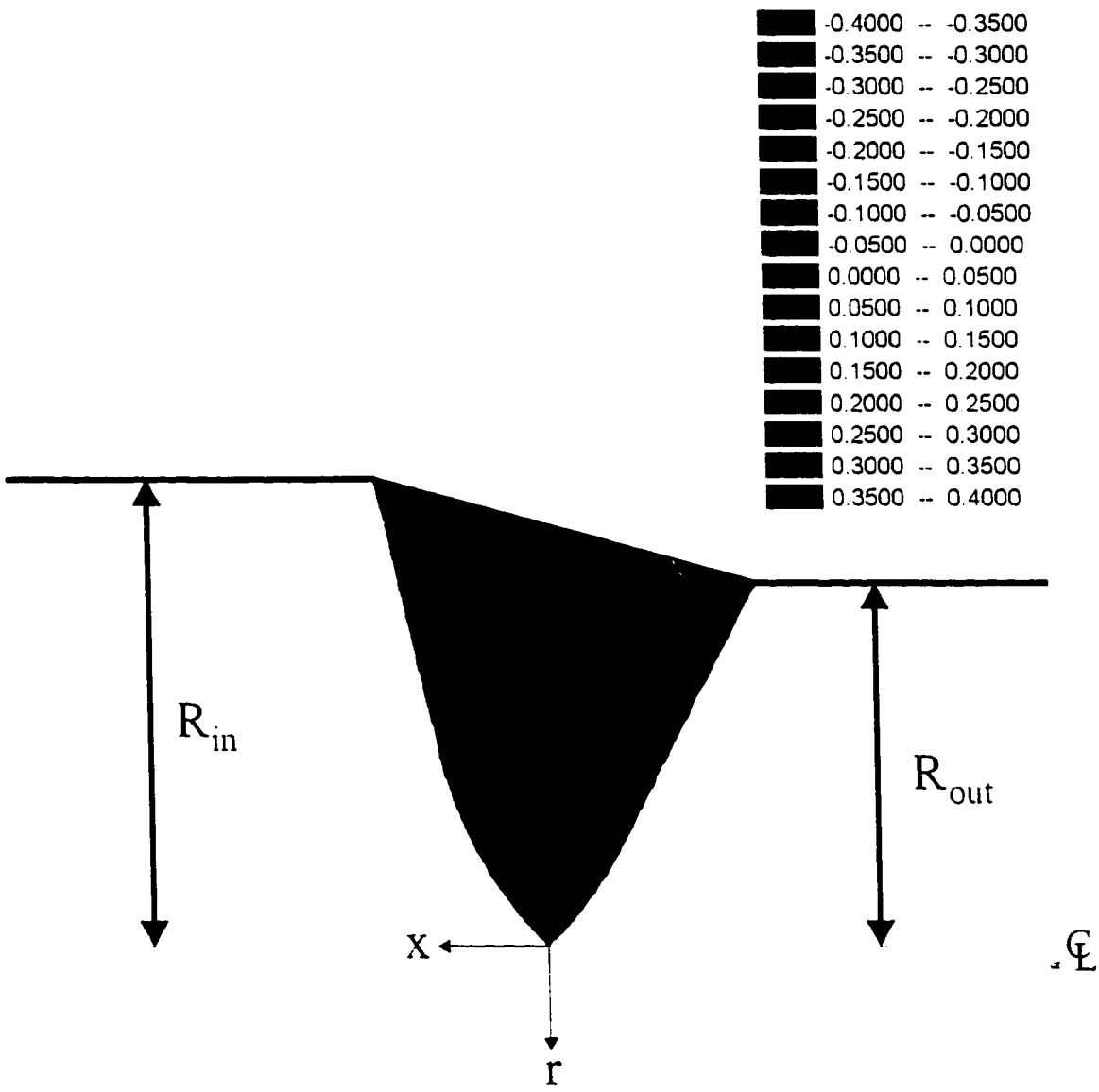

Figure 6.4 Map of the hydrostatic pressure ($\sigma_H/2k$) during extrusion in a 15° die for a reduction of 39.3%.

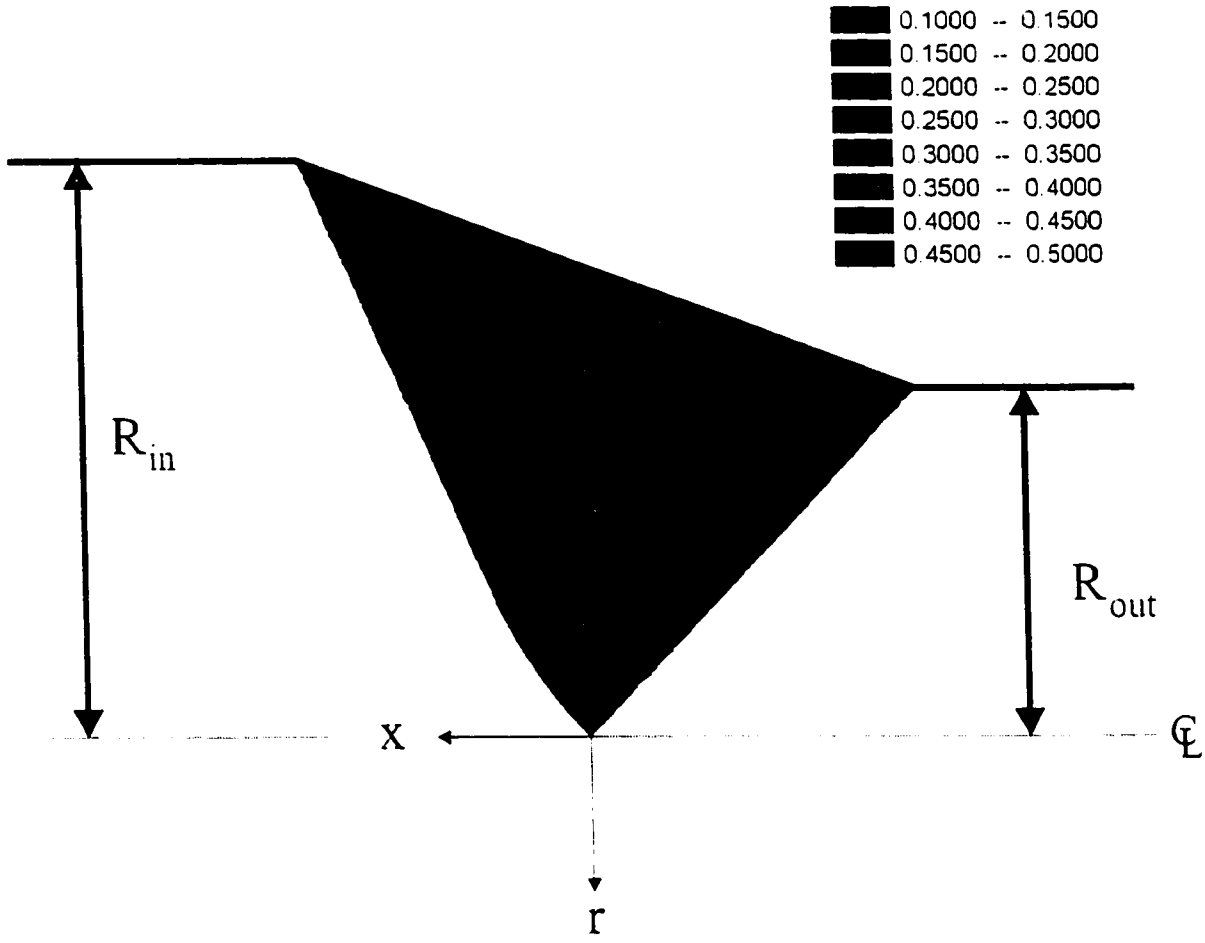

Figure 6.5 Map of the hydrostatic pressure ($\sigma_H/2k$) during extrusion in a 20° die for a reduction of 62.3%.

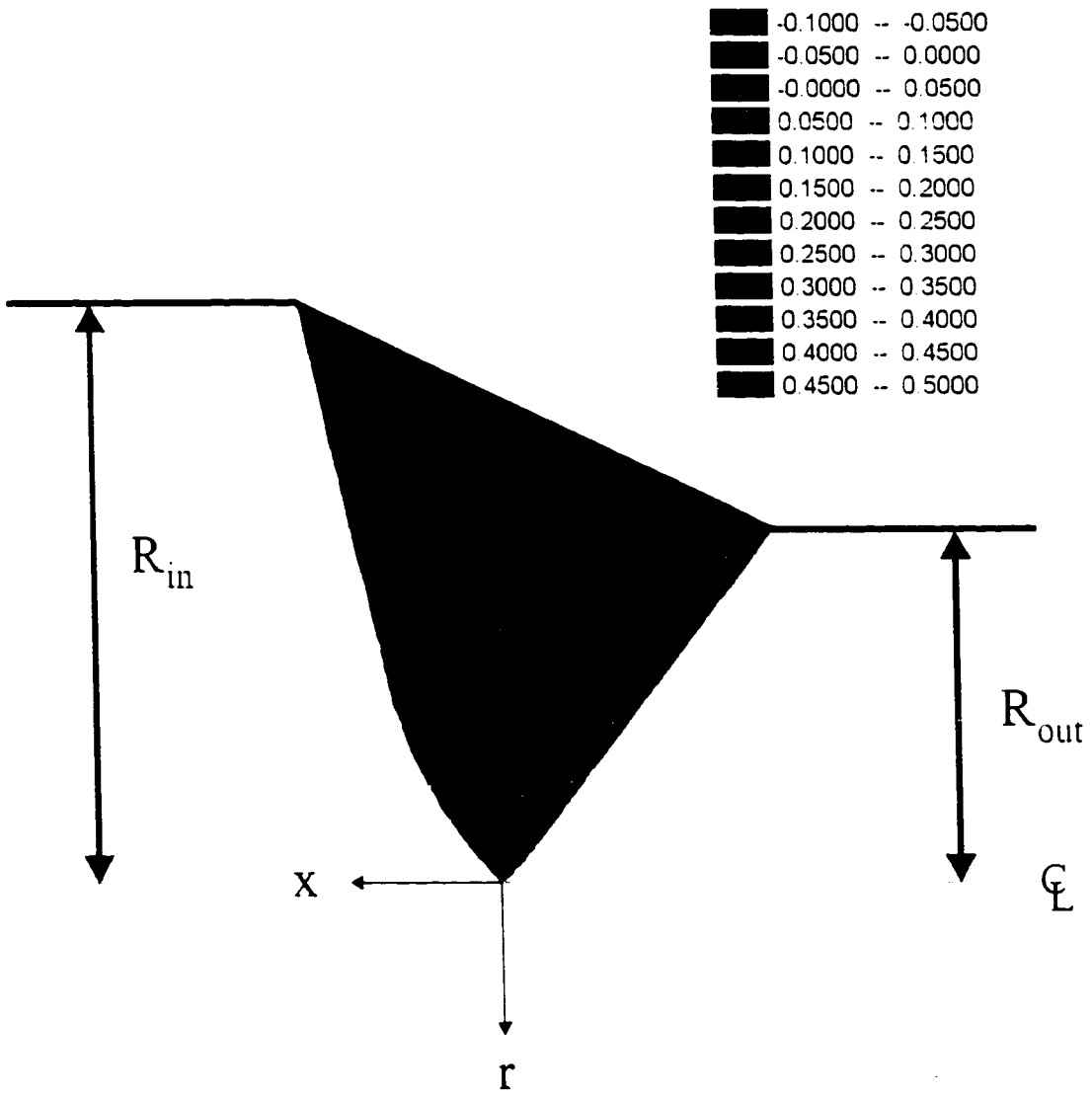

Figure 6.6 Map of the hydrostatic pressure ($\sigma_H/2k$) during extrusion in a 25° die for a reduction of 62.3%.

the pressure maps corresponding to the reductions of 39.3% (strain of 0.5) are more tensile in nature, both in terms of the magnitude of the hydrostatic pressures and the volume occupied by them, than the corresponding maps for reductions of 62.3% (strain of 1.0). These effects of die angle and reduction were also observed by Thomason (1969/70). It can be concluded that process parameters such as die angle and reduction have great importance in determining the hydrostatic pressure distribution in the extrusion dies and thus, considering the link between hydrostatic pressure and damage, will directly affect the initiation and evolution of damage.

It is worthwhile to examine the maximum range of hydrostatic pressure reached in all of these plots. The lowest tensile pressure has a value of $\sigma_H/2k$ not inferior to -0.4 from figure 6.4. The highest compressive pressure does not exceed a value of 0.5 for $\sigma_H/2k$.

At this point, it is important to examine the assumptions made in this analysis and how this will affect the ability of the present results to model the process of extruding MMCs. The assumptions refer to both global and local properties. The assumption made for the global flow of the composites will be discussed first. The first assumption of the slip line field analysis is that the material being extruded is rigid-plastic, which means that it has infinite rigidity up to its yield strength, and that past the yield point, plastic flow occurs without strain hardening. Generally, for large strain processes such as extrusion, ignoring elastic deformations does not lead to large errors since they constitute a very small fraction of the total strain. Thus, the assumption of infinite rigidity is a good one. However, in the present study, from the flow stress data of Table 4.2, it is obvious that work hardening of the composites occurs as a result of extrusion. The assumption of a non work hardening billet is not fulfilled and will lead to error. A correction for this effect is to use an intermediate shear yield strength $\bar{k}$ which lies between the shear yield strength of the undeformed and fully extruded composite. These are the assumptions made for the global properties of the deforming MMCs. The assumptions made for local

processes must also be examined. There is the problem that the composites consist of plastic matrices with linear elastic reinforcements embedded into them. The one exception to this was the one Cu-W billet where the W fibers were plastic, but, in general, the assumption of plastic deformation of a continuum fails if deformation is examined on the same scale as the reinforcement. This may not be important for the particulate reinforced MMCs where the particle size is of the order of 10 μm but may be more important in the Cu-W billets where the fibers have a diameter of 1 mm. Another source of possible error in the model is that it does not consider the effects of friction at the die walls. Although hydrostatic extrusion was chosen as the process to reduce the friction to the largest possible extent through the hydrodynamic lubrication effect of the pressurizing fluid, the results of Section 4.1 make it clear that friction was a significant factor in determining the extrusion pressure. The main effect of friction occurs locally near the die walls, and so it would be expected that the hydrostatic pressure would be most affected by this error at that location. Further, this analysis considers conical converging dies whereas the experiments were conducted using streamline dies. This differing geometry is another discrepancy between the model and experiments.

It was the goal of the slip line field model to determine the magnitude of the hydrostatic pressures in the die during extrusion and to link the results to the experimental observations of damage in hydrostatically extruded MMCs. Having an estimate of these pressures, we can try to evaluate whether their magnitude was high enough to suppress damage events such as decohesion and fracture of the reinforcement during the extrusion process. Considering the errors in the slip line field model, it was thought that a link between the hydrostatic pressure calculated in the dies and damage accumulation in MMCs should be made on a qualitative basis. As was discussed earlier, it has been shown that both the sense and magnitude of the hydrostatic pressure affects the appearance of damage in materials. Since damage is normally characterized by a dilatational event, it is self evident that a tensile hydrostatic pressure will always aid the process and that a compressive hydrostatic pressure will retard it. It was

concluded from microstructural analysis of the extruded particulate composites that the level of damage was linearly related to the amount of imposed strain. Since the imposed strain varied with the distance traveled in the die and it has been observed that there is an average drop in hydrostatic pressure in the slip line model from the die entrance to the die exit, the trend between damage and hydrostatic pressure is as expected. However, considering the observations of work hardening of the matrix with imposed strain and the observation of strain localization near the reinforcements during plane strain compression of Cu-W composites, it can't be ascertained what contribution the hydrostatic pressure may play in damage events. The more interesting goal may be to determine the level of the hydrostatic pressure that will suppress damage events.

It is first useful to consider under what conditions a material that is brittle in uniaxial tension may be extruded without fracturing by the suppressing effect of high compressive hydrostatic pressures. We assume that the uniaxial tensile fracture stress for this material is σ_f, that the uniaxial tensile flow stress is σ_o and that $\sigma_f < \sigma_o$. For extrusion, the material is subjected to a multiaxial stress state with principal components σ_1, σ_2 and σ_3. It is assumed that σ_1 is parallel to the extrusion direction and that it is always the highest tensile stress at any point and that the material will fail if $\sigma_1 = \sigma_f$. We further assume that the shear yield stress τ_o for the material follows the Tresca criterion and can be written as follows

$$\tau_o = \frac{|\sigma_1 - \sigma_3|}{2} = \frac{\sigma_o}{2} \qquad \text{eq. (6.10)}$$

where σ_1 and σ_3 are the highest and lowest algebraic principal stresses respectively. The situation in stress space can thus be constructed using a Mohr type plot as in figure 6.7. From this construction, it can be seen that in order to avert failure, the stress state during extrusion must be such that the shear yield stress τ_o is reached before $\sigma_1 = \sigma_f$. The critical point is the one where both σ_f and τ_o are reached

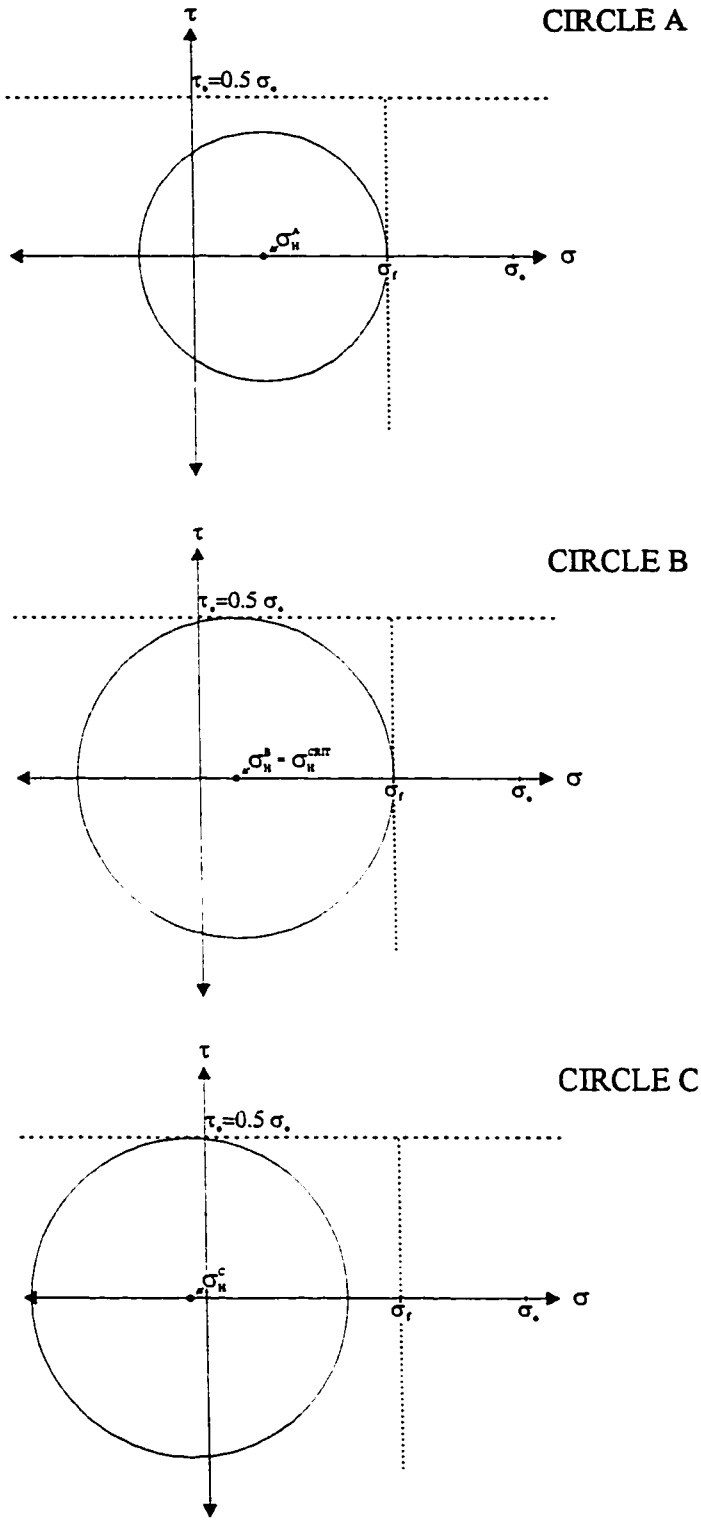

Figure 6.7 Mohr plots to represent the state of stress during extrusion for: a) fracture of the reinforcement, b) the critical point where the yield and fracture point of the reinforcement is reached and c) yielding of the reinforcement.

simultaneously. The critical hydrostatic pressure defined by that point, denoted σ_H^{crit} is the hydrostatic pressure below which fracture is never reached and the material deforms by plastic flow. It should be noted here that negative stresses are compressive in the present analysis. A graphical view of the stress states defined by the critical point is depicted in figure 6.7. The first possible situation is the one where the stress state is such that the fracture stress is reached before yield. The Mohr circle for this is denoted A, and the corresponding hydrostatic pressure for this state of stress is the stress at the center of the circle, denoted σ_H^A . The second circle illustrates the critical situation discussed previously and it is denoted by circle B with corresponding $\sigma_H^{crit} = \sigma_H^B$. The third situation, shown by circle C on figure 6.7, is one where plastic flow occurs and the material extrudes without fracture. The hydrostatic pressure for this stress state is σ_H^C, such that, $\sigma_H^C < \sigma_H^{crit} < \sigma_H^A$. As we are assuming that a damage event at σ_f will lead to catastrophic failure of the material, we have thus related damage to hydrostatic pressure. Damage will be suppressed when the hydrostatic pressure is algebraically smaller than

$$\sigma_H^{crit} = \frac{\sigma_{ii}}{3} = \frac{2\sigma_f + \sigma_2 - \sigma_o}{3} \qquad \text{eq. (6.11)}$$

since $\sigma_1 = \sigma_f$ and $\sigma_3 = -(\sigma_o - \sigma_f)$ at the critical point from figure 6.7.

From equation 6.11, it is seen that the critical hydrostatic pressure depends on the uniaxial fracture stress σ_f, the uniaxial tensile flow stress σ_o and the intermediate stress σ_2. In order to eliminate the latter from equation 6.11, different limiting cases must be examined. At the die walls, the material approaches a state of plane strain so that $\sigma_2 = 0.5\ (\sigma_1 + \sigma_3)$ and thus equation 6.11 becomes

$$\sigma_H^{crit} = \sigma_f - \sigma_o/2 \qquad \text{eq. (6.12a))}$$

At the billet center line, by symmetry, $\sigma_2 = \sigma_3$ and equation 6.11 becomes

$$\sigma_H^{crit} = \sigma_f - 2\sigma_o/3 \qquad \text{eq. (6.12b))}$$

In between the center line and the die walls σ_2 will take up an intermediate value and the critical hydrostatic pressure will be limited by equation 6.12a) and equation 6.12b). By inspection, because σ_f and σ_o are positive by definition, equation 6.12b) will always be smaller (algebraically) than equation 6.12a). Thus, if the hydrostatic pressures everywhere in the die are more compressive than the value calculated in equation 6.12b) from the uniaxial flow stress and fracture stress of the material, the extrusion will be successful in suppressing damage.

We can now estimate the effects of the hydrostatic pressures calculated in the slip line field analysis on the MMCs that were extruded. From eq. 6.12b), we can estimate whether the hydrostatic pressure in the die was high enough to suppress fracture of the brittle reinforcement. In order to accomplish this, values for σ_f and σ_o for the reinforcements used in this study must be found. For the model Cu-W composites, these can be estimated from experimental data. From Section 4.5, the hardness of the W fibers in the as-fabricated state was found to be 490 kg/mm^2. Using the hardness divided by 3 as a measure of σ_o, we obtain σ_o= 1.6 ± 0.1 GPa. The fracture stress σ_f can be estimated from the critical length calculated in Section 4.5 from dimensional measurements on W fibre fragments after extrusion to a total strain of 0.5. The critical length l_c was calculated as (2.0 ± 0.5) x 10^{-3} m. From Section 2.1, the expression for critical aspect ratio is

$$\frac{l_c}{d} = \frac{\sigma_f}{2\tau_y} \qquad \text{eq. (6.13)}$$

where τ_y is the shear yield strength of the matrix at the fibre/matrix interface and d is the fibre diameter, which is 1 mm in the present work. If we assume that the Cu matrix is fully hardened at the interface due to local plastic relaxation due to thermal expansion mismatch during fabrication and due to strain hardening during extrusion, we can estimate the interfacial shear yield stress as 225 ± 50 MPa. This value corresponds to the peak hardness measured in the Cu after extrusion, as shown in figure 4.25.

Thus, solving equation 6.13 for the fracture stress of W, a value of $\sigma_f = 900 \pm 300$ MPa is obtained. The error was estimated by an RMS error calculation, using the errors in l_C and τ_y. Thus, using the estimated values for σ_f and σ_o, it is found from equation 6.12b) that the critical hydrostatic pressure for suppression of fracture in the W fibers is -170 ± 300 MPa. This is a compressive pressure. In order to compare this to the results of the slip line field analysis, this pressure is made a dimensionless quantity by dividing by 2k, which is the uniaxial composite flow stress. This is estimated as the flow stress of the Cu matrix. In view of the fact that the Cu work hardens in the die during extrusion, from figure 4.25, it was estimated that 2k was approximately 300 MPa. Thus,

$$\frac{\sigma_H^{crit}}{2k} = -0.6 \pm 1.0$$

From the pressure plots for extrusion to a strain of 0.5, namely figure 6.4 and figure 6.5, remembering that compressive hydrostatic pressures are positive for that analysis, it is seen that none of the die volume has a hydrostatic pressure of $\sigma_H/2k$ of 0.6 or bigger. This seems to be consistent with the observation of fractured fibers in most of the Cu-W billets that were extruded. This result may also help explain the experimental observation of deformation of W fibers in one billet, as shown in figure 4.23. Before fabrication, the W fibers yield before fracture in tension. It is thus during composite fabrication that embrittlement occurred. The embrittlement of W fibers during fabrication of Cu-W composites has also been reported in the literature (Poole, 1993). No tensile data along the fibre axis is given in Poole's work other than the result that the fibre strength in tension is larger than 500 MPa. However, the transverse compressive strength of extruded W fibre was found to vary from one composite billet to the next. The range of strengths was found to vary between 700 to 1000 MPa. The variation in strength from one billet to another suggests that the degree of embrittlement is linked to the fabrication process. If this is true, then the magnitude of σ_f is dependent on fabrication parameters and it is possible that the billet that extruded without damaging was embrittled to a lesser degree. Possible fabrication process parameters that could cause this may be impurity diffusion or microstructural change such as matrix recrystallisation

while at the processing temperature. To illustrate, if we assume that this billet was fabricated in such a way that its uniaxial fracture stress was higher than 900 MPa, say 1200 MPa, the resulting critical hydrostatic pressure $\sigma_H/2k$ would become 0.44 (tensile) from equation 6.12b). This would mean that any hydrostatic pressure higher (more compressive) than 0.44 on the pressure maps shown on figure 6.3 and figure 6.4 would result in plastic flow of the tungsten. Every point of the 15° die is at that pressure or higher and all of the 10° die volume satisfies this condition. This may help explain the very different observations in seemingly identical Cu-W samples. Thus, it can be concluded that suppression of damage through the action of the high extrusion pressures may be an important factor for the model Cu-W composites, but also the thermo-mechanical history of the fibers. This has repercussions both for process design and the fabrication procedure.

The equivalent procedure can be carried out for the extruded Al based particulate composites. However, in this case, there is no experimental data available to estimate σ_f and σ_o for the ceramic reinforcements in these composites. For a rough estimate, the values of flow stress were obtained from the Cambridge Materials Selector™ database. The uniaxial flow stress for CMS and SiC were estimated as 12.0 GPa and 5.5 GPa respectively. Evidence in the literature for the fracture stress of the SiC particles (Maire et al., 1997) suggests that 1.5 GPa is a reasonable estimate for this value. The equivalent fracture stress for CMS was estimated at 1.0 GPa. If these values are substituted into equation 6.12b), the critical pressures are then calculated as -6.5 GPa and -2.7 GPa for SiC and CMS respectively. Assuming a composite flow stress of a few hundred MPa, it is clear from the pressure maps for all conditions of reduction and die angle that the hydrostatic pressure will never reach a value high enough to suppress fracture of the reinforcement by plastically yielding it instead. However, by comparison of the damage rates in tension and extrusion with applied plastic strain for 6061-20% CMS, the high hydrostatic pressures during extrusion clearly slow down the rate of damage accumulation with imposed

strain. The construction of figure 6.7 illustrates this point, as the compressive hydrostatic pressures shift the Mohr circle away from the tensile fracture stress.

Another parameter which affects the rate of damage accumulation besides continued nucleation of damage by particle cracking is the growth of the existing damage, or voids, in the material. The hydrostatic pressure component of the stress tensor strongly affects this dilatational process. An illustration of this effect can be obtained from the Rice and Tracey model for void growth under a remote applied strain rate field (Rice and Tracey, 1969). If the principal components of the strain field are denoted $\dot{\bar{\varepsilon}}_k$, the Rice and Tracey model predicts the rate of void growth $\dot{R}_k$ along the principal direction k as

$$\dot{R}_k = \left(C\dot{\varepsilon}_k + \sqrt{2/3\,\dot{\varepsilon}_L\dot{\varepsilon}_L}\,D\right)R \qquad \text{eq. (6.14)}$$

where R is the radius of the void, C is a constant related to the rate of hardening, the subscripts L refer to the two principal directions perpendicular to k and D is given by

$$D = 0.75\sigma_H/\sigma_o \qquad \text{for linear hardening}$$

$$D = 0.558\sinh\left(\frac{3\sigma_H}{2\sigma_o}\right) + 0.008v\cosh\left(\frac{3\sigma_H}{\sigma_o}\right) \qquad \text{for no hardening}$$

where v is the Lode variable and is defined in Section 2.7. The important aspect of equation 6.14 is that for whatever form it takes, it is strongly dependent on the hydrostatic pressure σ_H through the parameter D. When σ_H is negative (compressive), the growth rate of the void is predicted to be lowered and when it is tensile (positive) an increase in the void growth rate is expected. Thus, the combination of lower nucleation and growth rate during extrusion, compared to tension, can be explained through the action of the high compressive hydrostatic pressures.

6.2 MICROSTRUCTURAL ASPECTS OF DAMAGE ACCUMULATION DURING EXTRUSION

In the previous section, it was found that the hydrostatic pressures in the dies were not sufficient to suppress damage during the extrusion of the MMCs studied. This was verified experimentally for the pMMCs in the present study, where the amount of damage was found to be proportional to the imposed plastic strain in the die. Thus, the load transfer process from the plastic matrix to the elastic and brittle particles must be examined locally in order to understand the accumulation of damage in the composite microstructures. It is only with an appropriate view of this process that the effect of microstructural variables on the accumulation of damage can be understood.

For the loading of hard inclusions or particles by a plastic matrix, a modified Eshelby analysis for non-dilute systems can be used. The method is similar to the one used to evaluate thermal misfit stresses during cooling in that, for both cases, the shape of the hole after the cutting operation is determined by the applied strain tensor (Clyne and Withers, 1995). For loading by plastic flow, the transformation strain tensor is equal to the global applied strain tensor. Substituting the global applied strain tensor ε_M^P for the transformation strain tensor of the modified Eshelby method, the mean stress component in the matrix $\langle\sigma\rangle_M$ and particle $\langle\sigma\rangle_I$ are given by

$$\langle\sigma\rangle_M = -fC_M(S-I)\left\{(C_M - C_I)\left[S - f(S-I)\right] - C_M\right\}^{-1} C_I\varepsilon_M^P \qquad \text{eq. (6.15a))}$$

$$\langle\sigma\rangle_I = (1-f)C_M(S-I)\left\{(C_M - C_I)\left[S - f(S-I)\right] - C_M\right\}^{-1} C_I\varepsilon_M^P \qquad \text{eq. (6.15b))}$$

where f is the particle volume fraction, C_M and C_I are the matrix and particle stiffness tensors respectively, S is the Eshelby tensor and I is the identity matrix. The mean stresses in equation 6.15a) and equation 6.15b) must be added to the applied stress tensor σ^A to obtain the entire stress tensor. Hence, the stress state in the matrix σ_M and particles σ_I will be

$$\sigma_M = \sigma^{\wedge} + \langle\sigma\rangle_M \qquad \text{eq. (6.16a))}$$

$$\sigma_I = \sigma^{\wedge} + \langle\sigma\rangle_I \qquad \text{eq. (6.16b))}$$

Thus, the magnitude of the stresses in equation 6.15a) and equation 6.15b) are a measure of the efficiency of the load transfer process from the matrix to the reinforcements. This result is valid for uniform plastic flow in the matrix and it predicts, for a constant applied stress tensor, that the stresses in the particle will vary linearly with the imposed plastic strain. Considering the high stiffness of the ceramic reinforcements in the present work, equation 6.16b) predicts very high stresses in the particles for very small applied plastic strains. If this mechanism operated unimpeded, reinforcement cracking would occur at strains very much lower than the ones applied by hydrostatic extrusion. However, it is the magnitude of this stress build up which causes relaxation events to occur locally around the particles. The assumption of uniform plastic flow breaks down. In other words, the shape change of the hole due to plastic flow in the Eshelby cutting exercise will be a function of both ε_M^P and the local plastic strain caused by the relaxation mechanism.

An empirical form for this applied misfit strain tensor has been shown (Brown and Stobbs, 1976) to model pMMC strain hardening accurately and it is obtained by substituting $\sqrt{\varepsilon_M^P}$ for ε_M^P in equation 6.15a) and equation 6.15b). Thus, by considering relaxation events around particles, the build up of stress in the particles is now predicted to be roughly parabolic with the applied plastic strain.

It is now of interest to develop an expression from equation 6.16b) relating the transfer of load to the fracture of an embedded particle. If we assume for the moment that the particles are ellipsoidal, that the 3-direction is the axial direction during extrusion and that the particles have an axis of symmetry in that direction, a reasonable estimate for fracture would be that the component of the stress tensor in the 3-direction equals the uniaxial fracture stress. This fracture criterion is written as follows:

$$\sigma_{3l} = \sigma_f \qquad \text{eq. (6.17)}$$

Further, we assume that the principal matrix stress in the extrusion direction (direction 3) is the largest algebraic stress and that by symmetry, the stresses in the transverse directions (directions 1 and 2) are equal. For yielding by the Tresca criterion, the initial matrix flow stress σ_o is given by

$$\sigma_o = \sigma_{3M} - \sigma_{1M} = \sigma_3^\wedge - \sigma_1^\wedge + (\langle\sigma_3\rangle_M - \langle\sigma_1\rangle_M) \qquad \text{eq. (6.18)}$$

from equation 6.16a). Rearranging equation 6.18 to solve for the applied stress in the direction of extrusion $\sigma_3^\wedge$,

$$\sigma_3^\wedge = \sigma_o + \sigma_1^\wedge - (\langle\sigma_3\rangle_M - \langle\sigma_1\rangle_M) \qquad \text{eq. (6.19)}$$

Putting $\sigma_3^\wedge$ into equation 6.16b), we obtain an expression for σ_{3l}, the principal stress in the particle in the extrusion direction

$$\sigma_{3l} = \sigma_3^\wedge + \langle\sigma_3\rangle_l = \sigma_o + \sigma_1^\wedge - (\langle\sigma_3\rangle_M - \langle\sigma_1\rangle_M) + \langle\sigma_3\rangle_l \qquad \text{eq. (6.20)}$$

Equation 6.20 states that the axial stress in the extrusion direction depends on the initial flow stress of the matrix, the applied transverse stress during extrusion, two principal mean stress components in the matrix and one principal mean stress component in the particle. The initial flow stress of the matrix is a constant. As well, since the extrusion process occurs at a constant load and that the die pressure is a constant for conical converging dies in equilibrium analyses (Section 2.3), $\sigma_1^\wedge$ can also be considered to be constant. Thus, the axial stress in the particle varies as a function of the mean stress components only. Since all of the mean stress components vary as $\sqrt{\varepsilon_M^p}$ empirically, equation 6.20 can be written simply as

$$\sigma_{3l} = C + F\left(\sqrt{\varepsilon_M^p}\right) = \sigma_f \qquad \text{eq. (6.21)}$$

where C is a constant and F is some function which varies with $\sqrt{\varepsilon_M^p}$ only. Equation 6.21 implies that the load transferred to the reinforcement in not a function of the radial position in the die, but only of the applied macroscopic plastic strain. The evidence from metallographic observations of the fully extruded

composites seem to validate this assumption as no discernible radial variation in damage was observed. For particles of the same shape and orientation, the fracture criterion given by equation 6.21 predicts that fracture should occur at one strain, when the loads in the particles have built up so that σ_{11} reaches σ_f. Experiments show a gradual accumulation of damage with strain.

This discrepancy between model and observation may be explained by considering the fracture stress of the particles. The Eshelby tensor S in equation 6.15a) and equation 6.15b) is a function of the aspect ratio of the particles. It is not a function of size. Thus, the load transferred to the particle by an applied plastic strain depends on its aspect ratio, but not on its size. However, in the previous chapter, it was found that the strength of brittle materials depended on their scale. The size dependence of the particle fracture stress has been used previously in the literature (Maire et al., 1997) for the modeling of damage evolution during plastic flow. From equation 5.5, the size dependence was assumed to vary via a Griffiths type of relationship, where the fracture strength σ_f was related to the reinforcement size r by

$$\sigma_f \propto \frac{1}{r^{1/2}} \qquad \text{eq. (6.22)}$$

Equation 6.21 is an expression of the assumption that the flaw size in the material scales with its external dimensions. Thus, the amount of load transferred to a particle before it fractures will depend on its size. Preferential cracking of larger size particles has been observed in the literature (Tao, 1991 and Newell, 1990) for the A356-20% SiC and A356-10% SiC composites investigated in the present work. Thus, in order to account for the scale of the reinforcement, equation 6.21 can be modified so that σ_f is a function of particle size r as follows

$$\sigma_{11} = C + F\left(\sqrt{\varepsilon_M^P}\right) = \sigma_f(r) \propto r^{-1/2} \qquad \text{eq. (6.23)}$$

Thus, equation 6.23 predicts that the plastic strain required to fracture a particle will vary with its size r. This explains the gradual accumulation of damage in pMMCs with a distribution of reinforcement size. From equation 6.23, the functional form of the relationship is predicted to be

$$\varepsilon_M^P \propto r^{-1/4} \qquad \text{eq. (6.24)}$$

To verify the prediction of equation 6.24, the size distribution of the reinforcement materials in the present investigation were obtained from the literature. The size distribution of SiC particles was reported by Tao (1991) and the size distribution of the CMS was compiled by Lloyd (1995). From the latter study, the particle area distribution and the aspect ratio of the particles was measured. The aspect ratio of the nominally spherical particles was found to be 1.31 ± 0.44. The error was estimated from the standard deviation to the mean. Considering the error, for simplicity, an aspect ratio of 1.0 was assumed for all of the particles. This is equivalent to assuming that the particles are spherical. In the present study, damage was measured as the % area of particles fractured. As larger particles will fail at a smaller stress, from equation 6.22, the damage will be proportional to the % area of particles larger than r. Hence, the reported area distribution of the particles was converted to the % area of particles larger than r. In this way, the slope of a log-log plot of the % area of particles larger than r against r will show the functional relationship between the amount of damage and the size distribution. The plot is shown in figure 6.8, for the approximate range of damage observed in this study, namely from 0 to approximately 50% by area. The slope of the best fitting line to this data is -0.27 ± 0.03. Thus damage is found to be proportional to $r^{-0.27\pm0.03}$,where r is the reinforcement size. Within error, the exponent of r is -1/4. The best fitting line with a slope of -1/4 is plotted on figure 6.8 for comparison to the linear regression line. In view of this result with equation 6.24, we can write a relationship between damage and applied plastic strain in the following form

$$\text{DAMAGE} \propto \varepsilon_M^P \qquad \text{eq. (6.25)}$$

Equation 6.25 thus predicts a linear relationship between damage and applied strain by extrusion for

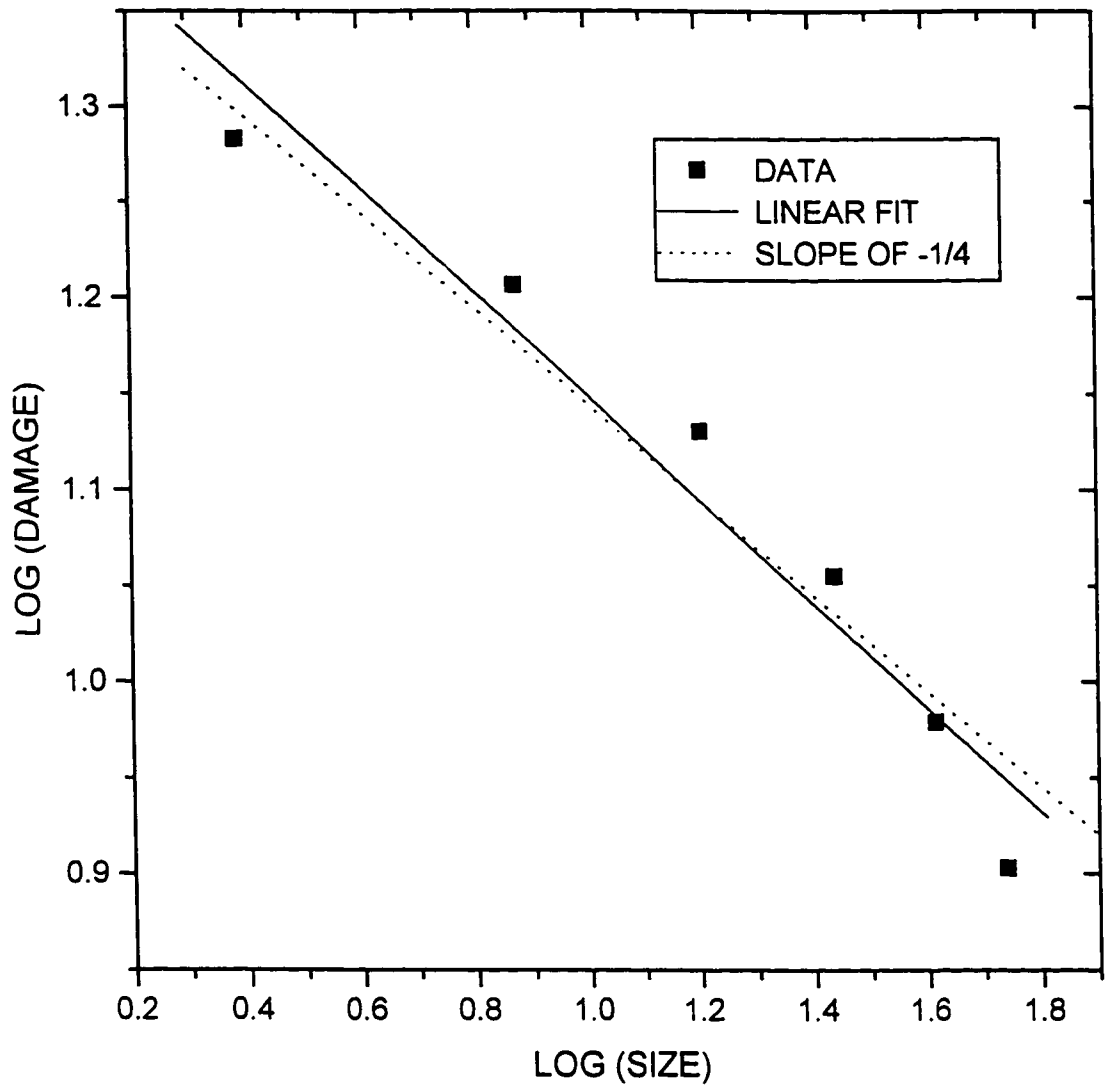

Figure 6.8 Log-log plot of damage in the CMS particles as a function of particle size r.

6061-20% CMS. The same procedure can be followed to plot the percent area of particles versus $r^{-1/2}$ from Tao's results (Tao, 1991). For SiC reinforcement volume fractions of 10% and 20% in A356, similar distributions in size and aspect ratio were found. The average aspect ratio was found to be approximately 1.9. It was assumed for the purpose of this estimate that the angular SiC particles had a constant aspect ratio of 1.9 and that their area was given approximately by the square of their size multiplied by the aspect ratio. In other words, it was assumed that the particles were aligned with respect to the extrusion direction and that they were rectangular in shape. Using this crude approximation, a plot of the logarithm of damage versus the logarithm of particle size r was constructed and the result is shown in figure 6.9. The slope of the best fitting line to this data is -0.25 ± 0.06. It is also seen from this plot that a best fitting line of slope -1/4 agrees roughly with the data. Thus, equation 6.25 also seems to apply to the A356-10% SiC and A356-20% SiC composites. As a consequence, for the reinforcement distributions reported, the linear relationship observed between damage and strain during extrusion of the particulate composites in the present work seems to be compatible with an empirical correlation for an Eshelby load transfer model.

The effect of microstructural variables on the accumulation of damage can now be examined from their effect in the Eshelby analysis given in equation 6.15a) and 6.15b). This will only be done on a qualitative basis since a quantitative model relating damage to applied plastic strain was not developed. The first variable of interest is the volume fraction of reinforcement, denoted f in equation 6.15a) and equation 6.15b). Although these aforementioned equations predict a lower mean stress $\langle\sigma\rangle_I$ for higher volume fractions of reinforcement, this does not mean that the stress will build up faster with imposed strain in composites with a lower volume fraction of reinforcement. The mean stresses are a measure of the efficiency of load transfer. At higher volume fractions of reinforcement $\langle\sigma\rangle_M$ is more negative from equation 6.15b), which means that for the same applied plastic strain, the applied stress σ^A needed to

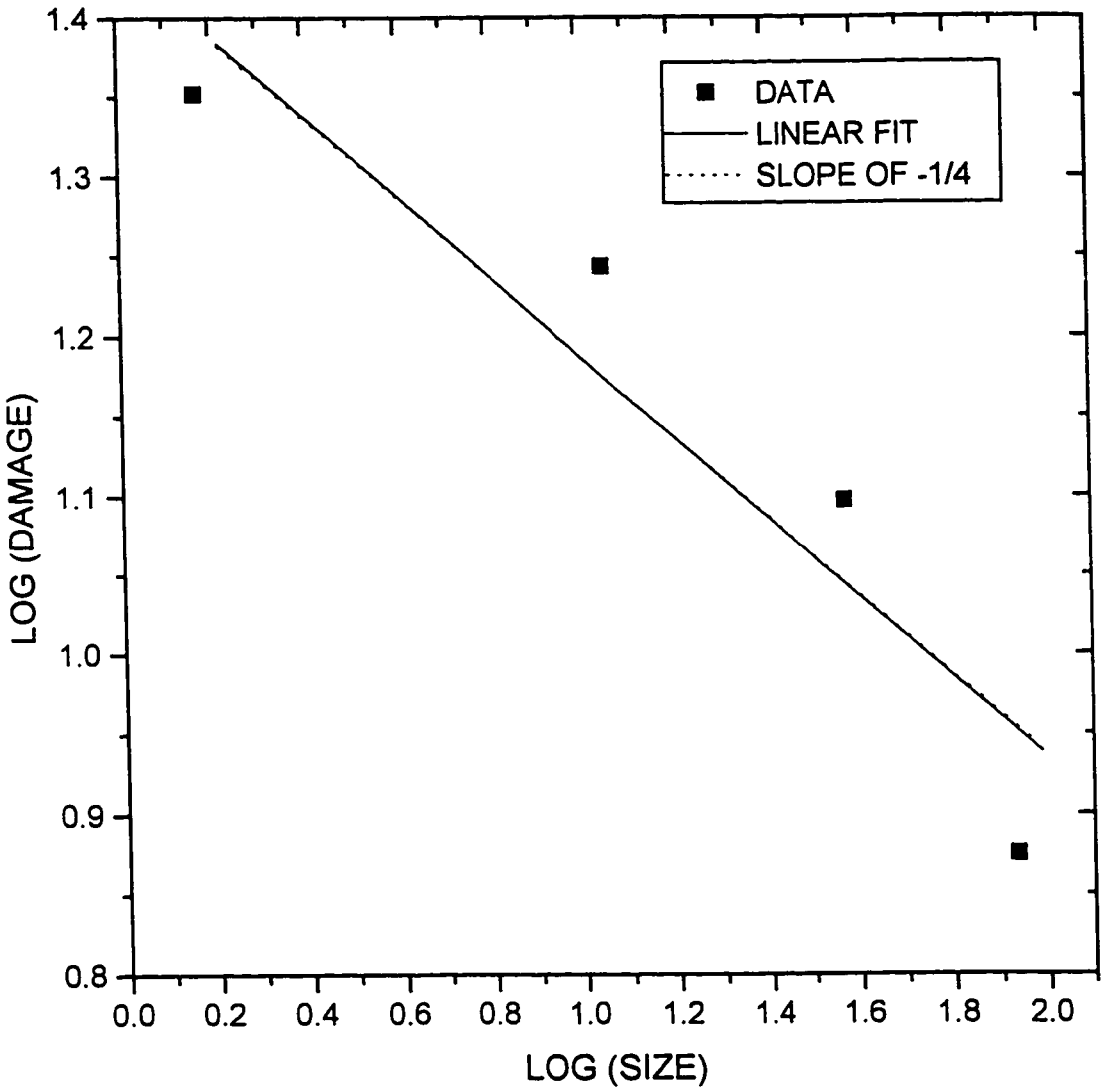

Figure 6.9 Log-log plot of damage in the SiC particles as a function of particle size r.

sustain plastic flow will increase. Thus, for a greater reinforcement volume fraction, the composite will work harden at a greater rate. From equation 6.15a) and 6.16b), it can be seen that the sense of the resultant stress state in the particles will depend on the magnitude of the increase in σ^A with increasing volume fraction and the magnitude of decrease in the mean stress $\langle\sigma\rangle_I$ with increasing volume fraction. The change in the component of the inclusion stress in the direction of extrusion, σ_{II}, with increasing volume fraction will determine the rate of damage accumulation. The evidence in the present study, from comparison of the damage levels in the A356-10% SiC and A356-20% SiC show that the damage level increases with increasing volume fraction, for the same applied plastic strain. This in turn would mean that the work hardening of the matrix more than compensates for the decrease in load transfer efficiency for an increase in reinforcement volume fraction.

The effect of particle shape is more definitive. Shape enters as a factor in equation 6.15b) through the Eshelby tensor S. The shape is characterized by the aspect ratio for particles idealized as ellipsoids. To illustrate this effect, equation 6.15b) can be solved for the A356-20% SiC and 6061-20% CMS composites which have angular and spherical particles respectively. It was assumed that the SiC particles were prolate ellipsoids of aspect ratio 1.9, oriented with their long axis in the extrusion direction. Further, it was assumed that the ceramic microspheres (CMS) had a composition consisting of 50% mullite and 50% alumina and the elastic properties of the mixture were estimated from the law of mixtures. Table 6.1 lists the Young's Modulus E, shear modulus G and Poisson's ratio ν for Al, SiC and CMS.

Table 6.1 Elastic Constants of Al, SiC and CMS

MATERIAL	E (GPa)	G (GPa)	ν
Al	69	26	0.34
SiC	415	185	0.15
CMS	250	90	0.26

It was assumed that all of the components of the composites were elastically isotropic. Equation 6.15b) was solved for an applied plastic strain $\varepsilon_M^P = 0.02$. The resultant mean stress tensor in the spherical CMS particles is (in MPa)

$$\begin{bmatrix} \langle\sigma\rangle_{11} \\ \langle\sigma\rangle_{21} \\ \langle\sigma\rangle_{31} \\ \langle\sigma\rangle_{41} \\ \langle\sigma\rangle_{51} \\ \langle\sigma\rangle_{61} \end{bmatrix} = \begin{bmatrix} -305 \\ -305 \\ 610 \\ 0 \\ 0 \\ 0 \end{bmatrix}$$

and the corresponding mean stress in the ellipsoidal SiC is given by the following tensor

$$\begin{bmatrix} \langle\sigma\rangle_{11} \\ \langle\sigma\rangle_{21} \\ \langle\sigma\rangle_{31} \\ \langle\sigma\rangle_{41} \\ \langle\sigma\rangle_{51} \\ \langle\sigma\rangle_{61} \end{bmatrix} = \begin{bmatrix} -90 \\ -90 \\ 1330 \\ 0 \\ 0 \\ 0 \end{bmatrix}$$

Thus, around twice the load transfer efficiency, in the extrusion direction (direction 3 in the Eshelby analysis), is predicted for the SiC particles. This would result in a proportional increase in the rate of damage accumulation with imposed plastic strain. However, it is clear that this increase in damage rate due to differing load transfer efficiencies of the two reinforcing materials (SiC and CMS) would be small compared to the experimentally observed 15 times increase in damage rate in A356-20% SiC compared to 6061-20% CMS. It is thus reasonable to assume that the large discrepancy in damage rate between the aforementioned MMCs is due to another factor.

Other factors must be examined to explain the effect of shape in damage accumulation during the extrusion process. The assumption that the angular SiC particles are ellipsoids may lead to error. An FEM study of the plastic strain distribution at a fibre end has shown that large local strains occur in the matrix near the corners (Christman et al., 1991). High local stresses in fibers near corners have been shown to occur by photoelastic experiments (Withers et al., 1992). These local stresses at sharp corners may be of import for the load transfer process to the angular SiC particles, leading to an intensification of the stresses. In such a case, fracture of angular particles would occur at lower applied plastic strains than for ellipsoidal particles. An FEM analysis of spheres and short fibre reinforcements has verified the enhanced load transfer and damage rate in angular particles (Llorca, 1997). Another variable of possible import in discussing the great difference in damage rate between A356 reinforced with 20% by volume SiC and 6061 reinforced with 20% by volume CMS is the flaw population in the particles due to their fabrication. The angular SiC particles were produced by mechanical attrition and the spherical CMS particles were made by spray drying of bauxite slurries and subsequent firing of the green spheres. Considering the severity of the mechanical attrition process, it is reasonable to assume that larger flaws were produced in the processing of the SiC. This population of proportionally larger flaws would lower their fracture stress and as a result, the rate of damage accumulation with imposed plastic strain could be increased significantly.

6.3 EFFECT OF EXTRUSION ON THE MECHANICAL PROPERTIES OF MMCs

Having now examined how the process of hydrostatic extrusion leads to microstructural damage in MMCs and what parameters determine the level of the damage, it is of importance to examine the change in tensile mechanical properties of extruded pMMCs. This section will deal with the changes in elastic modulus, flow stress, work hardening and tensile instability point. These changes will be

related to the plastic deformation in the matrix materials and damage level in the reinforcement materials produced by extrusion. This section will deal separately with the effect of extrusion on the matrix materials, reinforcement materials and finally on the composite materials made up of these components. The reason behind this subdivision is to separate the effects of extrusion on the components in order to better understand their combined effect in MMCs.

6.3.1 EFFECT OF EXTRUSION ON THE MATRIX MATERIALS

To illustrate the effect of hydrostatic extrusion on the matrices of the MMCs, the unreinforced alloy materials were hydrostatically extruded and subsequently tested in tension. The data obtained made it possible to compare the mechanical properties of the extruded alloys with the undeformed alloys. The mechanical properties will be discussed in terms of changes in the elastic modulus, flow stress, work hardening characteristics and tensile instabilities.

One mechanical property of interest is the elastic modulus. From Table 4.1, it is seen that no measurable change in elastic modulus was observed due to previous deformation by hydrostatic extrusion. This applies to both the A356 and 6061 alloy. The elastic modulus and damage level are related by considering the loss of load bearing area due to voids (Kachanov, 1986). If the amount of damage is defined as D, the ratio of the void area and load bearing area on a cross section perpendicular to the axis of uniaxial loading, then the elastic modulus E′ of the damaged material is related to the elastic modulus E_o of the undamaged state by

$$E' = E_o(1 - D) \qquad \text{eq. (6.26)}$$

Equation 6.25 predicts a loss of elastic modulus for a damaged microstructure. Therefore, in view of the observation that the elastic modulus remains unchanged after extrusion, it can be concluded that no significant microstructural damage is created in the alloys by this process.

Although the hydrostatic extrusion does not affect the elastic modulus, it has a significant effect on the 0.2% offset yield stress. In both the A356 and 6061, the same general effect of previous deformation by hydrostatic extrusion was observed. From Table 4.2, it is seen that in all cases, a large increase in the 0.2% offset yield stress is produced as a result of the hydrostatic extrusion process. The amount of the increase was also found to increase with the amount of previous strain by extrusion. This result is an indication of the strain hardening of the alloys during the extrusion process. For example, the hydrostatic extrusion to a total plastic strain of 1.0 leads to a 0.2% flow stress of up to 3x its original value.

The amount of strain hardening of the alloys during hydrostatic extrusion is related to the subsequent tensile work hardening rates. From the stress-strain curves for the unreinforced alloys, figure 4.6 and figure 4.10 for A356 and 6061 respectively, it is seen that the work hardening of the extruded alloys fall below the work hardening rate of the undeformed alloys. Further, increasing amounts of prior strain by extrusion lead to smaller work hardening rates over the entire tensile strain range. If, from Backofen's description of the materials-based strain hardening described in the literature review by equation 2.39, we assume that there is no contribution to the net hardening rate from the strain rate component or adiabatic component, the strain hardening in the alloys is only due to the applied plastic strain increment. Extrusion of the composite materials effectively applies strain to the matrix material. Thus, if we denote the total increase in flow stress possible in the alloy by strain hardening as $\Delta\sigma$ it is observed that

$$\Delta\sigma_{EXTRUDED} < \Delta\sigma_{UNDEFORMED} \qquad \text{eq. (6.27)}$$

That is to say, the extrusion process decreases the hardening capacity of the matrix material, compared to the alloy that was undeformed prior to tensile testing.

The $\Delta\sigma$ described above is a measure of a material's ability to resist geometrical tensile instabilities by work hardening. According to the Considere criterion, from Section 2.6, an external neck on a tensile sample will develop and the plastic flow will localize when

$$\sigma = \frac{d\sigma}{d\varepsilon} \qquad \text{eq. (6.28)}$$

This is a statement that an incipient neck will develop when the flow stress is equal to the work hardening rate. The point at which the Considere criterion is reached will depend on $\Delta\sigma$, the total possible increase in flow stress. From equation 6.27, the work hardening capacity of the undeformed alloys is higher and, from Table 4.2, their flow stress is lower than the corresponding values for the extruded alloys. Thus, the Considere criterion is satisfied at a higher strain for the undeformed alloys. From the instability data in Table 4.3, this was observed experimentally for both the A356 and 6061 alloys.

The work hardening rates and flow stresses at the point of tensile instability are reported for the matrix materials in Table 4.4 and Table 4.5. It was found that, within experimental error, the flow stress and work hardening rate coincide at the tensile instability for the undeformed 6061 alloys. In the undeformed A356 alloy, there is a small measurable difference between the work hardening rate and flow stress at the instability. It is thus not clear whether the tensile instability in this material satisfies the prediction of the Considere criterion. However, it is clear in the extruded A356 and 6061 alloys that the work hardening rate and flow stress do not coincide at the instability. A possible explanation for this result, considering the validity of the Considere criterion for the undeformed 6061, may be that the instability in the extruded 6061 and A356 was materials based. If the extrusion process saturates the flow stress in the alloys such that $\Delta\sigma_{EXTRUDED}$ approaches zero in all of the deforming body or some region of the microstructure, then the ability of the material to resist necking in tension is lost. Thus, the instability will be determined by the appearance of the first local fluctuation in cross-sectional area which

will quickly localize further deformation. In this way, the process will be determined by local flow processes in the material, as opposed to geometrical considerations in a homogenous plastic material. The stress-strain curves for the 6061 and A356 alloys previously deformed by extrusion show that in most cases, there is little, if any, hardening before the tensile instability is reached. It is thus possible that the tensile instabilities observed in the present work for extruded 6061 and A356 samples reflect the point at which a local materials based instability develops in the highly work hardened microstructure.

6.3.2 EFFECT OF EXTRUSION ON THE REINFORCEMENT MATERIALS

As opposed to the various effects of the extrusion on the matrix materials, there is only one main effect of extrusion on the reinforcement particles. From figure 4.2, it is seen that the particles fracture as a function of the applied strain by extrusion. If it is assumed that fractured particles will have no ability to sustain subsequent tensile loads after they fracture in the composite microstructure, then the hydrostatic extrusion effectively decreases the load bearing area of the particles. The proportion of this decrease depends on the damage rate with strain from figure 4.2.

At this point, the question which remains is how the separate effects of the extrusion process on the matrix materials and the reinforcement particles contribute to the global tensile properties of the extruded MMCs. This will be discussed in the following subsection.

6.3.3 TENSILE PROPERTIES OF HYDROSTATICALLY EXTRUDED MMCs

From the tabulated results in Section 4.3, it is apparent that the extrusion process has decreased the elastic modulus of the particulate composites investigated in this work. This decrease in elastic modulus can be simply related to the amount of damage created during extrusion. For a one phase

material, elastic modulus and damage are related by equation 6.26, which predicts a loss of elastic modulus for a damaged microstructure. For a composite, there is no simple expression such as equation 6.26 to relate the amount of damage to the loss of elastic modulus because of the more complex models to describe the contribution of matrix and reinforcement to the global properties. However, the general trend between stiffness and damage remains the same. Hence, increasing amounts of damage will lead to a decrease in the elastic modulus of the composites. The experimental results are thus consistent in reporting a loss of stiffness in the damaged hydrostatically extruded MMCs. This is only a qualitative argument, but considering the errors in the measurement of E reported in Table 4.1, a more accurate model could not be verified by the data in the present work.

Although the effect of extrusion on the elastic modulus was difficult to measure with precision, the effect that extrusion had on the flow stress of the composites was clear. For every composite tested, extrusion increased the flow stress significantly. In most cases, the flow stress was also found to increase with increasing applied plastic strain by extrusion. The same observations were made for the extruded unreinforced matrix alloys A356 and 6061. For the unreinforced alloy materials, assuming that there is no damage created during extrusion from the elastic modulus data, the increase in yield stress can be related to strain hardening. In the composites, the yield stress depends on both the intrinsic flow stress of the matrix σ_o and the efficiency of the load transfer process, which is described by equation 6.15a), the Eshelby expression for the mean stresses in the matrix. For uniaxial tension, equation 6.18 can be slightly modified so that the applied stress in tension σ^A is related to the intrinsic flow stress of the matrix σ_o by

$$\sigma_o = \sigma^A - \left(\langle\sigma_3\rangle_M - \langle\sigma_1\rangle_M\right) = P\sigma^A \qquad \text{eq. (6.29)}$$

where the 3 axis is in the tensile direction and the 1 axis is in the transverse direction. In this case, because the mean stresses in the matrix are elastic up to the yield point so that the misfit strain in the

Eshelby cutting exercise can be related to σ^A by Hooke's Law, the right hand side of equation 6.26 can be expressed as a scalar P times the applied stress. Rearranging equation 6.26, the flow stress of the composite σ^A is related to the intrinsic flow stress of the matrix σ_o by

$$\sigma^A = \frac{\sigma_o}{P} \qquad \text{eq. (6.30)}$$

The parameter P is thus an expression for the efficiency of load transfer to the particles. Equation 6.30 predicts a strengthening effect of the reinforcement if it is stiffer than the matrix. The results show that, indeed, the undeformed composites are strengthened by the addition of reinforcement particles. The results in Table 4.2 also show that there is still a reinforcing effect due to the particles for the materials extruded to a strain of 0.5 before tensile testing. Thus, even though there is damage created in the composites at this strain, according to the stress-strain curves in Section 4.3, the load transfer process still operates at a high enough level so that there is a general strengthening of the composite. The situation seems different for the materials extruded to a strain of 1.0 prior to tensile testing. In this state, the 0.2% offset flow stress was not available for A356-20% SiC due to failure at low strain. In the A356-10% SiC, a 0.2% offset flow stress of 365 ± 10 MPa was recorded, compared to a corresponding value of 385 ± 10 MPa for the unreinforced A356 alloy. Comparison of the 6061 alloy and the composite 6061-20% CMS shows that there is no measurable strengthening effect due to the particles. Thus, since the damage level increases with prior strain during extrusion, the loss of strengthening can be attributed to a decreased load transfer efficiency in the damaged microstructure. The effect of heat treatment of the composites back to the original T4 temper after extrusion to a strain of 0.5 leads to the conclusion that there is still a strengthening effect of the reinforcement. This is in agreement with the results for as-extruded composites. The only composite that was heat treated back to the T4 temper after being extruded to a strain of 1.0 was 6061-20% CMS. Compared to the unreinforced 6061 matrix, the composite is still stronger. This result is indicative of the low levels of damage measured in 6061-20% CMS. Much of the reinforcement particles are intact in this composite after extrusion to a strain of 1.0,

so that upon tensile loading, load can be shed from the matrix efficiently. However, this result seems to contradict the observation of no measurable strengthening in the as-extruded composite. This may be explained by examining the work hardening characteristics of the 6061 matrix. From the data in Table 4.2 for this alloy, the alloy is strongly strain hardened in the strain interval of 0.5 to 1.0. For extrusion in the strain interval, the composite strength remains essentially unchanged. From figure 4.22, it is seen that this plastic strain increment by extrusion creates approximately a 1% increase in the damage level. It is expected that this small change in damage level will not change the load transfer process appreciably. Rather, the absence of strengthening for the same increment in strain by extrusion may be an indication of the saturation of the intrinsic matrix flow stress σ_o in equation 6.30. Thus, the apparent lack of strengthening in 6061-20% CMS compared to unreinforced 6061 may be due to a much slower rate of strain hardening in the alloy. The work hardening characteristics of these materials will be discussed in more detail later.

To summarize, extruding the composites raises their flow stress in all cases. The increase is due in large part to the strain hardening of the matrix, from the data for the unreinforced matrix alloys. It was also found that the composites were stronger in tension than the matrix materials in the undeformed state and after extrusion to a strain of 0.5. No measurable strengthening was found in the composites extruded to a strain of 1.0 before tensile testing, as compared to the matrix materials extruded to the same strain. This may be due to a decrease in load transfer efficiency in the damaged A356-10% SiC and 6061-20% CMS. However, there is evidence from data for heat-treated 6061-20% CMS that this effect may be due in part to a saturation of the intrinsic matrix flow stress in 6061.

The strain at which the saturation of the intrinsic matrix flow strength will occur depends on the work hardening rate of the material. As there are implications for this saturation stress for the strength of the composites tested in the present study, it is of use to examine the work hardening rate

from the tensile tests. It is also of worth to examine the effect of prior strain by extrusion on the work hardening rate.

As discussed in Section 6.2, the Eshelby analysis for the loading of a particle by a remote applied plastic strain predicts that load is transferred strongly to stiff particles. This is only true if no plastic relaxation events occur locally. Therefore, because of this strong transfer of load, the model predicts higher initial work hardening rates in composites, as compared to the unreinforced matrix. This is verified by the experimental data in this work. If the work hardening rate in tension is examined at the 0.2% offset flow stress in the undeformed composites and matrix materials, it is found that in all cases, the composites have higher initial work hardening rates. However, the situation is reversed at higher plastic strains, where the unreinforced alloy exhibit higher work hardening rate than the composites. This has been observed previously (Kiser et al., 1996) and the lower hardening rates of the composites are thought to be caused by damage in the reinforcements. It has been found in the literature (Corbin and Wilkinson, 1994) that the work hardening rate of A356-10% SiC and A356-20% SiC in compression is higher than in tension. This is an indication of the link between work hardening and damage, since the rate of damage accumulation in compression is expected to be lower than the corresponding value in tension for the same applied strain. This behavior is expected in light of the effects of stress state and hydrostatic pressure on damage, as outlined in Section 6.1.

Further, the experimental results show that the tensile work hardening rates of composites after extrusion are lower than the work hardening rates in the undeformed composites. This behavior may be explained by two effects, the strain hardening of the matrix and the damage accumulation in the microstructure during extrusion. An analysis of damage in MMCs (Kiser et al., 1996) relates the net work hardening rate $\frac{d\bar{\sigma}}{d\varepsilon}$ to damage ρ in the following expression

$$\frac{d\bar{\sigma}}{d\varepsilon} = \frac{d\sigma_i}{d\varepsilon} - \rho\left(\frac{d\sigma_i}{d\varepsilon} - \frac{d\sigma_c}{d\varepsilon}\right) - \frac{d\rho}{d\varepsilon}(\sigma_i - \sigma_c) \qquad \text{eq. (6.31)}$$

where the subscripts i and c refer to intact and cracked cells in the FEM analysis. This analysis predicts a positive net hardening rate for an MMC that does not become damaged with strain. For a damaging microstructure, the net hardening rate will decrease proportionally to the level of damage and to the rate of damage accumulation. The effect of the rate of damage accumulation was verified by introducing over 50% damage into the composite microstructure in the T4 temper, heat-treating to the T6 temper and then testing in tension. Compared to the undamaged composite in the T6 temper, they found a higher work hardening rate in the damaged material at plastic strains above about 0.008. At these higher strains, introduction of a large amount of damage into the microstructure before testing reduced the last term in equation 6.31, thus increasing the net hardening rate. This net hardening occurs even though the damage level itself is very high. In the present work, damage was introduced into the composite microstructure via the extrusion process. When the composite was tested in tension after extrusion without heat treating, a lower hardening rate was observed, as compared to the intact composite. From equation 6.31, this can be attributed to a decrease in the first term due to the work hardening of the matrix material and an increase in the second term due to the level of damage. When the composites were heat treated back to the original T4 temper after extrusion and then tested in tension, the hardening rate was found to increase with respect to the as-extruded composite. However, contrary to the results of Kiser et al., the work hardening rate did not exceed its counterpart for the undamaged composite. The reason for this may be due to the amount of damage introduced in A356-10% SiC and 6061-20% CMS by extrusion. In all of these cases, from figure 4.2, no more than 5% damage was introduced into the microstructure of these composites by extrusion. This is an order of magnitude less than the amount of prior damage in the work of Kiser et al. From figure 4.21, there is a high rate of damage as a function of applied plastic strain in 6061-20% CMS in tension and the damage level quickly exceeds 5%. Thus, it

is thought that the small amount of damage introduced in the microstructure by extrusion did not affect the damage rate in equation 6.31 as strongly as the experiment by Kiser et al.

The work hardening rate discussed above describes a material's ability to resist geometrical tensile instabilities. The criterion for the tensile instabilities is given by the Considere criterion of equation 6.28. The criterion is derived for the assumption of constant volume plastic flow. However, from the density measurements on 6061-20% CMS in Section 4.3, it was found that the assumption of constancy of volume is not obeyed. Damage is created in the composites in the form of voids, thus decreasing the density. From the results of figure 4.19 on tensile specimens with hourglass shaped cross sections, the volume was found to increase with strain. It is thus of worth to derive the Considere criterion for a damaging material. The point of instability is defined where

$$dP = 0 \qquad \text{eq. (6.32)}$$

Thus, for an infinitesimal increment in strain, there is no increase in the load needed to continue plastic flow. At this point, any external constriction will propagate. The load is related simply to the applied tensile stress by

$$P = \sigma A \qquad \text{eq. (6.33)}$$

so that, combining equation 6.32 and equation 6.33

$$dP = Ad\sigma + \sigma dA \qquad \text{eq. (6.34)}$$

Solving for the stress σ and taking reciprocals of equation 6.34

$$\frac{1}{\sigma} = \frac{-dA}{Ad\sigma} \qquad \text{eq. (6.35)}$$

The volume V of the specimen is now defined as V=AL, where A is the cross sectional area and L is the length. Thus, the change in volume dV is given by

$$dV = AdL + LdA \qquad \text{eq. (6.36)}$$

Dividing equation 6.36 by the total volume V=AL, we obtain

$$\frac{dV}{V} = \frac{dL}{L} + \frac{dA}{A} \qquad \text{eq. (6.37)}$$

If the true strain in the sample is defined by the longitudinal strain as $d\varepsilon = dL/L$ and if equation 6.37 is rearranged to solve for $-dA/A$, the following expression is obtained

$$\frac{-dA}{A} = d\varepsilon - \frac{dV}{V} \qquad \text{eq. (6.38)}$$

Substituting equation 6.39 into equation 6.35,

$$\frac{1}{\sigma} = \frac{\frac{-dV}{V} + d\varepsilon}{d\sigma} = -\frac{d\ln V}{d\sigma} + \frac{d\varepsilon}{d\sigma} \qquad \text{eq. (6.39)}$$

where $dV/V = d\ln V$. Rearranging equation 6.40 to solve for $d\varepsilon/d\sigma$

$$\frac{d\varepsilon}{d\sigma} = \frac{1}{\sigma} + \frac{d\ln V}{d\sigma} = \frac{1}{\sigma}\left[1 + \frac{\sigma d\ln V}{d\sigma}\right] = \frac{1}{\sigma}\left[1 + \frac{d\ln V}{d\ln\sigma}\right] \qquad \text{eq.(6.40)}$$

where $d\sigma/\sigma = d\ln\sigma$. Taking the reciprocal of equation 6.40, the Considere criterion for a dilatational material is obtained

$$\frac{d\sigma}{d\varepsilon} = \frac{\sigma}{\left[1 + \left(\frac{d\ln V}{d\ln\sigma}\right)_{dP=0}\right]} \qquad \text{eq. (6.41)}$$

The method used to obtain equation 6.41 is similar to the procedure developed in the literature (Hart, 1967 and Semiatin and Jonas, 1984) for strain-rate sensitive plastic instabilities. However, in the literature, the total volume of the deforming body is assumed to remain constant. From equation 6.41, the differential of volume with applied stress must be estimated at the load maximum defining the instability. If the material is not damaging, which means that it is not increasing in volume, the differential in the denominator of equation 6.41 is zero, and the original form defined by equation 6.28 is returned. It is to be noted for this model that the volumetric expansion is assumed to have no effect on the homogeneity of plastic flow in the material. In other words, the local flow of the material near a void is assumed to be analogous to the macroscopic behavior.

The Considere criterion for a damaging material given by equation 6.41 predicts that the work hardening rate and flow stress will not be equal at the point of tensile instability. For a volume increase with increasing stress, the differential in equation 6.41 will be positive and so, at the instability, the work hardening rate is predicted to be lower than the flow stress. The model also predicts that the relationship between the applied stress and work hardening rate at the instability depends on the rate of damage accumulation (or dilatation) with stress at this point and not on the level of damage. In addition, equation 6.41 predicts, as does the original form of the criterion, that a drop in the work hardening rate of the material as a function of strain will cause the instability point to be reached at lower tensile strains.

This latter prediction has been verified experimentally. As discussed previously, it was found that the work hardening rate of all the composites that were extruded prior to tensile testing dropped below the corresponding work hardening rate for the previously undeformed material. From Table 4.3, it is found that extrusion prior to tensile testing reduced the strain at which the instability occurred.

It is worth examining other predictions of the Considere criterion for a damaging material defined by equation 6.41. The first is that the work hardening rate will not be equal to the flow stress at the point of tensile instability. A comparison of the results for the flow stress of the pMMCs at the instability, given by Table 4.4, and the results for the work hardening rate of the composite at the instability, given by Table 4.5, confirms this prediction. This finding is in contradiction to some observation of tensile instabilities in Al-SiC composites which validate the original form of the Considere criterion (Gonzalez and Llorca, 1996). In this aforementioned work, it was found that the flow stress matched the work hardening rate at the plastic instability. No estimates were given for the measurement error in the tests, nor of the procedure followed for the tensile testing. For the undeformed composites tested in the present study, the flow stress and work hardening rate at the point of tensile

instability were close, but from the error estimates, there was a measurable difference. For all of the composites extruded before tensile testing, the difference between the flow stress and work hardening rate at the tensile instability was large. Further, some literature results (Kiser et al., 1996) support the observations in the present work that the flow stress and work hardening rate do not coincide at the tensile instability for damaging materials.

Equation 6.41 predicts that, for a dilatational material, the flow stress will be larger than the rate of work hardening at the tensile instability. From the results in Table 4.3 and Table 4.4, the reverse was observed. However, a closer look was taken at how the properties in these tables were calculated. The data acquired in the tensile tests consisted of the load on the sample as well as the displacement of the gauge length measured by an extensometer. Thus, increments in strain were measured by the change in length of the specimen. The problem is in the stress measurement. It is common practice in tensile testing of materials to calculate the stress from the load using the strain defined above and assuming constancy of volume during plastic flow. This is how the data in Table 4.3 and Table 4.4 was compiled. However, this measurement is in error for a material such as the composites in the present study that expand during deformation. Thus, to verify the predictions of equations 6.41, it is important to measure the stress as the load divided by the cross sectional area of the specimen perpendicular to it.

This type of measurement was done during the tensile testing of 6061-20% CMS specimens with a tapered gauge section in an hourglass shape. The cross section was monitored by taking photographs of the specimen at regular intervals during the test. The true stress and true strain data for this test is shown in figure 4.17. In this experiment, the strain ε_D was measured as

$$\varepsilon_D = \ln\left(\frac{A_o}{A}\right) \qquad \text{eq. (6.42)}$$

To convert this to the longitudinal strain without assuming constancy of volume, equation 6.35 is integrated, giving

$$\varepsilon = \ln\left(\frac{A_o}{A}\right) + \ln\left(\frac{V}{V_o}\right) \qquad \text{eq. (6.43)}$$

Using the measurements of V/V_o made on the sample, from figure 4.19, the strains ε_D were converted to longitudinal strain ε. The resulting true stress true strain data is plotted on figure 6.10, along with a best fitting line of the form $\sigma = A + B\varepsilon^N$ for the data. Using this correlation, the stress-strain curve for a specimen with a standard section size in Section 4.3 was corrected to match the data for the hourglass specimen. The result is shown in figure 6.11. Using the corrected data from figure 6.11, it was found that the flow stress and work hardening rate at the tensile instability were 315 ± 10 MPa and 315 ± 50 MPa respectively. Without correction, the flow stress and work hardening rate at the tensile instability were 345 ± 10 MPa and 515 ± 50 MPa respectively. Thus, the correction applied to the data lowers the work hardening rate at the tensile instability so that the stress and work hardening rate are within experimental error. Further errors are introduced by this procedure due to the approximate nature of the corrections applied to the stress-strain curve for 6061-20% CMS.

Thus, due to the aforementioned errors, it is impossible with the present results to validate the applicability of the Considere criterion or the modified Considere criterion for previously undeformed 6061-20% CMS. However, it is of interest to estimate the magnitude of $(d\ln V/d\ln\sigma)_{dP=0}$ in equation 6.41, in order to gauge its possible effect on the instability data in the present study. From the density measurements of Section 4.3, it was found that a 0.42 ± 0.05 % increase in volume occurred at the tensile instability for 6061-20% CMS. This corresponds to a value of 1.0042 for V/V_o. From a best fit exponential line to the data in figure 4.19, it was found that this volume change occurred at a true stress of about 330 MPa. Re-plotting the data in figure 4.19 as $\ln(V/V_o)$ versus $\ln\sigma$, it was found that

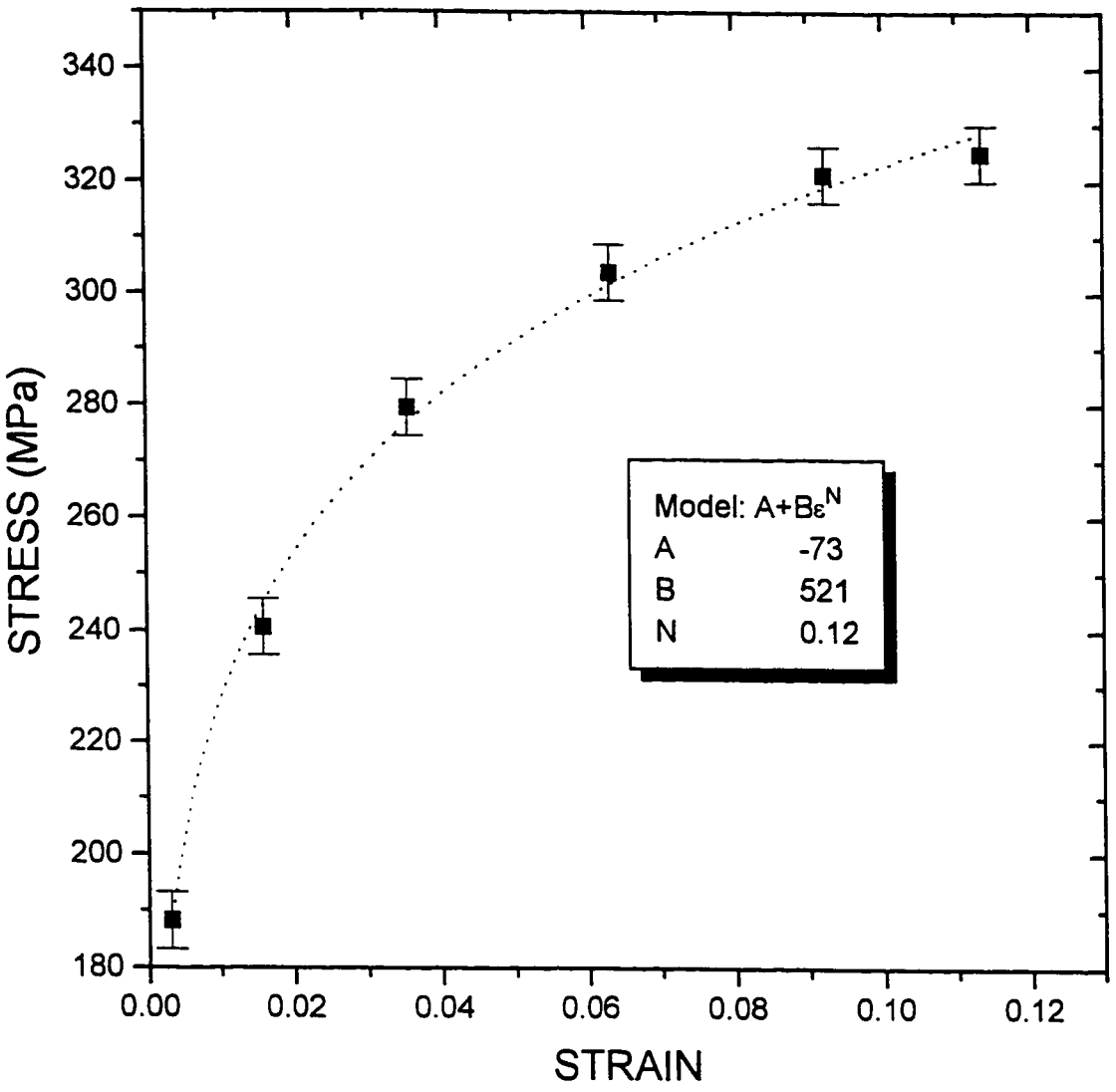

Figure 6.10 Plot of the data corrected for dilatation for stress and strain in the tensile hourglass shaped specimen made out of 6061-20% CMS.

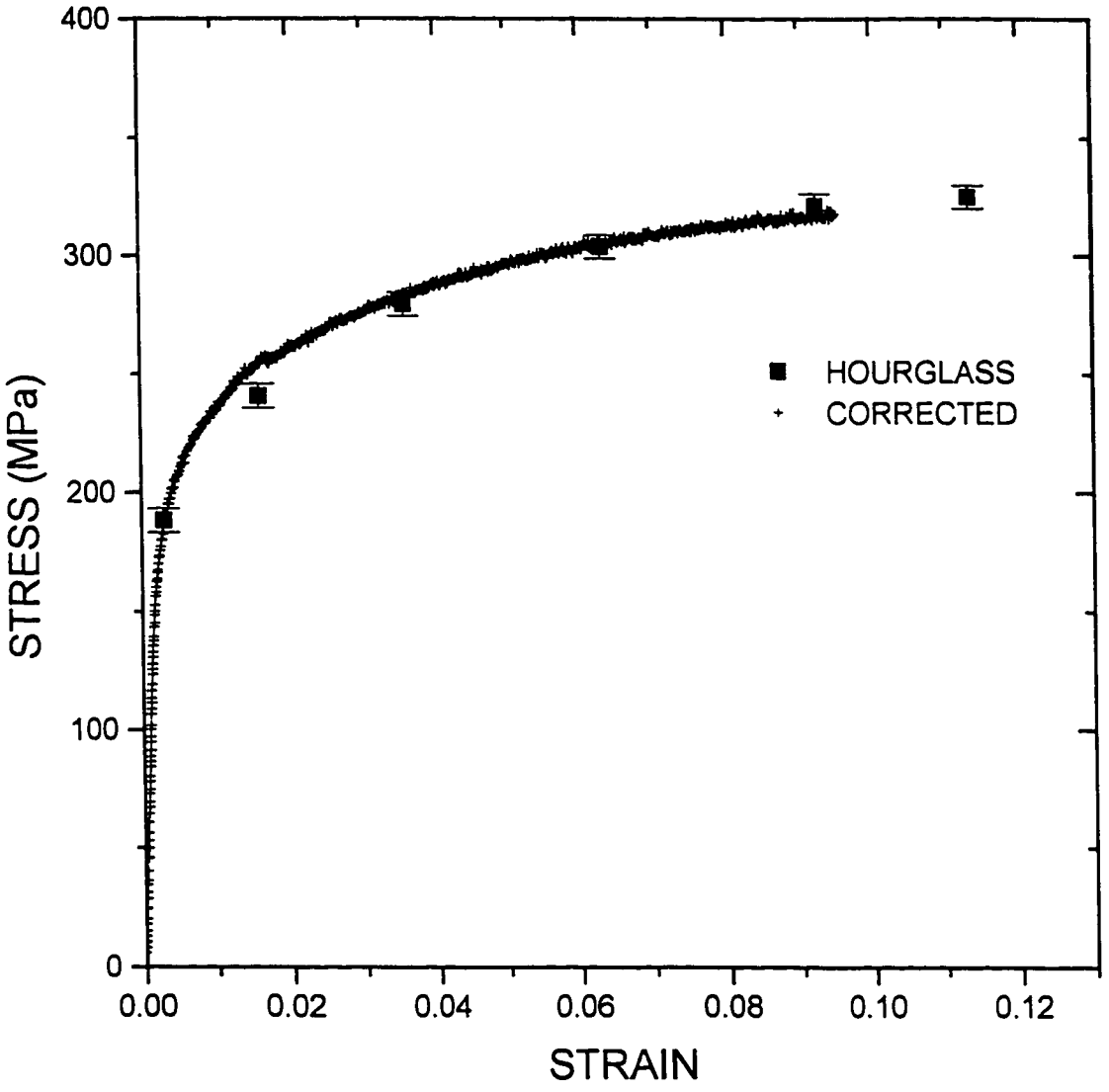

Figure 6.11 Stress-strain curve for 6061-20% CMS after correction for dilatation.

$$\left(\frac{d\ln\left(\frac{V}{V_o}\right)}{d\ln\sigma}\right)_{\dot{\varepsilon}_p=0} = \left(\frac{d\ln V}{d\ln\sigma}\right)_{\dot{\varepsilon}_p=0} = 0.055 \qquad \text{eq. (6.44)}$$

Thus, from equation 6.44, it is apparent that, at least for the case of 6061-20% CMS, the correction to the flow stress in equation 6.41 will be of the order of 6%.

It is unlikely from the results above that the correction to the flow stress and the correction for dilatational flow to the instability criterion would reconcile the large difference between the flow stress and work hardening rate at the tensile instability for all of the composites that were extruded prior to testing. In some cases, the flow stress and work hardening rate at the tensile instability differ by several hundred MPa and neither the Considere criterion nor the modification derived in the present work would adequately describe the conditions at this point. It is thus possible that instability in these materials is materials-based as opposed to the geometrically based instabilities described by equation 6.28 and equation 6.41. There is some evidence from Section 6.3.1 that the unreinforced and previously work hardened 6061 and A356 alloys do not become plastically unstable due to geometrical considerations, but due to local materials based instabilities. The reason for this behavior is possibly due to a saturation of the flow stress of 6061 and A356 by extrusion. If the extrusion process had a similar effect on the matrix materials of the composites, then these would also be prone to local materials based instabilities.

6.4 FIBRE DISTRIBUTION EFFECTS IN MODEL MMCs

In this section, the results of the plane strain compression tests on model Cu-W composites will be examined for information they might yield about the effect of reinforcement distribution in MMCs and the processes leading up to damage events. The various fibre distributions examined in this work will be discussed in order of complexity from 1 fibre composites to composites with multi-fibre arrays.

In order to describe the effects of distribution on the local plastic flow in MMCs, it is important to understand the effect of one fibre alone. The strain maps shown in figure 4.32 and figure 4.33 illustrate this effect. The observations clearly show that the strain distribution in Cu around a W fibre is very inhomogenous in nature. The presence of the fibre generated higher local strains than the macroscopically imposed strain. This has implications for the load transfer process. The assumption that the local plastic strain applied to the fibre is equal to the global strain breaks down. Local plastic relaxation occurs around the reinforcement so that continuum models such as the Eshelby model for load transfer cease to be applicable. Work on one-fibre Cu-W composites has been reported previously (Poole, 1993) and supports the evidence for inhomogenous flow around W and a decrease in load transfer efficiency due to plastic relaxation around the fibre. Poole's experimental and theoretical results by FEM show the same general features as the ones in the present work, both in terms of the magnitude and location of strain near the W fibers.

In light of this general agreement between the experimental strain maps for one fibre composites and the FEM strain results, the FEM results for the stress distributions can be examined. These numerical results can be used to gain insight into the load transfer process in the composite and the conditions which lead up to damage. It was found, from these stress distributions (Poole, 1993), that the stress generated in the W fibre in the direction of compression was of the same order as the corresponding stress in the matrix. Thus, for transverse compressive loading in plane strain, the load transfer efficiency is far below what is predicted by the Eshelby analysis of equation 6.15a) and equation 6.15b). The results from these stress fields also shed light into the observed damage events in the composites. In the present work, it was found that damage occurred in the form of decohesion at the fibre/matrix interface and that it initiated at 90° to the compression axis. This is consistent with Poole's FEM stress fields after 30% compression, where there is a maximum in tensile stress accross the

interface and a maximum in tensile hydrostatic pressure 90° to the axis of compression. It is reasonable to assume, given the dilatational nature of the debonding process, that the stress accross the interface and the hydrostatic pressure would be determining factors. Considering that both have their maximum tensile value where damage was observed experimentally, the damage can be related to the local stress state generated by the plastic flow around the fibre.

Having now some idea of the plastic flow process and stress state near one W fibre, changes in this pattern due to a second fibre can be examined. From the strain maps generated for the composites with 2 fibers, there is a clear difference in the pattern of flow compared to a one fibre composite. The strain pattern is also strongly dependent on the orientation of the 2 fibers with the compression axis. Generally, the distribution of the fibers to the compression axis affects the ease of penetration of plastic flow. The 0° and 90° arrangements create larger zones of lower than average strain than in the 1 fibre arrangement whereas the 45° arrangement has very few regions of lower than average strain. Reasons for this may be found. It is known that the macroscopic flow direction in compression experiments is 45° to the compression axis. The flow of dislocations occurs by shear, and the maximum component of shear is at 45° to the loading axis. Thus, the constraint exerted by the fibers depends on their orientation with respect to the maximum shear direction. In this way, it can be seen from figure 4.35 that there is an easy direction of flow along the direction of maximum shear for the 2 fibre arrangement at 45° to the compression axis. It was found experimentally (Poole, 1993) for arrays of W fibers in Cu that a triangular arrangement of fibers resulted in a more homogenous distribution of strain than a square packing of fibers. This result seems to parallel the observations for the 2 fibre arrangements. It was found by FEM analysis of the arrays considered by Poole that the triangular arrays shed load less efficiently to the fibers. Further, the experimental observations found more damage in the composite with square packing of fibers than for the triangular arrays for global deformation to the same strain. From these results, it is apparent that flow inhomogeneity, load transfer and damage are closely related

for transverse compressive loading in plane strain. Comparison of the present results for 2 fibre composites and literature results for arrays with various fibre distributions suggest that the ability of the fibers in constraining flow is related to the efficiency of impedance they offer to the development of macroscopic shear bands.

There is no published work on plastic transverse flow in two fibre composite arrangements and it is difficult to ascertain the difference between the present results and Poole's results for arrays. However, there seems to a similar trend of fibre distribution. The only known analysis of two fibre arrangements was by FEM for an elastic system (Lesne et al., 1995) in plane strain tension. The results are of limited use for comparison to the large plastic strains created during plane strain compression in this present study. Nevertheless, the study of the elastic system in the literature found that regions of higher stress than the global applied stress were created in the composites. It was also concluded that this anisotropy in the stress field would affect the onset of plastic flow and the operation of various damage modes. The importance of fibre distribution was found to depend on the relative stiffness of the fibre and matrix.

In comparison, there has been much more work on transverse flow in regular arrays of fibers in the literature. This work is thus related in a more or less direct fashion to the arrays tested in the present work. The most direct comparison can be made for the regular square array with an extra centered fibre, named the clustered array. There has been no published work on this exact distribution but much has been reported on square arrays (Poole, 1993, Adams, 1970, Hung and Kobayashi. 1992, Brockenbrough et. al., 1991 and Bohm et. al., 1993). A direct comparison between these published results and the strain map of figure 4.37 generated for a square arrangement of fibers away from the clustered region should be applicable. The influence of the extra fibre in the center should be small, according to Saint-Venant's principle. There seems to be general agreement for the strain distributions that evolve in composites

with square packing of fibers. The results are both experimental (Poole, 1993) and numerical by FEM (Hung and Kobayashi, 1992, Poole, 1992 and Brockenbrough et. al., 1991). In all of these, shear bands develop near the fibre/matrix interface at 45° to the compression axis. Also, extensive zones of low effective strain develop some distance away from the fibers, as shown in Figure 6.12. These are the same features observed on figure 4.37 and figure 4.39 for the square distribution of W in Cu-W.

The experimental results in this work can be compared most readily to Poole's FEM modeling since it considered explicitly the Cu-W system. In the present experimental work, the local volume fraction away from the cluster corresponded to 20% by volume of W. The numerical modeling for such a composite was reported by Poole, with the following conclusion for the efficiency of load transfer: the stresses in the fibers did result in a net strengthening effect, although the rate of hardening fell short of the Eshelby result given by equation 6.15a) and equation 6.15b). It was concluded that the load transfer in the transverse direction of the fibers was inefficient. The stress distribution generated by the FEM analysis also elucidates the observation of debonding in the composites at the fibre/matrix interface, 90° to the compression axis. The combination of radial stress and hydrostatic stress are at their maximum (tensile) value at this location, thus constituting the most dilatational stress state in the interfacial region. The effect of introducing a cluster in the square array of fibers can be gauged by comparing figure 4.37 and figure 4.38 which are the strain maps generated for locations far and close to the cluster respectively. The strain maps reveal the following differences: the low strain area is about 400 microns closer to the fibre near the cluster and the areas of very high strains above 40% are more limited near the cluster. This suggests that there is an effect of the extra fibre on the constraint to flow. It is difficult to conclude anything from the strain maps for the stress state that would result in this area, but it is reasonable to assume, considering the changes in the strain distribution, that it would be different than what has been calculated in Poole's work for square arrays.

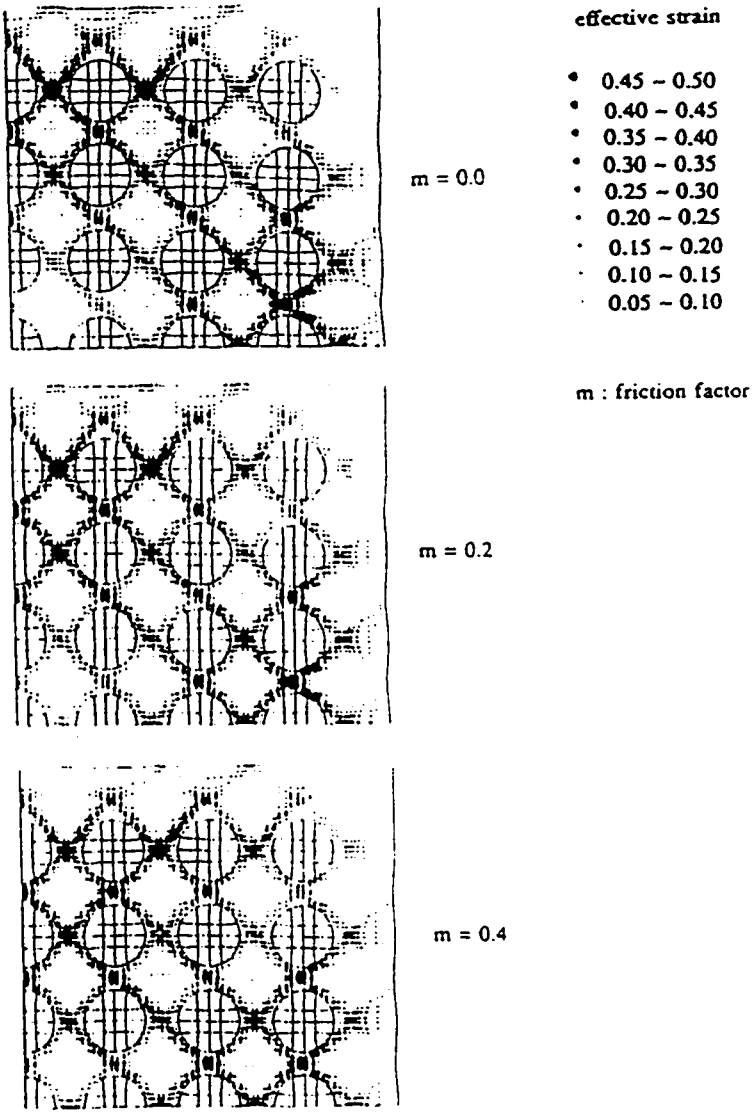

Figure 6.12 Numerical analysis for the pattern of flow for a square arrangement of fibres. (from Hung and Kobayashi, 1992)

The effect of a gradual increase in local volume fraction is another fibre distribution effect that was investigated in this study. The graded sample deformed to a strain of 13.9% was analyzed for local strain distribution in two areas of the graded composite. The resulting maps in a high local volume fraction area and a lower local volume fraction area are shown in figure 4.40 and figure 4.39 respectively. In the area of higher local volume fraction, the main observations were that the strain pattern was more inhomogenous than in the area of lower local volume fraction. There is a large region near the fibre with strains close to the globally imposed strain in the high local volume fraction region. The peak strain in the area of high local volume fraction was above 60%, whereas in the low local volume fraction region, the peak strain did not exceed 50%. However, the area of low strain from figure 4.40 suggests that, on the whole, the average strain in the matrix is lower in the high local volume fraction region than in the region of low local volume fraction. Although this would need to be verified experimentally or by modeling, this suggests that significant differences in the stress state of the composite would exist in the graded composite, and that this difference would vary with the local volume fraction of the reinforcement. This would then have repercussions on the load transfer process and the operation of damage mechanisms.

In summary, the investigation of reinforcement distribution effects in model composites has shown that stiff reinforcements in a plastic matrix inhomogenously distributes the amount of strain locally. The added constraint of one or many fibers in an array has also been shown to alter the flow patterns in the matrix. The effect of the orientation of the fibers with respect to the axis of loading in the 2 fibre composites, as well as the effect of a local cluster in an arrayed fibre composite and the effect of a graded reinforcement volume fraction have been discussed. The inhomogenous flow patterns have been related, when possible, to numerical simulations to solve for the stress distributions. These simulations yield quantitative information about the efficiency of load transfer from the matrix to the

fibre. From the distribution and magnitude of the stresses generated, an understanding of observed location and mechanism of damage was achieved.

6.5 LOAD TRANSFER IN Cu-SAPPHIRE

Plane strain compression tests were conducted on a model Cu-sapphire composite in order to make direct measurements of the stress state in the fibre as a function of the global applied plastic strain on the composite. The intent of these experiments was to get a measure of the load transfer process during plastic flow of MMCs. For ease of measurement, the residual stresses in sapphire were measured after plastic straining.

The results of these tests are shown in Table 4.8, in the form of the deviatoric stress tensor and hydrostatic pressure in the sapphire in the as-fabricated condition and after imposed strains of 0.6% and 1.2%. The results show that the residual stresses are modest in magnitude. This indicates that significant relaxation of the elastic stresses transferred to the fibers occurs upon unloading. This is a reflection of the very low flow stress of the matrix in the as-fabricated composite. For example, from the plane strain compression test, the maximum engineering stress applied to the composite was about 80 MPa after 0.6% strain and approximately 105 MPa after 1.2% strain.

The results indicate a build up of the stresses in the sapphire with imposed global plastic strain. The build up seems to occur on the basal plane of the sapphire, in the crystallographic directions 1 and 2. No variation of the residual stress along the c-axis (direction 3) of the fibre was measured. The sapphire basal plane in these experiments corresponds to the transverse direction of the composite. Since the plane strain compression experiments were designed to confine the plastic flow to the transverse

plane of the composite, it is to be expected that the load transfer would only occur on the basal plane of the sapphire.

The orientation of the sapphire fibre basal plane with the compression axis is not known. Therefore it is not possible to resolve the crystallographic stresses σ'_{11} and σ'_{22} on the orthogonal basis defined by the compression axis. Nevertheless, it is clear from the results that σ'_{11} is becoming more compressive with strain and that σ'_{22} is becoming more tensile with strain. FEM analyses (Poole, 1994) on isolated fibers predict compressive stresses in the fibers along the compression axis and tensile stresses perpendicular to it. This suggests that the crystallographic direction 1 in closer to the compression axis than direction 2 and that the results are consistent with the theoretical predictions.

The other component of the stress tensor to be considered is the hydrostatic component of the residual stress. The results suggest that plastic flow of the matrix surrounding the sapphire results in an increase in compressive hydrostatic pressure. In the as-fabricated composite, the hydrostatic stress is measured to be close to zero and builds up to a pressure of -25 ± 17 MPa (compressive) after 0.6% strain. The results also suggest that the residual pressure remains essentially unchanged by an additional plastic strain of 0.6%. These compressive pressures have been predicted by FEM (Poole, 1993) although it is not known at what rate they are predicted to build up with applied plastic strain of the composite. In any case, this evidence tends to indicate general agreement between the experimental results and numerical analyses.

As was reported in Section 4.7, the sapphire fibre fractured in the plane strain compression test to 1.8% strain. It is of worth to examine the possible reasons for this early fracture. By visual inspection of the transparent sapphire, it was observed that the fracture was in the transverse direction of the fibre. It was thus thought to estimate the maximum transverse stress on the fibre from the plane strain

compression data and the form of the residual stress tensor in the fibers. From the plane strain compression test, the highest applied engineering stress was approximately 130 MPa. If it is assumed that the load transfer efficiency for this composite is modest, we can imagine that the compressive stress in the fibre along the compression axis would be of the order of 300 MPa. Using the ratio of the residual stresses after 1.2% strain, $\sigma'_{11}/\sigma'_{22}$, we can estimate the highest transverse tensile stress as 200 MPa. From the literature (Kelly and MacMillan, 1986), a reasonable estimate for the fracture toughness K_{IC} of sapphire (Al_2O_3) is 4 MPa$\sqrt{m}$. Using the following relation between K_{IC} , the applied stress σ and the flaw size a

$$K_{ic} = \sigma\sqrt{\pi a} \qquad \text{eq. (6.45)}$$

we can estimate the flaw size as being of the order of 100 μm. As the surface of the sapphire fibre has a rough finish obtained by grinding, a 100 μm flaw along the length of the fibre is not out of the question. This rough estimate might thus explain the fracture of the sapphire fibers at low strains.

To summarize, it was found that the experimental residual stress measurements in a sapphire fibre were consistent with some theoretical and numerical predictions for load transfer in plane strain and that the transverse failure of the sapphire at low applied plastic strain could be attributed to surface flaws in the fibers.

CHAPTER 7

CONCLUSIONS

In this concluding chapter, a summary of the main findings of this thesis will be given. The salient features of the work on hydrostatic extrusion of MMCs, of plane strain compression of model MMCs and of scale effects in MMCs will be outlined separately. The final objective of this chapter will be to put the results of these separate investigations into the broader context of how the central issue of damage accumulation in MMCs is intimately related to the development of processing routes, the optimal design of microstructures and the spatial distribution of the reinforcement phase. This interlinking for the processing and design of MMCs to satisfy specific functional requirements will be highlighted.

As outlined in the introductory chapter to the present work, there were four main objectives for the research related to the hydrostatic extrusion of MMCs and these will be addressed in turn. The first goal of this investigation was to measure the damage evolution in hydrostatically extruded MMCs. It was found that damage occurred as reinforcement cracking in all of the composites that were hydrostatically extruded. The rate of damage accumulation in all three particulate systems investigated was found to vary linearly with applied strain. The relative rate of damage accumulation in the composite was found to be dependent on the volume fraction and particularly on the shape of the reinforcement in the MMCs.

It was shown that the behavior in hydrostatic extrusion can be rationalized by consideration of the effect of various parameters, and most importantly the hydrostatic component of the stress state, on the initiation and growth of damage. A slip-line field analysis was adopted based on the original work of Thomason (1969/70) to develop maps of the hydrostatic pressure in the extrusion dies. The magnitude

and distribution of hydrostatic pressure in the extrusion dies were found to depend on both the reduction and die angle and was in accord with the experimental observations. The estimates of hydrostatic pressure obtained from this analysis were used in conjunction with a simple criterion for the stress state required to suppress damage in the MMC microstructures during hydrostatic extrusion.

To account for the observation of varying rates of damage accumulation with imposed plastic strain by extrusion for the three particulate composite systems tested in this work, a micro-mechanical description of the response of MMCs during plastic flow was developed. This analysis was based on an Eshelby model of plastically induced stresses modified by an empirical correction for local plastic relaxations near the reinforcements and for non-dilute volume fractions. It was found, for the distributions of particles in the present work, that this model could explain the observed linear relationship between damage in the pMMCs and applied plastic strain by extrusion. The influence of microstructural variables such as reinforcement size, shape and volume fraction on this model were examined and compared to the experimental observations.

The last objective of the work on the hydrostatic extrusion of MMCs was to study the tensile response of the particulate reinforced composites subsequent to the extrusion process and to compare this response to the previously undeformed materials. It was found that the tensile mechanical properties of the MMCs could be linked to changes effected by the hydrostatic extrusion in both the matrix and reinforcement phase. The composite stiffness was found to be lowered by the damage introduced into the microstructure. The 0.2% offset flow stress of the MMCs was raised as a result of the extrusion process in all cases. This was attributed in large part to the strain hardening of the matrix materials during extrusion. Further, a loss of strengthening in the MMCs extruded to a strain of 1.0, as compared to the unreinforced matrix materials, was linked to the effect of damage on the load transfer efficiency and to a saturation of the matrix flow stress. As predicted by a model in the literature (Kiser and Zok, 1996),

these two effects and the effect of the rate of damage accumulation also accounted for the observed drop in the work hardening rates of the previously extruded composite materials. This drop in tensile work hardening rate of the previously extruded MMCs, as well as the increase in flow stress was found to lower the amount of tensile strain required to reach the point of plastic instability of the composites. It was also found that the prediction of the Considere criterion for the tensile instability was not met. In light of the observation of density changes in 6061-20% CMS, the Considere criterion was modified to account for a damaging microstructure. For the previously undeformed MMCs, comparison of the experimental results with the predictions of the modified Considere criterion were inconclusive, due to experimental error. However, since the modified Considere criterion clearly did not apply for the pMMCs tested in tension subsequent to extrusion, the tensile instabilities were thought to be based on materials behavior as opposed to the geometrical considerations of the Considere criterion and its modification in the present work. This conclusion is based on evidence for the saturation of the matrix flow stresses during the hydrostatic extrusion process.

In addition to the work on the hydrostatic extrusion of MMCs, the present thesis was concerned with two topics on the effect of plane strain plastic flow in model composite systems and the first was an investigation of spatial distribution effects transverse to W fibers in Cu-W MMCs. The patterns of flow in plane strain compression were presented as maps of equivalent strain for various fibre distributions. The general conclusion for the effect of the fibers was that the pattern of flow in the Cu was inhomogenous, both in terms of the magnitude and distributions of strain. Further, it was found that both the strain magnification near the Cu/W interface and the amount of plastic constraint to the direction of macroscopic flow depended on the spatial arrangement of the fibers. The results of the plane strain compression tests were related, where possible, to numerical simulations solving for the stress state in the deforming MMCs. From this analysis, it was possible to link the location of damage, in the form

of interfacial decohesion in these experiments, to the position of high tensile hydrostatic stresses and high axial stresses accross the interface.

To complement the results of the work on fibre distribution effects, an optical method for measuring internal stresses in chromium doped sapphire was used to monitor the residual stresses in a one-fibre Cu-sapphire composite as a function of applied plastic strain in plane strain deformation transverse to the sapphire fibre. The salient observations of this research were that there was a build up of internal stresses with increasing applied plastic strain and that this build up led to fracture of the sapphire at small strains. The build up of internal stresses was found to be consistent with predictions from load transfer analyses and the transverse fracture of the sapphire was thought to be consistent with simple calculations for the fracture stress due to surface flaws.

The relation between scale and strength in materials was examined in more detail in a general analysis of scale effects in MMCs. Scale dependent bounds for the strength of MMCs were developed using scaling laws for the metal matrices and for the strong reinforcements. These limits on strength were presented as scale dependent composite design charts. The results of this analysis served to illustrate the importance of scale parameters for MMC design. The scale dependent composite design charts further emphasize the importance of finding new processing routes capable of producing MMCs on a fine scale.

To conclude, the main findings of the present investigation have demonstrated how damage in MMCs links together issues of process design, of microstructural optimization and of the resultant mechanical properties of the composite. In order to exploit the potentially advantageous properties of MMCs, they must be produced in a way which suppresses or limits damage. Careful choices must be made for the fabrication of the MMCs. The way in which the constituents are produced is important, in

terms of both microstructural parameters such as size and shape and the flaws produced in them during fabrication. The primary MMC fabrication process must be chosen carefully to incorporate the two or more phases in such a way that good interfacial bonding occurs. Attention must also be paid to the volume fraction of reinforcement that should be added to the metal matrix for optimum resultant properties of the MMC, as well as the distribution of reinforcement in the microstructure. These considerations will be especially important if subsequent solid state processing steps involving large deformations are needed to produce a final component. It is clear from this work that, along with the microstructural variables of size, shape, volume fraction and reinforcement distribution, the solid state process parameters will also have to be optimized to produce undamaged MMCs. Of special interest for this choice is the effect of the process parameters on the hydrostatic pressures created during the deformation of the MMCs. Thus, the design of an MMC component to satisfy specific functional requirements will involve optimization of the composite microstructure and the processing steps to produce the material.

APPENDIX A

MAPLE™ PROGRAM TO GENERATE SLIP- LINE FIELDS

```
> Digits:=20;
> r:=1;
> nm:=`slf`;
> an:=`90`;
> ex:=`.txt`;
> fnam:=cat(nm,an,ex);
> of:=fopen(fnam,WRITE);
> fprintf(of,`%c %c %c %c \n`,`M`,`N`,`X`,`Y`);
> for n from 0 by 1 while n<=90 do
> oang:=n;convert(oang,float);
> roang:=evalf(oang*evalf(Pi)/180);
> for f from 0 by 1 while f<=90 do
> ang:=f;convert(ang,float);
> rang:=evalf(ang*evalf(Pi)/180);
> if n=0 then
> y:=evalf(-r*(1-cos(rang)));
> x:=evalf(r*sin(rang));
> fprintf(of,`%d %d %f %f \n`,n,f,x,y);
> elif f=0 then
> y:=evalf(r*sin(roang));
> x:=evalf(-r*(1-cos(roang)));
> fprintf(of,`%d %d %f %f \n`,n,f,x,y);
> else
> phi1:=evalf(-rang+roang+ .*evalf(Pi)/180);phi2:=evalf(-rang+roang);
> delx:=evalf(Int(cos(phi)*(-r*(BesselI(0,2*sqrt(abs((phi-roang)*roang)))+sqrt(abs(roang/(phi-
roang)))*BesselI(1,2*sqrt(abs((phi-roang)*roang))))),phi=phi1..phi2,10,_NCrule));
> dely:=evalf(Int(sin(phi)*(-r*(BesselI(0,2*sqrt(abs((phi-roang)*roang)))+sqrt(abs(roang/(phi-
roang)))*BesselI(1,2*sqrt(abs((phi-roang)*roang))))),phi=phi1..phi2,10,_NCrule));
> newx:=x+Re(delx);
> newy:=y+Re(dely);
> fprintf(of,`%d %d %f %f \n`,n,f,newx,newy);
> x:=newx;
> y:=newy;
> fi;
> od;
> od;
> fclose(of);
```

APPENDIX B

FORTRAN SOURCE CODE FOR ANALYSIS OF DEFORMED GRIDS

```
C   PROGRAM GRDAN
    INTEGER R,C
    REAL CF,GS,GA,AA
    DIMENSION X(100,100),Y(100,100),ST(100,100)
    OPEN(UNIT=12,FILE='INPUT.DAT')
    OPEN(UNIT=13,FILE='OUTPUT.DAT')
    REWIND(12)
    WRITE(*,*)'# OF ROWS,# OF COLUMS,CONV. FACT.?'
    READ(*,*) R,C,CF
    WRITE(*,*)'GRID SIZE, ANGLE OF GRID,ANGLE TO COMP. AXIS?'
    READ(*,*) GS,GA,AA
    DO 200 J=1,C
    DO 100 I=1,R
    READ(12,*) Y(I,J),X(I,J)
    X(I,J)=X(I,J)*CF
    Y(I,J)=Y(I,J)*CF
  100 CONTINUE
  200 CONTINUE
    DO 400 L=1,C-1
    DO 300 K=1,R-1
    IF(Y(K,L).GE.0.0 .AND. Y(K+1,L).GE.0.0 .AND. Y(K,L+1).GE.0.0
   +) THEN
    CALL BASIS(X,Y,K,L,X1,Y1,X2,Y2)
    CALL STRAIN(X1,Y1,X2,Y2,ST(K,L),GS,GA,AA)
    WRITE(13,*) X(K,L),Y(K,L),ST(K,L)
    ENDIF
  300 CONTINUE
  400 CONTINUE
    STOP
    END
*************************************************************************
    SUBROUTINE BASIS(A,B,I,J,X1,Y1,X2,Y2)
*************************************************************************
    IMPLICIT REAL (A-H,Q-Z)
    DIMENSION A(100,100),B(100,100)
    INTEGER I,J
    X1=A(I,J+1)-A(I,J)
    Y1=B(I,J+1)-B(I,J)
    X2=A(I+1,J)-A(I,J)
    Y2=B(I+1,J)-B(I,J)
    RETURN
    END
*************************************************************************
    SUBROUTINE STRAIN (A1,B1,A2,B2,EQS,S,DO,CA)
*************************************************************************
    IMPLICIT REAL (A-H,P-Z)
    PI=ACOS(-1.0)
```

```
      XX1=S*COS(PI*(CA)/180)
      YY1=S*SIN(PI*(CA)/180)
      XX2=S*COS(PI*(CA+DO)/180)
      YY2=S*SIN(PI*(CA+DO)/180)
      D=1.0/(XX1*YY2-XX2*YY1)
      F11=D*(YY2*A1-YY1*A2)
      F12=D*(-XX2*A1+XX1*A2)
      F21=D*(YY2*B1-YY1*B2)
      F22=D*(-XX2*B1+XX1*B2)
      C11=(F11**2.0)+(F21**2.0)
      C12=F11*F12+F21*F22
      C22=(F12**2.0)+(F22**2.0)
      GAM11=SQRT((C11+C22)/2.0+SQRT((((C11-C22)/2.0)**2.0)+(C12**2.0
     +)))
      GAM22=SQRT((C11+C22)/2.0-SQRT((((C11-C22)/2.0)**2.0)+(C12**2.0
     +)))
      E11=LOG(GAM11)
      E22=LOG(GAM22)
      EQS=SQRT((2.0/3.0)*(E11**2.0+E22**2.0))
      RETURN
      END
*************************************************************************
```

BIBLIOGRAPHY

Adams, D.F., 1970, J. Comp. Mat., 4, 310.

Alpas, A.T., Embury, J.D., Hardwick, D.A. and Springer, R.W., 1990, J. Mater. Sci. 25, 1603.

Armstrong, R., Codd, I., Douthwaite, R. and Petch, N.J., 1962, Phil. Mag., 7, 45.

Argon, A.S., Im, J. and Safoglu, R., 1975, Met. Trans., 6A, 825.

Ashby, M.F., 1992, Materials Selection in Mechanical Design, Pergamon Press, New York.

Ashby, M.F., 1993, Acta Met. et Mater., 41, 1313.

Attwood, D.G. and Hazzledine, P.M., 1976, Metallography 9, 483.

Avitzur, B., 1967, Metal Forming: Processes and Analysis, McGraw-Hill, Toronto.

Bohm, H.J., Rammerstorfer, F.G. and Weissenbek, E., 1993, Comput. Mat. Sci., 1, 177.

Bridgman, P.W., 1944, Trans. Am. Soc. Met., 32, 553.

Brown, L.M. and Clarke, D.R., 1975, Acta Metall., 23, 821.

Brockenbrough, J.R., Suresh, S. and Wienecke, H.A, 1991, Acta Met. et Mater., 39, 375.

Brown, L.M. and Stobbs, W.M., 1976, Phil. Mag., 34, 351.

Brusethaug, S. and Reiso, O., 1991, Proc. of the 12th Riso International Symposium on Materials Science, Riso National Laboratory, Roskilde, Denmark, N. Hansen et al. (eds.), 247.

Burger, G., Koken, E., Wilkinson, D.S. and Embury, J.D., 1987, Advances in Phase Transitions, Pergamon Press, Toronto, J.D. Embury and G.R. Purdy (eds.), 247.

Chawla, K.K., 1987, Composite Materials, Springer Verlag, New York.

Christman, T., Needleman, A. and Suresh, S., 1989, Acta Metall., 37, 3029.

Clyne, T.W. and Withers, P.J., 1995, An Introduction to Metal Matrix Composites, Cambridge University Press, New York.

Coffin, L. and Rogers, H., 1967, Trans. ASM, 60, 672.

Corbin, S.F., 1992, Ph.D. thesis, McMaster University.

Corbin, S.F. and Wilkinson, D.S., 1994, Acta Met. 42, 1329.

Cox, H.L., 1952, Brit. J. Appl. Phys., 3, 73.

Deschamps, A., 1994, M.Eng. thesis, McMaster University.

Drucker, D.C., 1965, High Strength Materials, J. Wiley, New York.

Embury, J.D., 1993, Proc. 3rd European Conf. on Advanced Materials and Processes (Euromat '93), Paris, France, R. Pichoir and P. Costa (eds.), 607.

Embury, J.D. and Lahaie, D., 1993, in Mechanical Properties and Deformation Behaviour of Materials Having Ultra-Fine Microstructures, Nato Series E: Applied Sciences, Vol. 233, Kluwer Academic Publishers, Boston, 287.

Eshelby, J.D., 1957, Proc. Roy. Soc., A241, 376.

Fan, Z., Tsakiropoulos, P. and Miodownik, A.P., 1994, J. of Materials Sci., 29, 141.

Gerold, V. and Haberkorn, H., 1966, Phys. Stat. Sol. 16, 675.

Gharghouri, M., 1996, Ph.D. thesis, McMaster University.

Griffith, A.A., 1920, Philos. Trans. R. Soc. London, 221A, 163.

Hall, E.O., 1951, Proc. Phys. Soc. London, 643, 747.

Hart, E.W., 1967, Acta Met. 15, 351.

Hull, D. and Bacon, D.J., 1984, Introduction to Dislocations, Pergamon Press, New York.

He, J. and Clarke, D.R., 1995, J. Am. Cer. Soc., 78, 1347.

Heymes, F., 1992, M.Eng. thesis, McMaster University.

Hill, R., 1967, The Mathematical Theory of Plasticity, Oxford University Press, Toronto.

Hung, C. and Kobayashi, S., 1992, Int. J. Mach. Tools Manufact., 32, 601.

Iosipescu, N., 1967, J. of Materials, 2, 537.

Johnson, W., Sowerby, R. and Haddow, J.B., 1970, Plane-Strain Slip-Line Fields, Edward Arnold (Publishers) Ltd., London.

Kachanov, L.M., 1986, Introduction to Continuum Damage Mechanics, Martinus Nijhoff, Dordrecht.

Kachanov, L.M., 1958, Izv. Akad. Nauk. SSR O.T.N., Tekh. Nauk, 8.

Kelly, A. and MacMillan, N.H., 1986, Strong Solids, Oxford Sci. Publications, Toronto.

Kiser, M.T., Zok, F.W. and Wilkinson, D.S., 1996, Acta Mater., 44, 3465.

Languillaume, J., Kapelski, G. and Baudelet, B., 1997, Acta Met. et Mater., 45, 1201.

Leckie, F.A., 1986, Engin. Fracture Mech., 25, 505.

Lemaitre, J. and Chaboche, J.-L., 1990, Mechanics of Solid Materials, Cambridge University Press, New York.

Lesne, P.-M., Allio, N. and Valle, R., 1995, Acta Met. et. Mater., 43, 4247.

Lesuer, D.R., Syn, C.K., Sherby, O.D., Wadsworth, J., Lewandowski, J.J. and Hunt Jr, W.H., 1996, Int. Mat. Rev., 41, 169.

Llorca, J. and Gonzalez, C., 1998, J. Mech. Phys. Solids, 46, 1.

Lloyd, D.J., 1995, private communication.

Maire, E., Wilkinson, D.S., Embury, J.D. and Fougeres, R., 1997, Acta Mater., 45, 5261.

Malzahn Kampe, J.C., Courtney, T.H. and Leng, Y., 1989, Acta Met. et Mater., 7, 1735.

Manthiram, A., Bourell, D.L. and Marcus, H.L., 1993, JOM 45, 66.

Nan, C.W. and Clarke, D.R., 1996, Acta Met. 44, 3801.

Nastasi, M., Parkin, D.M. and Gleiter, H., eds., 1993, Mechanical Properties and Deformation Behaviour of Materials Having Ultra-Fine Microstructures, Nato Series E: Applied Sciences, Vol. 233, Kluwer Academic Publishers, Boston.

Newell, J., 1990, M.Eng. thesis, McMaster University.

Nye, J.F., 1993, Physical Properties of Crystals, Clarendon Press, New York.

Onat, E.T., 1986, Engin. Fracture Mech., 25, 605.

Pederson, O.B., 1983, Acta Met. 31, 1795.

Petch, N.J., 1953, J. Iron Steel Inst. London, 173, 25.

Poole, W.J., 1993, Ph.D. thesis, McMaster University.

Poole, W.J., Embury, J.D., MacEwen, S. and Kocks, U.F., 1994, Phil. Mag,, A69, 645.

Pyrz, R., 1994, Composites Sci. and Tech., 50, 1.

Reed, J.S., 1988, Introduction to the Principles of Ceramic Processing, John Wiley and Sons, Toronto.

Reuss, A., 1929, A. Angew. Math. Mech., 9, 49.

Rice, J.R. and Tracey, D.M., 1969, J. Mech. Phys. Solids, 17, 201.

Sachs, G., 1927, Z. Angew. Math. Mech., 7, 235.

Schey, J.A., 1977, Introduction to Manufacturing Processes, McGraw-Hill, Toronto.

Semiatin, S.L. and Jonas, J.J., 1984, Formability and Workability of Metals, American Society for Metals, Metals Park.

Simmons, G. and Wang, H., 1971, Single Crystal Elastic Constants and Calculated Aggregate Properties - A Handbook, M.I.T. Press, Cambridge.

Smith, T.K., Shaw, R.W., Heathcock, C.J., Edwards, L.C., Couper, M.J. and Xia, K., 1993, Method of Making Ceramic Microspheres, U.S. patent 5,240,654.

Sowerby, R., 1985, Metal Forming and Impact Mechanics, S.R. Reid (ed.), Pergamon Press, New York.

Tao, S. and Embury, J.D., 1993, Met. Trans., 24A, 713.

Tao, S., 1991, M.Eng. thesis, McMaster University.

Taya, M. and Arsenault, R.J., 1989, Metal Matrix Composites, Pergamon Press, Toronto.

Thomason, P.F., 1969/70, Proc. Instn. Mech. Engrs., 184, 896.

Thomason, P.F., 1990, Ductile Fracture of Metals, Pergamon Press, Toronto.

Turner, G.I. and Lane, R.A., 1977, The Effect of Powder Particle Size on the Mechanical Properties of Hot Pressed P1 Beryllium, Paper I/15, in Proc. Beryllium 1977 Conf., Metals Sociey, Institution of Metallurgists and Royal Society, London.

Valiev, R.Z., Korznikov, A.V. and Mulyokov, R.R., 1993, Mat. Sci. and Eng. A168, 141.

Voigt, W., 1910, Lehrbuch der Kristallphysik, Teubner, Leipzig.

Was, G.S. and Foecke,T., 1996, Thin Solid Films, 286, 1.

Webster, D. and London, G.J., eds., 1979, Beryllium Science and Tech., Vol. 1, Plenum Publishing, New York.

Wiese, W.L., Smith, M.W. and Glennon, B.M., 1966, Atomic Transition Probabilities, Volume I, National Bureau of Standards, Washington.

Withers, P.J., Cecil, G. and Clyne, T.W., 1992, Proc. 2nd European conf. on Adv. Mats. and Processes (Euromat '91), Cambridge, U.K., T.W. Clyne and P.J. Withers (eds.), Inst. of Metals, 134.

Yip, T.-H. and Wang, Z., 1997, Mat. Sci. Tech., 13, 125.

Zok, F., 1988, Ph.D. thesis, McMaster University.